VIDEO CAMERA-BASED OVERHEAD LINE CONDITION MONITORING FOR ENHANCED ASSET MANAGEMENT

By

Mersedeh Maksabi

A thesis submitted to
The University of Birmingham
For the degree of
DOCTOR OF PHILISOPHY

School of Civil Engineering
College of Engineering and Physical Science

May 2021

UNIVERSITY OF
BIRMINGHAM

University of Birmingham Research Archive

e-theses repository

This unpublished thesis/dissertation is copyright of the author and/or third parties. The intellectual property rights of the author or third parties in respect of this work are as defined by The Copyright Designs and Patents Act 1988 or as modified by any successor legislation.

Any use made of information contained in this thesis/dissertation must be in accordance with that legislation and must be properly acknowledged. Further distribution or reproduction in any format is prohibited without the permission of the copyright holder.

Abstract

Having a direct impact on performance of the catenary-pantograph system, the reliability of the overhead contact line is crucial for continuous current collection, safe network operation, preventing delays and consequential financial losses. Contrary to condition assessment of the pantograph that can be performed off the track in rolling stock depots, condition monitoring of the contact wire comprises certain complexities and requires line closures. Although challenging, the consequences of catenary-pantograph system failure caused by bad positioning of the contact wire or its wear established a need within the railway industries for developing monitoring techniques to enable routine assessment of the distributed contact lines at the lowest disruption level. This significant need led to allocation of significant funding and deployment of inspection cars equipped with high-fidelity sensors for measurement of the parameters affecting the contact stability. The drawbacks of using sensors drawn attention towards a monitoring alternative that enables condition assessment of the asset non-invasively and through processing of video images. The most recent vision-based monitoring system aids in identifying probable anomalies within the pantograph collector strips through extraction of the contact wire stagger from the recorded data. Yet, the contact wire uplift is another key parameter affecting the contact stability and safe running of the train. As one of the predominant parameters affecting the performance of catenary-pantograph system, the focus of this thesis is on the contact wire uplift. Two vision-based monitoring approaches of trackside and on-board are considered and the feasibility of acquiring contact wire uplift parameter from the video images as well as reliance on the image data are investigated.

ای نام تو بهترین سرآغاز ...

Acknowledgements

I would like to express my appreciation to my supervisor Dr Charles Watson. It was an honour to work under his supervision. His positive outlook and confidence in my research motivated me in accomplishing the aim of the research regardless of the challenges involved for not having access to sufficient data for my experiments. I am thankful to him for his guidance, support and understanding.

I would like to extend my sincere thanks to my internal examiner Dr Stuart Hillmansen, my external examiners Prof Steven Duncan and Mr Chris O'Donnell. Having my work assessed by these gentlemen is a lifetime honour.

Many thanks to our industrial contacts Mr Brian Lee at London East ham depot and Mr Ndaba Mayo at Network Rail Sandwell and Dudley for providing me with data for my experiments as well as their valuable advice.

Special thanks to Dr Kasra Daheshpour for his support, encouragement and proof reading of this dissertation.

Finally, I want to show my love and appreciation to my family.

My father, who I sadly lost to cancer while I was writing this dissertation. He was my best friend and my greatest supporting system. I miss him so much and I hope I made him proud. My mother, for her unconditional love and for inspiring me in becoming a better version of myself. I indebted all of my achievements in life to her love, strength, guidance, support and patience. My sister Mahsa, for 33 years of sweet sisterhood and for being my strength especially after tragic loss of our father. I remain eternally grateful to her.

In memory of my beloved father, Hossein Maksabi.

I dedicate this dissertation to my wonderful mother, Irandokht Azimi.

Be a loner. That Gives you time to wonder, to search for the truth.
Have holy curiosity. Make your life worth living.

Albert Einstein (1879-1955)

Table of Contents

1. INTRODUCTION 1
   1.1 Background of the Research 1
   1.2 Aim of Research 9
   1.3 Objectives of Research 9
   1.4 Novelty of Research 10
   1.5 Structure of the Thesis 11
2. LITERATURE REVIEW 12
   2.1 Introduction 12
   2.2 Overhead Contact Line System 13
      2.2.1 OHL Failure Modes 14
         2.2.1.1 Contact Wire Wear 14
         2.2.1.2 Contact Wire Fatigue 14
         2.2.1.3 Catenary Wire Fatigue 15
         2.2.1.4 OHL Component Failures 17
   2.3 Common Incidents of OHL and Their Impact on Service Disruption 18
      2.3.1 Dewirement 18
         2.3.1.1 Deflection of the Contact Wire 18
      2.3.2 Arcing 19
         2.3.2.1 Breakage of the Wire at Insulated Overlaps 19
         2.3.2.2 Contact Wire Break Test 20
         2.3.2.3 Ways to Reduce Arc-related Deterioration 21
   2.4 Influence of Environmental Factors on Contact Line System 22
      2.4.1 Impacts of Wind 23
         2.4.1.1 Reported wind-related OLE Incidents in the UK 23
         2.4.1.2 Galloping Instabilities 24
         2.4.1.3 One Dimensional Aerodynamic Galloping 25
         2.4.1.4 Calculation of Wind Speed for Galloping 26
      2.4.2 Icing 27
         2.4.2.1 Reduction of Contact Wire Performance 28
         2.4.2.2 Divergence of Contact Wire 28
         2.4.2.3 Ice-induced Electric Arc 29
         2.4.2.4 Insulator Flash-Over 29
         2.4.2.5 Ice-induced Galloping 29
      2.4.3 Contact Wire De-icing Methods 29
         2.4.3.1 Manual de-icing 29

2.4.3.2 Chemical de-icing 30
2.4.3.3 Thermal Running 30
2.4.3.4 Resistive Wire Heating de-icing 30
2.4.4 Impact of Temperature Variation 31
2.5 Requirements for Routine Condition Monitoring of the Railway Infrastructure 31
2.5.1 Contact Wire Preventive Maintenance 32
2.5.1.1 Contact Wire Residual Thickness Calculation 32
2.5.2 Contact Wire Wear Measurement Methods 33
2.5.3 An Overview of the Developed Contact Wire Optical-based Monitoring Techniques 34
2.5.3.1 MEDES and ATON Systems 34
2.5.3.2 Japanese System 35
2.5.3.3 WWS101 35
2.5.3.4 Geocat 36
2.5.3.5 Contact Wire Thickness Measurement System 36
2.5.4 An Attempt to Predict Contact Wire Localized Wear 36
2.6 Monitoring the Quality of Current Collection 38
2.6.1 Detection and Measurement of Electric Arcs 38
2.6.2 Requirements of Interaction Between OHL and Pantographs 39
2.6.2.1 Static Contact Force 39
2.6.2.2 Mean Contact Force 40
2.6.2.3 Contact Force of the pantograph 40
2.6.2.4 Contact Force Measurement Technique 40
2.6.3 Oscillation of Contact Wire Caused by Pantograph Coupling 46
2.6.4 Contact-based Monitoring of the Contact Wire 46
2.6.5 Vision-Based Monitoring of Catenary-Pantograph System 47
2.7 Summary 49
3. METHODOLOGY 50
3.1 Introduction 50
3.2 An Ideal Overhead Contact Wire Condition Monitoring System 51
3.3 Outline of the System 53
3.4 System Approach 53
3.4.1 Digital Image Processing 54
3.4.2 Image Analysis 55
3.4.3 Analysis of the Trackside Data 57
3.4.3.1 Selection of a Suitable Thresholding Technique 57
3.4.4 Motion Detection in Static Background 60
3.4.4.1 Background Subtraction 60

3.4.4.2 Optical Flow 62
3.4.4.3 Difference Over Time 65
3.4.4.4 Point-based Analysis of the Contact Wire Height Variations 66
3.4.4.5 Measurement of the Contact Wire Static Uplift 67
3.4.5 Analysis of the On-board Data 69
3.4.5.1 Measurement of the Contact Wire Stagger via Hough Transform 72
3.4.5.2 Determining the CW Height Variation 77
3.5 Summary 88
4. VISION-BASED TRACKSIDE MEASUREMENT OF THE CONTACT WIRE DYNAMIC UPLIFT 90
4.1 Introduction 90
4.2 Measurement of the Contact Wire Uplift 91
4.3 Design of the Trackside Uplift Measuring System 92
4.3.1 System Input 92
4.3.2 Processes 92
4.3.3 System Output 93
4.3.4 Experimental Results 93
4.3.4.1 Analysis of the First Video Data 94
4.3.4.2 Analysis of the Second Video Data 96
4.3.4.3 Analysis of the Third Video Data 99
4.3.4.4 Analysis of the Fourth Video data 103
4.3.5 Investigation of the Damping Characteristics of the Contact Wire 105
4.4 Summary 109
5. TRACKSIDE MEASUREMENT OF THE CONTACT WIRE STATIC UPLIFT 110
5.1 Introduction 110
5.2 Experimental Setup 111
5.3 Data Acquisition 113
5.4 Experimental Results 113
5.4.1 First Registration Arm 113
5.4.2 First Dropper 116
5.4.3 Second Dropper 118
5.4.3.1 First Trial 118
5.4.3.2 Second Trial 120
5.4.3.3 Third Trial 121
5.4.4 Third Dropper 123
5.4.4.1 First Trial 123
5.4.4.2 Second Trial 125
5.4.4.3 Third Trial 127

5.4.5 Fourth Dropper 128
5.4.6 Fifth Dropper 130
5.4.6.1 First Trial 131
5.4.6.2 Second Trial 132
5.4.6.3 Third Trial 134
5.4.7 Second Registration Arm 135
5.4.7.1 First Trial 135
5.4.7.2 Second Trial 137
5.4.8 Investigation of the Contact Wire Stiffness Parameter 141
5.5 Summary 145
6. MEASUREMENT OF CONTACT WIRE UPLIFT USING ON-BOARD VIDEO DATA 147
6.1 Introduction 147
6.2 Current Application of the On-board Video Data 148
6.3 Monitoring of Contact Wire Height Variations 149
6.3.1 Processing of the First Video 151
6.3.1.1 Detection Results 155
6.3.1.2 Performance Evaluation 159
6.3.1.3 Contact Wire Height Variations 160
6.3.2 Processing of the Second Video 164
6.3.3 Trending Analysis of the CW Height Variations 165
6.3.3.1 First Scenario 166
6.3.3.2 Second Scenario 171
6.3.3.3 Third Scenario 176
6.4 Summary 179
7. Discussion 180
7.1 Introduction 180
7.2 Requirements for Vision-based Condition Monitoring of Contact Wire 181
7.2.1 Trackside Measurement of Dynamic Uplift 181
7.2.1.1 Segmentation of Image Data 181
7.2.1.2 Extraction of Contact Wire Motion Information 182
7.2.1.3 Ease of Use 182
7.2.1.4 Validation 183
7.2.1.5 Application 183
7.2.2 Contact Wire Height Variation Using On-board Data 185
7.2.2.1 Detection of the Pantograph from Dynamic Scene 185
7.2.2.2 Ease of Use 186
7.2.2.3 Limitations 186

7.2.2.4 Application 186
7.3 Summary 187
8. Conclusion 189
8.1 Accomplished work 189
8.1.1 Trackside 189
8.1.2 On-board 189
8.1.3 Conclusions 190
8.1.3.1 Trackside 190
8.1.3.2 On-board 190
8.1.4 Findings 191
8.1.5 Remaining Problems 193
8.2 Recommendations for Future Work 194
9. References 196

Table of Figures

Figure 2-1 Components of overhead contact line system (Kiessling, et al., 2002) 13
Figure 2-2 : a) Crack initiations in the contact wire surface; b) micrographic section of the contact wire: specks due to electrical arcs; c) micrographic section of the contact wire: surface defects due to friction (Masset, et al., 2011) 15
Figure 2-3 Catenary cable cross-section (Efanov, et al., 2016) 16
Figure 2-4: Broken strand due to aeolian vibration after removal of suspension clamp (Lilien, 2013) 16
Figure 2-5:Time history of current, voltage and tension of the contact wire (Wada, et al., 2019) 20
Figure 2-6: Appearance of the broken contact wires (Wada, et al., 2019) 21
Figure 2-7: Network Rail route-based regions (Network Rail, 2015) 24
Figure 2-8: CW worn cross section (Stickland, 2003) 25
Figure 2-9: Icing of the contact wire (Heyun, et al., 2012) 27
Figure 2-10:Contact wire manual de-icing operation (Heyun, et al., 2012) 30
Figure 2-11 Contact wire cross-section (Borromeo & Aparicio, 2002) 33
Figure 2-12:Force equilibrium in a pantograph (Koyama, et al., 2014) 40
Figure 2-13: The details of the inner force (Koyama, et al., 2014) 41
Figure 2-14: Contact wire condition and contact force waveform (Kusumi, et al., 2006) 42
Figure 2-15: Overlap structure with greater contact force (Kusumi, et al., 2006) 44
Figure 2-16: Overlap structure with normal contact force (Kusumi, et al., 2006) 44
Figure 3-1: Research Methodology 53
Figure 3-2: Intensity values of a small area of the image 54
Figure 3-3: Histogram of the trackside image data 58
Figure 3-4: Aperture problem 64
Figure 3-5: Schematic of the apparatus 68
Figure 3-6: Contact wire dynamic behaviour a) sliding view of the contact b) contact wire zig zag motion 69
Figure 3-7: Edge detection operation a) true-colour image b) input grey scale image c) output edge image d) output edge image (figure by author) 71
Figure 3-8: Hough transform, a) Line space, b) Hough space (Aydin, et al., 2014) 72
Figure 3-9: Detection of the contact wire via Hough transform. a) Input edge image, b) Line representation in Hough space, c) Detected contact wire (figure by author) 73
Figure 3-10: Detection results (figure by author) 74
Figure 3-11: Trajectory of the contact wire lateral movement on working range of the pantograph (figure by author) 75
Figure 3-12: False detection of the contact wire (figure by author) 76
Figure 3-13: Detection of the contact wire and upper side of the collector strip 77
Figure 3-14: Haar rectangular features (Guennouni, et al., 2015) 80
Figure 3-15: Discriminant features of the pantograph (figure by author) 81
Figure 3-16 Integral image sum 84
Figure 3-17 Integral image block 85
Figure 3-18:Cascade Classifier (Viola & Jones, 2001) 86

Figure 3-19: Trajectory of the pantograph, video length 29.39 seconds, bbox info at first frame [233,226,201,44] centroid [333.50,288], bbox info at last frame[252,233,172,37] centroid [338,251.50] (Figure by author) 87
Figure 4-1: Contact wire free oscillations under service condition 94
Figure 4-2: Contact wire oscillation a) CW oscillation in millimetre b) CW oscillation at different monitoring points, offset=56.645 95
Figure 4-3: CW oscillations caused by the passage of two pantographs 96
Figure 4-4: Position of the pantographs from the selected monitoring point at the moments of maximum uplift 97
Figure 4-5: CW upper side vibrations, offset = 122.92mm 98
Figure 4-6: CW Oscillations due to running of the two pantograph 100
Figure 4-7: Upper side oscillation of the CW, offset = 120.71 mm 100
Figure 4-8: CW response at the two monitoring points, offset1=120.24mm, offset2=117.81 102
Figure 4-9: Contact wire oscillations caused by running of the pantograph 104
Figure 4-10: CW upper side oscillations, offset = 259 mm 104
Figure 4-11: Single degree of freedom system (Stickland, 2003) 105
Figure 4-12: Vibration (Stickland, 2003) 106
Figure 4-13: the decaying amplitude of the CW vibration 107
Figure 4-14: Demonstration of the selected peaks for the calculation of the CW damping parameter 108
Figure 5-1: The static uplift measuring device in use (Location: Long Marston) 111
Figure 5-2: Schematic of a class two lever 112
Figure 5-3: Uplift data (location: first registration arm) 114
Figure 5-4: CW response characteristics at the first registration arm 115
Figure 5-5: Variability of the recorded uplift at the first registration arm 115
Figure 5-6: Uplift data (location: first dropper) 116
Figure 5-7: CW response characteristics at the first dropper 117
Figure 5-8: Variability of the recorded uplift at the first dropper 117
Figure 5-9: Uplift data (location: second dropper) 118
Figure 5-10: CW response characteristics at the second dropper 119
Figure 5-11: Variability of the recorded uplift at the second dropper 119
Figure 5-12: CW response characteristics at the second dropper 120
Figure 5-13: Variability of the recorded uplift at the second dropper 121
Figure 5-14: CW response characteristics at the second dropper 122
Figure 5-15: Variability of the recorded uplift at the second dropper 122
Figure 5-16: Uplift data (location: third dropper) 123
Figure 5-17: CW response characteristics at the third dropper 124
Figure 5-18: Variability of the recorded uplift at the third dropper 124
Figure 5-19: CW response characteristics at the third dropper 125
Figure 5-20: Variability of the recorded uplift at the third dropper 126
Figure 5-21: CW response characteristics at the third dropper 127
Figure 5-22: Variability of the recorded uplift at the third dropper 127
Figure 5-23: Uplift data (location: fourth dropper) 128
Figure 5-24: CW response characteristics at the fourth dropper 129
Figure 5-25: Variability of the recorded uplift at the fourth dropper 129

Figure 5-26: Uplift data (location: fifth dropper) 130
Figure 5-27: CW response characteristics at the fifth dropper 131
Figure 5-28: Variability of the recorded uplift at the fifth dropper 131
Figure 5-29: CW response characteristics at the fifth dropper 132
Figure 5-30: Variability of the recorded uplift at the fifth dropper 133
Figure 5-31: CW response characteristics at the fifth dropper 134
Figure 5-32: Variability of the recorded uplift at the fifth dropper 134
Figure 5-33: Uplift data (location: second registration arm) 135
Figure 5-34: CW response characteristics at the second registration arm 136
Figure 5-35: Variability of the recorded uplift at the second registration arm 136
Figure 5-36: CW response characteristics at the second registration arm 137
Figure 5-37: Variability of the recorded uplift at the second registration arm 138
Figure 5-38: Recorded Uplift at each test location 139
Figure 5-39: Static uplift of the contact wire under each load along the selected span 139
Figure 5-40: Recorded Uplift at each test location 140
Figure 5-41: CW Stiffness at the first registration arm 141
Figure 5-42: CW stiffness at the first dropper 142
Figure 5-43: CW stiffness at the second dropper 142
Figure 5-44: CW stiffness at the third dropper 143
Figure 5-45: CW stiffness at the fourth dropper 143
Figure 5-46: CW stiffness at the fifth dropper 144
Figure 5-47: CW stiffness at the second registration arm 144
Figure 5-48: CW vertical stiffness along the span 145
Figure 6-1: Breakage of the pantograph and its detachment from the train 148
Figure 6-2: System Processes 150
Figure 6-3: Pantograph Height Trajectory(8stages of training at 0.5 FAR) 152
Figure 6-4: Pantograph Height Trajectory (12 stages of training at 0.5FAR 153
Figure 6-5: Pantograph Height Trajectory (20 stages of training at 0.2FAR) 154
Figure 6-6: Performance evaluation on open-route equipment 155
Figure 6-7: Performance evaluation on open-route equipment 156
Figure 6-8: Performance evaluation at the first structure,(a) missing track due to the low contrast 157
Figure 6-9: Performance evaluation at the second structure, (a) missing track due to brightness severity 157
Figure 6-10: Performance evaluation at the third structure 158
Figure 6-11: Performance evaluation at the fourth structure 158
Figure 6-12: Detection challenges in poor and severe brightness level at the bridges 159
Figure 6-13: Measurement of the conversion coefficient 160
Figure 6-14: Pantograph Height Variations (mm), calib=0.4683 160
Figure 6-15: Image mapping technique 161
Figure 6-16: CW height variations considering movement of each pixel in reality 162
Figure 6-17: Calculation of the conversion factor 163
Figure 6-18: Estimation of the CW height variations 163
Figure 6-19: Performance evaluation of the system and its sensitivity to deviation of the pantograph 164

Figure 6-20: Estimation of the CW height variation from detected locations of the pantograph (89% estimated accuracy based on detection results in 1000 output frames).....165
Figure 6-21: Selected data for trending analysis of the CW uplift 166
Figure 6-22: CW uplift over a single span.....167
Figure 6-23: Variations of mean of uplift over time.....168
Figure 6-24: Prediction of the CW reliability 170
Figure 6-25: Trending analysis of the CW uplift over the full catenary length.....172
Figure 6-26: Difference graph of the CW uplift 173
Figure 6-27:Difference graph of the CW uplift 173
Figure 6-28: Difference graph of the CW uplift 174
Figure 6-29:Difference graph of the CW uplift 174
Figure 6-30: Difference graph of the CW uplift 175
Figure 6-31: Trending analysis of the CW uplift over the full catenary length.....176
Figure 6-32: Difference graph of the CW uplift 177
Figure 6-33: Difference graph of the CW uplift 177
Figure 6-34: Difference graph of the CW uplift 178
Figure 6-35: Trending analysis of the CW uplift.....178
Figure 7-1: Prototype of the trackside uplift measurement system 183

Table of Tables

Table 3-1: Identification of the potential stakeholders and their expectations according to the drawbacks of the conventional condition monitoring method.....52
Table 4-1: Calculated maximum uplift over the colour and the grey channels 98
Table 4-2: Measurement of the CW maximum uplift.....99
Table 4-3: Measurement of the Maximum Uplift at the moment of contact 101
Table 4-4: The computed uplift corresponding to each channel.....101
Table 4-5: Maximum uplifts at two monitoring points.....103
Table 4-6: Measurements of the CW uplift 105
Table 6-1: System Performance.....160

Chapter One

1. INTRODUCTION

1.1 Background of the Research

The British Railway has experienced an evolutionary history since the days of steam locomotives in the 19th century until today, the glory era of the electric trains. British railway as one of the most extensive railway networks in Europe is contributing to over 1.5 billion journeys per annum. Rail transport with 2% of carbon dioxide emissions associated with it, is a more environmentally friendly mode of transportation compared to road transport. Besides, allocation of Low Carbon Transport Innovation Strategy (LCTIS) announced in the Energy Review in summer 2006, shows the government desire for further reduction of emission-related climate change caused by rail transportation (Department for Transport, 2007). In the last seventeen years, there was an increase of approximately 100% in number of passenger journey. Whereas, this number is 60% for freight journey. This figure will be doubled for the passenger journey and reach to 140% for freight journey within the next thirty years (Network Rail, 2014). Modernisation of the UK railway network mainly began with installation of 25000V AC Overhead Line equipment (OHL) over the West Coast Main Line from Euston to the North West in the 1960s-1970s. Despite inevitable technical (i.e. alterations to tunnels with arched profiles and insufficient clearance) and legal restrictions (i.e. necessary amendments to OHL design and wires configurations) in the installation of the OHL, electrification of the UK's railway lines has been having a significant growth. Followed by Network Rail announcement in 2014, over two-thousand miles of tracks are to be put under high-voltage overhead wires by 2021 through Network Rail's £4bn national electrification programme (NetworkRail, 2014).

Standing substantial competition with other modes of transportation has made railway stakeholders to heavily invest on modernisation of their products and emerging innovative solutions for effective asset management. With the growing demand for rail transportation, condition-based and predictive maintenance turned to main concern for network operators. This emphasises the necessity for routine condition monitoring of the railway infrastructure, which is fundamental in implementing prognostics and health management solutions (Brahimi, et al., 2017).

As one of the main system that assures operability of railway infrastrucre, the OHL is aimed to provide an uninterrupted power supply to trains through coupling with the pantograph. With a designed life cycle of over 30 years, the OHL system has high availability. Yet the failure of the OHL can be catastrophic. The cause of OHL failure is usually a fault, damage or a bad-fitting of a component. Most OHL failures cause line closure. Seriousness of the fault, scale of breakage (mostly to the wires) and time of fault identification create different levels of disruption to rail traffic. For instance, the consequences of slackening or breakage of droppers vary from higher amount of uplift to serious damages to the pantograph and OHL structures. Despite customers' dissatisfaction, service-affecting asset failures make network and train operators as well as stakeholders liable to pay tremendous amount of money as delay compensation each year. Therefore, reduction of such events is a big concern for the railway industry (NetworkRail, 2017).

OHL fault occurrence can be mitigated by an effective asset management strategy through planning a suitable maintenance and renewal regime. Furthermore, installation and upgrading of OHL equipment require contemplation of their level of use in accordance with their operational life. Maintenance policies of OHL are based on preventive maintenance and involve planned inspections of the components that are highly disruptive to rail traffic (Brahimi, et al., 2017).

The main component of OHL is the contact wire that transmits the electric current along its length and supplies it to the train engine through the interaction with the pantograph. To assure continues power transmission to the vehicle engine, the contact wire should withstand the mechanical stresses and wear. The design of the contact wire should facilitate the connection with the dropper and registration arm. Despite the expected high conductivity from the component, the contact wire cross-section must be kept as small as possible to keep its weight down.

The contact wire material selection is a balancing of the mechanical and electrical requirements. Accordingly, the selected material must have high conductivity, tensile strength and anti-corrosion properties. Copper is an excellent conductor and has a good performance under different temperature. Alloy additives such as tin, silver and cadmium are added to copper to boost the mechanical performance which can sacrifice the conductivity to a greater or lesser extent (Dearman, 2019).

Performance of the contact wire can be evaluated through measurement of its three parameters of wear, height and stagger. Exposure to environment and frequent contact with the pantograph accelerates wear of the contact wire. As the traffic increases, the wear of the contact wire and the localised wear at hard spots increase. Accordingly, the probability of faults occurring increases at lines with higher amount of traffic and speed (Ahmed, 2017). Apart from the wear, bad positioning of the contact wire as result of substandard equipment installation or extreme weather condition affect the performance of the component and put safe running of the vehicle in danger. Excessive stagger and sag of the contact wire result in operation of the contact components (the contact wire and the pantograph) beyond their performance envelope. This leads to the pantograph dewirement that causes serious damages to OHL equipment and the train. For this reason, infrastructure managers schedule regular inspections to measure the stagger and height of the contact wire that considering the structural (i.e. slenderness) and operational (energisation level and height) features of the component involves certain challenges (NetworkRail, 2017). Because of the complexity in scheduling the inspection programme, most OHL are only assessed every 4-6 years. Even then, a high percentage of the lines remain uninspected (Dearman, 2019).

Wear mechanism of the contact wire is due to the combination of three physical phenomena listed below (Bucca & Collina, 2015):

- Electrical contribution to wear as a result of current flow at the moment of interaction with the pantograph and power dissipation that involves wear of both contact surfaces (the contact wire sliding surface and the pantograph graphite). Collector strips material, voltage and current levels affect this contribution.
- Mechanical contribution to wear as a result of friction and shocks at the moment of contact. Condition of the contact surfaces, tensioning of the contact wire, hardness of the collector strips, contact force of the pantograph, train speed and weather conditions affect this contribution.

- Electrical arcs caused by contact loss that leads to power dissipation and results in electrical erosion and fusion on both the contact surfaces. The root causal of the pantograph arcing is attributable to unexpected vibrations between the contact components caused by climate condition and geometry singularity (Wu, et al., 2016).

Wear estimation of the contact wire can be done through calculating its residual thickness. The threshold for renewal of the contact wire is set at 80%. This is the ratio between the original section and the worn area of the wire (Borromeo & Aparicio, 2002).

The contact wire useful operational lifecycle is generally between 25 to 30 years. This figure mostly depends on line speed, number of pantograph passages and type of tensioning (i.e. auto or fixed). Due to lack of reliable monitoring technique for condition assessment of the contact wire, the asset renewal operation is yet to become condition-based. The renewal cycles are usually between 35-40 years that considering the cost of the operation and high disruption level to rail traffic is not ideal (Dearman, 2019). The contact wire overhaul is the most expensive cost of the OHL maintenance budget (Brahimi, et al., 2017).

Identification of the wire, degree of wear and its wear rate aids in establishing an asset replacement plan as well as formulation of a wear control index to gauge the wire and see how close the component is from breakage (Shing & Pascoschi, 2006).

Complexities of working on high voltage contact lines at meters above the ground and limitations of manual inspection make optical-based measurement systems more desirable candidates for condition monitoring of the contact wire. These systems are designed upon two measurement disciplines of calculation of the wire thickness and width of the sliding surface (Borromeo, et al., 2003). The advantage of measuring the width of the contact wire sliding surface over measurement of its thickness is the ability of assessing more than one wire simultaneously. However, the main drawbacks of measuring the width of the sliding surface is its dependency to reflexive properties of the sliding surface that results in measurement errors. The advantage of measuring the contact wire thickness is its low cost and simplicity. Apart from being limited to measurement of one wire only, thickness measurement systems have limited measurement range (horizontal limitations of $\pm 250\ mm$), limited measurement speed (~ 5 km/h) and requires modification of the pantograph (installation of optoelectronic detector to the panhead).

MEDES, ATON, Shimada's systems and WWS are some of the developed optical-based system that determine the width of the wire wearing track. The measurement basis in MEDES

and ATON systems is through illumination of the contact surface of the wire using laser diodes, image capturing with CCD cameras and analysis of the images through parallel processing. The difference between these two systems is mainly the utilised type of optics. In Shimada's system, the laser beam hits the wire sliding surface and part of the emitted beam will be captured by a photoelectric transfer element that is then used to measure the reflection return time. Although the measurement basis in Shimada's system is more straightforward compare to other systems, its large size and requirement for installation on trains rooftop have limited its application. WWS enables contact-less measurement of degree of wear of up to ten contact wires simultaneously. This system calculates the residual thickness of the wire from width of its sliding surface using two cameras as well as an independent lighting unit that extend operability of the system to overnight monitoring, inside tunnels and under bridges. According to the system manufacturer (Fraunhofer IPM), high measurement frequency and fast data processing make WWS suitable for speeds of up to 350 km/h. Additionally, WWS is part of the multi-sensor system CIS (Contact Wire Inspection System) and its low-speed variant CIS-LS that record contact wire wear and position simultaneously (Reiterer & Olshausen, 2021). The drawback of WWS is its image processing system that leads to erroneous calculation of wear in case of sudden slope changes (for example: presence of portal frame or mast) in captured images.

With a direct impact on current collection, wear of the contact surfaces and noise reduction, maintaining a uniform contact between the contact wire and the pantograph improves the railway performance. Assuring uniformity of contact at high speed is a challenging task since the likelihood of contact-loss increases at high speeds (Ahmed, 2017).

Mechanically, the pantograph and the OHL are two separate dynamic systems acting as a spring-mass-damper system (Keenor, 2016) The OHL and pantograph interacting with each other by contact force acting on collector strip of the pantograph. This, to some extent, leads to examining the performance of two systems as a paired system (NetworkRail, 2017).

Contact force of the pantograph creates a vertical displacement on the contact wire, known as uplift. As the train moves, this uplift creates a wave in the contact wire. When the train speed reaches the wave propagation speed pantograph loses contact. To assure contact stability, OHL designers set the tensioning of the wire in a manner to maintain the wave speed lower than the train speed (Keenor, 2016). Apart from moving along the contact wire, the resultant force caused by pantograph coupling spreads across the collector strip from sideways through

staggered alignment of the contact wire (Dahlberg, 2007). The stagger or zig-zag movement of the contact wire above the track is allowed by attaching pull-off arms to the supporting structures. This leads to uniform wear of the collector strip graphite.

Depending on the contact wire elasticity and its wear degree, an excessive contact force creates higher level of dynamic excitation within the contact wire. This causes the wire to lift beyond the permitted range. Such condition can disturb the pantograph operation since it creates a supplementary acceleration that affects the contact stability and in severe cases lead to dewirement (Papi, et al., 2001).

The elasticity of the OHL is a key parameter when evaluating the performance of the catenary-pantograph system, which is measured as the amount of uplift per unit contact force (Keenor, 2016). For a better performance, ideally, the elasticity should be uniform throughout the span. However, in reality it changes along the span and is of lesser value at or near the OLE structures comparing to midspan. The OLE designers match the elasticity differential within the system according to performance requirements. For instance, for highspeed lines a lower elasticity differential is required. Pre-sag of the contact wire is often used to compensate the elasticity variations at the midspan (Cho, et al., 2010). Thereby, the uplift of the contact wire at midspan can be kept within the same range as at the supports. Another solution to compensate the contact wire stiffness variations is to use stitch wires.

Although the catenary-pantograph system is aimed to provide an uninterrupted current flow for trains operations, due to the oscillations of the contact wire and pantograph the contact force can sometimes be irregular. The following are the factors contributing to irregularity of the contact force (Dahlberg, 2007):

- Large amount of current drawn from a short section of the contact wire when starting the vehicle. The resultant heating is damaging to the wire and creates weak spots.
- Irregular vertical stiffness of the contact wire caused by droppers and sagging of the contact wire in between them.
- Irregular mass distribution along the contact wire. This is mostly induced by droppers and their clamps, which cause vibrations of the contact components. The attachment of clamps and registration arm to the contact wire reduce its elasticity and lead to hard spots. Each hard spot reflects part of the wave towards the train. Excessive hard spots cause contact-loss.

- Variations of height, stiffness and mass distribution of the contact wire at overlaps sections.

Contact force irregularities have known consequences. Too small contact force increases the likelihood of electromagnetic disturbances as results of arcing. When the contact force is too large, the contact wire uplift exceeds the planned range, its wear increases due to friction and in extreme cases it also might be torn down (Keenor, 2016).

The contact force of the pantograph is mainly the product of inner, inertia and aerodynamic forces. Measurement of the contact force at high speed is challenging. The main reason for this is having no practical approach for measuring the aerodynamic force whilst its interacting with the contact wire (Kusumi, et al., 2006). Low-speed test runs are the adopted strategy by the industry to measure the contact force of the pantograph. Such measurement practice involves installations of force sensors (for example: strain gauge load cells) to the pantograph. Within the industry, the low-speed test runs are usually conducted when commissioning a new OHL and testing of new or recently maintained pantographs. Contact-based monitoring techniques are subject to certain drawbacks. For instance, the measurements are performed under high current, temperature and vibration levels. Monitoring under such conditions not only is damaging to expensive measuring gadgets, it also lead to uncertainties within measurements. According to this existing gap, a substantial benefit can be gained from a non-contact vision-based monitoring system that enables measurement of the contact force from uplift of the contact wire at the moment of interaction with the pantograph. Considering the contribution of the aerodynamic force acting on the pantograph, the application of vision-based system in estimation of the contact force remains limited to low-speed test runs.

The traditional approach to measure the uplift and stagger of the contact wire is by conducting static tests and use of displacement transducers to determine the vertical and lateral movement of the wire at predefined locations. Such measurements are directly influenced by the tensioning of the contact wire. Furthermore, measurement of the contact wire dynamic lifting requires consideration of static positioning of the wire and impacts of local topology on its movement. Apart from limitations and high disruption levels, static measurements of the contact wire dynamic response are prone to errors that are often non-quantifiable (Stickland & Scanlon, 2001).

Despite the drawbacks of contact-based measurement techniques, limitations of manual inspections and lack of a reliable contactless technique, majority of existing monitoring

systems currently used by rail industries are contact-based. At the moment, Network Rail is performing condition assessment of the OHL infrastructure by a Mobile Maintenance Train (MMT). MMT is equipped with multiple sensors attached to the pantograph. The sensors take measurements from pantograph height, pantograph acceleration, dynamic forces, dynamic uplift and stagger. Another system utilised by Network Rail is an optical-based wear monitoring system (similar to WWS). The system is installed on the rooftop of one of Network Rail test coaches. This system propagates rows of white spotlights on the contact wire and captures images from the sliding surface. The images are then transferred to a control computer via optical fibre for further processing to identify the scale of any wear or crack within the wire.

The consequences of service disruptions caused by catenary-pantograph system failure led to installation of video cameras on trains rooftop. A common practice adopted by Network Rail and train operating companies (TOCs) to monitor the performance of the catenary-pantograph system is to watch the recorded videos. Due to size of the data and lack of suitable processing system, majority of the data are erased after a short period of time without being assessed. The videos are usually used as evidences to identify cause(s) for the system failure and to find liable party to pay for damages.

The reliability of the image data in condition assessment of the pantograph and contact wire have attracted researchers' attention, which resulted in development of several vision-based monitoring systems. Despite the direct impact of contact wire performance on the contact stability, applications of the majority of the monitoring systems are limited to condition assessment of the pantograph. To this date, most innovative vision-based monitoring approach suggested enables detection of the collector strip anomalies through extraction of the contact wire stagger from footages recorded by on-board line scan camera (Aydin, et al., 2014).

Uplift of the contact wire is one of the most important parameters both in evaluating condition of the contact wire and performance of the catenary-pantograph system. Contact force of the pantograph, train speed, type of tensioning and deformity of the contact wire are the main factors affecting the contact wire uplift (Keenor, 2016).

As the wire undergoes structural deformity, the reduction of its cross-section affects its stability against external forces and results in high amplitude oscillations. Thus, it is rational to monitor the deterioration of the contact wire by analysing its vibrational behaviours under similar excitation condition. To this end the conventional approach to measure the uplift is by attaching displacement transducers, which increase the dynamic excitation of the contact wire and leads

to measurement errors. The significant impact of the uplift parameter on the reliability of OHL and lack of contactless monitoring system for its measurement at lowest disruption to rail traffic are the incentives for proposing this research project.

The thesis addresses the following hypothesis:

Is it feasible to develop a vision-based monitoring system for measurement of the contact wire dynamic uplift without attaching markers/measuring gadget to OHL structures or the pantograph?

If so, what would be the reliance level on the acquired data from the images?

1.2 Aim of Research

This research investigates the possibility of extracting the contact wire height variations from the video data. The aim is to propose a monitoring approach that enables more routine assessment of the contact wire condition through measuring its uplift. Two vision-based monitoring approaches of trackside and on-board are considered. The feasibility of extracting the contact wire height variations through processing of the footages recorded by trackside and on-board cameras are examined. The monitoring systems are required to generate variations of the contact wire dynamic height through an automated procedure and in near real-time.

1.3 Objectives of Research

To achieve the aim, the objectives of this research project are determined as follow:

1. Carry out comprehensive literature review to identify the main OHL system components, their failure modes and vulnerability of the contact wire against external factors affecting its performance.
2. Identification of the knowledge gap and demand potential for monitoring approaches under consideration through perusing the developed condition monitoring techniques along with their pros and cons.
3. Propose a feasible methodology that enables extraction of the contact wire motion information from trackside videos.
4. Use suitable image processing techniques and develop a vision-based monitoring system that enables measurement of the contact wire dynamic uplift in near real-time.
5. Examine the reliability of the image data in determining the contact wire uplift.
6. Identify a feasible methodology that enables recognition and detection of the pantograph from background objects in the on-board videos.

7. Achieve contact wire height variations with respect to pantograph location.
8. Use the data from processing of on-board video and suggest a framework that enables monitoring of the contact wire degradation process through trending analysis of its uplift.

1.4 Novelty of Research

Despite the important function of the contact wire uplift in performance evaluation of the catenary-pantograph system as well as on the condition assessment of the asset itself, there has not been any contactless solution introduced for its measurement. This research proposes two new vision-based approaches to address this existing gap non-invasively and through processing of the video images.

The proposed trackside vision-based system uses the recorded observations from vertical movement of the contact wire and determines the dynamic uplift at a certain location of the line. The system allows assessment of the contact wire condition based on its uplift, frequency of oscillation and damping ratio. Compared to the conventional trackside monitoring techniques currently in use within the industry, the proposed system enables measurement of the contact wire uplift in its active state using an automated contactless procedure and in near real-time.

The effectiveness of vision-based monitoring systems depends on the reliance level on the image data and the utilised image processing technique. The reliability of the approach is evaluated by performing a static uplift test on the contact wire. To perform the static test, a new mechanical tool is designed. The designed tool enables measurement of contact wire static uplift in response to a range of known forces. The precision of the proposed vision-based trackside measurement system is evaluated by comparing the obtained results after processing of the trackside footages with the uplift data recorded by the apparatus.

The second proposed vision-based monitoring system determines the contact wire height variations along the entire catenary length through frame-by-frame detection of the pantograph from the on-board video data. This system is aimed to enable condition assessment of the contact wire through trending analysis of its uplift over time. The suggested on-board monitoring approach determines the contact wire height with respect to the location of the pantograph at each video frame. Although the high computational complexity involve in the processing of the video data will not allow real-time processing of the data, the processing time is reasonably fast.

1.5 Structure of the Thesis

This chapter discussed the importance of contact stability on the catenary-pantograph system performance. The impact of the uplift parameter on the contact stability and the parameters causing variations of contact wire uplift were explained. The complexities involved with the condition monitoring of the overhead contact lines and drawbacks of contact-based monitoring techniques were discussed. Through highlighting the parameters affecting the contact stability and knowledge gap in measurement of such parameters the motivation for proposing this research project was outlined.

The following is the outline of the subsequent chapters of this thesis:

- In Chapter Two, the main components of the OHL system, common OHL-related incidents and factors affecting the contact stability along with the solutions to avoid/mitigate them are discussed. The chapter introduces methods for evaluating the performance of the catenary-pantograph system and discusses the developed techniques for measurements of the contact wire parameters.
- Chapter Three establishes a feasible methodology to achieve the research aim. The chapter discusses the utilised image processing techniques for extraction of the uplift parameter through categorising the video data according to their background features.
- Trackside monitoring system designed to deliver the contact wire uplift under service condition is presented in Chapter Four
- Trackside measurement of the contact wire static uplift to examine the reliability of the image data along with the developed image processing technique in determining variations of uplift is presented in Chapter Five.
- On-board monitoring system designed to deliver the contact wire height variations over the entire catenary length is presented in Chapter Six.
- Chapter Seven discusses the usefulness and limitations of the suggested condition monitoring approaches.
- Chapter Eight is the conclusion of the research and recommendations for further work.

Chapter Two

2. LITERATURE REVIEW

2.1 Introduction

Under the pressure to improve the efficiency of railway operations at high speeds, network operators and TOCs have significantly contributed towards assuring continuality and high quality of current collection. This needs both the pantograph and contact wire to be free of imperfection (Forrest, et al., 2010). The contact wire structural and operational features complicate carrying routine maintenance inspections and restrict engineers in using measuring devices to effectively monitor the contact wire condition at low disruption levels to rail traffic (NetworkRail, 2017). Although challenging, early detection of defects within the contact wire is a must as it improves the level of preparedness of network operators to identify and avoid the probable defects before turning into service disrupting failures. This chapter defines the main components of the overhead contact line system, assesses the common overhead contact line incidents, and reviews solutions to prevent or mitigate the occurrence of such incidents. The definition of wear in the contact wire is described and the developed condition monitoring techniques along with their competency in measuring the contact wire parameters are evaluated.

2.2 Overhead Contact Line System

The Overhead Contact line System (OCS) contains an overhead contact line, cantilevers, poles, foundations as well as conductor wires to supply current for use by electric trains (NetworkRail, 2015).

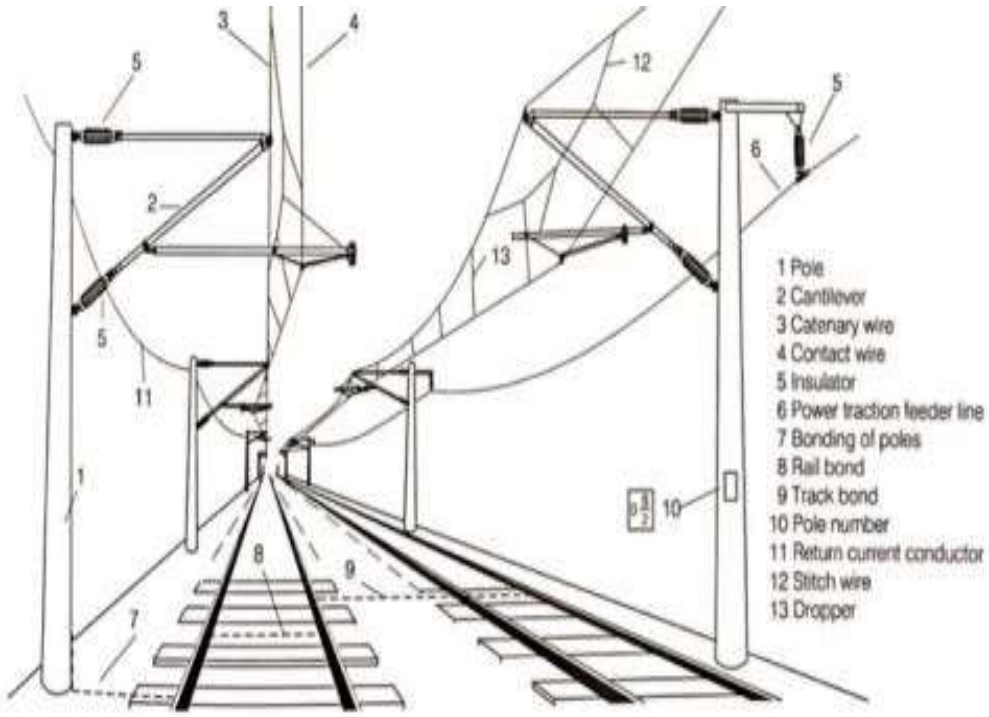


Figure 2-1 Components of overhead contact line system (Kiessling, et al., 2002)

The main components of the overhead contact line system are described as follow:

- *Contact wire* is the pre-tensioned wire through which pantograph collector strip travels. The primary purpose of the contact wire is to act as a contact slide ensuring continuous transmission of electrical energy to the pantograph (Kiessling, et al., 2002). The contact wire should withstand the mechanical stress caused by its tension, environmental conditions and trains passage (Keenor, 2016). For an even wear of the collector strips, the contact wire is aligned at alternating angles against the track axis in a zigzag arrangement.
- *Catenary wire* is the longitudinal wire that supports the contact wire from above.
- *Droppers* are the wires located at regular intervals and suspended from the catenary and connected to the contact wire to support the contact wire.
- *Stitched wire* compensates for changes in the contact wire height caused by varying temperatures and equalises the elasticity at the supports and midspan.

- *Cantilever* is a horizontal structure that supports catenary projecting from a single mast on one side of the track.
- *Fixed terminations* secure the contact and catenary wires to poles.
- *Tensioning devices* tension the contact and catenary wires at either ends to maintain good contact with the pantograph by keeping the contact wire as still as possible at all times and conditions. There are two tensioning mechanisms known as conventional and spring tensioning mechanisms. The conventional tensioning mechanism, also known as cast-iron balance weight, is highly prone to mechanical problems and vandalism that causes service disruptions (NetworkRail, 2015). The spring tensioning mechanism is a new generation of tensioning devices in which two springs are allocated for each wire at each end that are attached to frames spanning the line above the track.

2.2.1 OHL Failure Modes

Diagnosing the OHL system failure is challenging since in majority of cases information regarding the damage and failure of the system is obtained through manual inspections and maintenance practices. Investigation of the OHL failures led to specification of two major controlling issues. One is the magnitude of the lifting force by the pantograph on the contact wire and the other is the cyclic application of lifting forces that causes fatigue cracking failure (Shing & Wong, 2008).

2.2.1.1 Contact Wire Wear

Interaction with the pantograph and lateral movement of the contact wire across the collector strip produce wear within both the contact wire and the pantograph. This is proportional to the imposed load by the pantograph (Beagles, et al., 2016). As the system operates at higher contact force than it was originally designed for, the severity of wear of the contact wire changes from mild to severe. Lower contact force prevents the severe wear within the wire, however, it might cause contact-loss that produces an electrical arc (refer to Section 2.3.2). Electrical arcs increase the temperature of the contact wire and cause melting and vaporisation of the wire. If neglected, overtime the rate of wear increase and adversely affects the contact stability (Gonzalez, et al., 2008).

2.2.1.2 Contact Wire Fatigue

The cyclical loading causes contact wire fatigue, especially at location where there is a change in the wire gradient. The contact wire fatigue has a major impact on the contact wire uplift and therefore on contact stability. Detecting contact wire fatigue is not simple. Monitoring of the contact wire fatigue process requires quantification of the stress cycle present in the line.

According to Masset, et al. (2011) the risk of contact wire fatigue failure increases due to the following causes:

- Overloaded traffic
- The increase of applied tensile load to the contact wire at high-speeds
- Existence of bending waves within the loading cycle before and after passage of the pantograph due to low catenary damping
- Crack initiation and defects in the contact wire surface caused by pantograph friction, electrical arc and corrosion

Figure 2-2 demonstrates cracks initiation and defects in the contact wire surface caused by electrical arcs and pantograph friction.

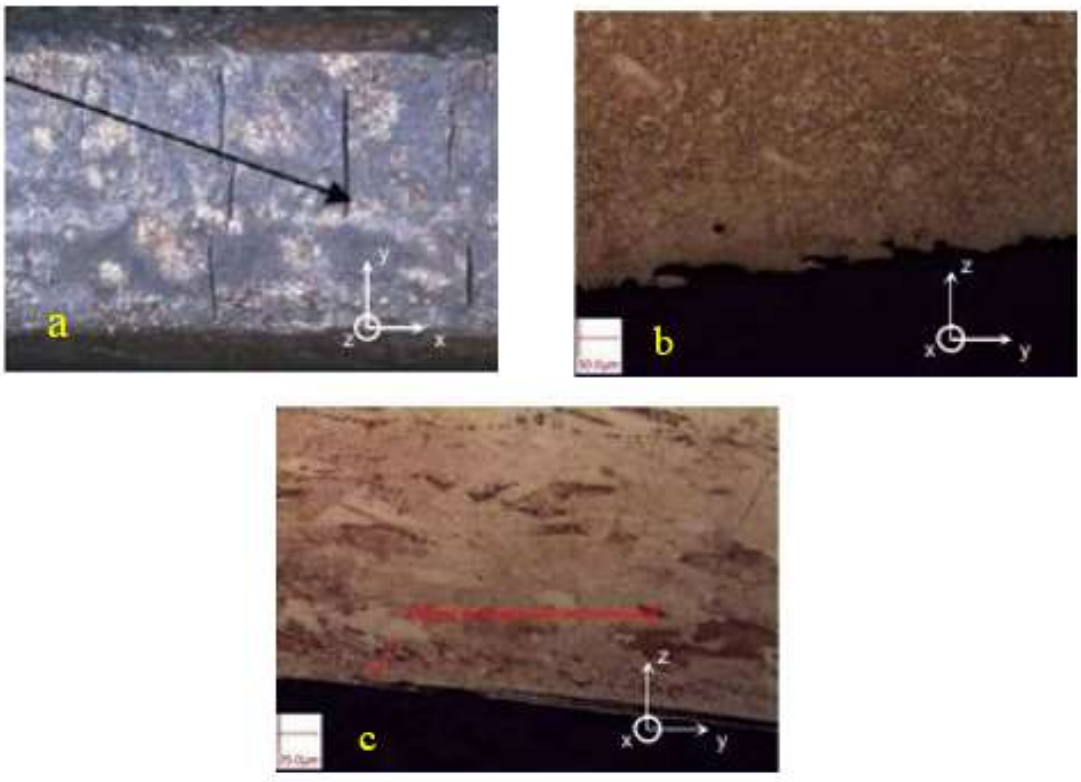


Figure 2-2 : a) Crack initiations in the contact wire surface; b) micrographic section of the contact wire: specks due to electrical arcs; c) micrographic section of the contact wire: surface defects due to friction (Masset, et al., 2011)

2.2.1.3 Catenary Wire Fatigue

Regardless of low likelihood of occurring, one of the probable incidents during train operation is breakage of the messenger wires. Despite having anticorrosion properties, the catenary wire is formed by nineteen layers of strands (see Figure 2-3) and constitutes a high mechanical

strength. If the wire cross-section reduces by more than 15%, it requires insertion or installation of new branch of wires (Efanov, 2016).

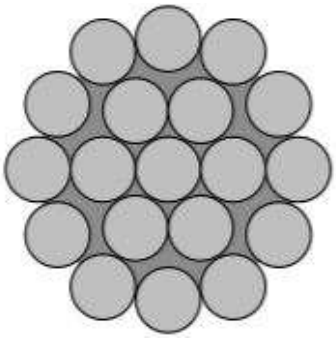


Figure 2-3 Catenary cable cross-section (Efanov, et al., 2016)

One of the reported failure events on the West Coast Main Line and East Anglia arose due to wear and fatigue of the catenary wires at locations where the wires pass over the pulley wheels. Although the pulley wheel enables longitudinal movement of the catenary wire as the wire heats up or cools down, they cause wear and initiate cracks within the catenary wire which eventually lead to the component failure (Taylor, 2013).



Figure 2-4: Broken strand due to aeolian vibration after removal of suspension clamp (Lilien, 2013)

Braided cables are often used that reduce the eddy losses in the catenary wire. Despite extensive application, braided wires are also subject to fatigue (Beagles, et al., 2016). This is due to the fretting formation between different layers of strands and their movements by different degrees as the wire bends. Overtime the fretting between different layers of strands at their contact area initiates and spreads cracks that leads to failure of cables (Lilien, 2013). As more number of strands break, the catenary wire load-bearing cross-section decreases. Therefore, there will be

higher tensile stress in the remaining strands which causes breakage of the catenary wire (Beagles, et al., 2016).

The located internal strands between the central and outer layers are subject to maximum load influence during train operations (see Figure 2-3). Sharp impact action directed along the cable axis occurs at the time of catenary wire layer breakage. To record such events, Efanov, et al., (2016) proposed a vibration-based monitoring technique with requirement to connect diagnostic gadgets to predefined control spots on the catenary wire. The diagnostic gadget is formed by an accelerometer, a temperature sensor, a radio module and a built-in controller. Six gadgets were allocated to monitor the catenary wire over a single span and distanced about one meter from the pulley wheels and on the middle of the anchorage. Once data are obtained and processed, the monitoring results will be transmitted to the data hubs of the line stations through a radio-frequency channel at a certain designated frequency. Notwithstanding the advantage of finding the deviations of the catenary wire from its standard condition, the disadvantages of the developed continuous monitoring system are as follow:

- Installation of measurement tools to overhead catenary cables
- High energy consumption for devices to exit from 'sleep' mode
- Longer time of connection to be set between the devices when operating in 'sleep' mode
- Network typologies related restrictions
- Not considering the critical effects such as fault of the pantograph and its impact on catenary wire condition and on system performance.

2.2.1.4 OHL Component Failures

Failure of other overhead contact line components can as well lead to serious consequences. As an example, when a dropper breaks, its broken part clamped to the contact wire will be unsupported from above and can hang below the contact wire. As the pantograph passes, the broken dropper tangles around and damages the pantograph (Beagles, et al., 2016). Such an incident not only imposes significant delays in the train services, the deviation of the pantograph from its position can also cause serious damages to the overhead line equipment. Breakage of the dropper clamps can also result in a higher amount of uplift and affect the contact stability.

2.3 Common Incidents of OHL and Their Impact on Service Disruption

2.3.1 Dewirement

One of the incidents that electrified railways continuously suffer from is dewirement. Dewirement happens when the contact wire and pantograph interaction exceeds their performance envelope (Keen, 1998). Dewirement incidents damage the overhead line components and in severe cases lead to service disruption. The UK's railway network experiences over ten dewirement incidents per annum. Each incident imposes significant average costs of £1m in the forms of penalties and liability to pay for the required maintenance or renewal of damaged equipment (Ricardo-Rail, 2017). The cause of dewirement can be driven by complex set of elemental conditions such as; anomalies within both contact wire and pantograph, local topographic, meteorological conditions and train speed (Evans, et al., 1990). Though, comprehensive solutions for the problem of dewirement are yet to be found. As today, the best solution offered is to put in place a set of control units to record measurements of parameters affecting the contact stability. To detect common elemental conditions causing dewirement, a monitoring system is used. The system collects data from control units. The data is processed to provide the probability of dewirement and is feeded to train control centres. Therefore, in cases of any high probabilities of dewirement occurrence suitable actions can be taken within control centres. The main causes of the dewirement are attributable to failure of the pantograph. In severe cases where there is an imminent risk of dewirement due to pantograph being faulty, the train is stopped by the responsible network control centre. In such cases actions taken are withdrawing it from service, lowering the faulty pantograph or switching the pantographs (Ricardo-Rail, 2017)

2.3.1.1 Deflection of the Contact Wire

As the speed increases, the impact of the sideway push from the pantograph uplift force on dynamic deflection of the contact wire increases. The level of increase depends on the following factors:

- Shape of the pantograph head
- Contact force of the pantograph, its uplift and tilt
- Tension of the contact wire, and
- Train speed

2.3.2 Arcing

As the contact between contact wire and pantograph becomes lost, the current continues to flow to the contact strip through a luminous electric discharge known as arc. Kinks and electrical welding are two conditions that increase the probability of arc occurrence. The uniformity of contact between the contact wire and pantograph is significantly affected by kinks (contact wire height variations) where at high speeds might lead to contact-loss.

Defective sliding contact creates a condition known as 'electrical welding'. Wear of the contact wire and pantograph collector strip create roughness on contact surface. This leads to irregularly in current distribution and collection. Under such conditions two phenomenon of hot spots and micro welding might happen. As the speed increases the welded spots start to break causing further deterioration of the contact wire. Wear of the contact wire results in continues sparking as it interact with the pantograph and progresses wear of the collector strip (Bruno, et al., 2001). Aydin, et al, (2014) categorised the main reasons of arcing as follow:

- Incorrect static contact force
- Incorrectly set aerodynamics
- Wear of contact surfaces
- Excess friction, and
- Poor geometric adjustment

When arc occurs at the certain spot of the contact wire, at that spot, the contact wire repeatedly heats up, softens, stretches by tension and becomes necked. The necked area of the contact wire cannot withstand the tension and as a result contact wire breaks (Wada, et al., 2019).

2.3.2.1 Breakage of the Wire at Insulated Overlaps

As the train approaches the insulated overlap, the pantograph riding the entering contact wire of the first power section suddenly transitions onto the parallel contact wires of the two power sections bridging the section. As the train passes through the overlap section, the entering contact wire rises, and pantograph begins to ride only on the second contact wire breaking contact with the first power section (White, et al., 2017). The breakage of the contact wire at insulated overlaps has become a big rail transport disorder. The main reason of the wire breakage at overlap sections is high number of arc incidents due to frequent stopping of the train at these locations (Wada, et al., 2019).

2.3.2.2 Contact Wire Break Test

Wada, et al., (2019) conducted a break test on the contact wire focusing on arc. The experiments were carried out under 30A to 300A arc current and tensions of 9.8 kN and 19.6 kN. The aim was to measure the relationship between the arc current, tension of the contact wire and necking length of the contact wire. The break test was performed on a new wire, which was pulled by a spring type tensioning device. The contact strip was fixed to an actuator with moving stage operating capability to move the contact strip vertically. A voltage of 35V to 40V was applied and a current of 55A to 405A was flown while changing the circuit resistance. To generate the arc, the contact strip was lowered at speed of 0.5 mm/s to break contact with the contact wire. The range of maximum gap between the two contact surfaces was set at 0.6 mm to 2 mm. As the contact strip was descending, it is possible that the arc moves to the direction of the contact wire axis. To prevent this, the contact strip was tilted towards and adjusted to make point contact with the sliding surface of the wire. A chromel-alumel thermocouple was also taped to the gripped surface of the wire to measure its temperature.

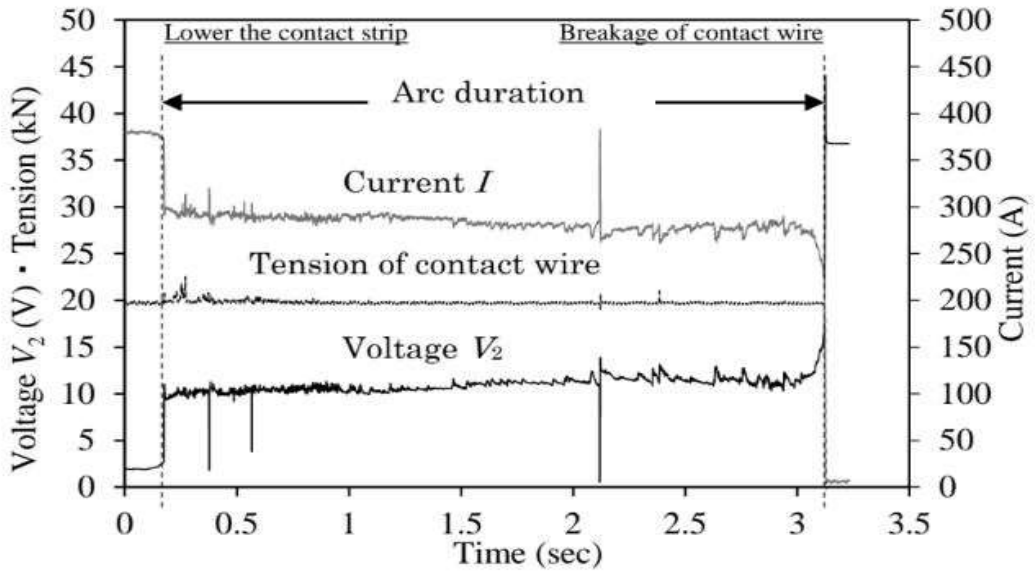


Figure 2-5:Time history of current, voltage and tension of the contact wire (Wada, et al., 2019)

As can be seen from Figure 2-5, the contact strip was lowered at 0.2 seconds, when, the arc happened between the two contact surfaces. At the same time, voltage drops occurred at the electrodes at both ends of the arc that increases the inter-electrodes voltage V_2 to 9V and decreases the circuit current to about 300A. Under such condition, contact wire broke at 3.1 seconds. The arc duration was calculated from the moment voltage V_2 exceeds 9V to the time

when the tension drops. The arc current and arc voltage were calculated as average values over the arc duration time.

Figure 2-6 shows the broken contact wire under the tension of 9.8 kN. As it can be seen from the figure, the tip of the breakage point is softened due to heat caused by the arc and necking length of the wire is stretched by the applied tension. From the appearance of the broken wires it was clear that the necking length decreases under large arc current condition. From the measured contact wire temperature distribution, it was concluded that, under lower current and longer arcing duration, the temperature of the contact wire increases over a wider range and so is the necking length of the contact wire.

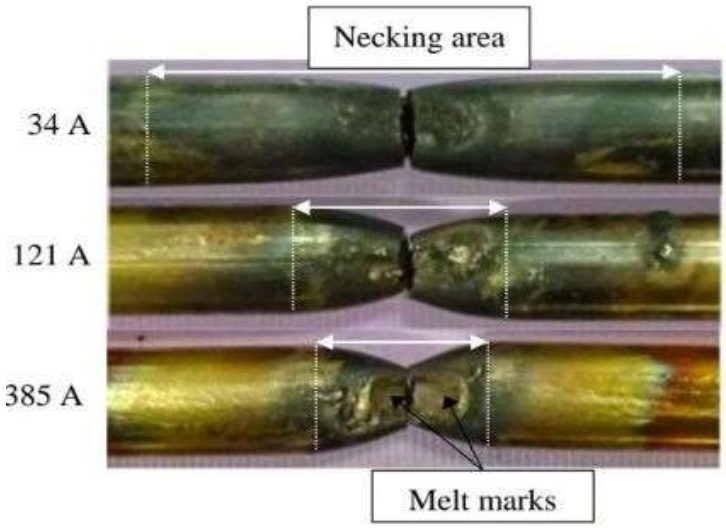


Figure 2-6: Appearance of the broken contact wires (Wada, et al., 2019)

2.3.2.3 Ways to Reduce Arc-related Deterioration

Bruno, et al., (2001) listed solutions to reduce arc-related deterioration within the contact surfaces. The followings are brief descriptions of the proposed solutions together with their possible drawbacks:

- Increase the uplift contact force. Such a solution shortens both collector strip and contact wire lifetime due to erosive and abrasive wear.
- Pantograph head mass reduction. Transmission of the high current confines such reduction.
- New design and modification of the overhead system. This solution can alleviate the problem, but it is too expensive to be implemented.

- Use of suitable monitoring technique to assess the status of the sliding contact between the pantograph and contact wire.
- To distribute the necessary current for the train operation between several pantographs. Such a practice reduces problems occurring due to high density current collected from a single pantograph. Italian Railways have tested this solution for the first time by placing two pantographs at both ends of a high speed train. The outcome of the trial shown reduction of the quality of the contact as the second pantograph interacts with the contact wire. This can be due to excitation level that contact wire experiences after passage of the first pantograph.

2.4 Influence of Environmental Factors on Contact Line System

Apart from the electrical and mechanical loads as results of electric currents and the lifting force of the pantograph, the contact line system is affected by environmental conditions. Parameters such as ambient temperature, wind velocity and ice accretion can affect the stability of the contact line system (NetworkRail, 2015). Thus, it is crucial that the components of the contact line system be reliable to withstand electrically and mechanically tolerate such external impacts. To maintain the performance of the catenary-pantograph system at acceptable level and control the impact of weather conditions, vulnerability of the OLE under different climate conditions have to be assessed. Network Rail has developed an evidence-based strategy to perform a detailed national assessment on OLE vulnerability through analysis of failures caused by climate conditions (Cox, 2015). For this reason, Network Rail uses Fault Management System (FMS). This system contains failure and maintenance reports of every asset including OLEs. In case of any faults the responsible user opens a new form and imports any information obtained regarding the incident and assigns a unique number to the report. With the asset number, the user can use the system to identify the geographical location of assets with GPS. Accordingly, using the system weather grid data can be mapped and relevant climate information can be imported to the report.

Such practice creates a database which includes both weather information and fault description. Therefore, using expert knowledge the influence of weather conditions on the relevant event/ incident can be investigated. The FMS can contain the following climate information (Cox, 2015):

- Wind (mph-daily mean max wind speed, hourly/daily maximum gust)

- Snowfall (mm-3 hourly)
- Temperature (°C-daily minimum/maximum, diurnal range)
- Precipitation (mm-3 hourly, daily total, 15-days total)

2.4.1 Impacts of Wind

Wind pressure may cause lateral deflection of the contact wire that in severe cases leads to pantograph dewiring. The problem of wind-induced dewirement was considered in modern OLE designs through assessing the local wind speed (known as OLE design wind speed). This was according to site-specific factors and by limiting the span length to control the maximum lateral deflection from centre of the track (Baker, et al., 2019). Excessive lateral deviation of the contact wire from the pantograph centre causes further displacement of the wire in response to the lifting force of the pantograph. As a result, the pantograph freely rises without restraint that is a damaging condition to the OLE and to the train. Deflection of the supporting structures, track and OLE tolerances are other causes of contact wire lateral deflection.

2.4.1.1 Reported wind-related OLE Incidents in the UK

The UK's railway network is classified into a route-based system which specifies ten regions demonstrated in Figure 2-7. Analyses of Britain weather data and the occurred OLE incidents between 1st April 2006 to 31st March 2015 proved that, wind-related OLE incidents were the most frequent. It was found that (Cox, 2015):

- Incidents of OLE increase, when wind gust is faster than 50 mph. As the wind speed is lower than the OLE designed wind resistance, it was more likely to be caused by vegetation and debris.
- Higher sensitivity to wind was observed for Scotland, LNE, and LNW (North & South). This could be due to the combination of long-stretches of OLE and high tree density.
- Reported OLE incidents as a result of tree fall due to storm and high speed winds which severely affected train services at LNW (both North and South), LNE and Anglia.

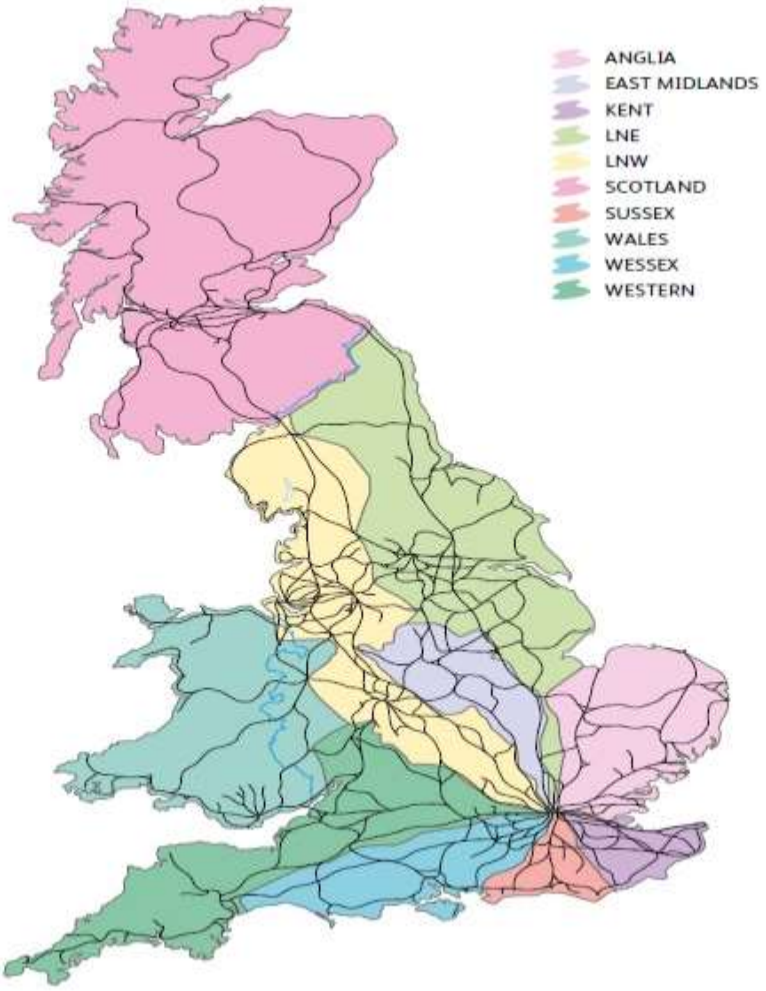


Figure 2-7: Network Rail route-based regions (Network Rail, 2015)

2.4.1.2 Galloping Instabilities

As the wire moves in the wind, its motion damps by both mechanical damping due to its support, self-weight and tension; and aerodynamic damping due to motion-induced aerodynamic velocities and forces. In contact wires with asymmetric cross-section about one or more axes, wind-induced displacement can cause galloping (Stickland & Scanlon, 2001). Galloping is created by the unsteady wind forces caused by structural deformity of the contact wire, which generates asymmetric lift and drag forces that leads to undamped oscillations. Negative aerodynamic damping with sufficient amplitude reduces the overall damping of the wire and leads to high amplitude oscillations. Apart from asymmetrical cross-section, the contact wire might undergo galloping oscillations due to progression of inevitable wear at its bottom section caused by contact with the pantograph and temporarily change of its cross-section shape by ice accretion in winter time (Baker, et al., 2019). Figure 2-8 shows the cross-sectional deformity of the contact wire.

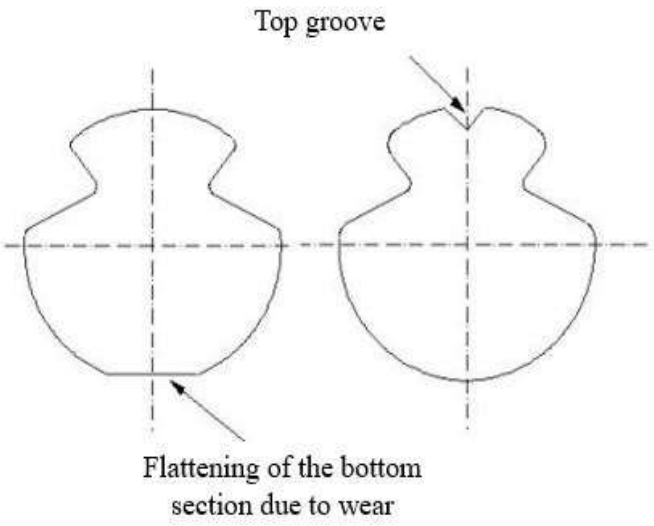


Figure 2-8: CW worn cross section (Stickland, 2003)

Sachs, (1987) introduced wind breaks and shelter belts as solutions for galloping instability. Physical constraints at locations with more reported galloping instability such as embankments made the construction of shelter belts impractical. Stickland & Scanlon, (2001) suggested modification to the contact wire profile. This was later on endorsed by Stickland, (2003) to be impractical. Stickland, (2003) suggested that the generation of additional mechanical damping forces within the OHL system increases the wind speed at which galloping happens.

2.4.1.3 One Dimensional Aerodynamic Galloping

Large amplitude oscillations of the contact wire at the moment of the contact and its oscillation prior to contact initiation can lead to dewirement. The aerodynamics of galloping instability is described by Stickland, (2003) through the formation of a one-dimensional equation of motion for this instability.

$$m[\ddot{y} + 2\zeta\omega\dot{y} + \omega^2 y] = -\frac{1}{2}\rho UB\left(\frac{dC_L}{d\alpha} + C_D\right)\dot{y} \qquad (2.1)$$

The right hand side term of Equation 2.1 determines the aerodynamic contribution to the overall damping of the system. The net damping coefficient of the system is achievable through rearranging of Equation 2.1 as follow:

$$2m\zeta\omega + \frac{1}{2}\rho UB\left(\frac{dC_L}{d\alpha} + C_D\right) = d \qquad (2.2)$$

The parameters of Equation 2.2 are:

m mass per unit length

ζ damping ratio

ω natural frequency

ρ density

U wind speed

B diameter of the contact wire

C_L lift coefficient

C_D drag coefficient

α angle of attack

d damping coefficient

The damping coefficients of a stable and unstable contact wire are of positive and negative values respectively. The mechanical damping ratio of the contact wire is usually positive, and the component will not gallop unless the below criterion is met:

$$\left(\frac{dC_L}{d\alpha} + C_D\right) < 0 \qquad (2.3)$$

According to Equation 2.3 also known as Glauert-Den Hartog criterion, when the mass and damping ratio of the contact wire are small, under sufficiently high wind speed, the wire develops galloping Stickland, (2003). The Glauert-Den Hartog criterion for the contact wire is determined through wind tunnel measurements. The outcomes of the carried wind tunnel tests shown the tendency of the contact wire to gallop at the lower angle of incidence as its wear increases.

2.4.1.4 Calculation of Wind Speed for Galloping

To calculate wind speed at or above which galloping occurs, Equation 2.2 is rearranged as follows:

$$U = \frac{d - 2m\zeta\omega}{\frac{1}{2}\rho B\left(\frac{dC_L}{d\alpha} + C_D\right)} \qquad (2.4)$$

As mentioned in Section 2.4.1.3, negative damping coefficient results in galloping. Thereby, if the value of d in Equation 2.4 is set to zero, the calculated U value determines the wind speed above which galloping occurs. Due to unavailability of a right measuring instrument in determining the damping ratio of the contact wire, Stickland (2003) assumed a reasonable damping value to calculate the wind speed. The carried experimental work has shown that at a right angle of attack, the component exhibit galloping in wind speeds as low as 19 mph.

In order to measure the contact wire damping ratio Stickland, (2003) recorded the displacement of the contact wire using a potentiometric displacement transducer with a range of 0 to 1 m. The utilised potentiometers were powered by 10v laboratory power supply, generating the

voltage output of 0v for 0 displacement and 10v for 1m displacement. The generated signals from the transducer were fed to a digital data recorder through the designated channel and then transmitted to a PC based data acquisition system for analysis. This set up was tested on a section of the UK East Coast Main Line that was known to gallop at around 40 mph wind speeds. After analysis of the contact wire dynamic response, recorded under moderate wind, the natural frequency and the contact wire damping ratio were measured as 1.4 Hz and 0.05.

Apart from complexities in contact-based measuring of the contact wire damping, there are known weaknesses in recording of contact wire response using displacement transducers. For example, the effect of draw string potentiometers on measurement of damping and frictional damping as the wire feeds in and out of the transducer housing. Quantification of the magnitude of these effect is not possible. Therefore, the calculated damping ratio by Stickland (2003) included the contribution of these effects.

2.4.2 Icing

In countries with cold climate conditions, the effect of ice accretion has numerously damaged the supporting structure and destroyed the overhead contact wires (Heyun, et al., 2012). Atmospheric icing significantly affects the overall design and safe running of the contact lines. The added burden of ice creates an intermediate layer that interferes with the contact between the contact wire and pantograph. This increases the aerodynamic interaction and triggers the wire to move beyond the permitted range (ADS, et al., 2016). Figure 2-9 shows ice accretion on the contact wire.

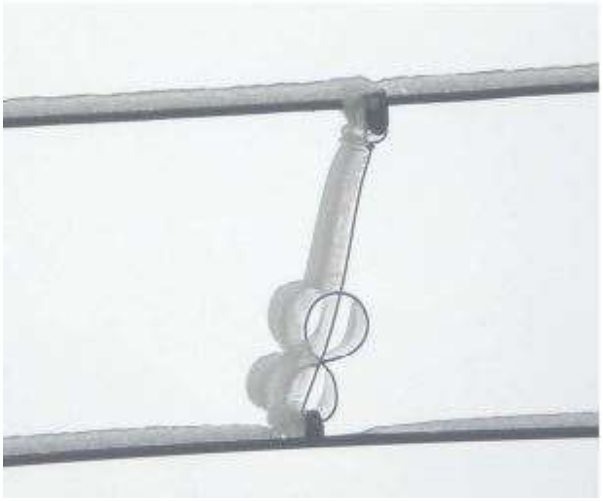


Figure 2-9: Icing of the contact wire (Heyun, et al., 2012)

The contact wire has many bearing points and is distributed through the span length (< 65 metres) often with an interval from 8 m to 12 m to support it from above. Thereby, unlike high-voltage transmission wires with longer span lengths of up to 500 m that twist when icing and wave in the wind, the contact wire does not twist or wave under icing conditions. Another consequence of cold climate condition is freezing of the moisture layer that exists between the contact surface and pantograph. This makes maintaining of the sliding contact between the two components difficult (Aydin, et al., 2014). Heyun, et al., (2012) classified the major hazards of contact line icing into five categories as:

- Reduction of contact wire performance
- Divergence of contact wire
- Ice induced electric arc
- Insulator flash-over
- Ice induced galloping

2.4.2.1 Reduction of Contact Wire Performance

The contact wire performance has two meanings of higher smooth and higher kilter. The former happens when the actual distance between the contact wire and the orbits plane is smaller than the distance of the ideal parallel state. The latter occurs when the wire is flat and straight, and pantograph can pass through it without any hurdles (Heyun, et al., 2012).

The ice load imposes additional weight to the contact wire. This increases the tension and can lead to breakage of the dropper clamp, deformation of the mid-anchor clamp and damage the swivel clip holder. Icicles formation at the bottom of the suspension clamp can increase the contact wire elasticity variation, weakens the performance of the contact wire and results in higher vertical contact force. When icicles form at the bottom of the contact wire running of the collector strip across the wire can cause severe wear on contact wire surface. This leads to volatility in collecting current and sparking. Such an event can damage the train.

2.4.2.2 Divergence of Contact Wire

The contact wire cross-section changes as it goes through icing and affects its aerodynamic characteristics. Existence of ice load under wind might diverge the contact wire. If the divergence exceeds the performance envelope (i.e. 480 ± 10 mm) it breaks contact with the collector strip. This affects the quality of current collection and increases the rate of wear progression within both contact surfaces.

2.4.2.3 Ice-induced Electric Arc

Electric arc is another consequence of icing, caused by the contact wire conductivity reduction due to its coverage by ice. In severe icing conditions the contact between the contact wire and collector strip might become lost. The thick layer of ice interferes with the contact between the contact wire and collector strip and no current flows. Such condition affects the train operation and cause service cancellations.

2.4.2.4 Insulator Flash-Over

Ice accretion on trains roof surface insulators mainly deposits on the upwind side (Heyun, et al., 2012). In general, the ice is 5-10 mm thick. However, at high speeds the maximum ice thickness can reach to more than 30 mm. As the train pulls in, the accumulated ice melts due to created heat. The contaminated medium in the ice forms a conductor causing short circuits and flashovers that not only damages the electrical equipment, but also affects the normal transport.

2.4.2.5 Ice-induced Galloping

Section 2.4.1.2 dealt with galloping and its effect on performance of the contact wire. Regardless of the rare likelihood of happening, ice-induced galloping can have hazardous consequences, such as:

- Breakage of positive feeder cable
- Breakage of cantilever insulators
- Breakage of dropper clamp
- Deformation of mid-anchor clamp
- Breakage of the steady-arm

2.4.3 Contact Wire De-icing Methods

There are four contact wire de-icing and anti-icing methods that are described in the following sections.

2.4.3.1 Manual de-icing

The most primitive yet time-consuming and unsafe de-icing operation is the manual de-icing. This is either performed by human or machines (Heyun, et al., 2012). Harsh environmental conditions bring much difficulties in manually removing the ice from the overhead contact wire. Regardless, this method has been repeatedly used by many domestic railways. Figure 2-10 shows manual de-icing operation on the contact wire.



Figure 2-10:Contact wire manual de-icing operation (Heyun, et al., 2012)

2.4.3.2 Chemical de-icing

To prevent icing, one way is to reduce the water freezing point by applying de-icing agents. The most common de-icier used for such application is calcium chloride (CaCl). The first attempt of coating the contact wire with antifreeze agents was by the Railroad Car Company in Germany. Despite occasional application on contact wires, chemical de-icing has been more frequently carried on airports and highways. The scale of environmental contamination due to spreading of the chemicals after each chemical de-icing activity should be contemplated in advance.

2.4.3.3 Thermal Running

Contact wire thermal running is another solution to melt the ice from the contact wire. The thickness of ice around the contact wire will be visually examined by a relevant engineer, who will notify the control centre when the ice thickness is close or passed the warning level. To remove the ice, the electric current has to flow through the contact wire while the collector strip is in idle mode and keeps touching the contact wire.

2.4.3.4 Resistive Wire Heating de-icing

A de-icing system of overhead contact line is developed in Japan. It comprises a built-in wire with insulation resistance characteristics. Once the power is on and current flows to the device power plate the power plate connects to the resistive wire. The created heating in the resistive wire heats the contact wire and melts its ice. Performance level of this de-icing method varies depending on weather conditions, ice thickness, melting current and melting time.

2.4.4 Impact of Temperature Variation

Expansion and contraction of the contact wire under influence of inclement weather condition can seriously affect its height and safe running of the train. Depending on the age of the contact wire, increase in temperatures (at/above 32℃) causes the wire to sag and in some cases to collapse completely. Under extremely cold weather condition contact wire might hog. These changes in profile affect the system dynamic, which enforces speed restrictions, causing service cancellations and hours of delays within the trains operation. The contact lines with fixed termination are more vulnerable against temperature deviations. Considering the potential disruption level to train operations caused by sag and hog of the contact wire, it is necessary to ensure the tension of the wire is kept constant (Keenor, 2016). Use of auto-tensioning mechanism (see Section 2.2) for lines prone to sagging increases the contact wire stability since the tension of the wire will be unaffected by the temperature variations.

2.5 Requirements for Routine Condition Monitoring of the Railway Infrastructure

The railway infrastructure is a complex multi-disciplinary engineering system involving track substructure, OHL, railway crossings and so forth. The interactions amongst components of railway infrastructure creates a situation where performance of a components correlates with the condition of other components. To avoid the effect of poor behaving component on others routinely monitoring of components must be undertaken. Owing to high complexity of railway engineering structures, the idea of developing highly intelligent continuous monitoring system and its enhancement through advanced diagnostic software is not yet feasible (Efanov, 2016). Accordingly, railway engineers paid more attention to routinely monitor each individual component of railway infrastructure.

According to Lykov, et al., (2012) more than 75% of railway overhead line incidents are caused by either failure of the overhead line equipment or pantograph. Routinely monitoring of the overhead contact lines allows detection of emerging defects within the contact line elements before they lead to the assets failures. This can significantly mitigate risk of service disruption (Lykov, et al., 2012).

Measurement methods are developed to examine the performance of catenary-pantograph system. Accordingly, three aspects of monitoring are classified (Kiessling, et al., 2009):

- Monitoring of the contact wire alone
- Monitoring of the pantograph alone

- Monitoring of the mechanical contact between the contact wire and pantograph

2.5.1 Contact Wire Preventive Maintenance

A considerable portion of the total maintenance expenditures in railways belongs to overhead line maintenance. If maintenance is not planned, irregular maintenance and replacement intervals requires line blockage which interfere with train services (Lykov, et al., 2012). Therefore, preventive maintenance of OHL is essential in effectively managing and maintaining the system reliability as set in standards. In order to monitor the performance of the contact wire condition of the high-current wire at meters above the ground should be assessed. This together with required access possessions to perform maintenance highlights the high demand of railway industries such as Network Rail to automatically detect probable defects within the wire under service conditions.

Increase of wear on the contact wire reduces contact stability. This results in higher amount of uplift under service conditions. There is a strong link between the line traffic and contact wire degradation. Increase in traffic and speed, increase wear. As a result, localised wear at hard spots and occurrence of faults becomes more probable.

Other factors contributing to the progression of contact wire wear are (NetworkRail, 2012):

- Contact force of the pantograph
- Type of alloy used for fabrication of the contact wore
- Collector strip material, and
- Traction current being drawn by the trains

2.5.1.1 Contact Wire Residual Thickness Calculation

In general, contact wires have a circular cross-section with two slightly opened longitudinally grooves that are formed above the horizontal centreline. Such geometry facilitates attachment of the dropper connections and registration connections at the cantilevers. Monitoring of the contact wire residual thickness helps in extending the contact wire lifetime and enables early detections and corrections of probable deterioration within the contact wire. Calculation of the contact wire residual thickness determines the degree of wear within the wire. Figure 2-11 is a schematic of the cross-sections of a new and a worn wire.

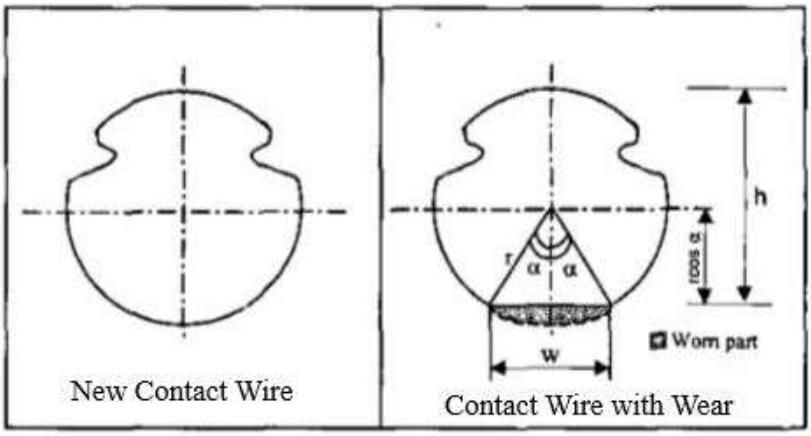


Figure 2-11 Contact wire cross-section (Borromeo & Aparicio, 2002)

Borromeo & Aparicio, (2002) calculated the residual thickness of the contact wire in the right-hand-side image of Figure 2-11 as follows:

Assuming r is the radius of the contact wire cross-section, the residual thickness h is calculated as follows:

$$h = r + r.cos\alpha = r.(1 + cos\alpha) \tag{2.5}$$

$$\alpha = arcsin\left(\frac{w/2}{r}\right) \tag{2.6}$$

According to Equation 2.5 and 2.6, h is obtained from the width of worn track w through:

$$h = r.\left[1 + cos\left(arcsin\frac{w}{2 \cdot r}\right)\right] \tag{2.7}$$

considering the worn section of the wire with central angle of 2α, the relationship between the worn section A and width of the track developing wear w, is:

$$A = r^2 \cdot arcsin\frac{w}{2 \cdot r} - \frac{r}{2} \cdot \sqrt{r^2 - \left(\frac{w}{2}\right)^2} \tag{2.8}$$

2.5.2 Contact Wire Wear Measurement Methods

The traditional contact wire wear measurement method is performed manually by personnel working from trackside and the platform of the ladder coaches. Apart from reliability of the measured data, manually performed measurements require un-powering of the contact lines and this is highly disruptive. Such a measurement method cannot be performed regularly due to access restrictions and monitoring challenges at locations such as tunnels, bridges, stations and so forth. More specifically, manual measurement is limited to sections with higher likelihood of wire defects which are found from historical data. The disadvantageous of manual measurement technique highlight the demand for automatic alternatives.

Various contactless measurement techniques are developed and amongst them, the optical-based measurement methods have been the most successful. Majority of the operative condition monitoring systems and those under development are optical-based that are designed by considering the following criteria (Borromeo & Aparicio, 2002):

- Number of contact wire in the measurement range. As an example, there are four wires in the overlap section and the system should monitor them at the same time.
- Measurement must be performed at train speed, which means the system should enable processing and archiving of acquired data in real time.
- The variations of the contact wire height must be considered.
- Contact wire lateral displacement must be taken into account.
- The system should operate at day and night and under different weather conditions.

2.5.3 An Overview of the Developed Contact Wire Optical-based Monitoring Techniques

Contact wire wear can be analysed by monitoring of the contact wire wearing track or calculating the wire residual thickness. The benefit of measuring the width of the wire sliding surface than calculating its thickness is the ability to measure the double wire systems. Additionally, modifications of the pantograph (for example, installation of photoelectric devices) is not required. The followings (Sections 2.5.3.1 to 2.5.3.5) are descriptions of some of the developed optical-based contact wire wear monitoring systems.

2.5.3.1 MEDES and ATON Systems

MEDES and ATON systems enable measurement of the width of the wearing track through illumination of the wire contact surface by laser diodes and capturing of the reflected image with CCD cameras. MEDES system is operative in laboratory coaches used by RENFE (National Network of Spanish Railways) and SNCF (French National Railway Company). Measuring coaches of the Dutch Railways are equipped with ATON system. Due to contact wire height variations, both systems are enhanced with a focus system that positions the cameras with respect to lenses. A band-pass filter is used in both the systems that suppress the background light in the image data.

MEDES system takes and processes 250 images per second. Considering the number of pixel of each CCD camera, there are large amount of data to be processed in real time. To enhance processing capability in both systems, parallel processing was performed. The difference between ATON and MEDES systems is in the utilised type of optics. Telescopic and

conventional optics are used in ATON and MEDES systems respectively. The main advantage of telescopic optics is in providing a constant optical resolution. However, compare to conventional optics, telescopic optics are more expensive and complicated.

Borromeo & Aparicio, (2005) developed a version of MEDES system modelled in VHSIC Hardware Description Language (VHDL) and implemented it in Field Programmable Gate Array (FPGA). This system has the capability of a minimum of 1000 measurements per second and is compatible with MEDES system. The advantage of FPGA over DSPs parallel processing adopted in MEDES system is simultaneous execution of the control procedures and its technology independence.

2.5.3.2 Japanese System

The Japanese optical measurement system developed by Shimada, et al., (1997) determines the contact wire wearing track by measuring the reflection return time. The Japanese system uses a laser that scans the stagger zone with a rotatory mirror. As the laser beam hits the contact wire sliding surface, irregular reflection will be emitted and part of it will return to the light source. The returned beam will be captured by the photoelectric transfer element and is used to measure reflection duration. The laser beam scans at a constant speed. Therefore, the calculated reflection duration is proportional to the width of the wearing track. The Japanese system comprises several mirrors and lenses. Moreover, it incorporates a servomechanism to adjust the lenses with respect to height of the contact wire. Compare to MEDES and ATON systems, the measurement basis of the Japanese system is simpler. The disadvantages of the Japanese system are its large size ($2500 \times 1000 \times 400\ mm$), complexity of the deployed optic system and installation of bulky measurement instruments on the train rooftop.

2.5.3.3 WWS101

WWS101 is another optical-based contact wire monitoring system developed by Fraunhofer IPM (Institute of Physical Measurement). The system is equipped with two cameras that are positioned with their lens views oriented toward the contact wire. The illumination source propagates rows of white spotlights and the images of the illuminated sliding surface of the contact wire will be captured by cameras. Each recorded frame shows 25mm of the length of contact wire. WWS101 system embeds a device that measures the contact wire position and provides better control of the scan angle of the mirror and camera zoom. The captured image data is transferred via optical fibres to the control computer for processing. The processing system utilises image processing algorithms that enhance quality of images and signify the present edges in the image to better identify the sliding surface. The direction of edges is

calculated and averaged for each 25mm of the wire length (Hoefler, et al., 2001). The problem of the utilised processing system is that sudden slope changes (for example, presence of mast) in the image data leads to measurement errors.

2.5.3.4 Geocat

Geocat is an integrated diagnostic prototype system designed by Fumi & Forgione, (2001) and was installed in one of FS special trolleys in Italy. This system enables measurement of the width of the contact wire wearing track through installation of measurement devices to the pantograph. Installation of the measuring devices to the pantograph can be counted as a disadvantage as the measurement will be performed under high-voltage, and measurement errors caused by pantograph vibrations will be inevitable.

2.5.3.5 Contact Wire Thickness Measurement System

On the contrary to wearing track measurement systems, contact wire thickness measurement system does not allow measurement of more than one wire to be carried simultaneously. Cybernetix in France developed a system that operates at the maximum speed of 5 km/h and uses a device that lifts one of the wires to enable simultaneous measurement of both the wires. This system has a horizontal limitations of $\pm 250\, mm$ and cannot cover the entire stagger zone of approximately $\pm 400\, mm$ (Borromeo & Aparicio, 2002). This approach requires provision of sideway parallel laser illumination and is in need of installation of measuring instrument (optoelectronic detector) to the pantograph. Hence, the measurements are subjected to high-voltage related disturbances and vibrations.

2.5.4 An Attempt to Predict Contact Wire Localized Wear

It is vital to replace the wires before they reach the end of their useful operational lifecycle. Replacement of contact wires is expensive since wires need to be replaced in lengths of tens of meters to become connected to the rest of the contact line. During this time, to gain possession on track and undertake renewal, the line must be kept out of service. To extend the useful lifecycle of wires, inspections must be carried on a timely basis in order to set maintenance at correct intervals efficiently. To achieve this there is a need for a method to enable prediction of the localised wear points within the wire.

Local wear of the contact wires with rapid progression is mainly caused by the separation of pantographs, sliding of the contact strip due to gradient of the wire, the wire excessive deviation, double ear connection point and point with connector. Takahashi, et al., (2014) suggested an on-board monitoring approach that uses wear detector unit with high-intensity infrared light source that measures contact wire thickness at predefined locations. The device

examines whether the wire thickness has reduced beyond the permitted range. Takahashi, et al., (2014) deployed a method to predict the contact wire localised wear based on the correlation between the amount of wear and other parameters such as deviation and height of the contact wire. The contact wire height and its deviation were measured through installation of rooftop measurement unit on a test train. The following are the list of the utilised sensors and instruments along with the desired parameters to be obtained through their application:

- Pantograph accelerometer: to detect the impact of pantograph with metal fittings and obstructions.
- Optical separation sensor: to detect the generated arcs caused by the separations of contact components.
- Pantograph monitoring camera: to check the status of the pantograph and contact wire.
- Rotatory laser device: to measure the height and deviation of the contact wire.
- Infrared LED device: to measure the contact wire residual diameter.

The measuring devices were located both on a rooftop and in an underfloor unit cabinet. The control unit installed under the floor was linked to the train control system and to rooftop devices. This system records information such as time, location, kilometrage, speed, train number and adds them to the collected data. This supplement the classification of data through an unmanned operation. The height and deviation of the contact wire were measured by a potentiometer linked to the vertical movement of pantograph and a laser unit fitted inside the car respectively. The beam intensity of the adopted laser device falls under class 3B of JIS C 6802 (Safety of laser products). To protect people around the station from high intensity laser beam whilst train enters or exits the station, the laser beams were not emitted when train speed is less than 5 km/h. After scrutinising the differences between the measurements graphs obtained with interval of three months Takahashi, et al., (2014) identified the following problems:

- In some cases, the contact wire residual thickness has increased over time instead of decreasing.
- The measurement graphs were distorted by noise and other offsets generated by a uniform error along the overall measurement data.
- Significant differences were observed between the actual and predicted results.

The reasons behind the observed measurement errors were identified as:

- Error of the laser positioning device caused irregular reflection noise of laser beams as they hit contact wire rough surface
- False measurement positions (i.e. difference of wheel diameter used in counting kilometrage)

Description regarding monitoring of the contact wire wear from the contact force waveform is laid out in Section 2.6.2.4.

2.6 Monitoring the Quality of Current Collection

The challenges in evaluating the performance of the catenary-pantograph as a coupled system in supplying the required electric current into the vehicle engine are firstly the operation of trains at high speeds and secondly the energisation level of 25kV. Presence of uncontrolled variables such as wind and aerodynamic effects on a running line as well as track condition affecting the current collection should be taken into account while performing full-scale testing on the system (Kiessling, et al., 2009).

To quantify the quality of current collection, Bruno, et al., (2001) gathered an index based on a statistical analysis of the properties achieved through three fundamental measurement activities listed in the below:

- Detection of the arcs due to contact-loss
- Measurement of the contact force between the pantograph head and contact wire
- Measurement of the contact wire dynamic raising with respect to the line being at rest condition

The degree of impact of these properties on performance of the catenary-pantograph varies. It is unusual to detect poor current collection caused by one property alone. Accordingly, a reliable global index is a product of careful analysis of measured data properly correlated (Bruno, et al., 2001).

2.6.1 Detection and Measurement of Electric Arcs

Contact behaviour is usually assessed by the number and duration of the arcs, measured as voltage loss. There are three main reasons which make measuring of arcs inadequate for evaluating the quality of contact. Firstly, when there are no arcs or number of arcs are relatively low, measuring of the arcs cannot compare variations of the contact line systems. Secondly, arcing cannot be simulated. Thirdly, even under identical conditions, measurements of arcs are not reproducible (Kiessling, et al., 2009). To evaluate the quality of the current collection, the

percentage of contact loss as a ratio of the time that the pantograph is not interacting with the contact wire to total time of the train operation needs to be calculated. Higher percentage of contact loss results in poor current collection and increases wear within the contact wire. Bruno, et al., (2001) measured the duration of the ultraviolet emission propagated by arcing at the time of contact loss. The measuring tool is made of photomultiplier tubes (phototube sensors) formed by a photocathode and a series of electrodes placed in an evacuated glass enclosure. The measurement instrument was tested on an ETR500 high-speed train with double pantographs equipped with phototube sensors fixed on the top deck of the locomotive at a distance of four meters away from the pantograph. Equipotential wire (i.e. a conductor wire that connects the front and rear pantographs) on top of the ETR500 compensates for current conduction when one of the pantographs loses contact with the contact wire. The obtained data from phototube sensors was validated based on equipotential wire (EW) current measurement. The collected data from phototube sensor and those obtained from EW during test were used to calibrate the phototube sensors to assess their selectivity. The suggested measuring technique has limited application inside the tunnels and was not suitable for overnight tests. To gain an insight to the current collection where the visibility degrades a TV camera was also installed on top of the train. The recorded footages were only used to visually monitor the pantograph operation.

2.6.2 Requirements of Interaction Between OHL and Pantographs

Hundreds of regulations and standards are defined for contact line systems. However, the most important standards for designers and operators of OHL are Technical Specification for Interoperability (TSI) Energy, EN 50 119, EN 50 121, EN 50 122, EN 50 163 and EN 50 367 (ADS, et al., 2016). In order to meet requirements for the interoperability of the European rail system, TSI and EN 50 367 set out the technical and operational standards that must be met by each subsystem (EuropeanUnionAgencyforRailways, 2016).

The interaction of the contact wire with pantograph creates an aspect that needs specifying some of the requirements relating to the static contact force, the mean contact force and the quality of the current collection (Kiessling, et al., 2009).

2.6.2.1 Static Contact Force

EN 50 206-1 defines the static contact force as the mean vertical contact force exerted upwards by the collector strip on the contact wire when the pantograph is raised, and the vehicle is at standstill. The static force for the AC systems is between 40 N and 120 N. For DC 1.5 kV systems, a higher static force (between 50 N and 150 N) improves the quality of the contact

and avoids dangerous heating of contact wire when the train is at standstill with its auxiliaries working (The Commission of the European Communities, 2002).

2.6.2.2 Mean Contact Force

According to EN 50 206-1, the mean contact force comprises the static and aerodynamic components of the pantograph contact force with dynamic correction applied to the contact wire as a function of running speed. For trains with multiple pantographs, the mean contact force should not exceed the defined range. Each pantograph should satisfy the current collection criteria, and the design of overhead contact lines and condition of the contact wire should sustain this force for all the pantographs on the train (Kiessling, et al., 2009).

2.6.2.3 Contact Force of the pantograph

Condition monitoring of the contact between the contact wire and pantograph is known as one of the key indices when evaluating the performance the catenary-pantograph system (Koyama, et al., 2014). Extreme contact force fluctuations between the two contact components result in unstable current collection conditions. Since condition of OHL affects these fluctuations, the OHL state of repair can be investigated by assessing the characteristics of the contact force waveform (Kusumi, et al., 2006).

2.6.2.4 Contact Force Measurement Technique

The developed contact force measurement methods in the literature are based on the force equilibrium in the pantograph. A background on this matter is divided into three main sections explained below:

Force Equilibrium in a Pantograph

To describe the analytical model of the pantograph, the pantograph is divided into two subsystems of panhead and an articulated frame with the panhead support. Figure 2-12 demonstrates the force equilibrium in the pantograph.

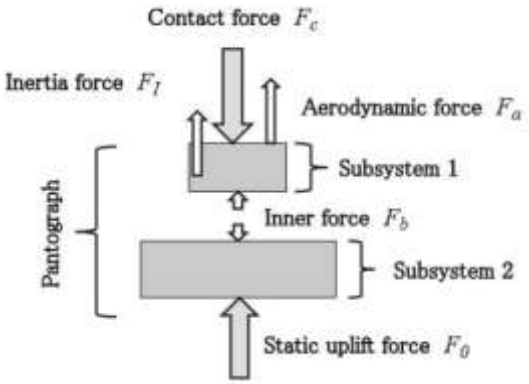


Figure 2-12:Force equilibrium in a pantograph (Koyama, et al., 2014)

From Figure 2-12, the contact force F_c, and inner force F_b, act on the interface between the subsystems one and two respectively. Since the equilibrium of subsystem one is affected by the aerodynamic force F_a, and the inertia force F_I, the contact force is the sum of the three forces acting on subsystem one. There is no practical way to measure the aerodynamic force while interacting with the contact wire. Hence, the aerodynamic force is estimated according to its proportionality to the square of the flow velocity against the pantograph denoted as V_t in Equation 2.10. The proportionality constant C_a, in Equation 2.10 is achievable though a wind tunnel test. Thereby, to evaluate the contact force two forces of inner and inertial should be measured (Koyama, et al., 2014).

$$F_c = F_b + F_a + F_I \tag{2.9}$$

$$F_a = C_a V_t^2 \tag{2.10}$$

The inner force can be measured by attaching built-in-sensors such as load cells and strain gauge to the panhead. When the friction force between the panhead and its support is negligible, the inner force comprises spring reaction forces of the panhead (denoted as $F_{bs,i}$ in Equation 2.11).

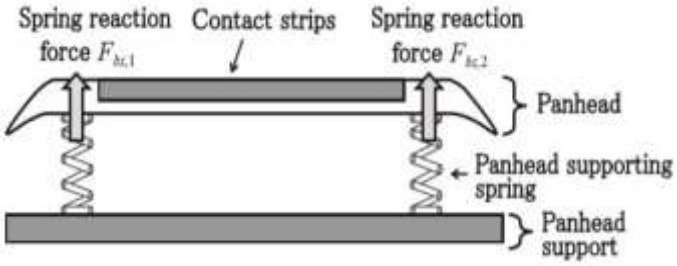


Figure 2-13: The details of the inner force (Koyama, et al., 2014)

$$F_b = \sum_{i=1}^{n} F_{bs,i} \qquad (i = 1,2,..,n) \tag{2.11}$$

The inertia force can only be obtained in a low frequency range. m and a are the panhead mass and acceleration respectively and the inertia force is therefore calculated through Equation 2.12.

$$F_I = ma \tag{2.12}$$

In order to measure the contact force in a high frequency range, the inertia force would be the product of the accelerations of plural positions on the panhead and the corresponding equivalent mass m_i, as stated in Equation 2.13. To measure the acceleration a common way is to connect built-in accelerometers onto the panhead.

$$F_I = \sum_i m_i a_i \qquad (2.13)$$

Monitoring of the OCL using Contact Force Waveform

The contact wire height variation significantly affects current collection performance. Kusumi, et al., (2006) studied the relationship between the contact force and wire height. This was done by measuring the contact force on-board the train, and the static height plus the contact wire wear on a maintenance wagon. To measure the contact force, the inertia force is first achieved through installation of four accelerometers on the panhead and measuring the strain on the pan-spring. To obtain the aerodynamic upward force, the pantograph was lowered to get separated from the contact wire. The overall aerodynamic upward force was measured by a load cell with a string attached to the pantograph underframe. The average force was measured by ignoring the inertia force through sum of the aerodynamic force and inner force. Accordingly, the aerodynamic upward force was calculated equal to the negative value of the inner force. A good match between the results of the carried load cell running tests and wind tunnel tests was observed. The contact force was measured as sum of the inner and inertia forces as well as the aerodynamic force acting on the panhead corresponding to the train speed.

The contact force, the pantograph height and contact loss was measured from the first pantograph at speed of 280 km/h. Figure 2-14 demonstrates the contact wire height, wear and the contact force waveforms.

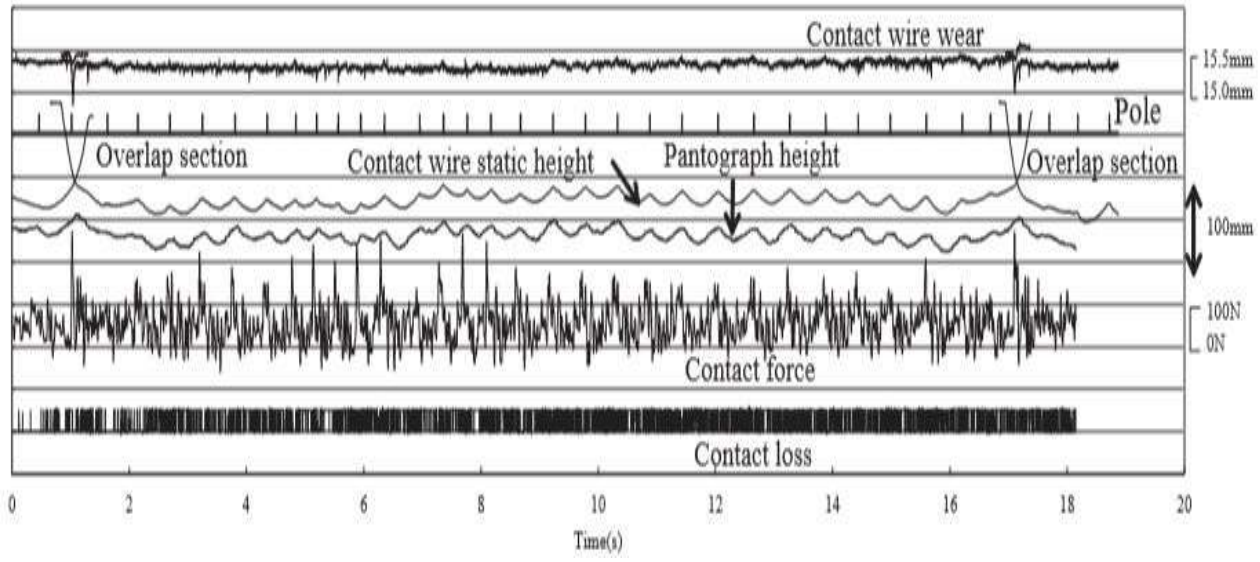


Figure 2-14: Contact wire condition and contact force waveform (Kusumi, et al., 2006)

By analysing the low frequency up-and-down motion of the pantograph and considering the pantograph as a mass of pantograph head and frame, the contact force can be expressed through Equation 2.14 (Kusumi, et al., 2006).

$$F_c = P_0 - m\frac{d^2y}{dt^2} \tag{2.14}$$

Where, y, m and P_0 are pantograph displacement, mass of the pantograph, and static uplift force respectively. In low-frequency domain, the contact force decreases when the acceleration is positive, and increases when the acceleration is negative. The acceleration can be calculated using Equation 2.15.

$$a = \frac{y_{i-n} - 2y_i + y_{i+n}}{(n\Delta x)^2} \tag{2.15}$$

Where, y_i is sample data of i number of pantograph height, Δx is sampling interval and n is data space for calculation. The relationship between the pantograph acceleration, contact force and contact wire height profile at support points shows that the negative higher acceleration leads to larger contact force. This determines the correlation between the acceleration and the contact wire height. It is also found that the contact force is greater at places with greater curvature of static contact wire height profile.

Kusumi, et al., (2006) studied the relationship between the contact force and contact wire wear at overlap structures. The comparison was made between two different overlap structures where normal and higher than normal contact forces existed. Figure 2-15 is a closer demonstration of the overlap section on right-hand-side of Figure 2-14. Accordingly, a force greater than the normal contact force was applied and local wear was detected at the junction point on the B line. Figure 2-16 shows a good overlap structure where normal contact force occurred.

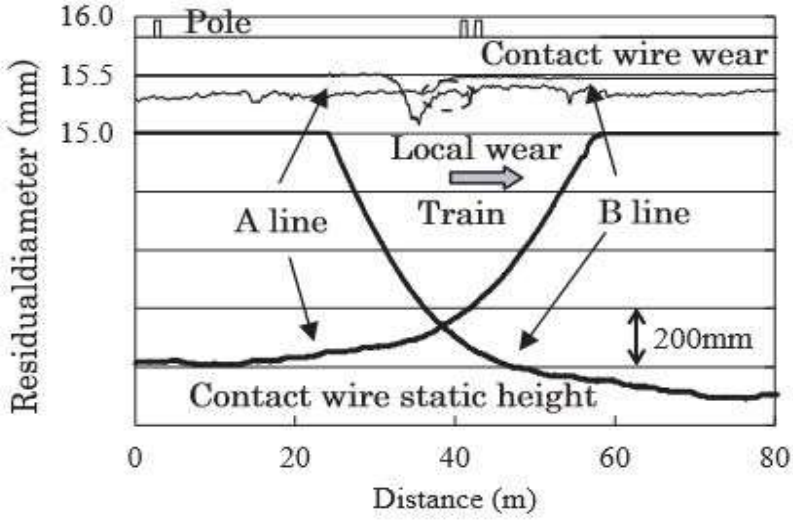


Figure 2-15: Overlap structure with greater contact force (Kusumi, et al., 2006)

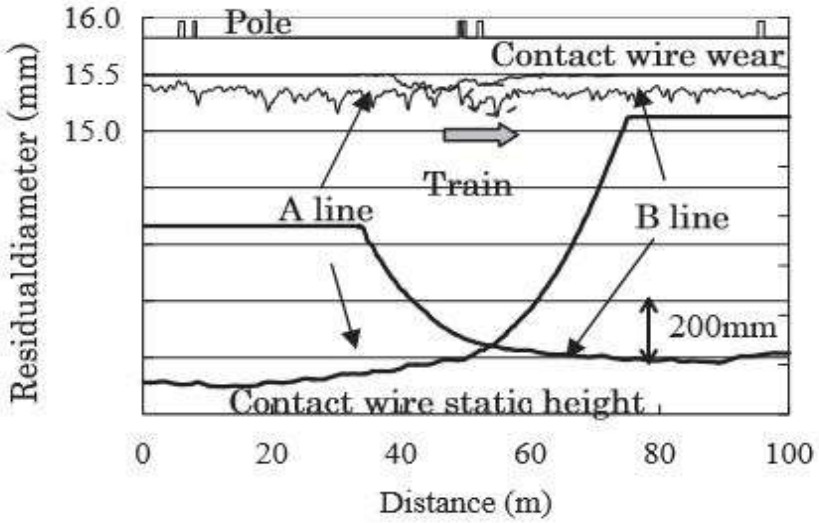


Figure 2-16: Overlap structure with normal contact force (Kusumi, et al., 2006)

Contact Force and Contact Wire Strain

The strain on the contact wire increases with speed. Frequent strain in excess on the contact wire results in its fatigue and might lead to its breakage. Measurement of the contact wire strain is challenging under high voltage condition. Accordingly, by assuming the overhead contact line as a tensioned elastic beam model, the amount of strain, ε, in response to the constant contact force, F, can be expressed as follow:

$$\varepsilon = \frac{F}{2ZE}\sqrt{\frac{EI}{T}}\frac{1}{\sqrt{1-(V/c)^2}} \qquad (2.16)$$

The parameters of Equation 2.16 are as follow:

EI the rigidity (young's modulus and moment of inertia) of the contact wire

Z the contact wire section modules

T the contact wire tension

c the wave propagation velocity, and

V the running speed

According to Equation 2.16, the amount of strain at the contact wire is proportional to the contact force and is proportional to the invert of $\sqrt{1-(V/c)^2}$.

To find the relationship between the contact force and contact wire strain, Kusumi, et al., (2006) calculated both parameters during the running test while calculating the theoretical value corresponding to the running test speed using Equation 2.16. The obtained results during the test run and the theoretical value, determined a good correlation between the contact force and contact wire strain. Hence, it was concluded that the contact force enables detection of the locations with higher contact wire strain.

This proposed method for measuring the contact force is one of the few developed contact force measurement methods that require sensors to be installed on the panhead. Estimation of the contact force above 100 mph is still a challenging task for Network Rail (Duncan & Arthington, 2018). Recently in the UK, DB Systemtechnik (DBST) and ESG Rail have been supporting Hitachi Rail Europe with testing and commissioning of new trains for the Intercity Express Programme (IEP), through providing facilities for pantograph and OHL testing. The interaction between the OHL and pantograph can be monitored by on-board test engineers and according to European standard EN50367 and requirements of various TSIs, including ENE (energy) and LOCPAS (Locomotive and Passenger). In November 2018, ESG made a contract with Network Rail for monitoring of the OHL. DBST was in charge of providing monitoring equipment such as high-fidelity sensors, which will be connected on the panhead to measure the contact force (Wordsworth, 2018). Sensor-based condition monitoring techniques share common drawbacks. These are (Koyama, et al., 2014):

- Sensors along with their auxiliary cables influence the dynamic characteristics of the pantograph
- Use of telemetry devices requires electric power supply units because sensors are installed in high-voltage conditions
- Accommodating sensors and the telemetry devices requires large space
- The way that some pantographs are designed restricts the installation of sensors

- Such measuring devices are expensive, and their lifetime are shorter in presence of high temperature and vibration level under high speeds.

2.6.3 Oscillation of Contact Wire Caused by Pantograph Coupling

When oscillations of the contact line and pantograph are not coupled, raising of the pantograph leads to contact-loss. Buksch (1979) described the behaviour of the contact wire as the pantograph presses against it by assuming the wire as a tensioned string. In order to examine the propagation of a transverse impulse, it is assumed that the contact wire has negligible stiffness, a longitudinal stress of σ and a specific mass of γ. Knowing the applied stress and the contact wire mass, the wave propagation speed can be achieved through:

$$c_p = \sqrt{\sigma/\gamma} \qquad (2.17)$$

As an example, the wave propagation speed for an AC-100 copper that is subject to a force of 10kN is $\sqrt{10000/0.89} = 106\ m/s$. This is approximately equal to 380 km/h. The practical tests at high speed shown that, as the train speed reaches the wave propagation speed, the contact wire uplift increases beyond the permitted range. This results in current interruption and restricts speed. The tests results showed that for a stable contact the wave propagation speed should be at least 1.4 or 1.5 times greater than the expected train speed (Kiessling, et al., 2009). For continuous contact, the difference between the maximum operating speed and wave propagation speed should be sufficient. This can be assured via a proper selection of the contact wire design and the applied tensile force.

Buksch (1979) considered the propagation of the reflected waves along the contact wire using d'Alembert wave equation, and obtained the motion of the catenary elements from the superposition of individual waves. By considering the contact wire as a taut string between the droppers, Popa, et al., (2012) described the attenuation of contact wire waveform using the reflected wave at dropper positions mathematically.

2.6.4 Contact-based Monitoring of the Contact Wire

BARWELL (1960) measured the vertical and lateral movement of the contact wires at predefined locations. Measurements were done by a galvanometer recorder that is activated by the transmitted A.C signal from the attached potentiometric displacement transducers to the wires. The applied transducers were insulated from high current conductor wires by resin bonded glass fibre tubes and were selected as light as possible to minimise their impact on the performance of the equipment. The recorded response provided information about the contact

wire maximum uplift and its lateral displacement caused by wind. Installation of more than a certain number of transducers is not beneficial. This is due to a high possibility of distressing the contact wire dynamics. The friction and changes in diurnal temperature on tensioning of the contact wire affect the performance of the contact wire. Thereby, measuring tension variations of the contact wire is of necessity while investigating component excitation levels in response to the external forces. Papi & Violi (1997) measured variations of tension in the contact wire using strain gauge dynamometers. They assessed the impacts of local topology on the movement of the wires based on the recordings of wind direction, wind velocity and ambient temperature. To measure the contact wire dynamic lifting, the static positioning of the contact wire during low speed test run was measured first. Regardless of high disruption level to rail traffics and complexity, monitoring of the contact wire dynamic uplift variations using this method is widely used by railway companies particularly to test the performance of new pantographs.

2.6.5 Vision-Based Monitoring of Catenary-Pantograph System

Ideally, to assure a uniform contact, performance of the overhead contact lines and pantograph needs to be monitored as a coupled system. Pantograph optical measurement systems are developed to examine goodness of current collection in an active state. This is done through installation of a video camera on the car flat roof surface which records pantograph operation.

Cho & Park (2016) proposed an optical-based monitoring technique that evaluates the current collection performance. This is done by assessing the contact stability through measurement of the stagger and height of the contact wire. The proposed optical-based stagger/height measurement system by Cho & Park (2016) shares interface with contact-loss rate measurement system through which the electronic waves outside of the visible wavelength range are detectable with an arc sensor. The effectiveness of the proposed technique was examined through offline processing of a limited number of frames (i.e. 300 frames from three tests runs over three days). The identified errors in the analysis of the selected video frames are:

- Similarity between the OHL components made automatic recognition of the contact wire from the images cumbersome.
- Variations of background objects as well as ambient lighting conditions resulted in partial/full deformation of the pantograph features in images and made extraction of its features impossible.

- Problems in distinguishing between the operating contact wire at sections with more than one contact wire.
- Fast movement of the contact wire across the working range of the collector strips and low sampling rate of the utilised CCD camera made detection of the contact point difficult.
- Detection difficulties in the vicinity of structures with complex features such as mountain and train stations.

Cho & Park (2016) analysed the selected frames by categorising the background scene with respect to illumination variations of fixed areas of the frames into three classes of normal, background interference and tunnel. By taking the average intensity of the images, a linear classifier was applied to the obtained data and enabled recognition of the pantograph from the background objects. The accuracy of the proposed monitoring technique in determining contact wire parameters is stated to involved 8 millimetres error for image resolution of 720×480. The observed measurement errors are claimed to be mostly due to blurring caused by rapidly changing images at high speed and limitations of the utilised camera.

Duncan & Arthington (2018) designed an OLE video analyser software that assists manual analysis of footages recorded by a GoPro camera. The software was developed to identify contact wire stagger and variations of the pantograph height. The effectiveness of the software was assessed by GoPro software analysis. The advantage of this software is in enabling detection of the missed non-conformances from manual analysis. The processing of the footages involves frame-by-frame detection of the pantograph. This requires the pantograph to be defined by the user to the system prior to running the detection process. Although this software monitors the height of the pantograph and is an alternate method to conventional analysis of the footages, the performance of the system involves two limitations:

- Interactive control of the system by experts due to lack of automatic recognition of pantograph features.
- Long processing time (analysis of a 20-minute footage take up to 6 hours).

The state of art in the camera-based monitoring of the pantograph-catenary system is the fault diagnosis approach developed by Aydin, et al. (2014). The aim was to prevent dangerous situations occurring as a consequence of fault of either the pantograph or contact wire. The developed system enables routinely inspection of the catenary-pantograph system through online processing of the images acquired from a digital line-scan camera. The system

simultaneously processes the data by performing edge detection operation to generate edge images. This way the contact wire and upper side of the collector strips are detected based on their line features using Hough transform (see Section 3.4.5.1). The post-processing of data involves provision of the obtained features which are coordination information of detected contact point at each frame formed as a signal to a D-Markov based state machine. Using D-Markov-based state machine the related disorders such as irregular positioning of the contact wire can be diagnosed. This vision-based monitoring system enables detection of the position of more contact between the pantograph and contact wire through which the wear points on the collector strip can be recognised.

2.7 Summary

The consequences of service interruption caused by failure of overhead contact line system and unplanned maintenance activities highlights the need for more routine assessment of this railway infrastructure. Condition of the contact wire has a direct impact on current collection and the reliability of OHL. Although contact wire uplift is of high importance when it comes to the reliability of OHL, lesser attention has been given to actually develop a reliable system for its measurement. The amount of uplift in response to the contact force is a critical parameter that affects the contact stability. Measurement of the contact wire uplift helps in identifying probable defects within the contact components before they develop into more severe faults and put safe running of the train in danger. Safety considerations, access restrictions, dependency on human judgement and train speed are the main challenges involved in measurement of the contact wire uplift. The next chapter determines whether it is feasible to measure the uplift from video data. This is done by evaluating suitability of different image processing techniques in enabling extraction of the contact wire motion information from video images.

Chapter Three

3. METHODOLOGY

3.1 Introduction

The conventional approach to measure the contact wire uplift is through the application of potentiometric transducers. Apart from considerable disruption level to the train services, installation of the measuring devices to the light overhead wire with slender structure triggers further variations within the component dynamic response and leads to measurement errors. The challenges of monitoring the overhead line equipment, the complexity of scheduling for health monitoring of the contact wire and the broad consequences of service disruptions caused by faults of either the pantograph or the overhead line equipment led to the installation of video cameras on the trains rooftops. Despite the potential usefulness of the image data in monitoring of the parameters affecting the contact stability, the reliability of the image data in determining the variations of such parameters yet needs investigating. In reality, the application of the on-board cameras has only extended the Network Rail and TOCs observation zone on the performance of the pantograph operating across the contact wire. In case if particular incidents require further inspections, the recorded video footages will be played back and assessed by suitable users to guess or confirm the cause of event. Nevertheless, after a short period the majority of the recorded videos are discarded without getting analysed further, said a senior member of a train operating company which was confirmed by the head of OLE team at

Network Rails. This current gap in the railway industry creates a need of establishing an appropriate methodology to be efficiently used to better determine condition of the contact wire. This chapter explains the need of establishing a non-disruptive condition monitoring approach and introduces the adopted techniques to be used over the stored video data to aid in efficiently using the recorded database in the industry and remotely condition monitoring the contact wire. To investigate the possibility to extract the contact wire height variations from analysis of the recorded video footages, two camera-based monitoring approaches of trackside and on-board are considered. The chapter describes the employed techniques and evaluates the suitability of different image/video processing methods in extracting the desired parameter from the video data.

3.2 An Ideal Overhead Contact Wire Condition Monitoring System

Ambiguous system specifications and not considering the stakeholders' requirements when finalising the application of a system can create unrealistic expectations to existing/potential stakeholders, impose additional costs and might postpone the project completion date. Table 3-1 identifies features of an ideal contact wire monitoring approach by highlighting the problem domain and the stakeholders' requirements for developing the monitoring techniques under consideration.

Table 3-1: Identification of the potential stakeholders and their expectations according to the drawbacks of the conventional condition monitoring method

Stakeholder Requirement(s)	**Problem Domain**	**Stakeholder's Perspective**	**Desired Achievement(s) through the use of the System**	**Potential Stakeholder(s)**
Contactless monitoring approach	High-disruption level of manual inspection programme and drawbacks of installing measuring gadget to the light overhead wire	Is it safe to be adopted? (Impacts on Human factors)	To perform monitoring safely, accurately and without disturbing trains operation	Government Network operators (Network Rail) Railway Inspectors
Prevent manpower & optimise monitoring cost	Existing monitoring approaches are time-consuming, costly and require human intervention in collecting and analysing the asset condition data	Cost optimisation by investing in developing automatic monitoring means with the capability to monitor the asset condition faster with less/no requirement for human intervention	Efficient asset management through automated monitoring method that is cheaper in the long term	Network Rail Government Railway Inspectors
Capability to monitor the condition of the contact wire over the entire length of the spans series	The challenges of monitoring the asset condition near the structures (tunnels and bridges) and in the vicinity of the train stations	Due to limitations of the conventional monitoring programme, the state of the contact wire at particular sections of the track remains unknown	Can it create a better insight into stability assessment of the contact wire in challenging environments where the height and illumination suddenly changes	Government Railway Operator Network Rail OHL and pantograph maintainer
Can it determine the dynamic response of the contact wire to the pantograph force?	Lower stability of the contact and a higher likelihood of contact-loss at high speeds might lead to electric arc, contact wire localised wear, and noises when the pantograph interacting with the worn section of the contact wire	Impact on current collection performances? Can it improve the asset life cycle?	Investigating the component dynamic response and height variations under service condition	Network Rail Railway maintainer and inspectors Neighbours
Fast processing time	Massive amount of video data to monitor the condition of the distributed contact wire over thousands of miles of track?	How fast the processing time will be? Less/no requirement for human intervention while processing data	How accurately it can determine height variations under service condition	Network Rail Railway Operators OHL and pantograph maintainer

3.3 Outline of the System

As specified in Section 1.2 and 1.3, the aim is to investigate the feasibility of using the video data to measure the contact wire uplift at predefined locations along the span and over the full catenary length. Both monitoring approaches, trackside and on-board, are expected to determine the asset height variations through automated timely-efficient operations. To fulfil the Section 1.3, this research is driven through three phases as demonstrated in Figure 3-1.

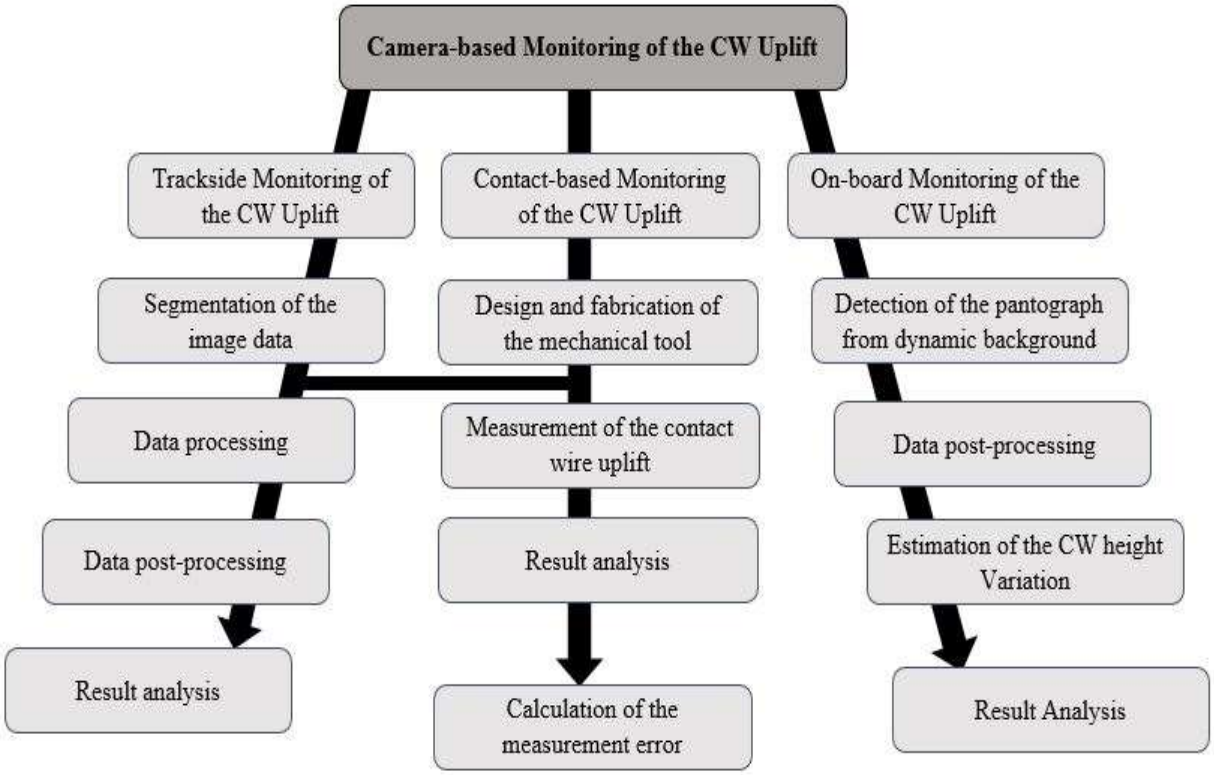


Figure 3-1: Research Methodology

3.4 System Approach

The following sections evaluate the suitability of different image/video processing techniques in determining the contact wire height variations according to the appearance features of the contact wire in the scene and type of the background.

3.4.1 Digital Image Processing

Digital images are recorded by a variety of devices including still and video cameras and have extensive applications in many fields such as security, military, medical and so forth. Under any application, the observer's goal (human or machine) is to extract the desired information from the scene that is imaged.

Digital image processing is a subset of the electronic domain through which an image is converted to an array of small integers (pixels), representing physical quantities such as radiance within the scene, stored in a digital memory and processed by computers or other digital hardware (Kang, 2007). Each pixel within an image stores an intensity value and has a unique location address, determined by its row and column number in the two dimensional (2-D) image (Stipanicev, 1994). Let $f(x, y)$ be the image 2-D function, where, x and y are the pixel spatial coordinates, and f is the intensity value at each pair of coordinates.

$$f(x,y) = \begin{pmatrix} f(0,0) & f(0,1) & \cdots & f(0,N_y-1) \\ f(1,0) & f(1,1) & \cdots & f(1,N_y-1) \\ \cdots & \cdots & \cdots & \cdots \\ f(N_x-1,0) & f(N_x-1,1) & \cdots & f(N_x-1,N_y-1) \end{pmatrix} \quad (3.1)$$

As can be seen from Figure 3-2, the pixels' intensity values of a digital image are finite discrete quantities.

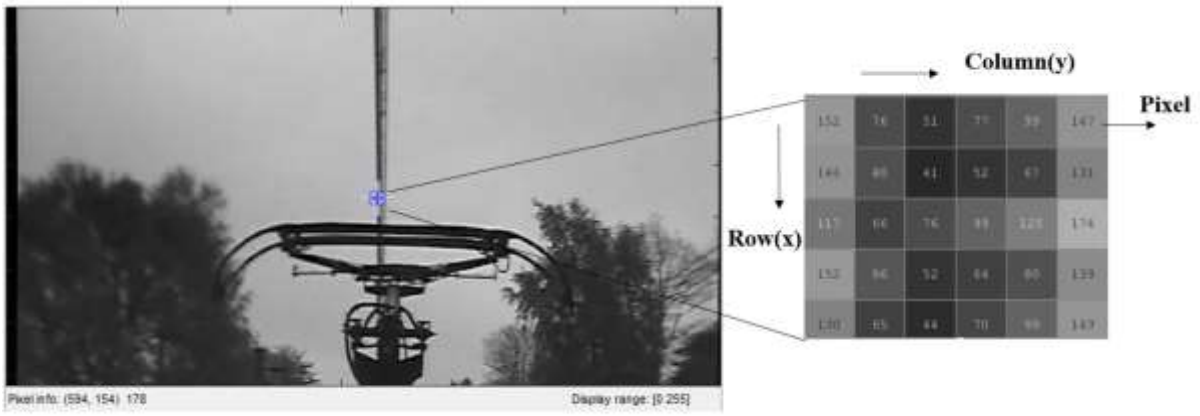


Figure 3-2: Intensity values of a small area of the image

In general, there are four types of images knowns as; colour image, intensity image, binary image and indexed image (Pratt, 2007).

Colour Image

Colour image is represented through a three colour channels of Red, Green and Blue (RGB). Each pixel of the image has 24 bits (8 bits per channel) and determines three intensity values, one for each colour.

Intensity Image

The brightness information and intensity values of an image is represented through intensity or greyscale image. The number of bits per each pixel in a greyscale image depends on the variation of the brightness level within the image. In general, each pixel of a greyscale image has 8 bits that creates 2^8 possible grey levels from 0 to 255. The brightness level of each pixel can be determined by double class or unit8 through which a floating number between range 0 to 1 and an integer within the range 0 to 255 is assigned to each pixel respectively. Although double class requires bigger storage compared to class unit8, the majority of the mathematical function are only applicable on double class.

Binary Image

The binary image is the product of the thresholding of a greyscale image. With only two possible grey values of 0 and 1, the binary image is represented by a single bit per pixel.

Indexed Image

An indexed image (type double or unit8) represents the colour image by storing it as two matrices. While the first matrix of the indexed image has the same size of the colour image, the size of the second matrix (or colour map) might differ depending on the spectrum of the visible colours in the image. The colour map matrix has m rows and three columns, where, each column specifies red, green and blue components for every single colour within the image. The contained numbers in the first matrix are direct indices of colour map matrix values, mapped to the corresponding colour within each image pixel.

3.4.2 Image Analysis

Extraction of meaningful information from image using computational techniques and algorithms is called image analysis. In contrast to other image processing methods such as image enhancement and restoration, image analysis has a numerical output rather than a modified picture.

A crucial step in image analysis is image segmentation. Segmentation is the process of the partitioning of an image into regions or categories based on features that makes the regions meaningful and disjoint (Cheng, et al., 2001). Pal & Pal, (1993) presented a formal definition of image segmentation based on homogeneity control of the pixels through general formulations of "split-and-merge method" as follows:

if $P(\ )$ is a homogeneity predicate defined on groups of connected pixels and F represents the entire image. Segmentation allows portioning of F into N disjoint regions, $F_1, F_2, \dots, F_N$ such that:

1. $\sum_{i=1}^{N} F_i = F$, F_i is a connected region, $i = 1,2,..,N$, meaning the segmentation must be completed.
2. $F_i \cap F_j = \emptyset$ for all i and j, $i \neq j$, meaning the regions must be disjoint.
3. $P(F_i) = True$ for all $\forall\, i$, meaning the entire pixels in a segmented region must satisfy the assumed homogeneity predicate.
4. $P(F_i \cup F_j) = False$ for $i \neq j$, indicating the difference in distinct regions according to the predicate.

Based on the above conditions, proper segmentation is usually the one through which pixels in the same category contain similar greyscale values and form a connected region, whereas the neighbouring pixels of different categories have dissimilar values. There are three main segmentation methods, known as thresholding, edge-based segmentation and region-based segmentation that are briefly described in the following:

- Thresholding enables partitioning of the regions within the image through binarisation of the greyscale image based on pixel intensity values. There are three general types of thresholding, known as, global, local and adaptive thresholding.
- Edges are points where there is a boundary between two regions within the image. Edge-based segmentation enables categorisation of the formative pixels of the image to edge or non-edge by applying an edge filter (Prewitt's, Canny and etc.) to the image. Accordingly, those pixels which are not separated by an edge are assigned to the same category.
- The basis of region-based segmentation techniques relies on identification of regions within the image with similar features such as; grey level, texture and etc. The two main region-based segmentation techniques are knowns as, region growing (merging) and region splitting.

3.4.3 Analysis of the Trackside Data

The raw data in the trackside monitoring approach are recorded by a video camera that was fixed on a tripod at around three meters away from the track while having a sideway view to the contact wire at the elevation angle of 30 degrees. The videos show the vertical movement of the contact wire under service condition. In the recorded footages the contact wire is featured as a thick horizontal line imaged in a way that every single column of each video frame contains some pixels that store information about the presence of the contact wire in the scene. According to the desired parameter under measurement, appearance characteristics of the contact wire and properties of the background, the classification of the image data is performed through threshold-based segmentation.

3.4.3.1 Selection of a Suitable Thresholding Technique

The global thresholding becomes in use when the pixel values of the object and the background are relatively consistent over the entire image (Bhargavi & Jyothi, 2014). The intensity distribution of the contact wire and background pixels in the image data under analysis are sufficiently distinct. Thus, it is expected that a single threshold t can be applied to the entire image that partitions the formative pixels depending on their intensity values to two categories of contact wire and sky. This section evaluates the effectiveness of global thresholding in segmentation of the trackside data according to the properties of the image histogram.

The input of a thresholding operation is usually a greyscale image that will be converted to a binary image upon completion of the segmentation operation. Accordingly, there are two possible values of either 0 or 1 assignable to each pixel that categorises the image into two classes of foreground and background.

$$g(x,y) = \begin{cases} = 1 & if\ f(x,y) \geq t \\ = 0 & otherwise \end{cases} \quad (3.2)$$

The threshold value can be chosen manually by setting different values to t and observing their success in segmentation of the desired object from the scene. However, this is not always the best practice since the illumination variations within the scene might lead to misclassification of some areas of the object in consideration as the background. Accordingly, the output of the segmentation operation cannot determine the boundaries of the object (i.e. the contact wire) as fine straight lines. Additionally, there can be a possibility of wrong classification of some of the pixels that are located in between the objects boundaries. The best way of selecting a suitable value for thresholding operation is through assessing the image histogram (Raju & Neelima, 2012). The image histogram determines the distribution of the greyscale value within

the image, constructed by splitting the range of data into bins with equal size. Figure 3-3 demonstrates the histogram of the greyscale trackside image data.

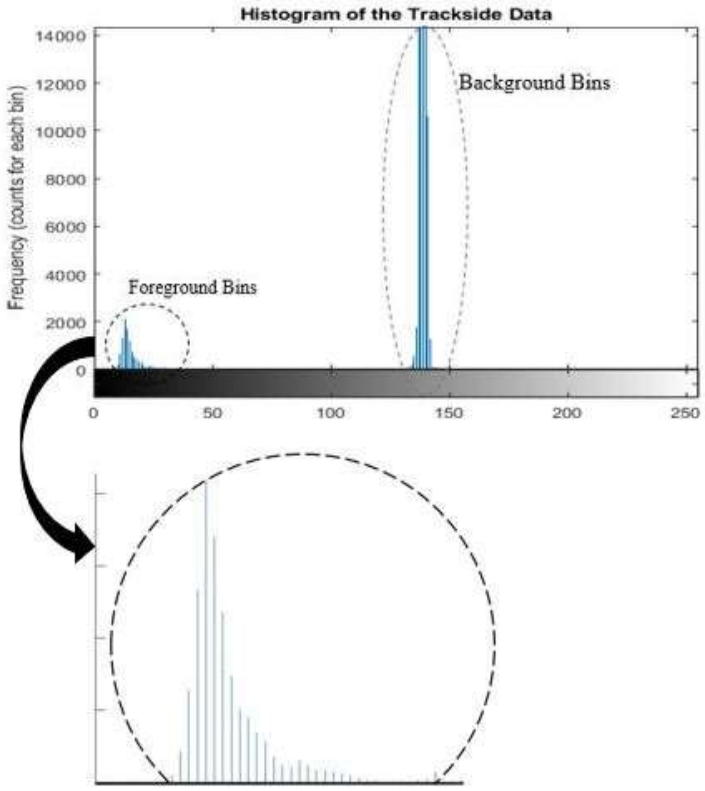


Figure 3-3: Histogram of the trackside image data

As it can be seen from the figure, the histogram of the trackside image data is characterised by two distinct dominant modes that make the histogram bimodal. Thereby, the image can be partitioned by applying one threshold to the entire pixels within the image. Ideally, the histogram should have a deep and sharp valley between its two peaks, representing the object and background respectively (Prewitt & Mendelsohn, 1966). The two peaks of the image histogram in Figure 3-3 are considerably unequal in height and produced no traceable valley. Several solutions are proposed to overcome such difficulties, as an example, Watanabe & CYBEST (1974) developed a difference histogram method that selects the threshold at the grey level with the maximal amount of difference. Another thresholding technique is the valley sharpening technique proposed by Weszka, et al. (1974), that restricts the histogram to the pixels with large absolute value through applying a Laplacian operation to the image. Both these methods aimed to determine the edges of objects in the image using the pixels information to modify the histogram such that it becomes suitable for thresholding.

Parametric techniques are other types of thresholding that enable the image partitioning through some statistical principles. An example of the parametric techniques is the thresholding technique developed by Chow & Kaneko (1972), to detect boundaries in radiographic images. The idea was to develop an automatic boundary detection that is not sensitive to shading or gradually varying interference. This was achieved through characterisation of the image regions containing a portion of boundary by applying a mixture of two Gaussian intensity distributions to the regions histogram. Although the developed thresholding technique by Chow & Kaneko (1972), enabled successful segmentation of the boundaries in the low-quality radiographic images, the technique involves extensive statistical decision procedures that not only make the operation tedious, but it can also lead to weak approximations of the real modes of the histogram.

The state-of-art in histogram dependent thresholding technique and the adopted approach for segmentation of the trackside image data is the nonparametric threshold selection method proposed by Otsu (1979). On the contrary to the mentioned histogram-based thresholding techniques, the focus in the Otsu's method is on the regions inside the object rather than the edges. The Otsu's method enables selection of an optimal threshold by a discriminant criterion that maximises the separability of classes in grey levels through minimisation of the weighted within-class variance, summarised in the following formulations:

Assuming $\sigma_w^2(t)$ and $q_1(t)[1-q_1(t)][\mu_1(t)-\mu_2(t)]^2$ are the within-class and between-class variances, the total variance σ^2 of the image can be calculated through Equation 3.3.

$$\sigma^2 = \sigma_w^2(t) + q_1(t)[1-q_1(t)][\mu_1(t)-\mu_2(t)]^2 \qquad (3.3)$$

Where t is the threshold value selectable from the range of 0 to 255, the weighted within-class variance is a product of the summation of the probability of each class q_n multiplied by the corresponding variance of each class σ_n^2 as follow:

$$\sigma_w^2(t) = q_1(t)\sigma_1^2(t) + q_2(t)\sigma_2^2(t) \qquad (3.4)$$

If n_i is the number of pixels at level i and N is the total number of pixels with grey values from 1 to I. The probability of each class is obtainable through normalization of the histogram using Equation 3.5.

$$P_i = n_i/N, \quad P_i \geq 0, \quad \sum_{i=1}^{I} P_i = 1 \qquad (3.5)$$

Accordingly, from the probability distributions of the pixels in the image histogram, the probability and mean of each class can be achieved using Equations 3.6 and 3.7.

$$q_1(t) = \sum_{i=1}^{t} P(i) \quad and, \quad q_2(t) = \sum_{i=t+1}^{I} P(i) \tag{3.6}$$

$$\mu_1(t) = \sum_{i=1}^{t} \frac{iP(i)}{q_1(t)} \quad and, \quad \mu_2(t) = \sum_{i=t+1}^{I} \frac{iP(i)}{q_2(t)} \tag{3.7}$$

Hence, the variance for each class is obtained via Equation 3.8.

$$\sigma_1^2(t) = \sum_{i=1}^{t} [i - \mu_1(t)]^2 \frac{P(i)}{q_1(t)} \quad and, \quad \sigma_2^2(t) = \sum_{i=t+1}^{I} [i - \mu_2(t)]^2 \frac{P(i)}{q_2(t)} \tag{3.8}$$

Thereby, the weighted within-class variance is achievable by substituting the calculated probabilities and variances of the classes into Equation 3.4. The above mentioned operations will be iterated and σ_w^2 will be calculated corresponding to each t until the lowest value of σ_w^2 is achieved. Accordingly, the most suitable threshold value for segmentation is identified.

3.4.4 Motion Detection in Static Background

Video is a collection of discrete images that appear continuously in sequence and create motion effects. Each second of a video is created from 24 (or more) still images. The human eye, with retinal image retention mechanism of 1/24 second, continuously observing the motion images is incapable of distinguishing details on the processes through which the object has changed its location (The & Shashev, 2017). An effective way of displaying the object motion is pattern detection based on the objects history of motion at each video frame over time. Majority of the developed motion detection techniques share common characteristics. The most common motion detection techniques are background subtraction, optical flow and difference over time.

3.4.4.1 Background Subtraction

Background subtraction (BS) enables detection of the motion regions by subtracting the pixels values of background image from those in the current image. The absolute difference between two consecutive images is stored in a matrix called distant matrix. Using this matrix, the obtained differences are compared to a threshold value calculated based on the supplied initial frames. In BS technique, it is assumed that the video sequence I is formed by a static background B in front of which moving objects are observed (Migliore, et al., 2006). By considering the difference between the colour distribution of a moving object and the background, the general BS algorithm is described through Equation 3.9.

$$x_t(S) = 1 \; if \; d\left(I_{s,t}, B_s\right) > \tau \quad otherwise \; 0 \tag{3.9}$$

Where d is the distance between $I_{s,t}$ and B_s, $I_{s,t}$ is the colour intensity of pixel s at time t and B_s is the background model at pixel s. Pixel s will be labelled as part of the motion field or motion mask, x_t, when the computed absolute difference is larger than the threshold value τ. Ideally, the supplied background image should be taken while the objects are not present in the

scene. Accordingly, the background model is initialised based on the first few frames of the video, which then trains over a set of selected frames. In this way, the created background model is tightly formed by the selected initial frames. Therefore, the resultant background model is subjected to unstable quality (The & Shashev, 2017).

An alternative way to generate the background model is the background estimation by considering the repeatability of the intensity of the background pixels, and applying a pixel-wise Temporal Median Filter (TMF) on the image. The drawbacks of the background estimation using TMF are:

- Failure in generating background estimation when a sequence is highly cluttered.
- The background should be fixed and ideally free of noise which is not feasible in every real life scenario.

Liu, et al., (2016) tried to improve TMF using of Gaussian filtering. As the illumination changes, the strong correlation among the components of RGB space leads to instability. To address this, Liu, et al., (2016) converted the video frames from RGB to HSV space that is formed by separate components knowns as Hue (H), Saturation (S) and Value (V). Hue remains unchanged as the illumination changes and the background estimation will be more stable as the HSV space enables separation of the brightness from the chromaticity. To reduce the noise, each background pixel was modelled with a Probability Density Function (PDF) learned over a series of given frames. The corresponding pixels to the object or noise were identified based on their low probabilities and thereby filtered from the operation. Consequently, the background model was achieved by applying TMF on the remaining pixels.

The main challenge in the BS method is frequently changing background due to changes in illumination, motion, and change of the background geometry. These make the inter-frame differencing a poor solution in identifying the moving objects from the scene (Desai & Gandhi, 2014). A common way to handle the illumination variations is background updating by using the Infinite Impulse Response (IIR) filter through Equation 3.10. According to Equation 3.9, when pixel s is classified as foreground, α (small constant [0 to 1]) will be set to zero. If the pixel is classified as background, a low non-zero value will be assigned to α which slowly updates the background. Consequently, when the pixel is classified as a moving pixel, a higher value will be assigned to α which triggers an immediate restoration of the background (Migliore, et al., 2006).

$$B_{s,t+1} = (1 - \alpha).B_{s,t} + \alpha.I_{s,t} \quad (3.10)$$

Background updating through use of IIR filter reduces the adverse impact of the illumination variations on the inter-frame differencing operation. However, depending on the proportionality of the object size to the background and the corresponding object intensity areas, the BS technique might suffer from foreground aperture problem regardless of how fast the object moves.

Despite the effectiveness in the BS method in detecting moving objects and determining the domain in which the object has moved across the frames over time, severe foreground aperture due to properties of the contact wire in the images (i.e. homogeneity of the contact wire pixels in the scene leads to its categorisation as background in the differencing operation and cause discontinuities/holes in the result), and disturbances caused by the presence of the pantographs in the scene make this approach inappropriate for analysis of the trackside video data.

3.4.4.2 Optical Flow

Optical flow is another class of motion detection technique used in computer vision to characterise and quantify the motion of objects in a video (Agarwal, et al., 2016). Horn & Schnuck, (1981) described optical flow as the distribution of apparent velocities of movement of brightness pattern in an image. This technique enables estimation of the object movement by considering the magnitude and direction of the flow vectors in two consequent video frames. Depending on the values of the flow vectors and observed discontinuities, the moving parts in the images can be recognised from the static background (Agarwal, et al., 2016).

Let $f(x, y, t)$ be the brightness function at point (x, y) in the image plane at time t. By considering the two fundamental assumptions of brightness constancy (i.e. pixel intensity remains the same along motion trajectory) and motion constraint (i.e. very small movement of a point in two consecutive frames), the motion velocity vector is estimated using the following formulations (Popescu, et al., 2016). Brightness constancy motion (BCM) model is expressed as:

$$f(x, y, t + T) = f(x - \Delta x, y - \Delta y, t) \qquad (3.11)$$

By applying a Taylor series on the right-hand term of Equation 3.11, the motion constraint or the optical flow equation is derived as:

$$f(x, y, t + T) = f(x, y, t) - \Delta x \frac{df}{dx}(x, y, t) - \Delta y \frac{df}{dy}(x, y, t) + o(|\Delta x| + |\Delta y|) \qquad (3.12)$$

Assuming D is the displacement vector defined as; $D = \begin{pmatrix} \Delta x \\ \Delta y \end{pmatrix}$, the spatial gradient of the image is determined as a vector of partial derivatives of illumination field f with respect to x and y.

$$\nabla f(x, y, t) = \begin{pmatrix} \frac{df}{dx}(x,y,t) \\ \frac{df}{dy}(x,y,t) \end{pmatrix} \quad (3.13)$$

Using Equation 3.13, the vector form of the Equation 3.12 would be:

$$f(x, y, t + T) = f(x, y, t) - D^T \nabla f(x, y, t) \quad (3.14)$$

Where $D(x, y)^T \nabla f(x, y, t)$ is the inner product of two vectors, the velocity vector can be achieved as:

$$V = \begin{pmatrix} u \\ v \end{pmatrix} = \lim_{T \to 0} \frac{D}{T} \quad (3.15)$$

and the optical flow equation would be:

$$V^T \nabla f(x, y, t) + \frac{df}{dt}(x, y, t) = 0$$

$$or \quad (3.16)$$

$$u(x, y) \frac{df}{dx}(x, y, t) + v(x, y) \frac{df}{dy}(x, y, t) + \frac{df}{dt}(x, y, t) = 0$$

The optical flow is defined as a matrix with identical height and width as in the image. u and v, the two unknowns of Equation 3.16 form the two layers of this matrix, defined to determine the offset of the movement of the pixels along axial x and y respectively. The two unknown variables of the optical flow Equation 3.16 originate aperture problem, in which objects physical motions appear indistinguishable. Figure 3-4 demonstrates this phenomenon by observing a section of a moving bar through a small aperture. Despite the bar moving in vertical and horizontal directions, its appearance remains the same and direction of the movement will not be distinguishable.

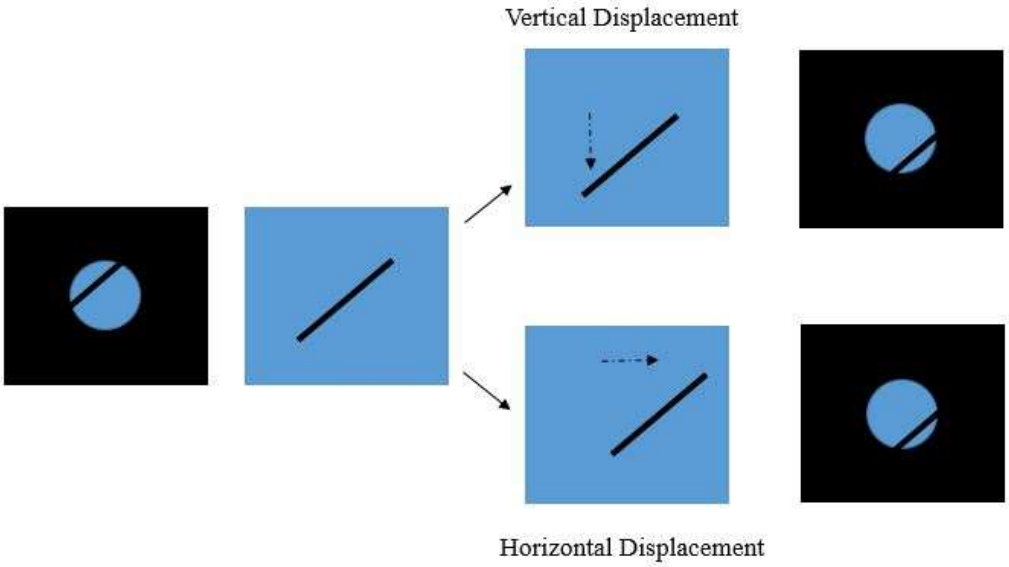


Figure 3-4: Aperture problem

In order to solve the optical flow equation, a homogeneity constraint for the displacement must to be applied. The optical flow is estimated through two methods of variational method and patch-based method developed by Horn & Schnuck (1981), and Lucas & Kanade (1981), respectively. The variational method using Horn & Schnuck (HS) algorithm in Equation 3.17, is a differential approach based on global optimisation that estimates the optical flow through minimisation of the cost function $J_{HS}(V)$.

$$J_{HS}(V) = \iint_{\Re} \left[u\frac{df}{dx} + v\frac{df}{dy} + \frac{df}{dt}\right]^2 dxdy + \lambda \iint_{\Re} \left[\|\nabla u\|^2 + \|\nabla v\|^2\right]dxdy \qquad (3.17)$$

Where, $\Re$ is the image region on which the optimisation is performed, and λ is a regularisation constant. The first term of the HS algorithm is a mean square error of the motion constraint and the second term is a regularisation term to ensure the gradient of the motion vector takes small values. Accordingly, the solutions for the two components of the optical flow are achieved as:

$$\lambda\nabla^2 u = \frac{df}{dx}\left[u\frac{df}{dx} + v\frac{df}{dy} + \frac{df}{dt}\right] \qquad (3.18)$$

$$\lambda\nabla^2 v = \frac{df}{dy}\left[u\frac{df}{dx} + v\frac{df}{dy} + \frac{df}{dt}\right] \qquad (3.19)$$

The two drawbacks of HS algorithm are the complexity of solving the optical flow equation through global optimisation and the sensitivity of selecting regularisation constant in smoothness variation and the numerical stability of the system. Instead of applying smoothness constraint, Lucas & Kanade, (1981) assumed the constancy of the motion vector in the local

region $\Re$, and expressed the optical flow equation for the entire pixels locations inside the region. The optical flow is then obtained through least-squares minimisation of the cost function $J_{LK}(V)$.

$$J_{LK}(V) = \sum_{i=1..n} w_i(u\frac{df}{dx}(x_i, y_i) + v\frac{df}{dy}(x_i, y_i) + \frac{df}{dt}(x_i, y_i))^2 \qquad (3.20)$$

Herein, the weighting factor w_i assigns larger weights to pixels locations that are closer to the centre of the region.

In the patch-based method, the optical flow is estimated by dividing the two video frames into patches of the same size and by applying variations of LK on the frame. The biggest drawback of the patch-based method is the challenge of detecting small moving object in the presence of other high amplitude movements such as movement of the camera. The recent advancements in both the variational and the patch-based methods involve different computation of the descriptor functions. Scale Invariant Feature Transform (SIFT) and Histogram of Oriented Gradients (HOG) are the two descriptors commonly used in the estimation of the optical flow (Savian, et al., 2020).

Although the displacement of the contact wire in the first few frames of the trackside video is relatively small, at the moment of the interaction with the pantograph the component vertical displacement increases significantly that generates errors in calculating the motion vectors. This is due to the second assumption of motion constraint that considers very small motion in between the frames, and derivation of the optical flow equation using the first-order Taylor series (Popescu, et al., 2016). Apart from part occlusion of the contact wire by the pantograph head (Panhead) at the moment of contact, the movement of the pantograph greatly disturb the motion vector field that make detection of the wire movement impossible. The solutions of smoothness constraint by Horn & Schnuck and local uniformity constraint by Lucas & Kanade also result in a poor accuracy along the boundaries of the moving object. This means the technique suffers to determine the contact wire movement variations at its' edges. These weaknesses make this technique inappropriate for analysis of the trackside data.

3.4.4.3 Difference Over Time

Difference over time is a technique of detecting the motion regions in videos based on the differences between the pixels of successive frames. Bobick & Davis, (1996) proposed a representation and recognition theory through developing an appearance-based recognition strategy that enables motion-based recognition by describing where there is motion and how the object moves. Motion energy image (MEI) (also known as binary motion region 'BMR')

was constructed to identify the location of motion in the image. The MEI represents the motion-shape and its spatial division, achieved through the computation of the optical flow of two consequent frames using a local gradient-based technique similar to Lucas & Kanade approach (described in Section 3.4.4.2). Then, the motion history image (MHI) is generated. Taken together, the MEI and the MHI can be viewed as two-components of the sample over time, where every component of each pixel is a function of the motion at that pixel location (Ahad, et al., 2010). The unification of MEI and MHI was constructed using MHI method with historical motion function $H_\tau(x, y, t)$, calculated from the differences in the image via an update function $\Psi\ (x, y, t)$.

$$H_\tau(x, y, t) = \begin{cases} \tau & if\ \ \Psi\ (x, y, t) = 1 \\ max(0, H_\tau(x, y, t-1) - \delta) & otherwise \end{cases} \qquad (3.21)$$

Where, (x, y) and t represent position and time, $\Psi\ (x, y, t)$ is the motion in the current video frame, τ determines the temporal extent of the motion, and δ is the decay parameter.

The update function was called for every frame of the sequence and generates a scalar-valued image in which recently moving pixels create brighter/darker regions, separating the motion regions from the background. Apart from being subject to the drawbacks of the optical flow (see Section 3.4.4.2), this method is limited in terms of:

- High sensitivity to object occlusions and improper implementation of the update function cause the recognition to fail.
- Failure to separate motion information in case of motion self-occlusion or overwriting.

3.4.4.4 Point-based Analysis of the Contact Wire Height Variations

Notwithstanding the drawbacks of the motion detection techniques described in Sections 3.4.4.1, 3.4.4.2 and 3.4.4.3, the non-trajectory nature of these techniques make extraction of the contact wire motion information across the video frames inefficiently challenging. Point-based analysis of the trackside images is developed by considering the appearance characteristics of the contact wire, the contact wire direction of motion and properties of the background. This approach enables the extraction of the contact wire height variations through frame-by-frame processing of the video data and identification of the contact wire location at each video frame. Occlusion of the contact wire by the pantograph is a significant obstruction in determining the contact wire uplift at or near the moment of contact. To mitigate the adverse impact of the presence of the pantograph on the monitoring performance, it is decided to restrict the operation to one column of the image matrix.

The trackside videos show the contact wire vertical vibrations as the pantograph moves along the span and passes by the section of the wire that is filmed. To achieve the contact wire vertical displacement, the video vertical resolution is remained untouched, while examining all the pixels value row-by-row correspond to the specified column number. Therefore, instead of N matrices (where $N = NumofFrames$) with a size of $[VidHeight \times VidWidth]$, there will be N matrices with a size of $[VidHeight \times 1]$ for processing.

Binarisation of the trackside image data is achieved by converting the images from their original true-colour format to greyscale and then, from greyscale to black and white using the Otsu's method (explained in Section 3.4.3.1). The global thresholding of the trackside image data after applying the computed threshold value allows categorisation of the image data into two classes of the contact wire and sky with pixels values of 1 and 0 respectively. After thresholding, the three-dimensional array of each video frame with the size of $[VidHeight \times 1 \times 4]$ is developed into a two-dimensional cumulative logical array with the size of $[VidHeight \times NumofFrames]$. From the developed 2-D logical array, the number of row pixels at logic one is counted for the mutual column number across the entire video frames. By taking to account both the returned number of pixels at logic one and the contact wire thickness in millimetre, the conversion factor is calculated, and the contact wire displacement graph is plotted in millimetre. The shape of contact wire across the frames remains almost the same that leads to the same number of pixels at logic one to be returned into the assigned cumulative array. Accordingly, the identification and removal of the noises caused by the passage of the pantograph from the monitoring point is possible based on the returned number of pixels at logic one, which present the contact wire in the scene.

3.4.4.5 Measurement of the Contact Wire Static Uplift

The contact-based trackside approach is developed to verify the reliability of the point-based analysis of the contact wire movement (explained in Section 3.4.4.4) in determining the amount of uplift in response to a known range of forces. For this reason, a mechanical tool is designed that applies a series of external forces to the contact wire and determine the amount uplift under each imposed force. Figure 3-5 depicts the designed apparatus for this purpose.

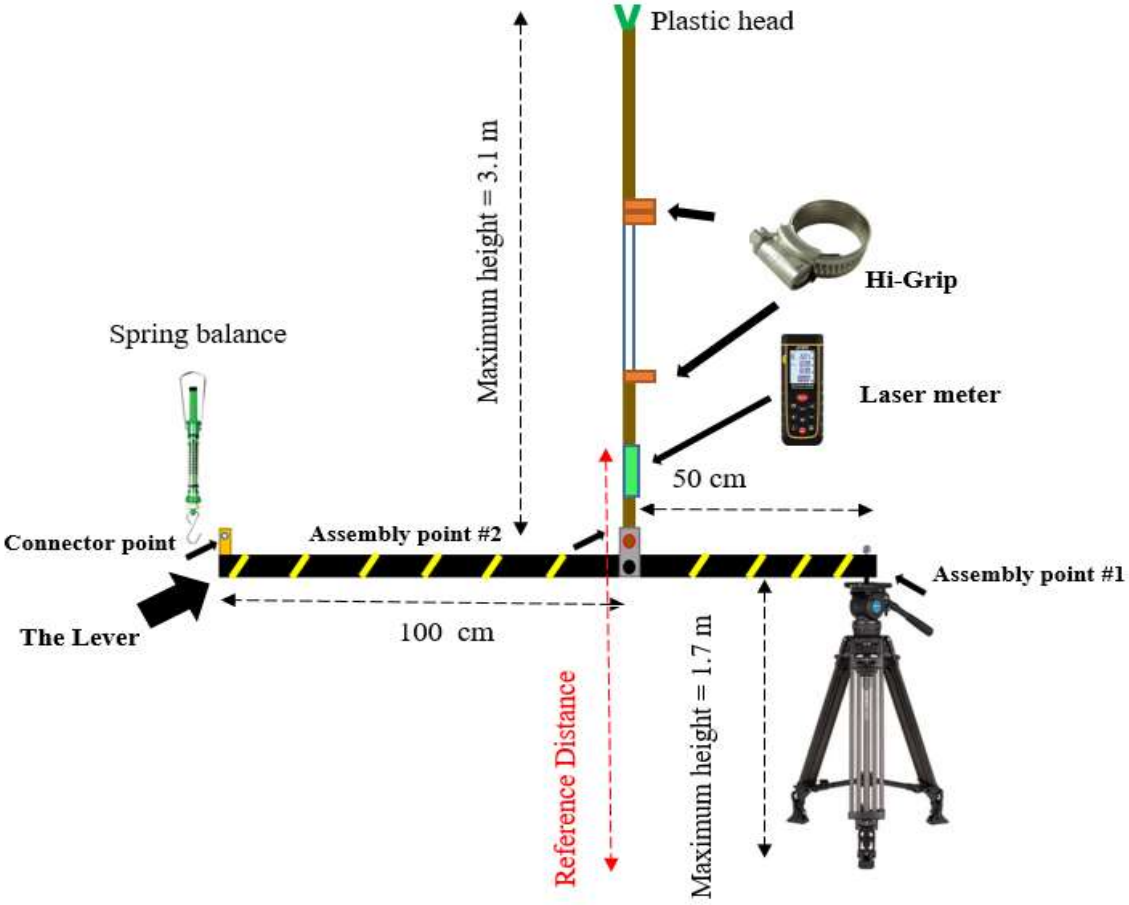


Figure 3-5: Schematic of the apparatus

The experiments are performed on seven locations along a 48.1meter span with dead wires located at Long Marston. The uplift of the contact wire at each test location is measured by a laser meter that is positioned above the holding bracket on the lifting arm of the apparatus, whilst the video camera records footages from the contact wire vertical movement. The apparatus and the video camera fixed on top of the tripod were moved from one test location to another until measurements over the entire span is completed. The recorded contact wire responses using the apparatus determine the contact wire uplift under four applied forces of 30N, 60N, 90N and 120N. The recorded videos from each test location are processed, and the contact wire uplift under each force is extracted and then compared to the recorded uplift from the laser meter. The detail of the verification process of the point-based monitoring approach is explained in more detail in Section 5.4.

3.4.5 Analysis of the On-board Data

Object detection in the dynamic background is still a globally challenging task for many, in artificial intelligence field. Cameras movement and the similarity between the background features has created different perceptions of dynamic backgrounds in the related literature. The on-board data are recorded by a camera fixed at certain angle that moves with the train. The specificity of the recorded video stream by the on-board camera is that static background objects appear to be moving. This is originated from the motion of the camera also known as 'ego-motion'. The on-board data shows the pantograph operation along the span series, up and down movement of the panhead, and the zig-zag motion of the contact wire across the working range of the panhead. In contrast to the trackside data that enables analysis of the contact wire vertical movement from the detection of the wire itself, the detection of the contact wire in the on-board video data can only determine its lateral movement. Figure 3-6 demonstrates the border of the contact wire movement across the panhead and its zigzag motion.

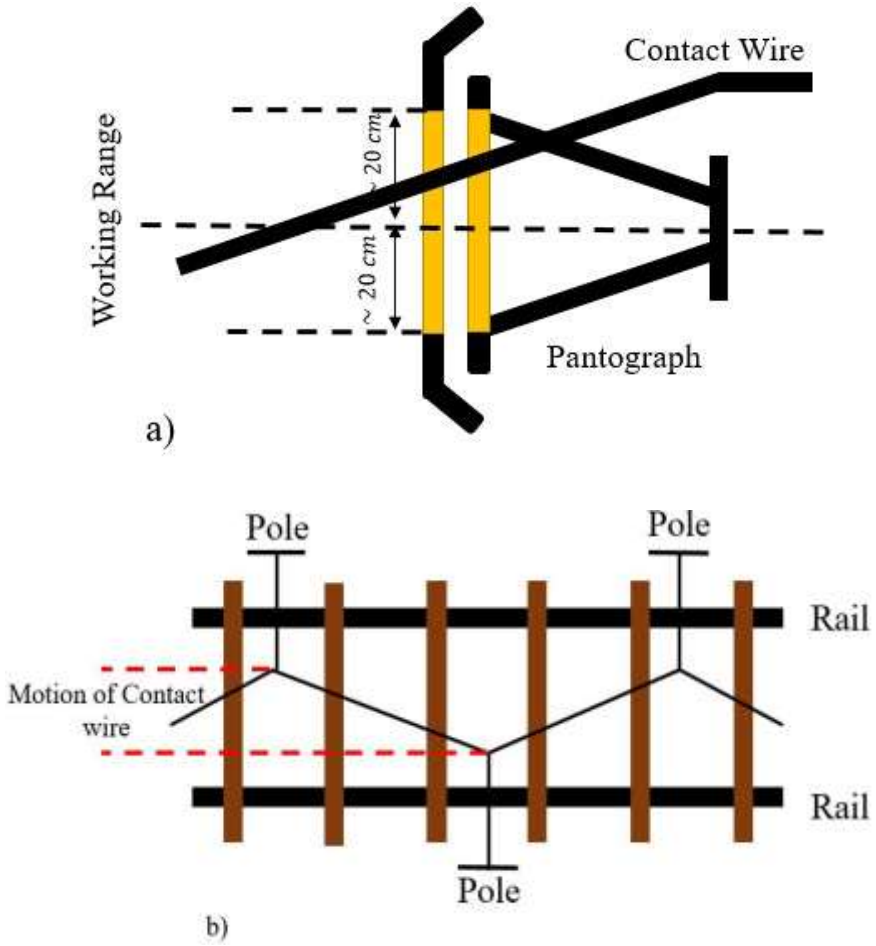


Figure 3-6: Contact wire dynamic behaviour a) sliding view of the contact b) contact wire zig zag motion

The lateral movement is one of the three parameters of the contact wire considered when monitoring the catenary-pantograph system performance. Monitoring of the contact point between the contact wire and the pantograph is possible through detection of the contact wire and the panhead based on their features in the image data. Detection of the contact wire is possible based on its line feature and using of Hough transform. Pre-processing of the data usually involves conversion of the video frames from their original true-colour format to greyscale and applying an edge filter to the greyscale data to reduces the amount of data in the image whilst preserving the important structural information.

In the images, the edges are defined as pixels at which the brightness values suddenly changes. The two commonly used edge detection algorithms are known as Sobel and Canny. In general, the Sobel operator is a kernel convolution process that returns a high response in case of sharp intensity changes in the greyscale image (Othman, et al., 2009). This process involves applying a Gaussian blur to the input image, removing the details/noises and enabling a smooth edge detection operation. The sobel operator runs in both x and y directions and calculates the gradient and orientations of the edges in the image. An enhanced version of sobel is canny edge detector that takes the produced edge image by sobel operator, applies a thresholding operation on the image to reduce the details further and generate finer edges. Figure 3-7 is a demonstration of a single frame of the on-board video and its conversion to an edge image through the use of the canny edge detector.

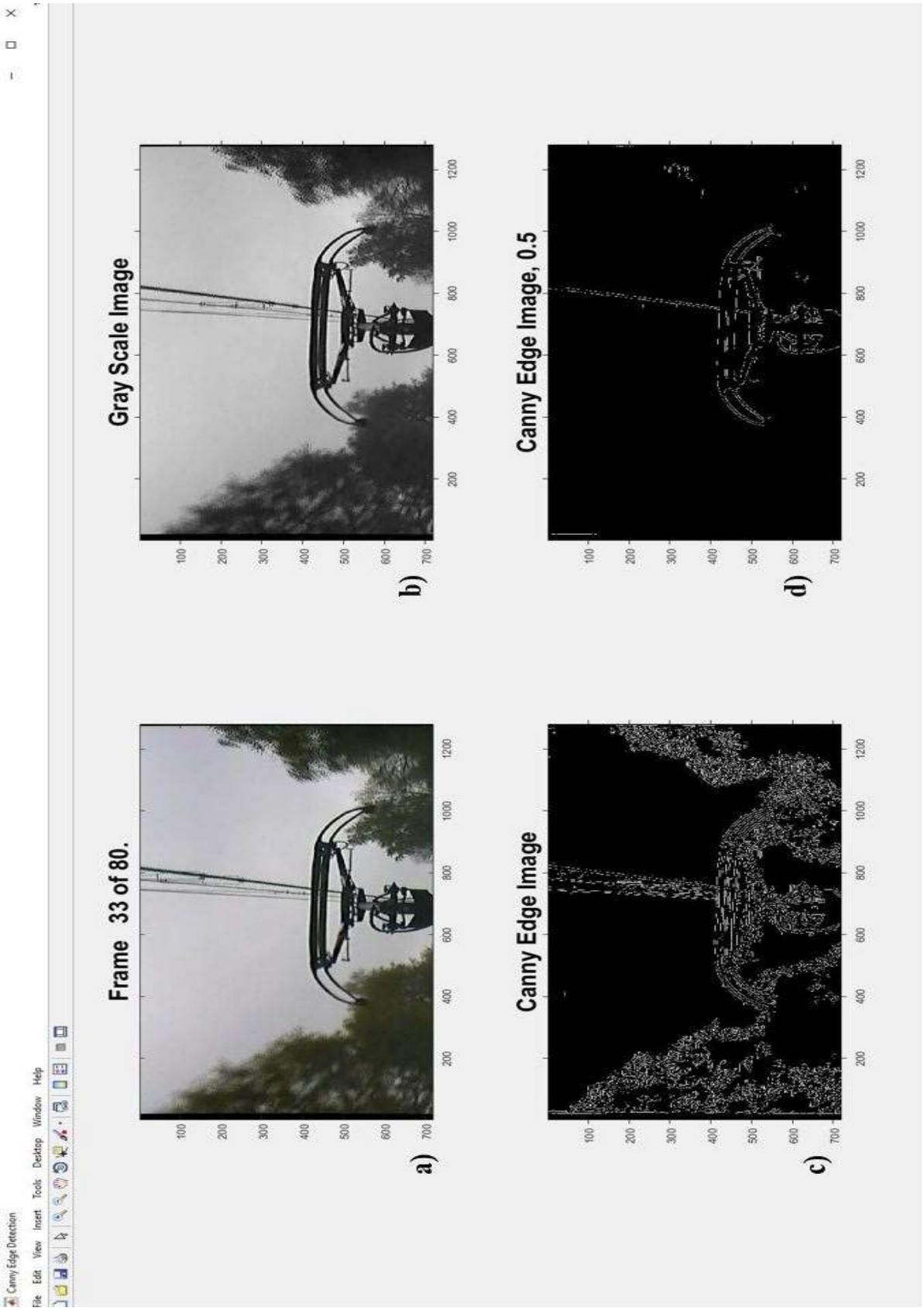


Figure 3-7: Edge detection operation a) true-colour image b) input grey scale image c) output edge image d) output edge image (figure by author)

3.4.5.1 Measurement of the Contact Wire Stagger via Hough Transform

Hough transform enables the recognition of straight lines by converting the edge image at pixel-level into a new space known as Hough or parameter space. A straight line is often described by its two parameters of slope a, and intercept b as follow:

$$y = a \cdot x + b \tag{3.22}$$

As vertical lines can give rise to unbounded values of the parameter a and b, the above line equation cannot represent vertical lines. In Hough space, lines are described by their polar coordinate parameters θ (theta) and r(rho), denoting the angle of perpendicular projection from the image origin to the line, and distance from the line to the origin respectively (Ballard, 1981).

Figure 3-8 demonstrates the polar transform of the straight line.

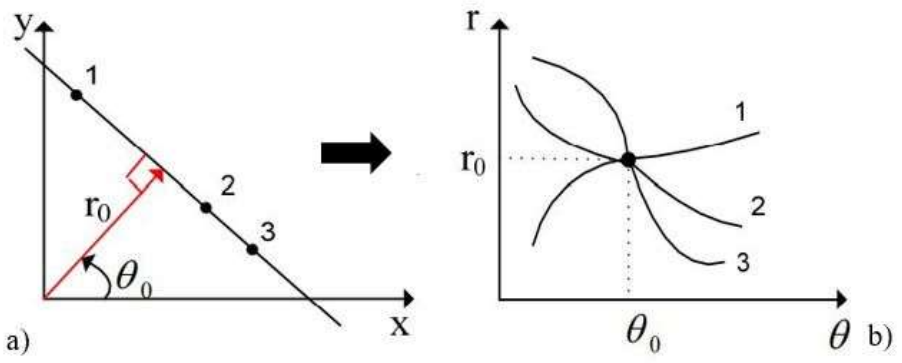


Figure 3-8: Hough transform, a) Line space, b) Hough space (Aydin, et al., 2014)

The polar coordinate of the straight line is expressed as:

$$r = xcos(\theta) + ysin(\theta) \tag{3.23}$$

In Figure 3-8 (b), a straight line in the polar coordinate system is plotted as a point with several other points passing through it. Each point forms a unique sine-like curves in Hough space, that share a common intersection point. Hough transform algorithm uses the voting method to determine the intersection point. The voting method uses a parameter space matrix whose rows and columns values are the returned r and θ respectively. At the beginning of the operation, the value of each cell of the transform matrix is zero. Throughout the operation, the value of each cell for the non-background points is obtained by calculating r for every θ, where, the θ range is $-90^{\circ} \leq \theta < 89^{\circ}$. The r value is then rounded off to the nearest allowed row in the transform matrix, and the accumulator cell is incremented.

Points with more Hough lines passing through them determine peaks of the Hough space. Each peak in the Hough space is specified by unique r and θ, representing potential lines of interest in the edge image. Figure 3-9 illustrates detection of the contact wire using the Hough transform.

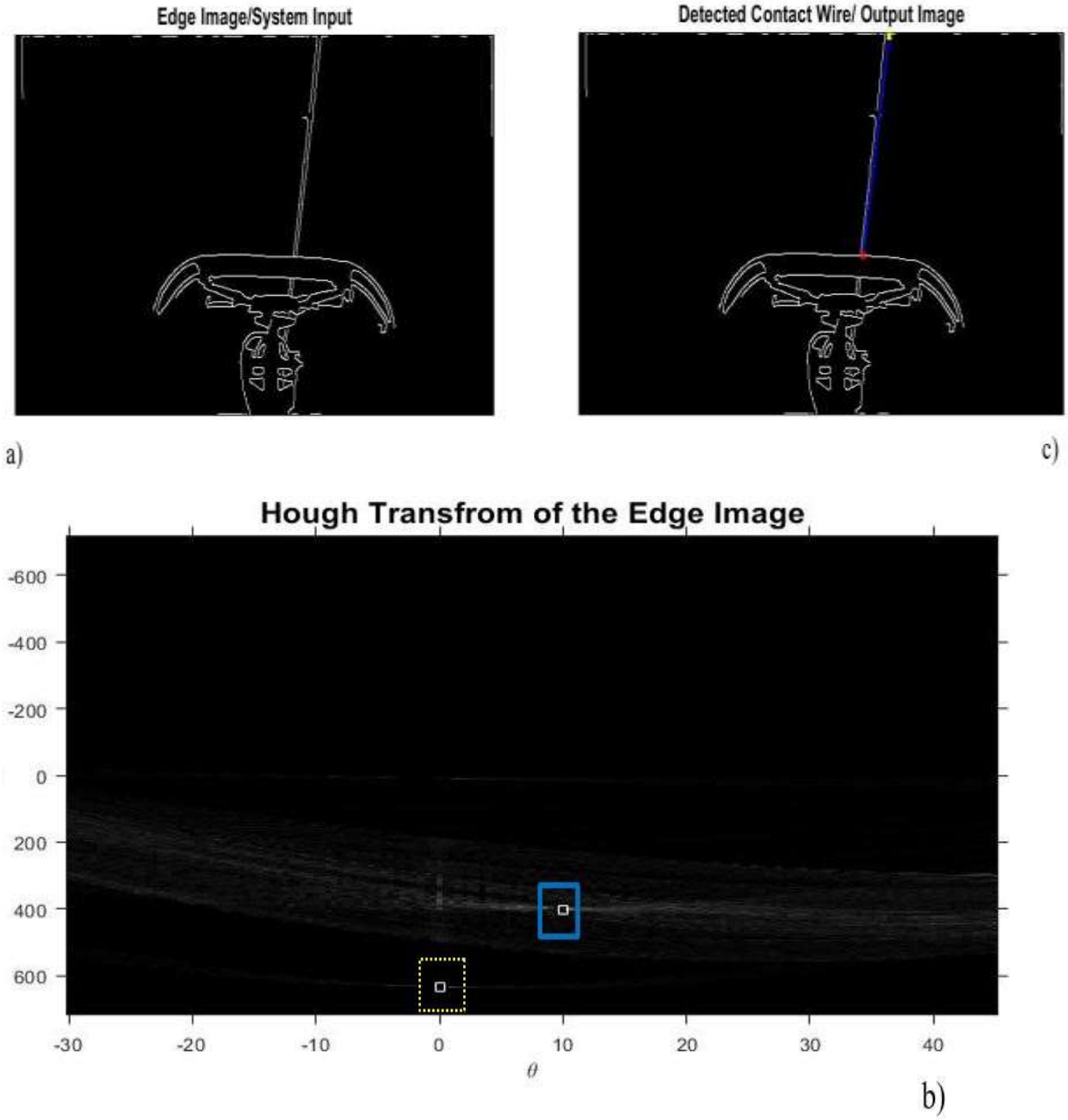


Figure 3-9: Detection of the contact wire via Hough transform. a) Input edge image, b) Line representation in Hough space, c) Detected contact wire (figure by author)

The performance of Hough transform is examined through implementation of line detection operation on a cropped version of the on-board data. The developed detection algorithm loops through every frame of the video and generates the output image along with displaying the

detected line as the video is streaming in real-time. Once the line detection at each video frame is completed, the computed specifications of the detected line are returned as a structure array with four components of Point1 (line startpoint), Point2 (line endpoint), θ and r. Figure 3-10 shows the performance of Hough transform in detecting the contact wire from the other background objects with line features.

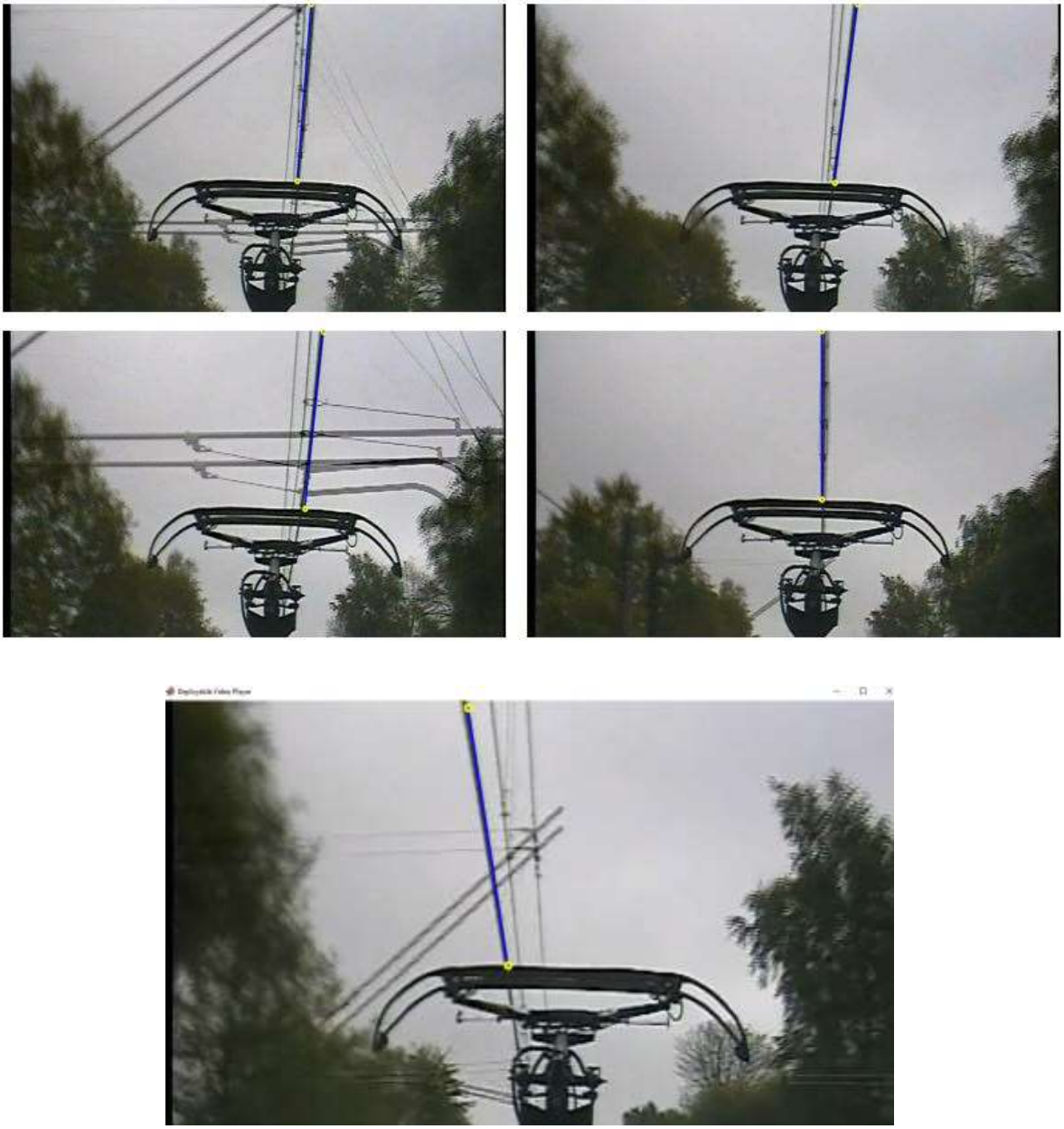
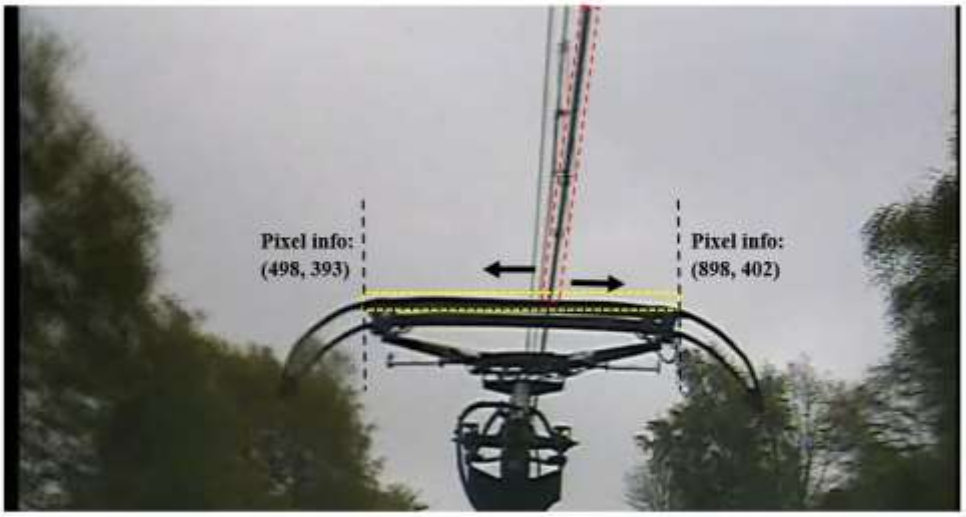
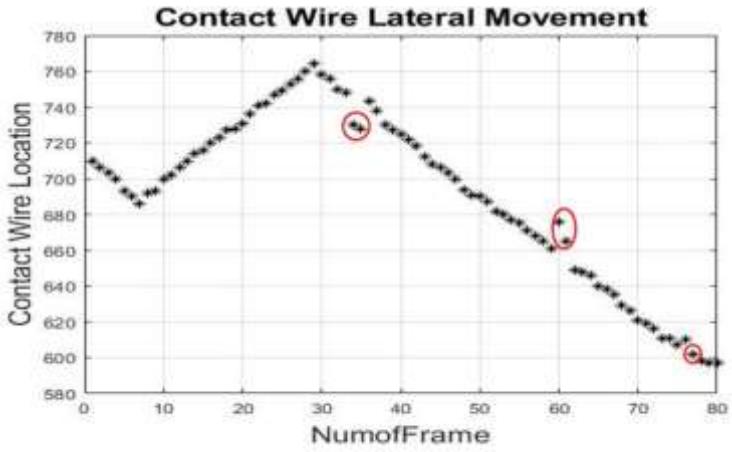


Figure 3-10: Detection results (figure by author)

The post-processing of the on-board data involves plot of the contact wire motion across the collector strips from the extracted x-values of the returned endpoint of the detected line. Figure 3-11 illustrates the contact wire lateral motion, obtained through performing the line detection operation on 80 video frames.



a)



b)

Figure 3-11: Trajectory of the contact wire lateral movement on working range of the pantograph (figure by author)

Although the developed line detection algorithm enables detection of the contact wire in the majority of the supplied samples, at some of video frames the tuned parameters for line detection cannot function as adequate. The red circles around some of the detection results show the errors in detecting the contact wire location across the panhead. This is mainly due to the brightness variations and changes in the intensity of the corresponding pixels to the contact wire. Such variations affect the performance of the canny operator and result in the edge image to be generated differently. Figure 3-12 demonstrates the corresponding errors to the points of false tracks shown in Figure 3-11.

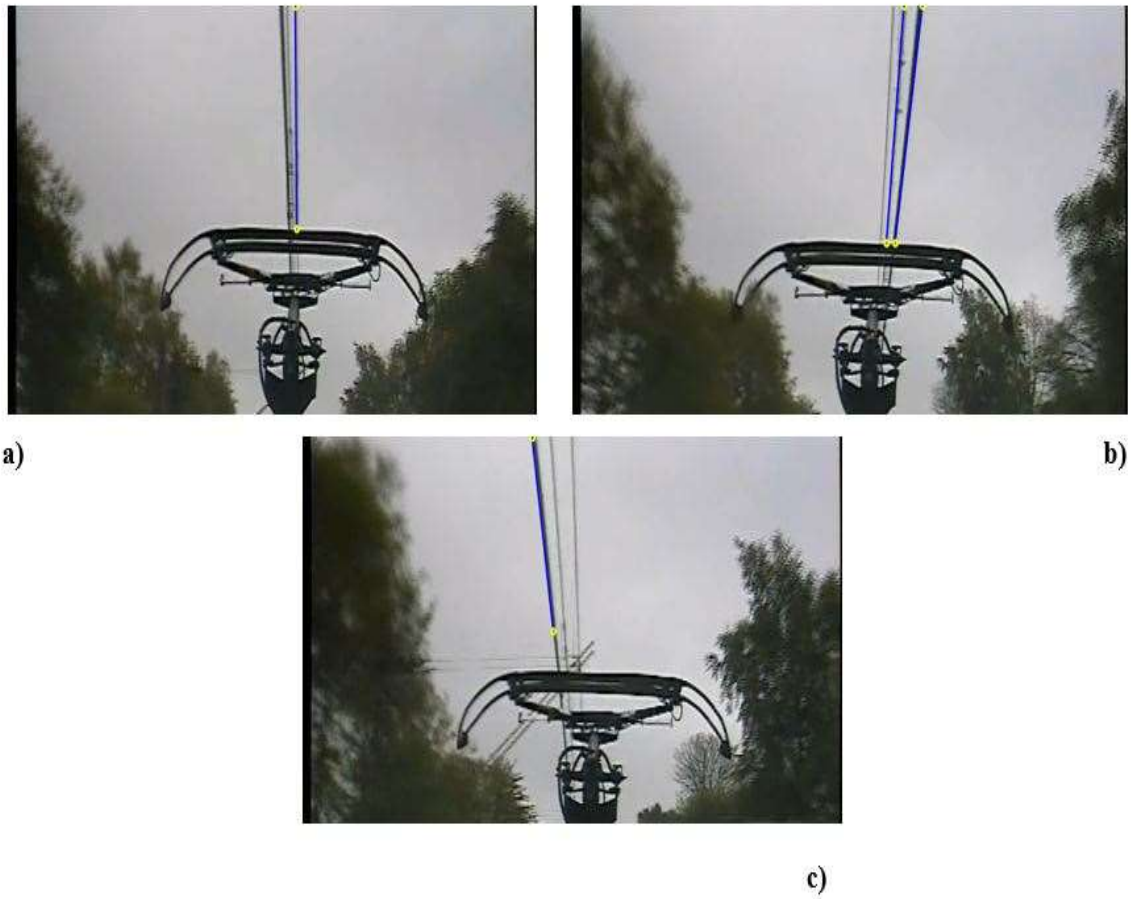


Figure 3-12: False detection of the contact wire (figure by author)

The errors within the illustrated plot in Figure 3-11 (b) are due to fast movement of the contact wire across the collector strip, discontinuities of the line representing the contact wire and the limitations of the detection parameters in handling the differences within the generated edge images. As a result, in Figure 3-12 (a) and (b), the similarity of the messenger wire to the contact wire and its location within the Hough transform search region have either caused false detection of the contact wire or, detection of both the wires simultaneously. To avoid such false detections, the neighbouring pixel around the detected Hough peak must be set to zero. In Figure 3-12 (c), part of the contact wire is detected. Although such an error causes insignificant differences within the contact wire displacement graph, the endpoint of the detected line does not reach the panhead. This means the adopted procedures lack to monitor the position of the contact wire based on its contact point with the panhead at some of the video frames.

Ideally, the contact wire lateral displacement graph should be plotted from the returned contact point coordination where the wire reaches the panhead. Detection of the contact point needs identification of both the contact wire and the panhead based on their line features. In the edge image, the pantograph upper side is presented as a horizontal line. To detect the pantograph

upper side, the image is tilted. This puts the desired line within the Hough transform projection angel ($-90^{\circ} \leq \theta < 89^{\circ}$).

Figure 3-13 demonstrates detection of both the contact wire and the panhead.

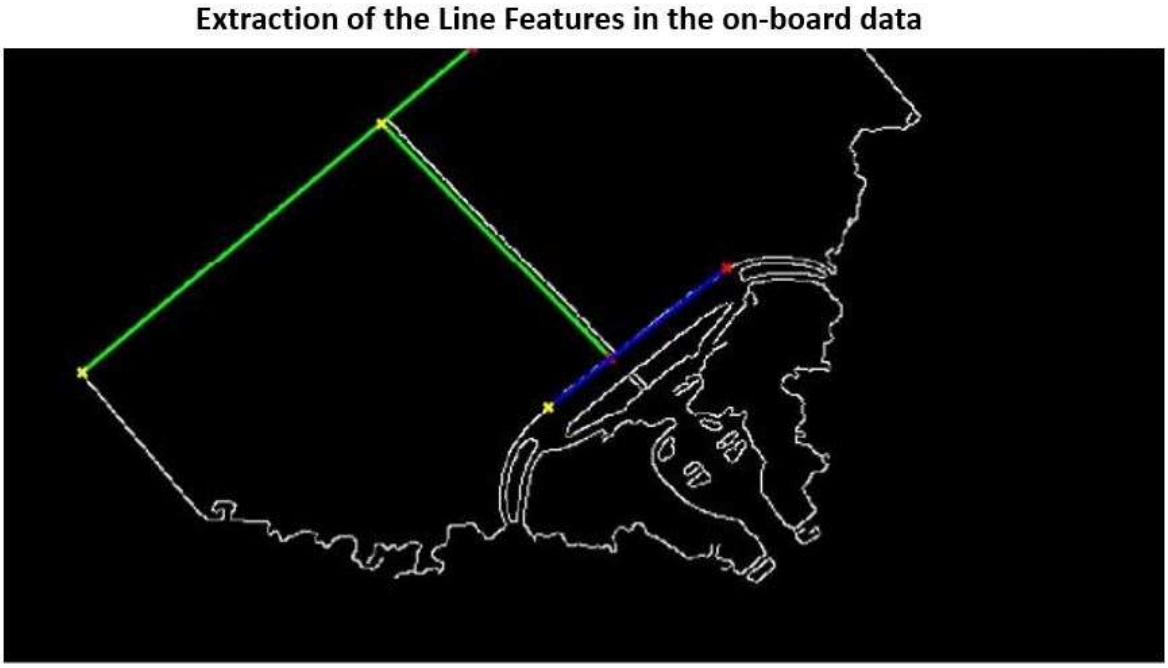


Figure 3-13: Detection of the contact wire and upper side of the collector strip

As can be seen from Figure 3-13, the rotation of the input image caused detection of the image boundaries, which highlights the need for restricting the search region to only locate the desired lines. The developed fault diagnosis approach by Aydin, et al. (2014), see Section 2.6.5, enables detection of the contact point through restricting the search space of the contact wire using the information of the returned pixels at the start and endpoint of the corresponding line to the panhead. The proposed monitoring algorithm by Aydin, et al., (2014) searches for the contact wire position based on the number of the edge pixel in the specified horizontally neighbourhood. Once the position of the contact wire in each video frame is found, the contact wire coordinates are saved to a diagnostic array. The elements of the diagnostic array are then used to plot the motion trajectory and to identify probable disorder between the two contact surfaces.

3.4.5.2 Determining the CW Height Variation

Estimation of the contact wire vertical displacement is possible through detection of its location at each frame of on-board video data. Detection of the contact wire in the on-board data can only help in measuring its lateral movement (see Section 3.4.5). For this reason, measurement

of the contact wire height variations is achieved by estimating its location through the detection of the panhead.

Object Recognition

Object recognition is the visual perception of objects despite changes in their colour, texture, size and form. The challenge of object recognition is detecting the object of interest from the scene and classify it according to its visual features. The recognition mechanism involves a visual sensor that acquires the information from the environment in which the object exists, a pre-processing unit that enables easier and faster recognition of the object, and a classification unit that classifies the detection results in the same categories or classes (Ghobadi, 2010).

Object recognition is more challenging when the background is not static; the followings are reviews regarding this matter (Chapel & Bouwmans, 2020):

- Existence of background objects that are not completely static such as waving trees.
- Complexities in separating the moving objects from static ones due to camera ego-motion.
- As the camera moves, the static background objects (buildings, bridges and etc.) move as well and should not be classified as foreground.
- Camouflage due to low contrast and fewer colour information cause the foreground to blend with the background and result in false negative (wrong classification of the foreground pixels).
- When the object moves long after the beginning of the video, the newly moving object and its old position in the background cause its recognition as foreground (known as ghosting)
- As the object stops moving it merges into the background and results in false negative.

The data obtained by the imaging sensors are often large and redundant and therefore cannot be supplied as input information to a system with real-time application. Feature extraction is a known technique that is usually applied in pre-processing of the data to extract the formative part of the data and boost the computational processing.

Feature Extraction

The processing time increases with the increase in the dimension of the input data. This is a major concern in designing systems with real-time applications. To address this issue, a set of information are derived from the original data known as feature vectors. Feature vectors hold the contents of each observation taken by the imaging sensor and reduce the dimensionality of

the input data. A proper feature extraction technique increases the efficiency of the object recognition process.

Machine Generated Features

Machine generated features are the similarities and the dissimilarities within the large data that cannot be usually seen by the human eye, but they can be highlighted by mathematical approaches such as Principal Component Analysis (PCA) and Linear Discriminant Analysis (LDA) (Ghobadi, et al., 2010).

Human Generated Features

Human generated features are knowledge-based data and are extractable via different heuristic approaches. Knowledge-based features provide abstract information regarding the object of interest that can be applied as the lower dimension features in detection algorithms. The knowledge-based features are application dependant and can be obtained either from the parametric visual data, or from the statistical properties of the data.

Parametric visual data provide information about shape, size, position and colour of the object which can be derived from the images using different image processing techniques. Some of these features are listed below:

- Corners in the Region of Interest (ROI)
- Lines in the ROI
- Edges in the ROI
- Colour

Statistical properties can be defined by the user based on the knowledge about the object of interest. Statistical properties provide information about the distribution of the data, such as variance of the pixel values, the number of non-zero pixels after the segmentation, standard deviation of the data and so forth.

The effectiveness of knowledge-based features in object detection is application dependant and they cannot always yield to satisfactory results (Ghobadi, 2010). To provide accurate information for classification of the object, the knowledge-based data can be integrated with the machine generated features. The product of this integration is called hybrid features.

Haar-Like Features

Haar-like features are rectangular features that are originated from Haar-wavelets, and are used in this work to enable recognition of the pantograph from the background objects in the on-board data. These features encode information about the object of interest which is difficult to

be extracted using the raw pixel data. Principle of Haar-like features relies on detection of the object information based on the adjacent rectangles in particular part of the image (Guennouni, et al., 2015). Figure 3-14 demonstrates the main types of Haar-like features known as; edge feature (the two top blocks in the figure), line feature (the block on the bottom left in the figure) and centre-surround feature (the block on the bottom right in the figure).

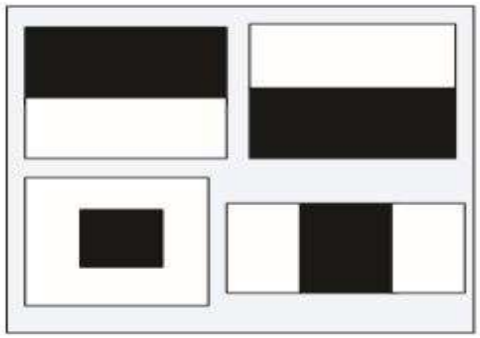


Figure 3-14: Haar rectangular features (Guennouni, et al., 2015)

The value of each Haar like feature is calculated through subtraction of the sum of pixel values in the black subregion from the sum of pixel values in the white subregion as:

$$f(x) = \sum_{black}(pixelvalue) - \sum_{white}(pixelvalue) \quad (3.24)$$

To detect the desired object, a search window that contains a Haar-like feature scans the image. The presence of Haar-like feature is then examined by comparing the value of the feature $f(x)$ with the threshold value θ computed in the training phase. When the value of $f(x)$ is above the computed threshold value, it means the feature exists within the search region and vice versa. Accordingly, the binary classifier for Haar-like feature would be:

$$h_t(x) = \begin{cases} 1 & if\ f(x) > \theta \\ 0 & if\ f(x) < \theta \end{cases} \quad (3.25)$$

Where $h_t(x)$ is a binary classifier for the Haar-like feature t.

Figure 3-15 illustrates the application of the edge features, the centre surround and the line features in extracting features of the pantograph within the scene.

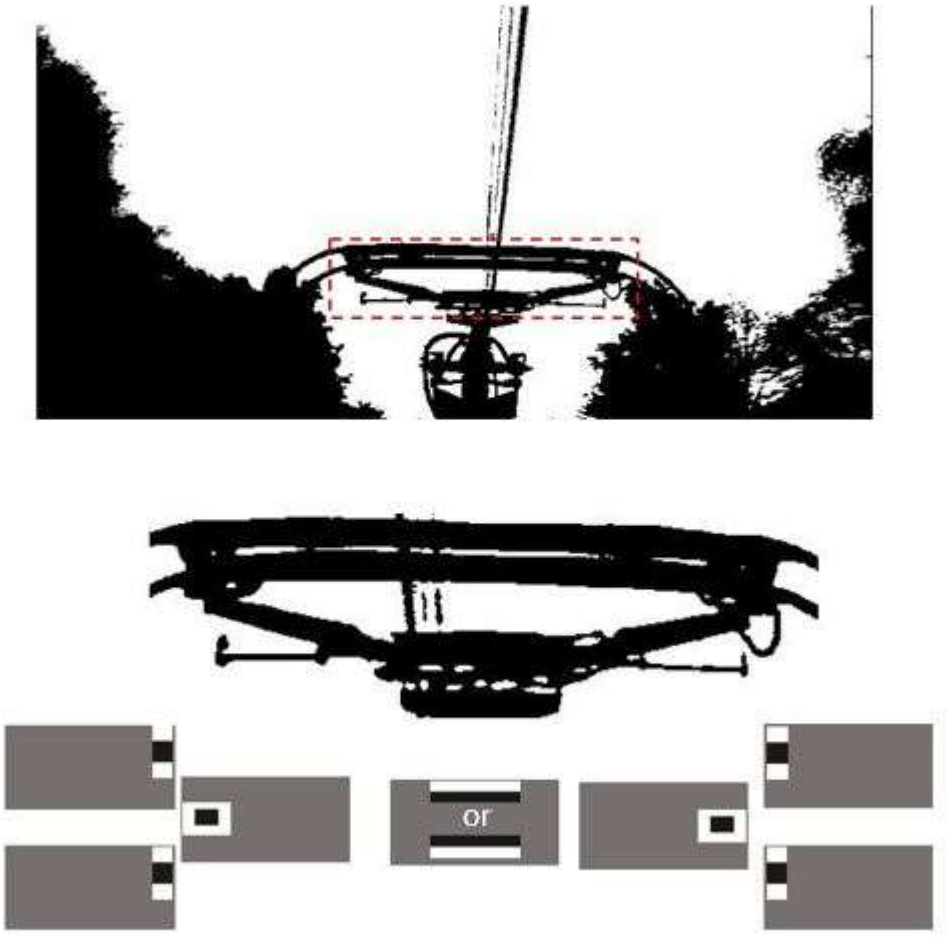


Figure 3-15: Discriminant features of the pantograph (figure by author)

Object Classification

Object classification is known as a procedure in which some decisions or forecasts are made according to the acquired observations (i.e. extracted features). Then, the decisions are applied to a new set of observations that classifies the data to the defined categories or classes. The proposed solutions for the object classification are grouped into three main categories of statistical models, neural networks and machine learning techniques. Due to lack of access to sufficient video data, the adopted approach to solve the classification problem in this work is a supervised learning classification using machine learning algorithm. On the contrary to an unsupervised learning in which instances are unlabelled, in supervised learning the decision function is built from the labelled training data. These decision functions or classifiers are applied to assign new observations to the defined classes. A classification system is implemented through three steps of (Ghobadi, 2010):

1. **Creating the dataset:** the training data D is created from the extracted features of m observations as:

$$D = \{(X_1, y_1), (X_2, y_2), \dots, (X_m, y_m)\}$$

where $X_j = (x_1, x_2, \dots, x_n)$ is an observation with n features and $y = (1,2, \dots, k)$ shows the output domain with k classes.

2. **Training:** depending on type of the problem, a training algorithm is selected to build a classifier from the created training dataset.
3. **Evaluation:** the generated classifier is tested with a test dataset that should ideally contain the same features used in the training dataset.

The followings are some of the known issues in the implementation of a classifier:

- **Generalisation:** the ability of the classifier in correctly assigning new observations that are not in the training set. In brief words, generalisation is the accuracy of a classifier in labelling the test data.
- **Speed:** speed of the classifier is an important factor when designing systems with real-time applications. For instance, a classifier with 90% accuracy might be preferred over a classifier with 95% accuracy if it operates 100 times faster in testing (Michie, et al., 1994).
- **Complexity:** A classifier should not be too complex else it might fit the noise and ultimately result in overfitting problem (Ghobadi, 2010). The key to avoid overfitting is to supply a lot of training data.
- **Size of the training data:** size of the training dataset is another important issue. Supervised learning techniques usually require a large training dataset for construction of strong classifier.
- **Time to learn:** time to learn is a vital factor when a classifier should be learned in real-time under a rapidly changing environment. This might indicate that a small number of observations would help in quicker learning of the classifier.

The two most popular supervised learning techniques are Support Vector Machines and AdaBoost technique (Kaur & Kaur, 2014).

Classification using AdaBoost

The utilised technique to classify the pantograph from background objects in on-board video data is a modified version of the adaptive boosting which was initially developed by Freund &

Schapire, (1999). In the original form of AdaBoost technique, the algorithm takes as input a training set of $(x_1, y_1), \dots, (x_m, y_m)$ where $x_i \in \mathbb{R}^m$ and $y_i \in \{\pm 1\}$, and then produces a strong classifier $H(x)$ by combining weak classifiers $h(x)$ through the following operation (Ghobadi, 2010):

$$H_T(x) = sign(\sum_{t=1}^{T} \alpha_t h_t(x)) \qquad (3.26)$$

For a uniform distribution of the data, the training samples are given with an equal weighting parameters w_i . This indicates all the samples have the same level of importance for the learning algorithm at the beginning of the training procedure. In each iteration the weak classifier is derived from the weighted training data. Once computation at each round is completed, the weighting coefficients α_i are updated so that the weights of the incorrectly classified samples in the previous round are increased. Accordingly, the weak learner is forced to focus on the hard sample data that are not correctly classified in the previous training round (Viola & Jones, 2001). The details of the AdaBoost technique are:

Given the training set D = $\{(x_1, y_1), \dots, (x_m, y_m\} \in \mathbb{R}^m \times \{\pm 1\}$

1) Initialise the same weighting factor of $w_i^{(1)} = 1/m$ for the entire samples
2) For $t = 1, \dots, T$:
    - Train a weak classifier by minimising the weighted error function as follows:

      $J_t = \sum_{i=1}^{m} w_i^{(t)} I(h_t(x_i) \neq y_i)$, $I(h_t(x_i) \neq y_i) = \begin{cases} 1 & if\ h_t(x_i) \neq y_i \\ 0 & otherwise \end{cases}$
    - Evaluate the error and compute the weighting coefficient as follows:

$$\epsilon_t = \frac{\sum_{i=1}^{m} w_i^{(t)} I(h_t(x_i) \neq y_i}{\sum_{i=1}^{m} w_i^{(t)}} \quad , \qquad \alpha_t = ln \frac{1-\epsilon_t}{\epsilon_t}$$

    - Update the weighting coefficient and increase the weights of the incorrectly classified samples

$$w_i^{(t+1)} = w_i^{(t)} exp\{\alpha_t I(h_t(x_i) \neq y_i)\}$$

3) construct strong classifier from the weak classifiers

$$H_T(x) = sign(\sum_{t=1}^{T} \alpha_t h_t(x))$$

Viola-Jones Method

One of the fastest yet most accurate approach in object recognition and classification is the detection technique proposed by Viola & Jones, (2001). This technique has been successfully used mostly to detect human faces from images or from the videos recorded by surveillance cameras. The performance level of the Viola-Jones method has extended its use in developing other computer vision applications such as vehicle tracking, analysing the traffic scene and traffic management (Moghimi, et al., 2018). The surveillance cameras are usually fixed at a certain angle, which means regardless of insignificant changes of the background objects the background remains the same. The developed on-board monitoring approach in this study uses the Viola-Jones method that enables recognition and classification by a strong classifier trained over thousands of training samples. The detection result at every single frame is displayed in the shape of a bounding box around the panhead. Once processing of each frame is completed, the returned coordinates of corner pixels around the bounding box (bbox) are saved into an array. From the returned pixels coordinates, the centroid of bbox in each video frame is calculated. The $calib\left[{}^{pixel}/_{mm}\right]$ is calculated using the length of the collector strips in reality and by counting the number of pixels featuring the collector strips in the image data. The movement of the pantograph is calculated based on the distance between the camera and the pantograph, camera coverage area and degree of the camera span (see Section 6.3.1). The contact wire height is estimated by considering the number of pixels between the centroid of the bbox and the upper side of collector strip.

Despite the successful application of Haar-like features in extracting information regarding the presence of the desired object in the scene, their computation can be time consuming. To speed up the computation time Viola & Jones, (2001) employed an intermediate representation of the image that is known as integral image, Figure 3-16.

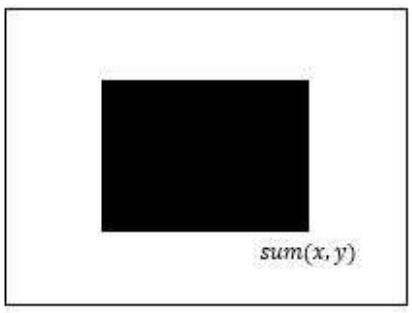


Figure 3-16 Integral image sum

The integral image at location x, y in Figure 3-16 is the sum of the pixels above and to the left of x, y, which is defined in Equation 3.27.

$$ii(x, y) = \sum_{x' \leq x, y' \leq y} i(x', y') \quad (3.27)$$

$ii(x, y)$ and $i(x, y)$ denote the integral and original images, that are achieved through Equations 3.28 and 3.29.

$$s(x, y) = s(x, y - 1) + i(x, y) \quad (3.28)$$

$$ii(x, y) = ii(x - 1, y) + s(x, y) \quad (3.29)$$

Where $s(x, y)$ is the cumulative row sum. Accordingly, when $s(x, -1) = 0$, and $ii(-1, y) = 0$, the integral image can be computed in one pass over the original image.

Integral image enables computation of any rectangular sum. For example, in Figure 3-17 the value of the integral image at location 1 is the sum of the pixels in rectangular A and the value of integral image at location 2 is the sum of the pixels in rectangular A and B.

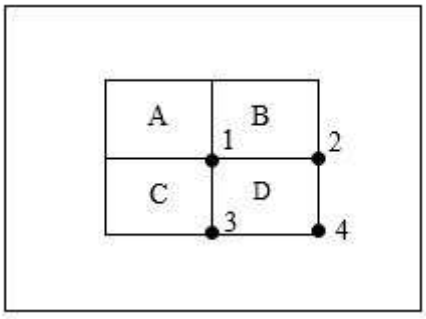


Figure 3-17 Integral image block

Accordingly, sum of the pixels in rectangular D is (Viola & Jones, 2001):

$$Sum(D) = ii(4) - ii(3) - ii(2) + ii(1) \quad (3.30)$$

In Equation 3.30, sum of pixels in rectangular D is the product of pixels values in rectangles $A + B + C + D$. Accordingly, $ii(4)$ is the sum of the pixels in rectangle D, $-ii(3)$ is the integral image of rectangle $A + C$,$-ii(2)$ is the integral image of $A + B$ and $+ii(1)$ is the integral image of rectangle A. The integral image of A is added to $sum(D)$ as it is subtracted twice in $ii(3)$ and $ii(2)$.

Although the integral images enable fast computation of Haar-like features, due to high number of these features, computation of all of them in a rapid object detection problem would not be feasible. Furthermore, majority of these features in the search window do not represent any

information about the desired object. To select a small set of Haar-like features and construct a strong classifier AdaBoost was applied. By applying AdaBoost to the training samples the best features with minimum error rate is iteratively selected throughout the procedure. Once the first best features are selected, the training samples are re-weighted such that the correctly classified samples gain smaller weights and the incorrectly classified ones are assigned a higher weight. At each iteration of the system a new best feature is selected and the samples are re-weighted accordingly. The product of running the algorithm after each round would be a weak classifier that corresponds to the best feature in that round. The final product is a strong classifier which is constructed from the weak classifiers.

For each feature a weak classifier is defined by:

$$h_j(x) = \begin{cases} 1 & if P_j f_j(x) < P_j \theta_j \\ 0 & otherwise \end{cases} \quad (3.31)$$

where x is the search window, f_j is the absolute value of the feature, P_j is the similarity that determines the direction of inequality and θ_j is the computed threshold throughout the AdaBoost procedure.

The performance of the constructed classifier by AdaBoost is not quite applicable in real-world object classification problems. Better detection performance and less the computational time is offered using Viola & Jones (2001) by arranging several classifiers in a cascaded form, shown in Figure 3-18.

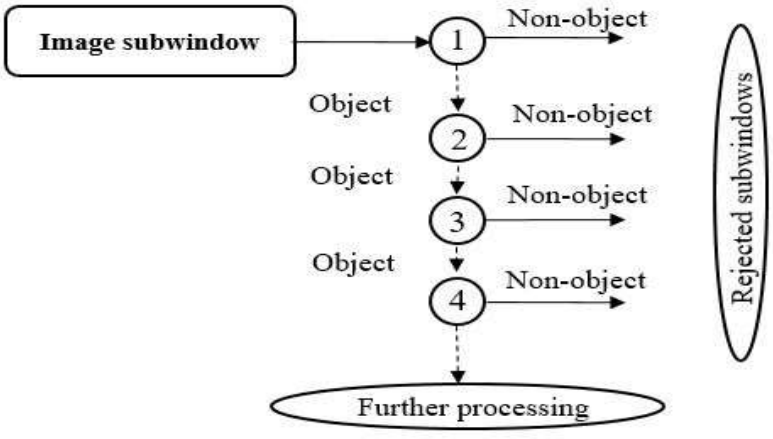


Figure 3-18:Cascade Classifier (Viola & Jones, 2001)

Using the cascade structure, the negative samples are rejected as fast as possible at the earliest stages. The first stage has a high detection rate of about 100% and an approximate false positive rate of 50% which means all the positive samples are detected correctly while half of the negative samples are rejected. Each stage reduces the false positive rate and decreases the detection rate. Since the detection rate at each stage is close to one, their multiplication yield to a final detection rate close to one, while the multiplication of the false positive rates approaches zero (Ghobadi, et al., 2010).

Figure 3-19 demonstrates the plot of the pantograph height trajectory, achieved from the processing of a cropped version of the on-board data. The graph shows the pantograph location based on the coordination of the bbox and the computed centroid of bbox in each frame. Herein, the obtained trajectory illustrates the reduction of the pantograph height (with respect to the image origin) towards the end of the video as the train starts to enter to the tunnel. Sections 6.3.1 and 6.3.3 discuss the application of the pantograph trajectory in estimating the contact wire height variation.

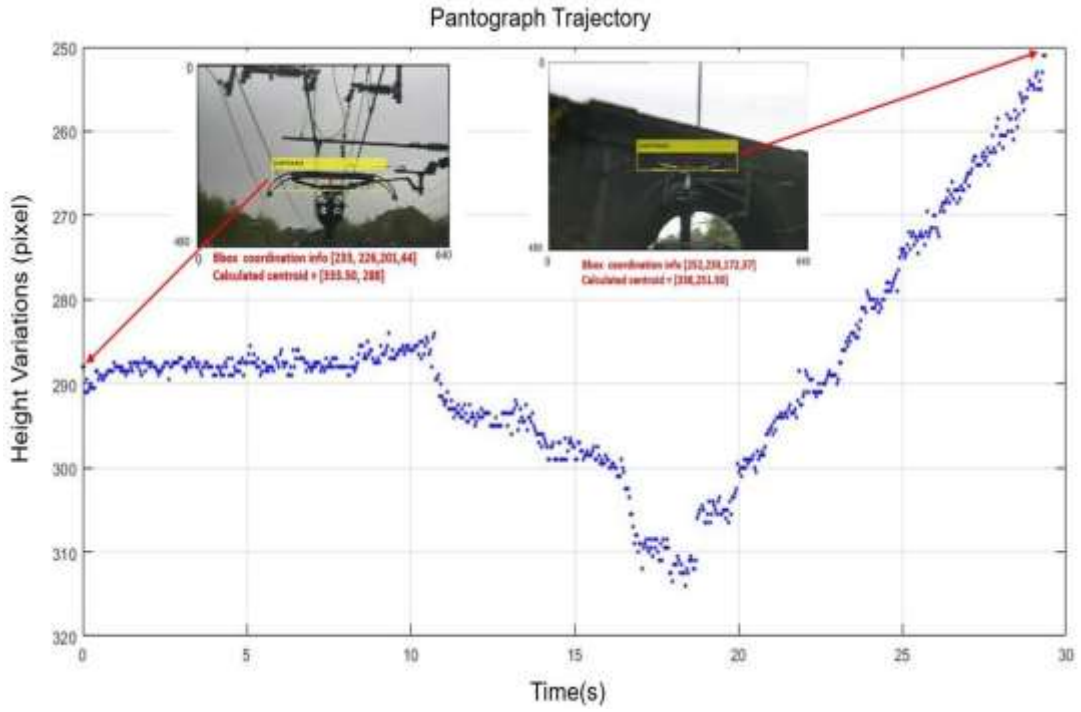


Figure 3-19: Trajectory of the pantograph, video length 29.39 seconds, bbox info at first frame [233,226,201,44] centroid [333.50,288], bbox info at last frame[252,233,172,37] centroid [338,251.50] (Figure by author)

Evaluation Metrics

The performance of an object detection algorithm is examined through three measures of precision, recall and quality. These measures are defined by quantitative metrics that classify the detection results into one of the three following categories (Moghimi, et al., 2018):

- True Positive (TP): the number of correct detection of the object.
- False Positive (FP): the number of wrong detection of a non-object, also known as false alarm.
- False Negative (FN): incorrect labelling of the object as background that appears as a missing track.

According to the above categories, the performance of the system in detecting the panhead across the video frames are evaluated through the following three measures:

$$Precision = \frac{TP}{TP+FP} \tag{3.32}$$

Precision is the proportion of correct detection of the panhead to the entire wrong and correct detections results.

$$Recall = \frac{TP}{TP+FN} \tag{3.33}$$

Recall determines the number of panhead correct detections across the video frames by considering the missing tracks.

$$Quality = \frac{TP}{TP+FP+FN} \tag{3.34}$$

Quality determines the overall accuracy of the detection method.

3.5 Summary

This chapter established a feasible methodology to enable the use of video data in determining the contact wire dynamic uplift by considering two aspects of monitoring. The classification of the trackside image data is achieved through a histogram-based thresholding technique that enables optimal selection of the threshold value for segmentation of the image data (see Section 3.4.3). The developed motion detection techniques were evaluated and the competency of the techniques in extracting the contact wire motion information through parametric assessment of each method were compared and assessed. Based on the assessments carried in Sections 3.4.4.1 to 3.4.4.3, it was discussed the contact wire appearance characteristic and its relatively fast up and down movement as the pantograph passes by the monitoring point have made these methods inefficient for the desired task. A new approach was established in Section 3.4.4.4

which enables measurement of the contact wire dynamic uplift through point-based analysis of the component response. The effectiveness of the developed vision-based trackside approach is examined through the design and fabrication of a mechanical tool that measures the contact wire static uplift in response to the exerted lifting forces described in Section 3.4.4.5. It was concluded in Section 3.4.5 that although, the trackside data enables the extraction of the contact wire height variations via detection of the wire itself, the positioning of the on-board camera on the train rooftop and the appearance characteristic of the contact wire in on-board data can only aid in monitoring the component lateral movement. For this reason, it was decided to achieve the component height variations through detection of the panhead. The broad obstacles of object detection in dynamic background discussed in Section 3.4.5.2, and the expected near real-time application of the system led to construction of a strong classifier using Viola-Jones method. The chapter discussed the key elements of Viola-Jones method and explained the impact of each element in an efficient construction of a strong classifier. The performance of the utilised detection technique is examined through three measures of precision, recall and quality.

Chapter Four

4. VISION-BASED TRACKSIDE MEASUREMENT OF THE CONTACT WIRE DYNAMIC UPLIFT

4.1 Introduction

This chapter introduces a novel vision-based monitoring approach that enables measurement of the contact wire dynamic uplift via a non-disruptive yet timely efficient operation. The footages are recorded by a video camera that is located at the side of the track with a sideway view to the contact wire. The recorded observations by the camera show the vertical oscillations of the contact wire before the arrival of the pantograph, at the moment of the contact and after the passage of the pantograph. Real-time analysis of the recorded footages not only allows examining the contact wire stability in response to the force of the pantograph, but also helps in identifying probable defects (e.g. crack initiations, wear of the wire, breakage of the dropper clamp and so forth) before they cause current interruptions or service cancellations at severe occasions. The chapter describes the processes through which the contact wire motion information is extracted from the videos and evaluates the goodness of the utilised segmentation technique by comparing the obtained response through analysis of the video data over each colour channel.

4.2 Measurement of the Contact Wire Uplift

Keeping the interaction between the contact wire and the collector strips of the pantographs healthy at all times is crucial to both infrastructure maintenance engineers, TOCs and TOFs. Damage of the pantograph (e.g. skew collector position) and wear of the contact wire affect the contact stability and result in contact-loss that further increases the wear rate within both the contact surfaces (Moeller, et al., 2002).

When the static uplift force is set too low, the low mean value of the contact force will trigger arcing that causes excessively low or unduly high uplift of the contact wire (Kiessling, et al., 2009). Excessive variations of the contact wire uplift from the planned range ($\sim 60\ mm$) result in disturbances within train operations, imposes speed restrictions and adversely affects the asset operational lifecycle. In addition to the important function of the uplift parameter in assuring the contact stability, measurement of the contact wire uplift is of a particular interest to infrastructure managers since it enables condition assessment of the asset itself and identification of faults affecting the performance of the contact components.

As mentioned in Sections 2.4.1.3 and 2.6.3.1, measurement of the uplift is usually performed through contact-based techniques with the requirement for installation of the measuring gadgets to the overhead line structures. For instance, the Jernbaneverket railway in Norway records the uplift by mounting the measuring arrangement at the cantilever. The recorded uplift data from the live contact line is then transmitted to the transfer unit at the base of the pole via an optical cable for further analysis of the recorded response (Thoresen, 2008). In Deutsche Bahn railway in Germany the uplift is also recorded through the installed measuring gadgets to the cantilevers. The arrangement includes an insulating rope that is fixed to the contact wire and leads to a potentiometer by a pulley. The rotation angle at the potentiometer is transformed into an electrical signal that determines the amount of uplift (Moeller, et al., 2002).

Measurement of the contact wire uplift together with the measurement of the contact force is of a particular necessity when commissioning the overhead contact line or testing the pantograph. In this way, the interaction between the contact wire and the pantograph can be examined, and the amount of uplift at different locations of the span (i.e. close to the supports and at midspan) can be calculated in accordance with the applied tensioning, train speed and the contact force. The planned uplift of the contact wire is then determined by evaluating the recorded uplift according to the requirements of the TSI energy (refer to Section 2.6.2).

The importance of measuring the contact wire uplift in monitoring of the asset condition and the drawbacks of the techniques that are currently in use by the industry indicate the demand for the monitoring technique under consideration in this work. In the continue, the chapter demonstrates the development of a vision-based system capable of extracting the contact wire uplift from the recorded trackside data through a fast yet efficient strategy with less/no requirement for human interventions

4.3 Design of the Trackside Uplift Measuring System

Development of the vision-based trackside monitoring system begins by investigating the possibility of extracting the contact wire height variations under service condition from the recorded videos. The proposed point-based analysis of the contact wire vibratory motions in Section 3.4.4.4 enables measurement of the contact wire uplift at its boundaries as the pantograph is pressing against it in real-time. The followings are descriptions of the input data, the processes and the expected output.

4.3.1 System Input

The data acquisition is performed by a video camera, which was fixed on a tripod and located around three meters away from the track, facing the contact wire from sideways at an elevation angle of 30 degrees. From the side of the track, the up and down motions of the contact wire in response to the pantograph force is recorded. In the recorded footages the contact wire is filmed as a thick horizontal line in a way that every single column of the image matrix contains a certain number of pixels that stores information of the presence of the wire in the scene. Data are recorded in MPEG-4 format and can be interactively selected by the user for the processing. Four datasets are utilised in this part of the research, enabling the measurement of the contact wire uplift in daylight condition. The recorded footages are the only source of information provided to achieve the expected output from the system.

4.3.2 Processes

Despite the cylindrical structure of the contact wire, the calibration set up, makes the component appear in more of a rectangular structure with sharp boundaries rather than round ones. The contrast between the contact wire and the background creates a good differentiation between these two in terms of their colours intensities. The following are the procedures through which the contact wire uplift is extracted from the videos.

- Segmentation of the image data.

- Identification of the contact wire location at each video frame from the returned pixel intensity values after binarisation of the image data using the computed threshold value.
- Plot of the contact wire vertical oscillations from the obtained cumulative array once the processing of the video data is completed.
- Removal of the disturbances caused by occlusion of the monitoring point by the pantograph at the moment of the interaction.
- Calculation of the uplift in millimetre based on approximation of the contact wire thickness in reality.

4.3.3 System Output

According to the system input and the processes, the expected output is the trend of the contact wire oscillatory motion under service condition that is used in calculating the amount of uplift under force of the pantograph and is of high importance to asset managers and senior decision makers.

4.3.4 Experimental Results

This section assesses the performance of the utilised logic, discussed in Section 3.4.4.4, in achieving the contact wire height variations. The data are in true-colour format, and the pre-processing of the data includes conversion of the data from its original format to greyscale. According to the colour intensity distribution and properties of the foreground (the contact wire) and the background (sky), segmentation of the trackside data is achieved through analysis of the histogram of greyscale images (see Section 3.4.3.1, Figure 3-3). The applied histogram-based thresholding enables binarisation of the greyscale data through minimisation of the within-class variances that determines an optimal value for the thresholding operation. After thresholding, depending on the stored amount of grey colour at each pixel, two values of one and zero are assigned to the corresponding pixels of foreground and background respectively. The contact wire oscillation in response to the pantograph operating along the contact line is obtained at a single column of the image matrix for every frame of the video. Apart from the selected column and its corresponding row values, the rest of the data at each frame are not considered in the analysis of the contact wire response that effectively optimises the processing time.

Since the contact wire oscillates vertically, the vertical resolution is remained untouched. The entire row values corresponding to the defined monitoring point are then stored in the allocated cumulative arrays. The contact wire initial response to the contact force is generated as a plot

of the positions of the corresponding cells to the contact wire at logic one. The post-processing of the data includes removal of the disturbances caused by occlusion of the monitoring point by the pantograph, and the plot of the height variations in millimetre considering the actual thickness of an unworn contact wire.

4.3.4.1 Analysis of the First Video Data

The first video data with the duration of 25 seconds and resolution of $[640 \times 480\ pixels]$ shows free oscillations of the contact wire after the passage of the pantograph. With the frame rate of 25 $frame/second$, monitoring of the contact wire oscillations is performed through identification of its location across 648 video frames. Binarisation of the image data is achieved through thresholding over each channel. To store the desired information, four cumulative arrays are assigned to the colour and grey channels before the system runs through the video frames extracting the pixels values. In every iteration of the system, the extracted values of each colour channel for the defined column in the current frame are stored inside the allocated array for each channel. This iterative process is repeated until the system is exhausted. The generated logical arrays with size $[480 \times 648]$ are then used to plot the contact wire response.

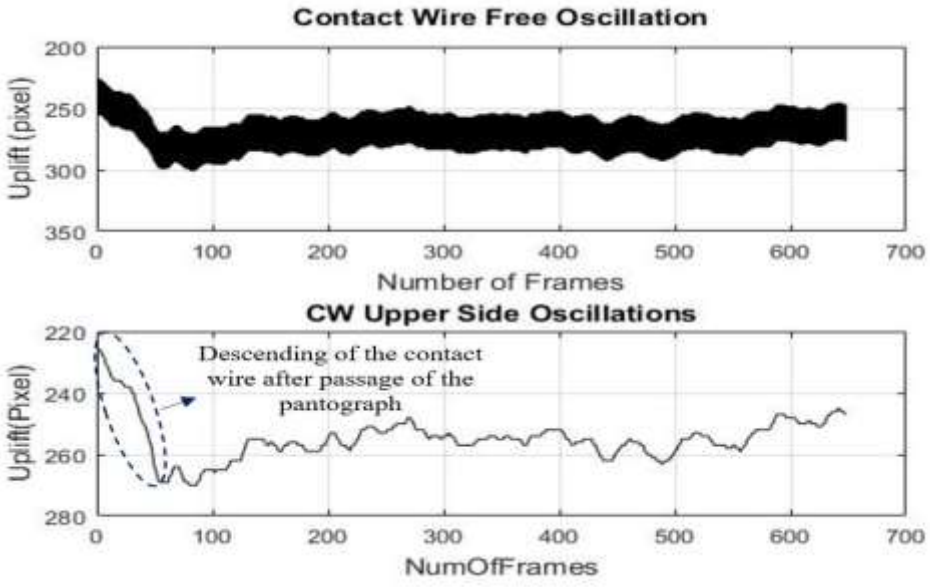


Figure 4-1: Contact wire free oscillations under service condition

From the constructed logical matrix, the returned number of pixels at logic one, representing the contact wire in the scene are counted as 31 pixels. Considering the contact wire actual thickness of 16 millimetres, the value of each pixel in millimetre is measured as approximately 0.5.

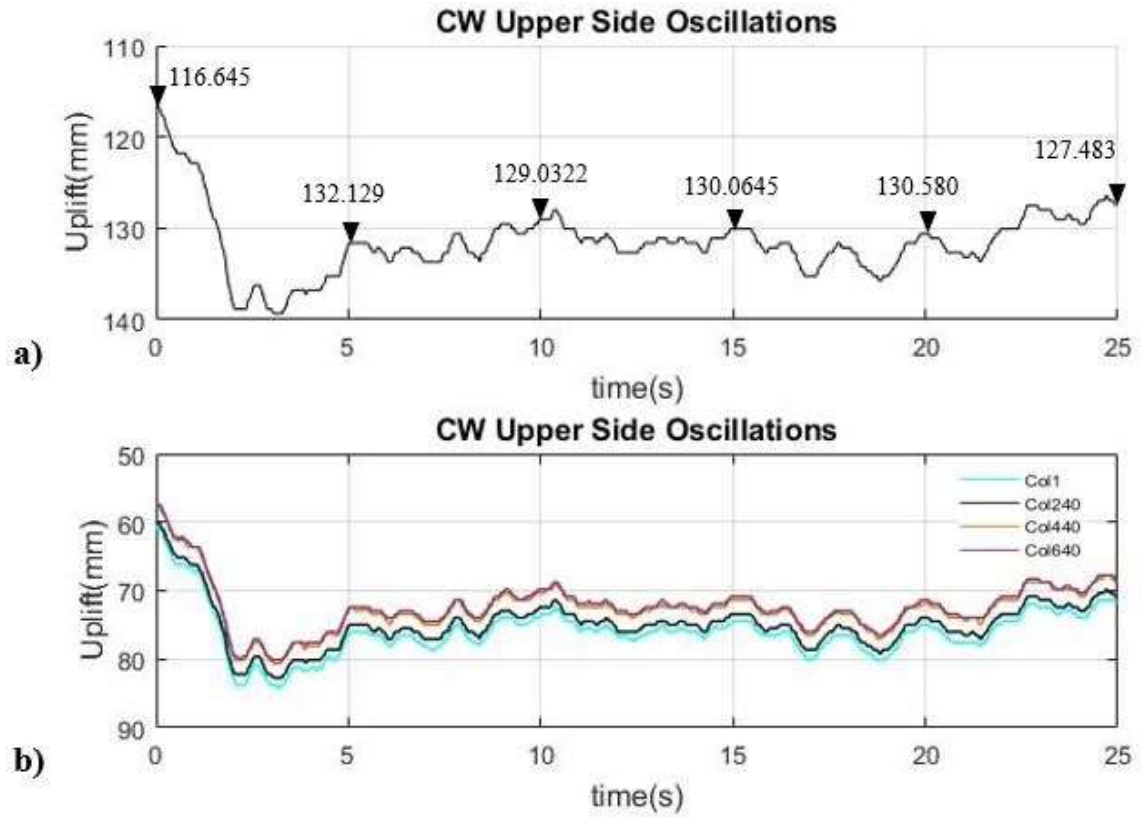


Figure 4-2: Contact wire oscillation a) CW oscillation in millimetre b) CW oscillation at different monitoring points, offset=56.645

Figure 4-2 (a) demonstrates conversion of the contact wire response to millimetre. As it can be seen the contact wire has a descending trend at the first two seconds of the video. Although there is no observation of the pantograph, from the recorded audio in the video file it was identified that the pantograph has just passed from the monitoring point. Accordingly, the descending trend of the contact wire movement at the beginning of the video is a demonstration of the component returning to its equilibrium state after the passage of pantograph. The total length of the contact wire under monitoring is 33 cm. To assure the similarity of the response at different locations of wire, the contact wire oscillation is obtained at four different monitoring points of 0.5 cm, 12.3 cm, 22.7 cm and 33 cm. As illustrated in Figure 4-2 (b), the trend of the contact wire oscillation follows a similar pattern amongst the selected monitoring points. The figure also shows a noticeable height difference between the first two (i.e. col1 and col240) and the second two (i.e. col440 and col640) monitoring points. This is related to the greater impact of the lifting force depending on the time lapsed after the passage of the pantograph and the gradient of the contact wire in the images.

4.3.4.2 Analysis of the Second Video Data

The second data with the duration of 14.88 seconds shows oscillations of 54.8 cm of the contact wire caused by running of the two pantographs. The contact wire response to the contact force is obtained through processing of 372 extracted frames from the video data. Figure 4-3 demonstrates the initial plot of the contact wire response.

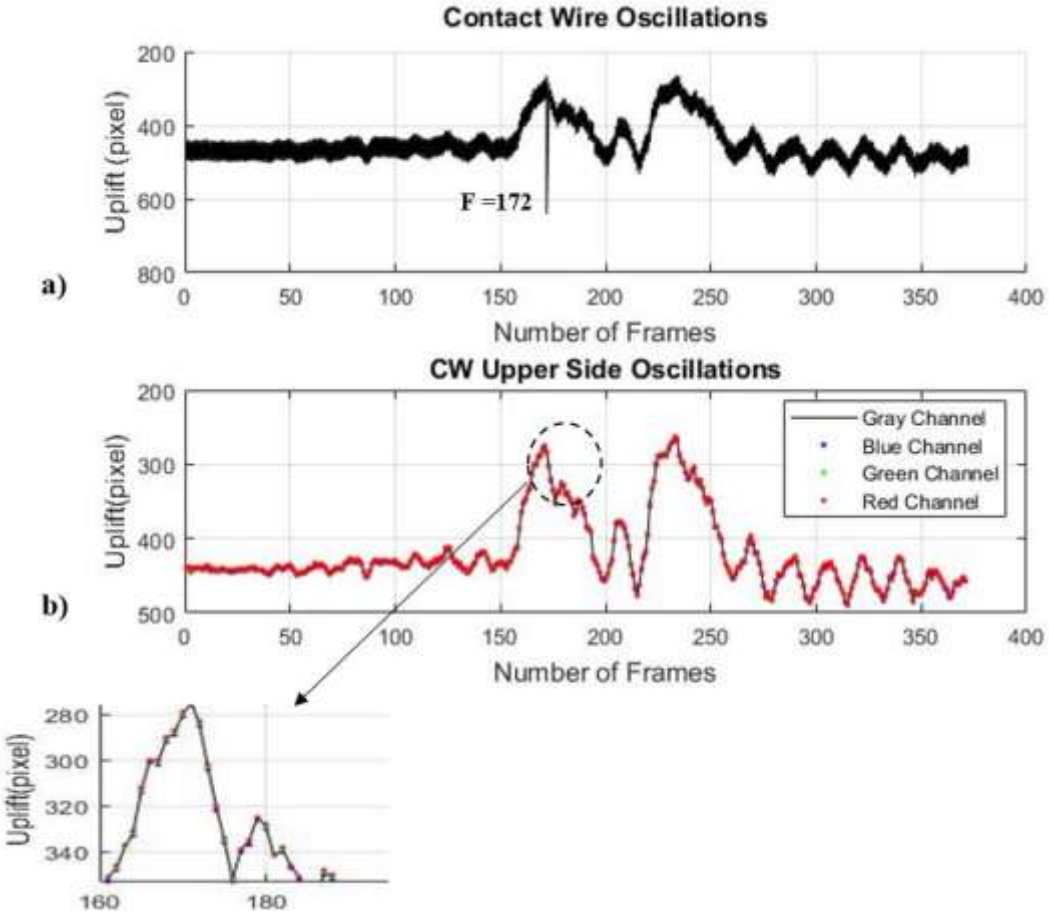


Figure 4-3: CW oscillations caused by the passage of two pantographs

The resolution of each extracted frame is $[1080 \times 1920]$. This means the oscillation is the plot of the logical matrix with a size of $[1080 \times 372]$. In Figure 4-3 (a), occlusion of the monitoring point by the pantograph resulted in returning of higher number of pixels at logic one to the assigned cumulative array. In this video, the occlusion only occurs when the first pantograph was passing by the selected monitoring point. Figure 4-4 demonstrates the location of the pantographs from the monitoring point in the two frames of the video at which the occlusion of the contact wire happened.

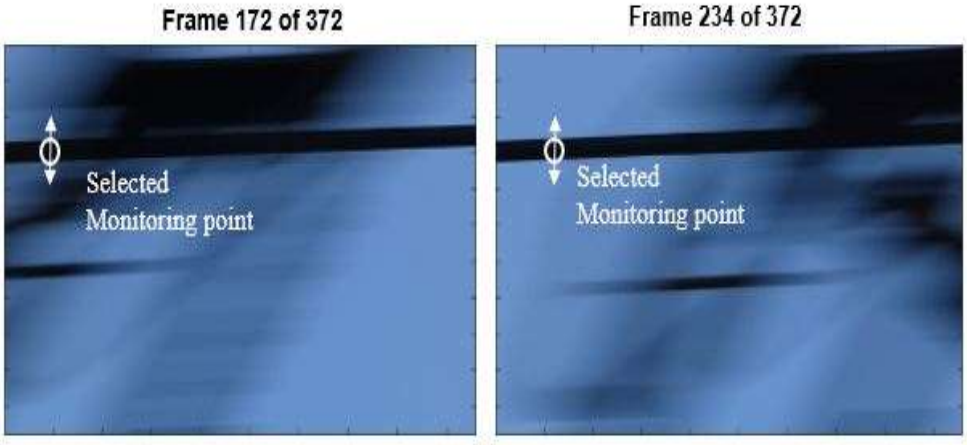


Figure 4-4: Position of the pantographs from the selected monitoring point at the moments of maximum uplift

The disturbance caused by the presence of the pantograph on the monitoring point is filtered out from the response plot based on the counted number of the pixel at logic one in the reference column. The developed system checks the number of the returned pixels at logic one at every single column of the generated logical matrix and outputs the frame number at which the disturbance occurred.

In order to examine the goodness of the utilised thresholding in segmentation of the image data, the contact wire response is obtained according to the amount of red, green and blue colours, stored at each corresponding pixel to the contact wire. Figure 4-3 (b) demonstrates the initial plot of the contact wire oscillations obtained over each channel. The similarity of the response characteristics verifies the goodness of the utilised thresholding over the grey channel in determining the contact wire oscillations and measuring its uplift.

The number of the corresponding contact wire pixels at the selected column matrix is counted as 56 pixels, which together with the actual thickness of the wire determine the conversion coefficient of approximately 0.28 $mm/pixel$. Figure 4-5 is the contact wire oscillation in millimetre, plotted for the colour and grey channels.

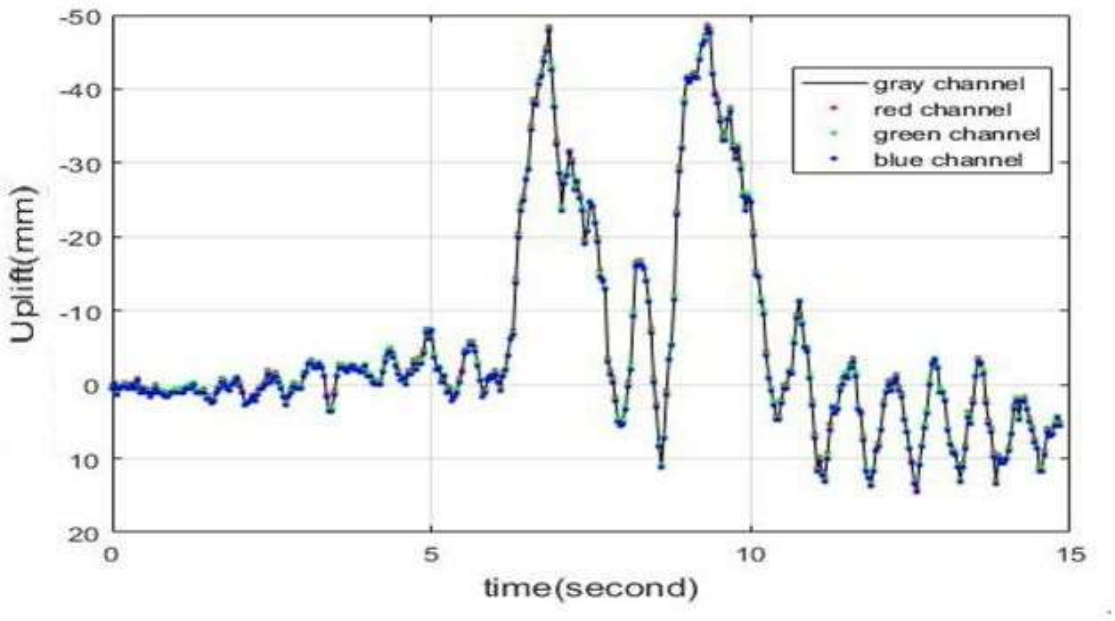


Figure 4-5: CW upper side vibrations, offset = 122.92mm

Since the height of the contact wire under no-load condition is unknown, the maximum uplift of the contact wire is calculated for the first three seconds of the video when the wire is not yet considerably displaced from its equilibrium position.

Table 4-1: Calculated maximum uplift over the colour and the grey channels

Reference Column Matrix		**Channel(s)**	**First Contact (F =172, t= 6.88 seconds)**	**Second Contact (F=234, t= 9.36seconds)**
Frame Number	**CW Vertical Location**	Grey	48.16	48.04
Frame = 25 time = 1second	−0.84	Red	48.44	48.72
Frame =50 time = 2seconds	1.12	Green	48.16	48.44
Frame=75 time= 3 seconds	−0.28	Blue	48.16	48.44

According to Table 4-1, the maximum uplift of the contact wire in response to the contact force is measured as approximately 50 mm. This is the height difference of the location of the contact wire between frames 50 and 234 (i.e. moment of the interaction with the second pantograph) over the red channel. The maximum uplift of the contact wire calculated over the grey channel between frames 50 and 172 (i.e. moment of the interaction with the first pantograph) shows a displacement of 49 mm. Taking into account the measurement error when calculating the uplift

over each channel, it is found that the maximum uplift of the contact wire has a range of between 47 and 50 mm.

Table 4-2: Measurement of the CW maximum uplift

Channel	**Measurement of the Contact wire uplift**					
	First pantograph (t = 6.88 seconds)			**Second pantograph (t = 9.36 seconds)**		
	t = 1s, −0.84 mm	**t =2s, 1.12 mm**	**t = 3s, −0.28 mm**	**t = 1s, −0.84 mm**	**t = 2s, 1.12 mm**	**t = 3s, −0.28 mm**
Grey	47.32	49.28	47.88	47.2	49.16	47.76
Red	47.6	49.56	48.16	47.88	49.84	48.44
Green	47.32	49.28	47.88	47.6	49.56	48.16
Blue	47.32	49.28	47.88	47.6	49.56	48.16

4.3.4.3 Analysis of the Third Video Data

The third video data with the duration of three minutes and five seconds, and resolution of $[480 \times 640]$ shows oscillations of 31 centimetres of the contact wire caused by the running of two pantographs. With the frame rate of 25 f/s, the contact wire response is calculated through processing of 4632 frames. After the thresholding operation, the number of pixels at logic one at the reference column is 33 pixels. This combined with the assumed wire thickness of 16 mm define the value of each pixel as 0.48 $mm/pixel$. The system counts the returned number of black pixels at every single column of the generated matrices with the size of $[480 \times 4632]$ and then outputs the frame numbers consisting more than 33 black pixels in their reference column structure. After processing of the data, a total number of nineteen frames have been traced that are generating the disturbances in the response plot. Out of the nineteen returned frames with disturbances, ten frames are subjected to the occlusion of the monitoring point by the first pantograph and the remaining nine frames are due to the occlusion by the second pantographs. Figure 4-6 demonstrates the initial trend of the contact wire uplift as well as some of the frames causing the disturbances at the moments of interaction with the pantographs.

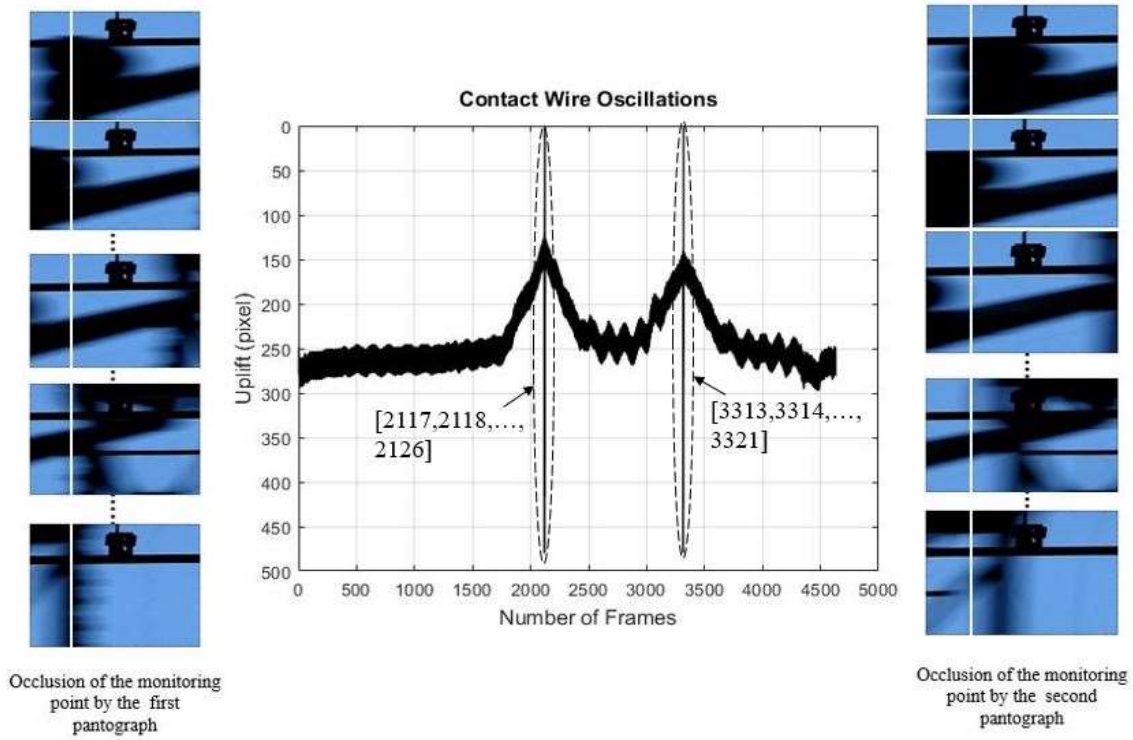


Figure 4-6: CW Oscillations due to running of the two pantograph

Figure 4-7 shows the contact wire oscillation after the conversion of each pixel to its value in millimetre.

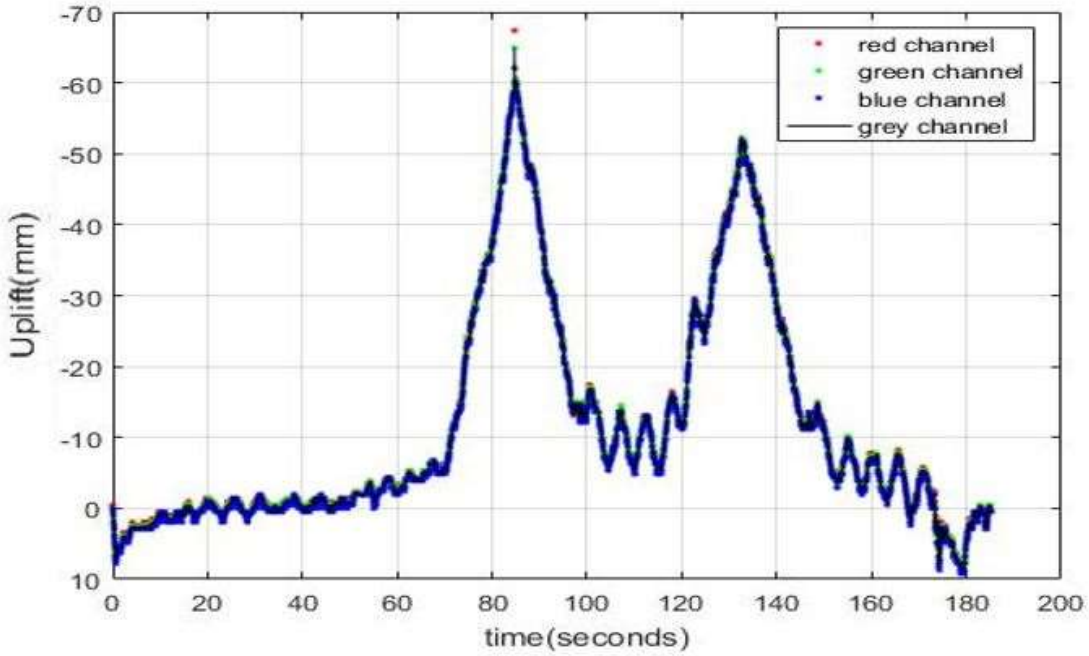


Figure 4-7: Upper side oscillation of the CW, offset = 120.71 mm

Table 4-3: Measurement of the Maximum Uplift at the moment of contact

Reference Column Matrix		**Channel(s)**	**First Contact (F =2118, t= 84.72seconds)**	**Second Contact (F=3325, t= 133 seconds)**
Frame Number	**CW Vertical Location**	Grey	64.963	51.388
Frame = 500 time = 20 (s)	0.969	Red	67.387	51.873
Frame = 2875 time =115 (s)	5.332	Green	64.963	51.873
Frame= 4000 time= 160 (s)	7.271	Blue	62.054	51.388

Table 4-4: The computed uplift corresponding to each channel

Channel	**Measurement of the Contact wire uplift**					
	First pantograph (t = 84.72 seconds)			**Second pantograph (t = 113 seconds)**		
	t = 20s, 0.969mm	**t =115s, 5.332mm**	**t = 160s, 7.271mm**	**t = 20s, 0.969mm**	**t =115s, 5.332mm**	**t = 160s, 7.271mm**
Grey	63.99	59.631	57.692	50.419	46.056	44.117
Red	66.418	62.055	60.116	50.904	46.541	44.602
Green	63.994	59.631	57.692	50.904	46.056	44.602
Blue	61.085	56.722	54.783	50.419	46.056	44.117

Table 4-4 determines the amount of uplift at the moments of the first and the second contacts with the pantographs. The values are calculated based on the locations of the contact wire at the specified frame intervals. The contact wire uplift due to running of the first pantograph has an approximate range of [61 66] millimetre compared to its location at t = 20 seconds. The maximum uplift of the contact wire in response to the pantograph force is measured as 66 millimetres, which is the height difference between frames 500 and 2118 (selected from the frame intervals at the moment of the first interaction) over the red channel. The highest uplift of the component corresponding to the grey channel is also observed between frames 500 and 2118 with an approximate amount of 64 millimetres. The calculated maximum uplift at the moment of the second interaction is approximately 50 millimetres.

Section 4.3.4.1 contains the functionality of the proposed approach at different monitoring points. The plot of the contact wire response at four different monitoring points (refer to Figure

4-2) validated the similarity of the contact wire response at different points of the wire. A noticeable height difference between the first two and the second two monitoring points was also observed. To examine the effect of the observed height difference in the measuring of the maximum uplift, the contact wire response is further investigated for an additional monitoring point, and the maximum uplifts are calculated and compared accordingly. Figure 4-8 demonstrates the contact wire oscillations at the selected monitoring points.

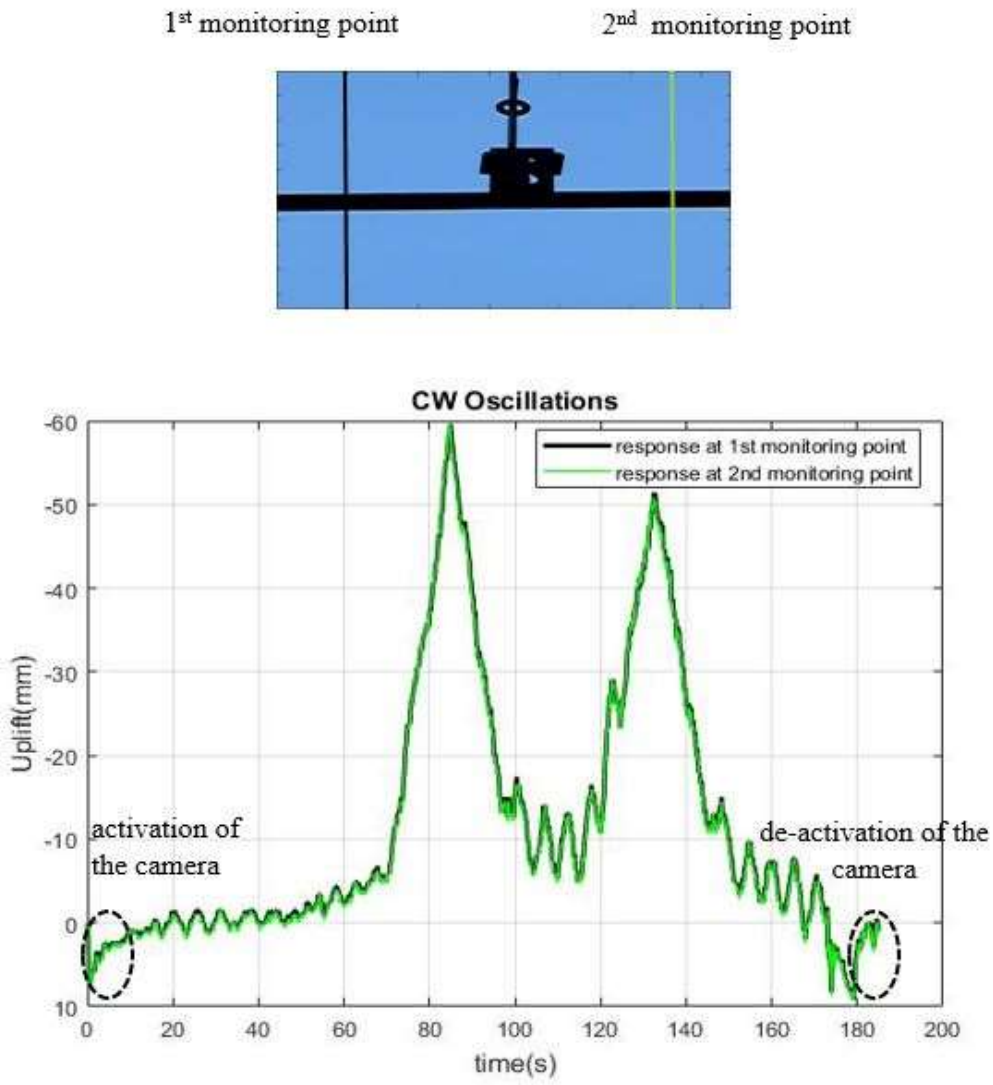


Figure 4-8: CW response at the two monitoring points, offset1=120.24mm, offset2=117.81

As can be seen, the obtained responses are overlapped and the trend of the contact wire oscillation at the selected monitoring points is almost identical. Accordingly, the effect of the gradient of the contact wire in the images on the analysis of the responses is insignificant. Table 4-5 determines the measured maximum uplifts corresponding to the selected monitoring points.

Table 4-5: Maximum uplifts at two monitoring points

Measurement of the contact wire uplift	**the first pantograph (t = 84.72 seconds)**			**the second pantograph (t = 113 seconds)**		
	t = 20s, 0.969	**t =115s, 5.332**	**t = 160s, 7.271**	**t = 20s, 0.969**	**t =115s, 5.332**	**t = 160s, 7.271**
1st monitoring point	63.99	59.63	57.69	50.41	46.05	44.11
2nd monitoring point	62.09	57.69	55.99	48.45	43.95	42.38

Based on Table 4-5, the maximum difference in measuring the contact wire uplifts at the selected monitoring points is 2 mm.

4.3.4.4 Analysis of the Fourth Video data

The fourth video data with the duration of four minutes and thirty seconds, and the resolution of $[480 \times 640]$ shows oscillations of 68 cm of the contact wire. With the frame rate of 25 f/s, the contact wire response to the contact force is obtained through processing of 6768 frames. After the thresholding operation, the number of pixels at logic one in the reference column is counted as 16 pixels that together with the assumed wire thickness define the value of each pixel as 1 $mm/pixel$. After processing of the data, a total number of seventeen frames have been traced that are causing disturbances in the plot of the response. Figure 4-9 demonstrates the initial plot of the trend of the contact wire oscillations along with some of the frames generating the disturbances at the moment of contact with the pantograph.

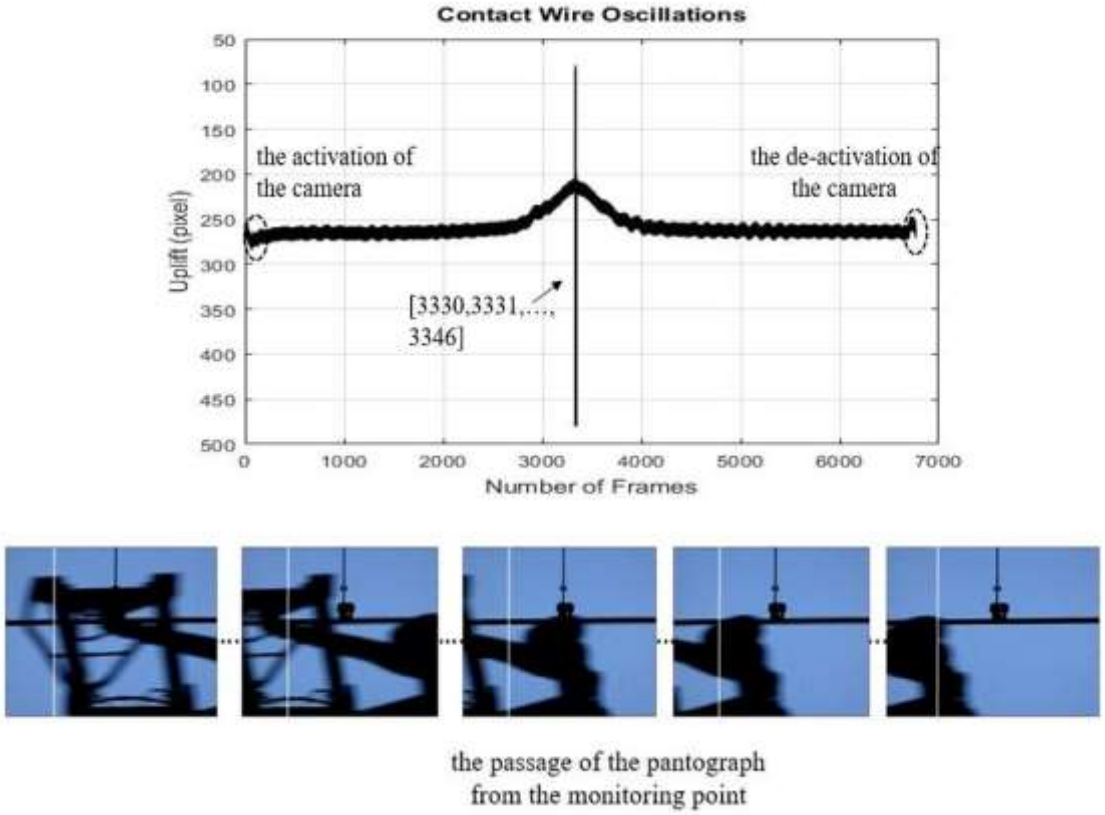


Figure 4-9: Contact wire oscillations caused by running of the pantograph

Figure 4-10 demonstrates the response characteristics corresponding to each channel.

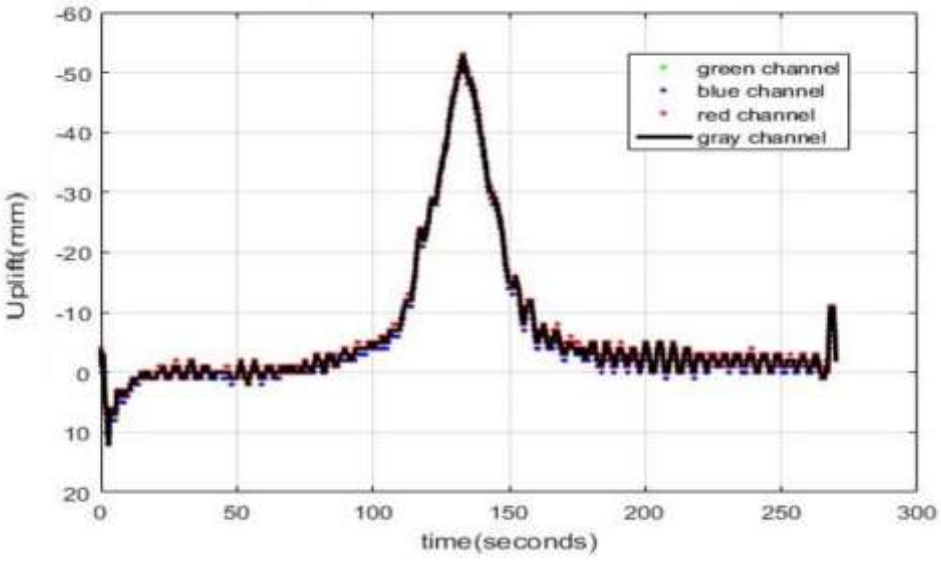


Figure 4-10: CW upper side oscillations, offset = 259 mm

Table 4-6 determines the uplift, measured in accordance to the locations of the contact wire before the arrival of the pantograph to the selected monitoring point.

Table 4-6: Measurements of the CW uplift

Reference Column Matrix		**2:22 ≤ max uplift ≤ 2:23**
Frame Number	**CW Vertical Position**	Observed Uplift (Grey Channel)
Frame = 1000 time = 40 seconds	0	53mm
Frame =2000 time = 1:20 seconds	2 mm	51mm
Frame=2500 time= 1:40 seconds	4 mm	49 mm

4.3.5 Investigation of the Damping Characteristics of the Contact Wire

The contact wire is a distributed parameter with multiple degrees of freedom. Considering the oscillations are occurring at the vertical plane, the contact wire response can be represented as a single degree of freedom (SDOF) system (Figure 4-11)

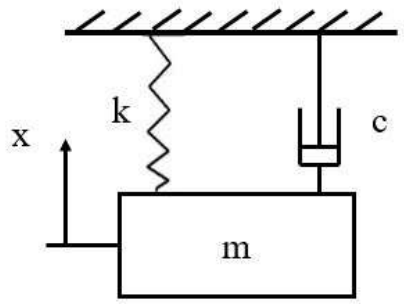


Figure 4-11: Single degree of freedom system (Stickland, 2003)

In this manner, the equation of motion can be expressed as (Stickland, 2003);

$$m\ddot{x} = -kx - c\dot{x} \tag{4.1}$$

where m is the mass per unit length, k is the spring stiffness and c is a constant value. Under no external forces, solution of Equation 4.1 takes a form of:

$$x = Ae^{-\sigma t}sin(\omega_d t + \phi) \tag{4.2}$$

where A and ϕ are the constants dependent on the initial conditions, $\sigma = c/2m$, and ω_d is the damped natural frequency.

For a slightly damped system, the damped natural frequency is almost similar to the undamped natural frequency ω_n.Therefore the damping ratio of the system can be achieved through

$$\zeta = \frac{\sigma}{\omega_n} = \frac{c}{2\sqrt{k \cdot m}} \tag{4.3}$$

The damping of the contact wire is usually obtained through its excitation by an impulse and measuring of its response that forms a vibration signal with a decaying amplitude as in Figure 4-12.

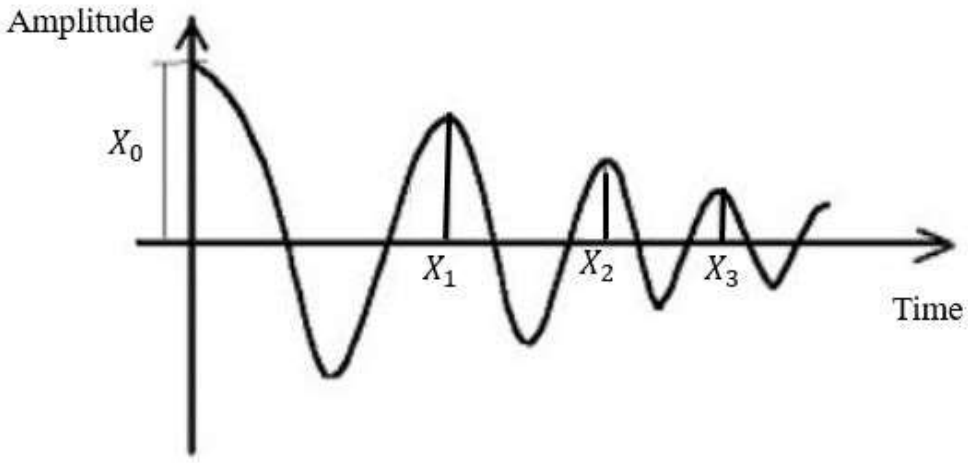


Figure 4-12: Vibration (Stickland, 2003)

The sine term in Equation 4.2 at each vibration peak must be equal to 1, the amplitude of each peak can be obtained through:

$$X_0 = Ae^{-\sigma t(0)}$$

$$X_1 = Ae^{-\sigma t(1)} = Ae^{-\sigma(t(0)+Td)} = X_0 e^{-\sigma Td} \tag{4.4}$$

$$X_2 = Ae^{-\sigma t(2)} = Ae^{-\sigma(t(0)+2Td)} = X_0 e^{-\sigma 2Td}$$

hence, after n cycles the peak amplitude would be:

$$X_n = X_0 e^{-\sigma nTd} \tag{4.5}$$

where the term σTd is the log decrement δ , that can be used to determine the damping in the system. Thereby, Equation 4.5 can be rewritten as:

$$\delta = \frac{1}{n} ln \frac{X_0}{X_n} \tag{4.6}$$

The dependency of the log decrement to the damping ratio is expressed as:

$$\delta = \frac{c2\pi}{2m\omega_d} = \frac{2\pi\zeta}{\sqrt{(1-\zeta^2)}} \tag{4.7}$$

For a slightly damped system, the log decrement can be calculated through:

$$\delta = 2\pi\zeta \tag{4.8}$$

The procedures throughout Section 4.3.4 determined the contact wire oscillations in response to the force of the pantograph at a certain monitoring point, selected from the video horizontal resolution. The obtained response after processing of the trackside videos showed the component excitations before the arrival of the pantograph to the monitoring point, at the moment of the mechanical interaction and after the passage of the pantograph. To investigate the damping of the contact wire, the log decrement is calculated by measuring the amplitude of the successive peaks from the obtained contact wire response. Figure 4-13 demonstrates the trend of the energy dissipation after the passage of the pantograph. This is achieved through processing of the fourth video (see Section 4.3.4.4).

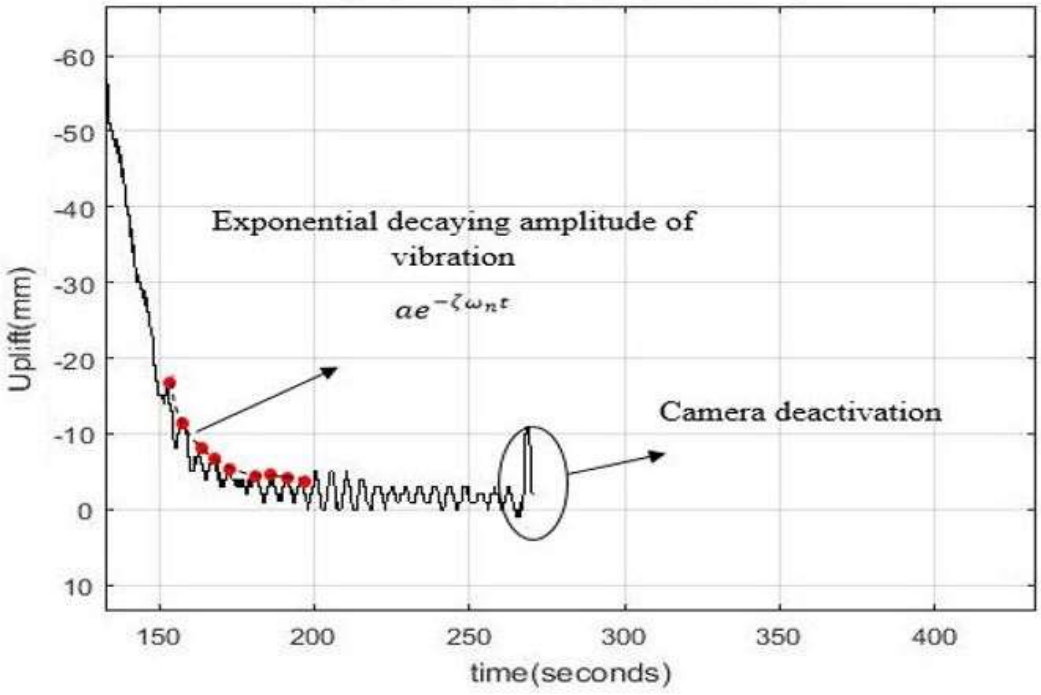


Figure 4-13: the decaying amplitude of the CW vibration

The log decrement is calculated through analysis of the contact wire post oscillations after the passage of the pantograph (Figure 4-14).

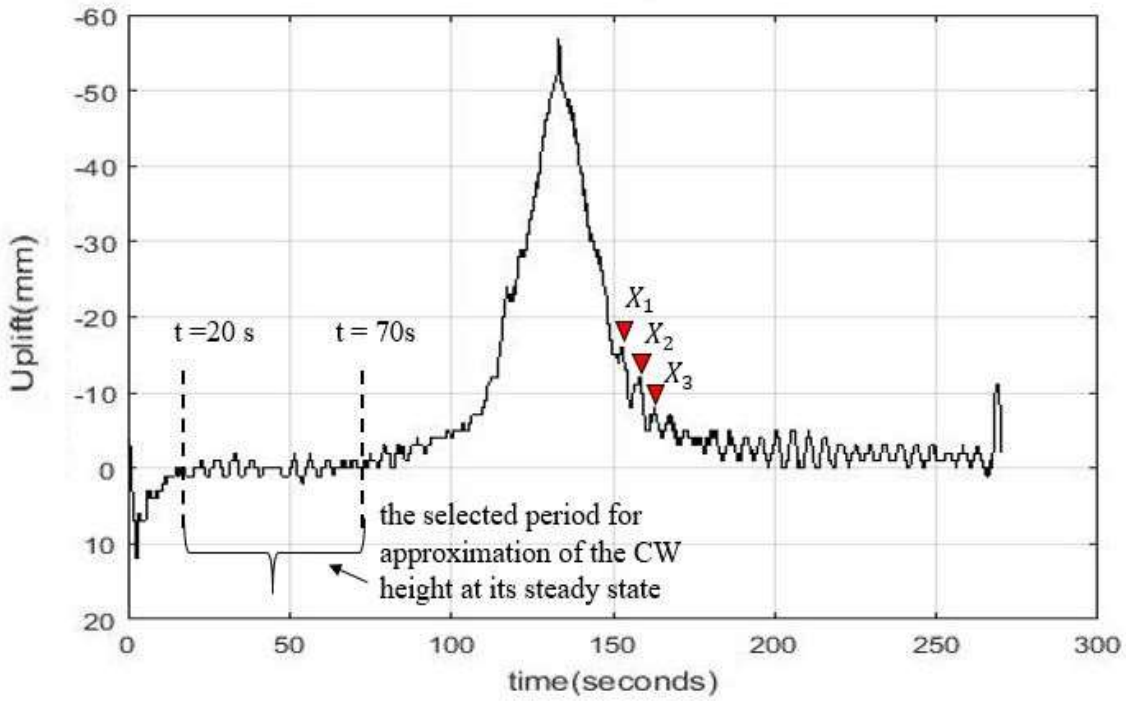


Figure 4-14: Demonstration of the selected peaks for the calculation of the CW damping parameter

According to Equation 4.6, measuring of the log decrement requires amplitude and time interval of the selected peaks to be known. The first peak of the oscillations denoted as X_1 in the figure has the amplitude of 16 mm, which occurred at 152.8 seconds. Amplitude and time of occurrence of the second peak are 12 mm and 157.9 seconds. For the third peak, the amplitude is measured as 8 mm, and it occurred after163 seconds. The contact wire height at its steady-state is approximated based on its positions during the 50 seconds of the video that is roughly 15 seconds before the pantograph reaches the monitoring point. According to the time interval of 0.04 seconds, the height of the contact wire at its steady-state is the average of its position across 1250 frames. This way, the height was calculated to be close to 3 mm. Hence, the log decrement of the three consecutive peaks and the contact wire damping ratio are calculated as following:

$$ln\frac{X_1}{X_3} = ln\left(\frac{X_1}{X_2} \times \frac{X_2}{X_3}\right) = 2\delta = 2 \times 2\pi\zeta = ln\left(\frac{13}{5}\right)$$

$$\zeta = \frac{1}{2\pi \times 2}\, ln\left(\frac{13}{5}\right) = 0.076 \qquad (4.9)$$

The calculated period of oscillation and the damped/undamped natural frequency are 5.1 seconds and 0.196 Hz respectively.

The range of the calculated damping ratio through post-processing of the obtained response is the same as the range that was measured through the application of the displacement transducers by Stickland, (2003) (see Section 2.4.1.3). The drawbacks of attaching the displacement transducer to the contact wire, the complexity of recording the dynamic response of the contact wire, as well as the uncertainties in the measurement of the contact wire uplift and damping ratio caused by the frictional damping and the draw string of the potentiometer indicate the additional usefulness and feasibility of the proposed vision-based trackside monitoring approach in better management of galloping and consequences of this instability.

4.4 Summary

Section 4.2 explained the importance of measuring the uplift in evaluating the performance of the catenary-pantograph system, condition assessment of the contact wire as well as in planning of the uplift range when commissioning new contact wire or testing pantographs. For this reason, a novel vision-based monitoring system was suggested which measures the contact wire uplift using the trackside video data (see Section 4.3.4). The performance of the developed system showed satisfactory results in determining the component oscillations under service condition. The goodness of the selected threshold value in segmentation of the image data was evaluated through analysis of the responses over each channel. Apart from measuring the uplift, further analysis of the contact wire post-oscillation after the passage of the pantograph enabled calculation of the component natural frequency and its damping ratio. This indicates further practicality of the system in monitoring probable defect within the wire and better management of the high amplitude oscillations. The validity of the proposed method and reliability of the image data in determining the contact wire uplift is evaluated in Section 5.4.

Chapter Five

5. TRACKSIDE MEASUREMENT OF THE CONTACT WIRE STATIC UPLIFT

5.1 Introduction

This chapter examines the reliance on the image data and the accuracy of the proposed vision-based monitoring approach in measuring the amount of uplift in response to the pantograph force. The precision of the developed point-based analysis of the trackside data is evaluated through defining a new aspect of monitoring that enables measurement of the static uplift under different loading conditions. A mechanical tool is designed which enables measurement of the uplift under each imposed force with reference to the contact wire height in no-load condition. The fabricated apparatus has a maximum adjustable height of 4.8 metres and an approximate weight of 10 kilograms (see Section 3.4.4.3, Figure 3-5). The experiments are performed on seven locations along a 48.1 metres span with dead wires at Long Marston. The chapter analyses the compliance characteristic of the contact wire uplift, measured both manually and automatically through analysis of the recorded trackside footages. Since the amount of uplift at each test location is measured for a known range of forces, the stiffness of the contact wire along the selected span is as well investigated.

5.2 Experimental Setup

The designed and fabricated mechanical measurement tool is made of an adjustable arm, formed by two wooden bars and a glass tube that connects to the wooden bars from both sides using two hi-grips. The arm is supported at one end, where it attaches to a class two lever with two assembly points at its both ends. One end connects the rig to the camera mount and the other is for the attachment of the spring balance. Once the rig is located on the track, the height of the mechanical arm and the tripod are adjusted in a manner to maintain the contact wire at its position. Afterwards, a range of known forces are exerted to the contact wire, causing the wire to lift. The contact wire uplift in response to the applied forces is recorded by the laser metre that is secured to the lifting arm of the apparatus above the holding brackets, where the arm and the lever are connected.



Figure 5-1: The static uplift measuring device in use (Location: Long Marston)

Depending on the type of the pantograph and the line speed, the approximate pantograph force is between 90N and 120N (Baker, et al., 2019). To measure the contact wire uplift under the same range of uplift forces, a 50N spring balance is used. The magnitude of the input force, exerted by the spring balance is increased through the design of a class two lever with a total length of 1.5 metres.

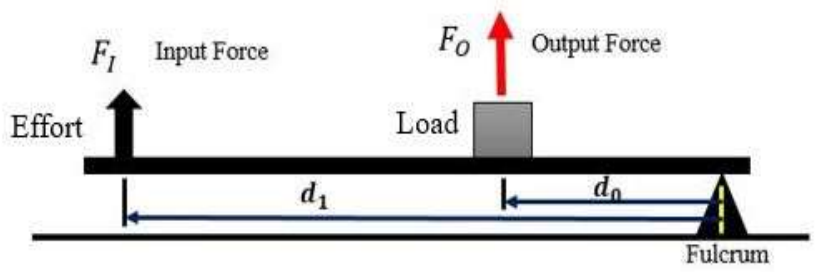


Figure 5-2: Schematic of a class two lever

Considering negligible resistive friction at the support, the relationship between the input force and the load is expressed as the ratio of the length of the effort arm to the load arm:

$$F_O/F_I = d_I/d_o \quad (5.1)$$

$$MA_F = F_O/F_I \quad (5.2)$$

where, MA_F denotes the force mechanical advantage of the lever. To increase the force of the spring balance, the ratio of the length of the effort arm to the load arm is considered in a way that the force mechanical advantage of the lever results in the output force to be triple the magnitude of the input force. The uplift of the contact wire in response to the force of the spring balance is measured with respect to the height of the contact wire under the rig self-load of 10N. The contact wire uplift is measured under the forces of 30N, 60N, 90N and 120N at predefined test locations. The measurement error due to the reflection of the laser beam against the uneven surface of the ballast gravels is avoided by placing a thin solid board on top of the track, where the propagated beam hits the surface and reflects to the source.

5.3 Data Acquisition

Measurements of the contact wire uplift were recorded during a dry summer day under no/light wind. The temperature was measured to be approximately 17°C, and the test locations were selected as follows:

Location 1: At the first registration arm.

Location 2: At the first dropper, located 3.8 metres away from the first registration arm.

Location 3: At the second dropper, located 8.8 metres away from the first dropper.

Location 4: At the third dropper, located 8.4 metres away from the second dropper.

Location 5: At the fourth dropper, located 9.6 metres away from the third dropper.

Location 6: At the fifth dropper, located 10 metres away from the fourth dropper.

Location 7: At the second registration arm, located 7.4 metres away from the fifth dropper.

The apparatus was moved to each test location and placed at the centre of the track beneath the contact wire. The lifting arm of the apparatus was extended to its maximum height. The contact wire was held by the V-shaped plastic hook on top of the upper wooden bar. To measure the uplift, force was applied, and contact wire was lifted. The amount of displacement was recorded according to the distance shown by the laser meter. To avoid the possibility of error in manually recording the contact wire uplift, measurements under each applied force were repeated five times at each test location. A camera was placed by the trackside to record footages from the movement of the contact wire throughout the entire test procedure. The camera was set at a 30-degree elevation angle and was located around three metres away from the track.

5.4 Experimental Results

This section investigates the reliability of the proposed trackside monitoring approach in calculating uplift of the contact wire by comparing the recorded responses using each measuring method.

5.4.1 First Registration Arm

The variability of manually recording the uplift during each test to the mean of the data recorded under each load is measured as maximum of three millimetres. The recorded uplift under 30 N and 90 N with 1.92 mm and 3 mm calculated standard deviation respectively

determine the smallest and the largest variability of the recorded data. Figure 5-3 shows the recorded uplift at the first registration arm.

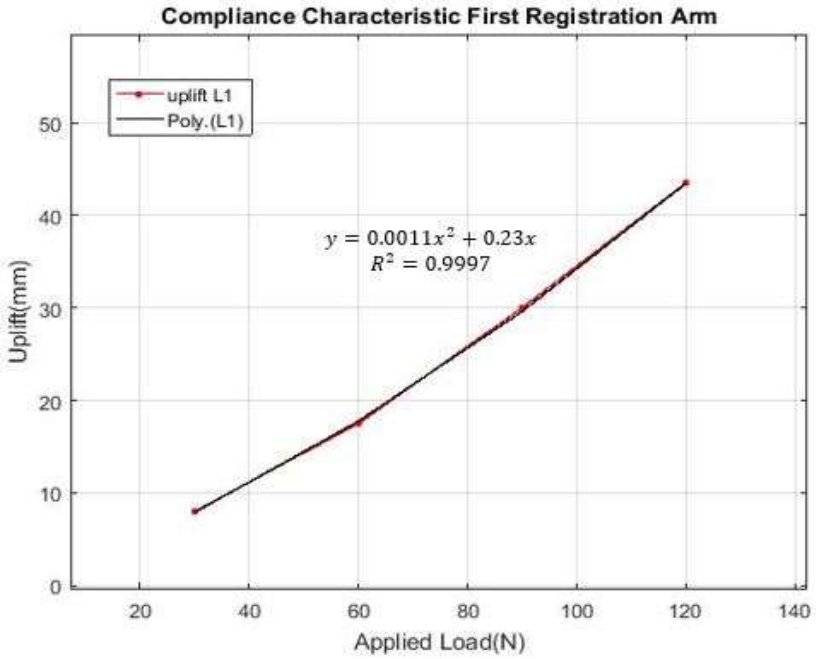


Figure 5-3: Uplift data (location: first registration arm)

After processing the video, small fluctuations were observed in the recorded responses. To better interpret the contact wire response, a non-parametric curve is fitted to the data. This regression process aims at preserving the peaks of the displacement graph whilst attenuating the fluctuations under each load. The adopted algorithm slices the data into sections of equal width that vary depending on the number of the data points. The algorithm then sums the data points at each section and averages the data to produce a smooth version of the plotted response.

Figure 5-4 demonstrates the impulse response of the contact wire after processing of the video recorded at the first registration arm.

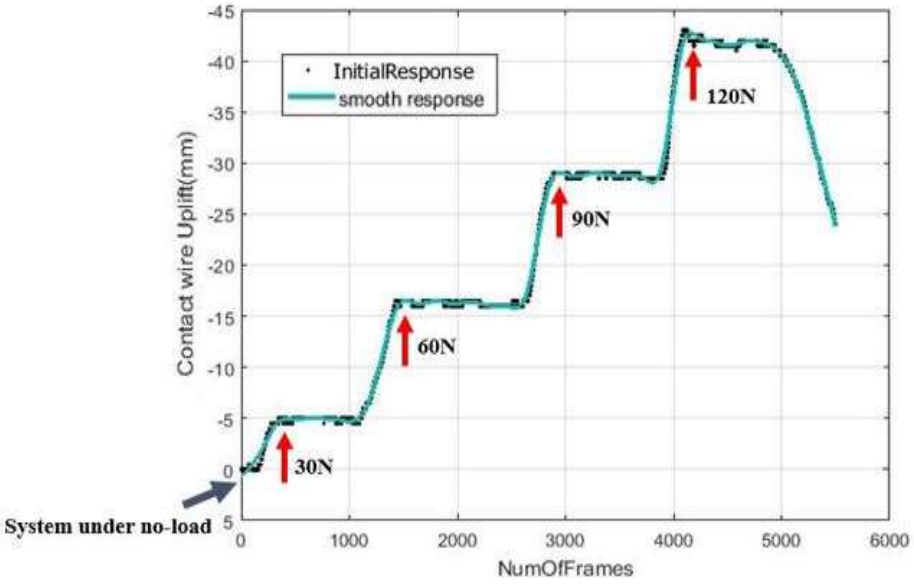


Figure 5-4: CW response characteristics at the first registration arm

Figure 5-5 demonstrates the variations of the contact wire uplift under each load at the first registration arm.

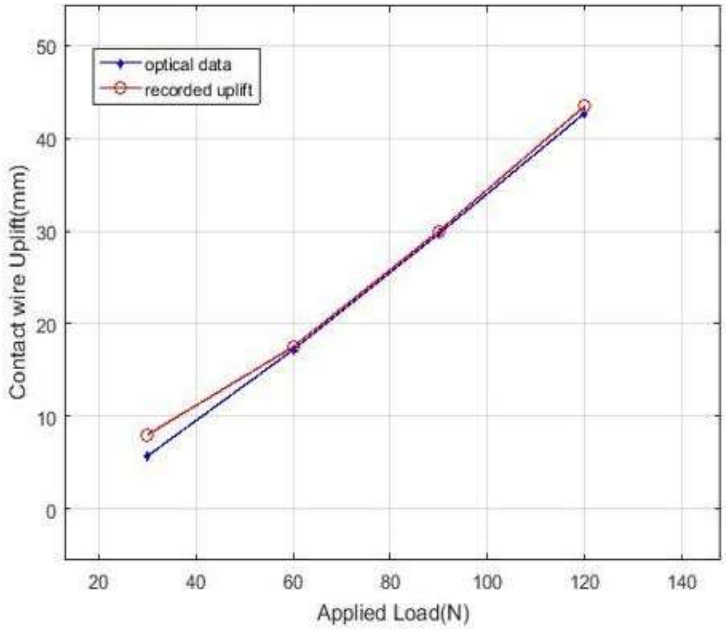


Figure 5-5: Variability of the recorded uplift at the first registration arm

According to Figure 5-5, the variability of the contact wire displacement in between the lifts under each load is as follows:

- As the force increases from 30 N to 60 N, the recorded uplift measured by the apparatus and the camera increases by 118 % and 230% respectively.
- As the force increases from 60 N to 90 N, the recorded uplift measured by the apparatus and the camera increases by 71% and 72% respectively.
- As the force increases from 90 N to 120 N, the recorded uplift measured by the apparatus and the camera increases by 45 % and 50 % respectively.

5.4.2 First Dropper

The variability of the recorded uplift during each test to the mean of the data recorded under each load is measured to be maximum of 16 millimetres. The uplift data recorded under 90 N and 30 N with 6.47 mm and 16.29 mm calculated standard deviation determine the smallest and the largest variability of the recorded data respectively. Figure 5-6 shows the recorded uplift at the first dropper.

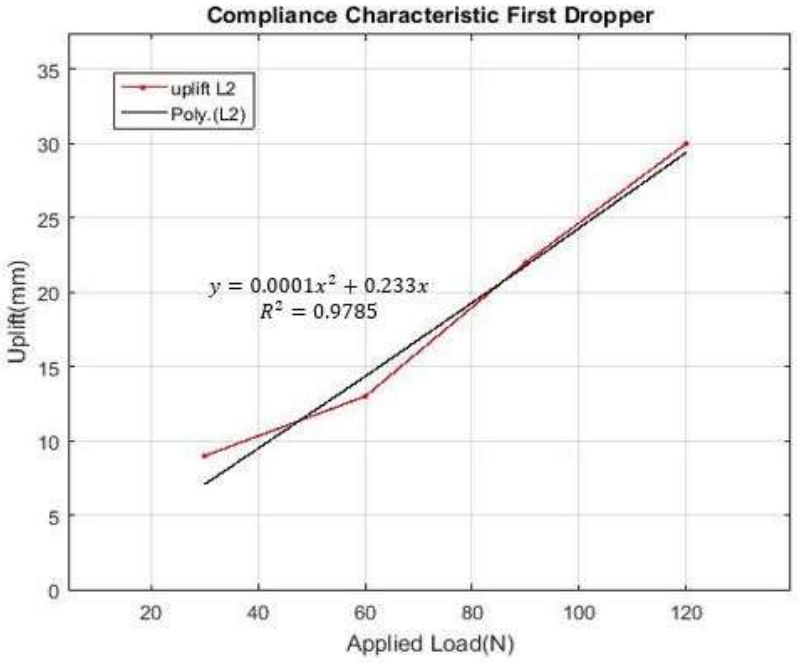


Figure 5-6: Uplift data (location: first dropper)

Figure 5-7 demonstrates the impulse response of the contact wire after processing of the video recorded at the first dropper.

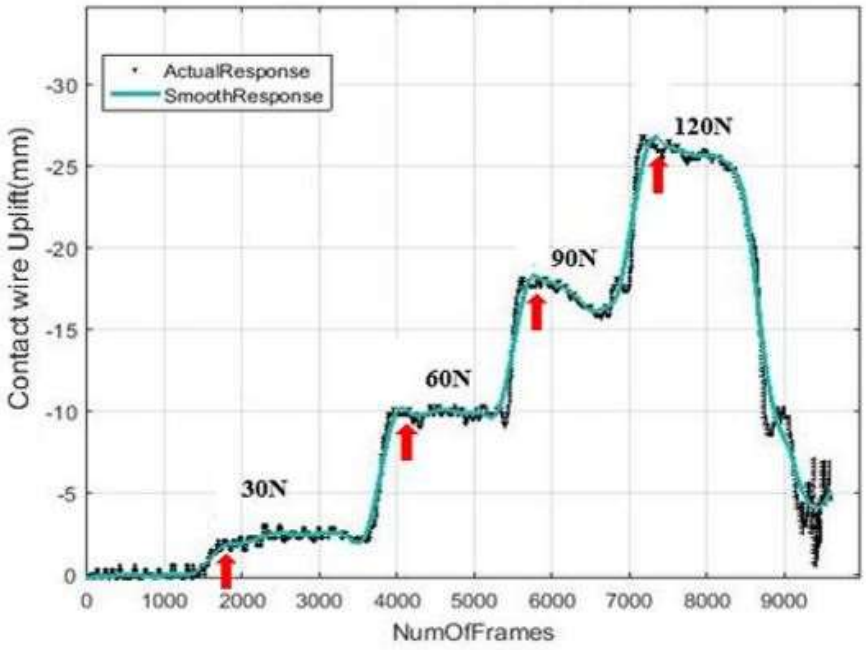


Figure 5-7: CW response characteristics at the first dropper

Figure 5-8 demonstrates the variations of the contact wire uplift under each load at the first dropper.

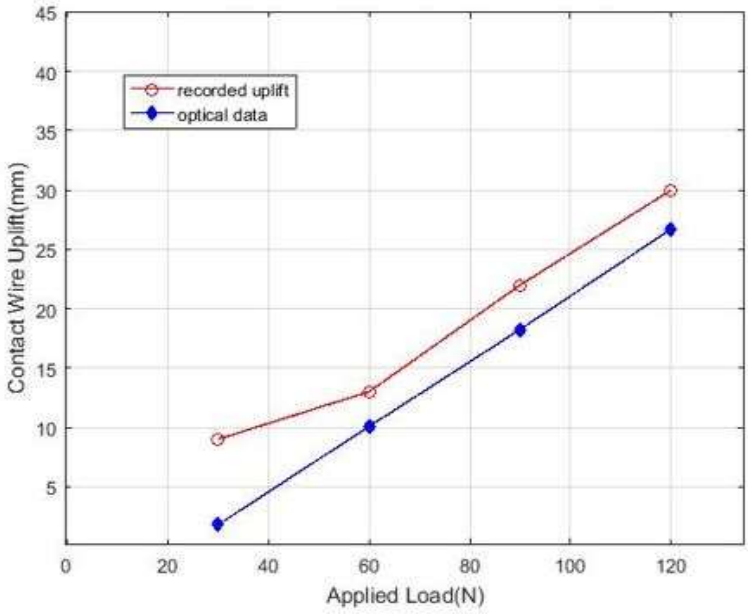


Figure 5-8: Variability of the recorded uplift at the first dropper

According to Figure 5-8, the variability of the contact wire displacement in between the lifts is as follows:

- As the force increases from 30 N to 60 N, the recorded uplift measured by the apparatus and the camera increases by 44 % and 420% respectively.
- As the force increases from 60 N to 90 N, the recorded uplift measured by the apparatus and the camera respectively increases by 69% and 71%.
- As the force increases from 90 N to 120 N, the recorded uplift measured by the apparatus and the camera increase by 36 % and 49 % respectively.

5.4.3 Second Dropper

The variability of the recorded uplift during each test to the mean of the data recorded under each load is measured as maximum of approximately 5 millimetres. The uplift data recorded under 30 N and 60 N with 2.77 mm and 5.1 mm calculated standard deviation determine the smallest and the largest variability of the recorded data, respectively. Figure 5-9 shows the recorded uplift at the second dropper.

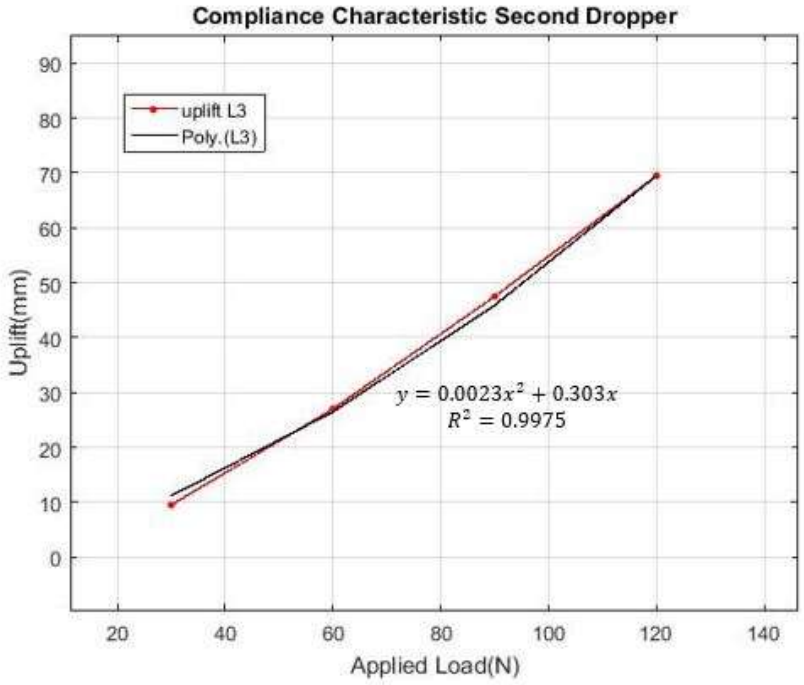


Figure 5-9: Uplift data (location: second dropper)

5.4.3.1 First Trial

Figure 5-10 demonstrates the impulse response of the contact wire after processing of the first video recorded at the second dropper.

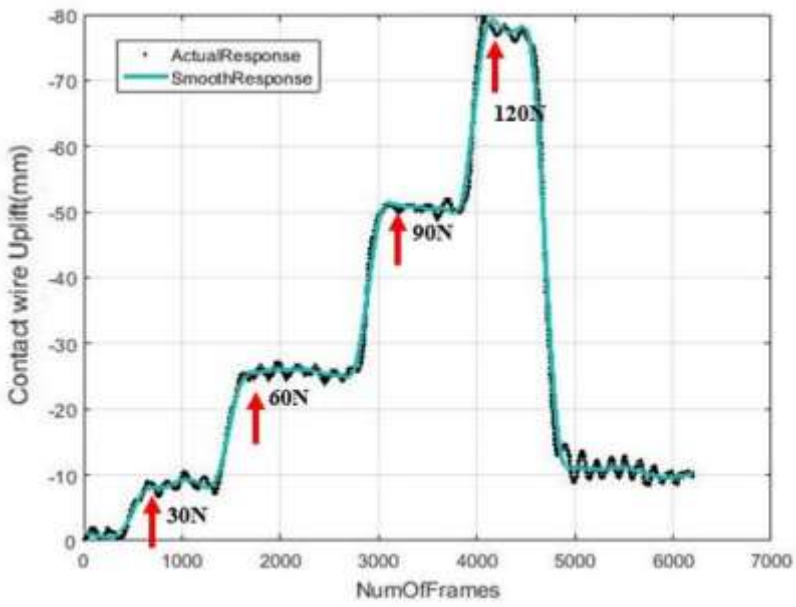


Figure 5-10: CW response characteristics at the second dropper

Figure 5-11 demonstrates the variations of the contact wire uplift under each load, recorded through each method.

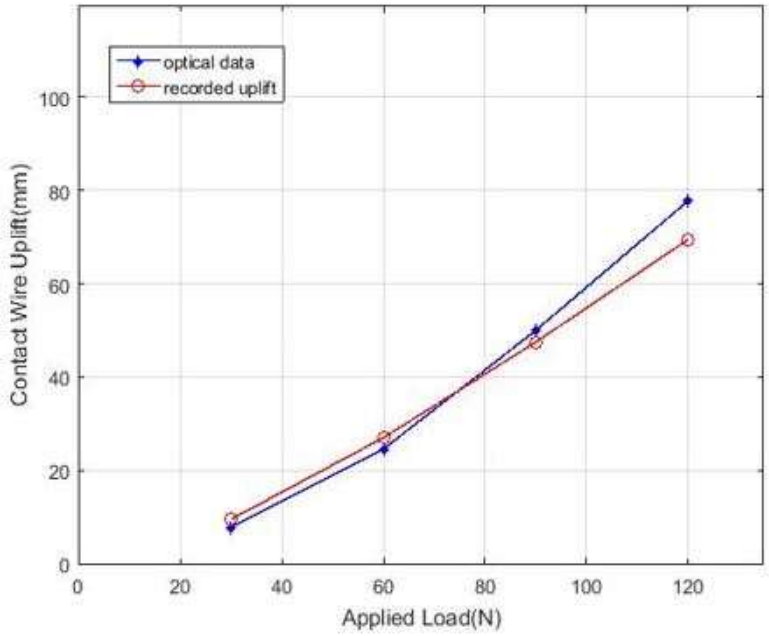


Figure 5-11: Variability of the recorded uplift at the second dropper

According to Figure 5-11, the following describes the variability of the contact wire displacement in between the lifts:

- As the force increases from 30 N to 60 N, the recorded uplift measured by the apparatus and the camera increases by 188 % and 180 % respectively.
- As the force increases from 60 N to 90 N, the recorded uplift measured by the apparatus and the camera increases by 76% and 105% respectively.
- As the force increases from 90 N to 120 N, the recorded uplift measured by the apparatus and the camera increases by 46 % and 54 % respectively.

5.4.3.2 Second Trial

Figure 5-12 demonstrates the impulse response of the contact wire after processing of the second video recorded at the second dropper.

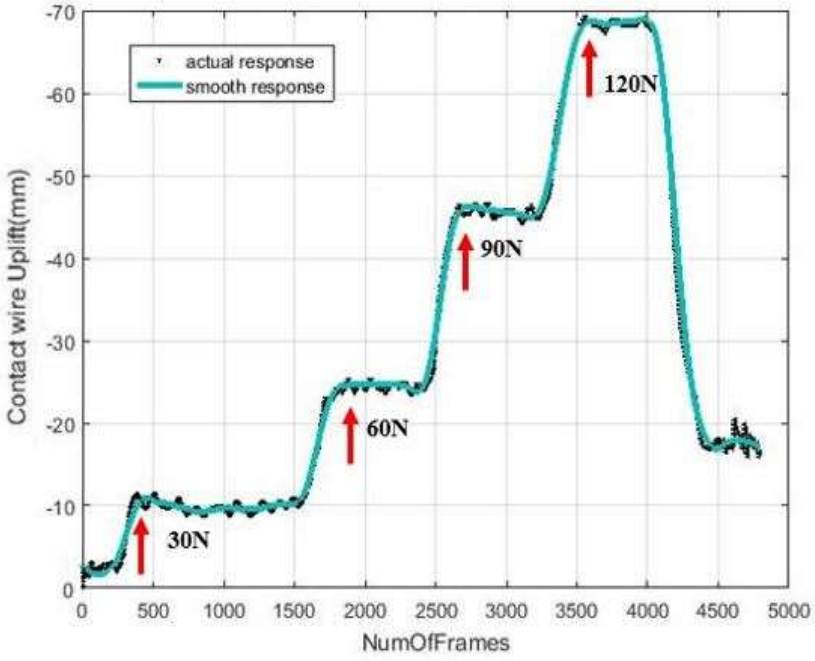


Figure 5-12: CW response characteristics at the second dropper

Figure 5-13 demonstrates the variations of the contact wire uplift under the applied loads, obtained after processing of the second video.

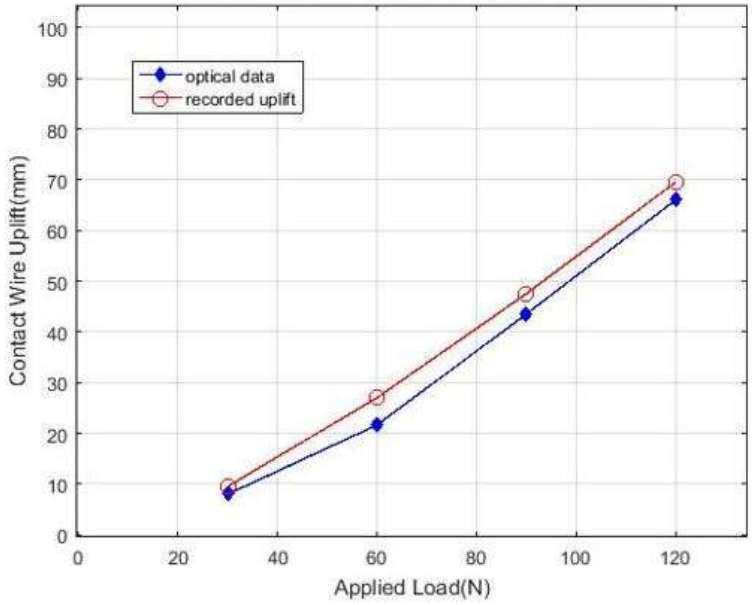


Figure 5-13: Variability of the recorded uplift at the second dropper

According to Figure 5-13, the variability of the contact wire displacement in between the lifts is described in accordance to the applied loads in following:

- As the force increases from 30 N to 60 N, the recorded uplift measured by the apparatus and the camera increases by 188 % and 125 % respectively.
- As the force increases from 60 N to 90 N, the recorded uplift measured by the apparatus and the camera increases by 76% and 86% respectively.
- As the force increases from 90 N to 120 N, the recorded uplift measured by the apparatus and the camera increases by 46 % and 49 % respectively.

5.4.3.3 Third Trial

The impulse response of the contact wire after processing of the third video, recorded at the second dropper is illustrated in Figure 5-14.

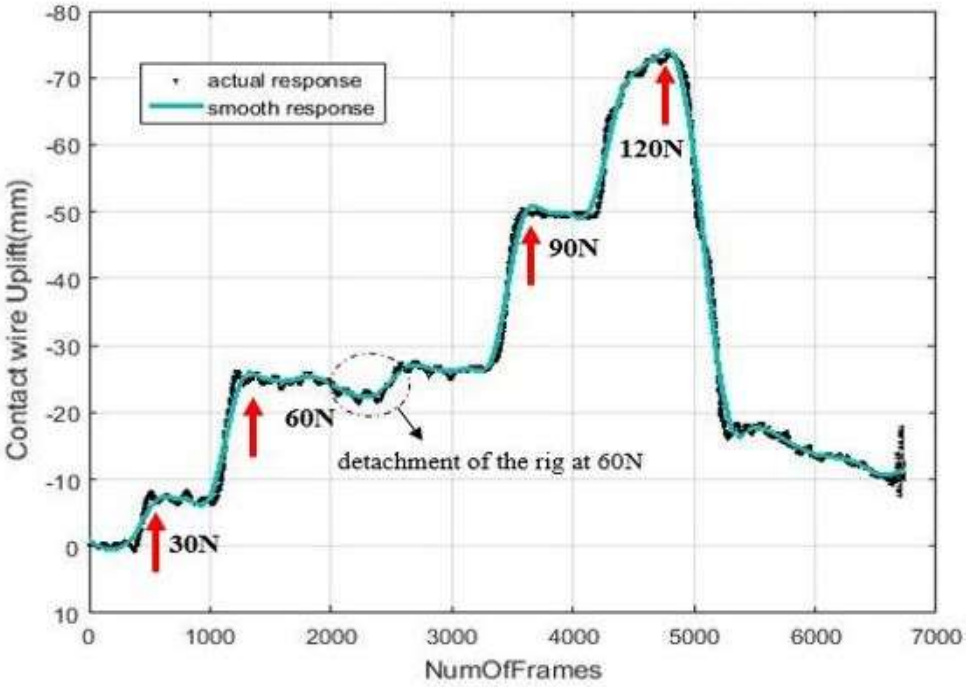


Figure 5-14: CW response characteristics at the second dropper

Figure 5-15 demonstrates the variations of the contact wire uplift under the applied loads, obtained after processing of the third video.

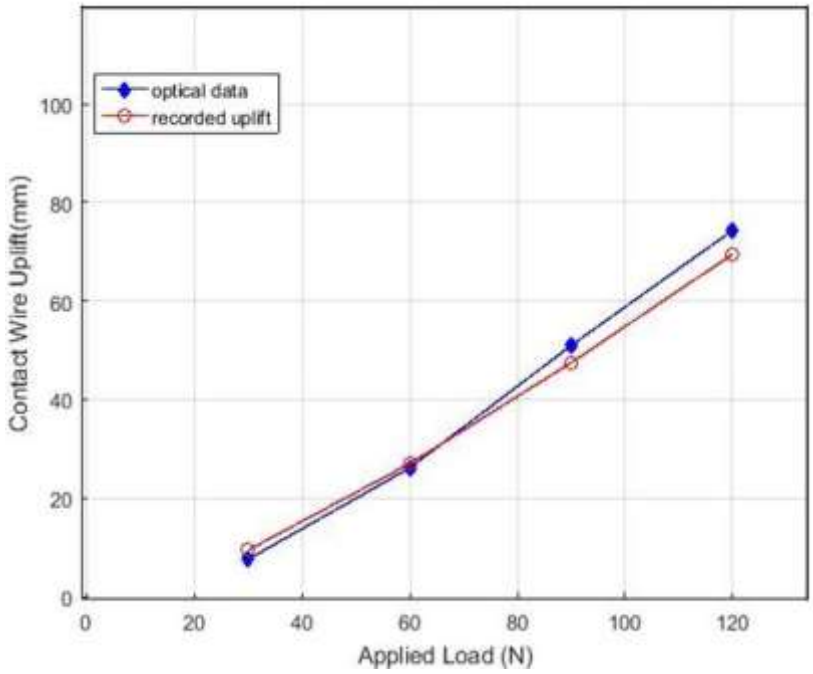


Figure 5-15: Variability of the recorded uplift at the second dropper

Using Figure 5-15, the variability of the contact wire displacement in between the lifts is as:

- As the force increases from 30 N to 60 N, the recorded uplift measured by the apparatus and the camera increases by 188 % and 208 % respectively.
- As the force increases from 60 N to 90 N, the recorded uplift measured by the apparatus and the camera respectively increases by 76% and 91%.
- As the force increases from 90 N to 120 N, the recorded uplift measured by the apparatus and the camera increases by 46 % and 48 % respectively.

5.4.4 Third Dropper

The variability of the recorded uplift during each undertaken test to the mean of the data recorded under each load is measured as maximum of approximately 3 millimetres. The uplift data recorded under 60 N and 120 N with 1.92 mm and 3.31 mm calculated standard deviation respectively determine the smallest and the largest variability of the recorded data. Figure 5-16 shows the recorded uplift at the third dropper.

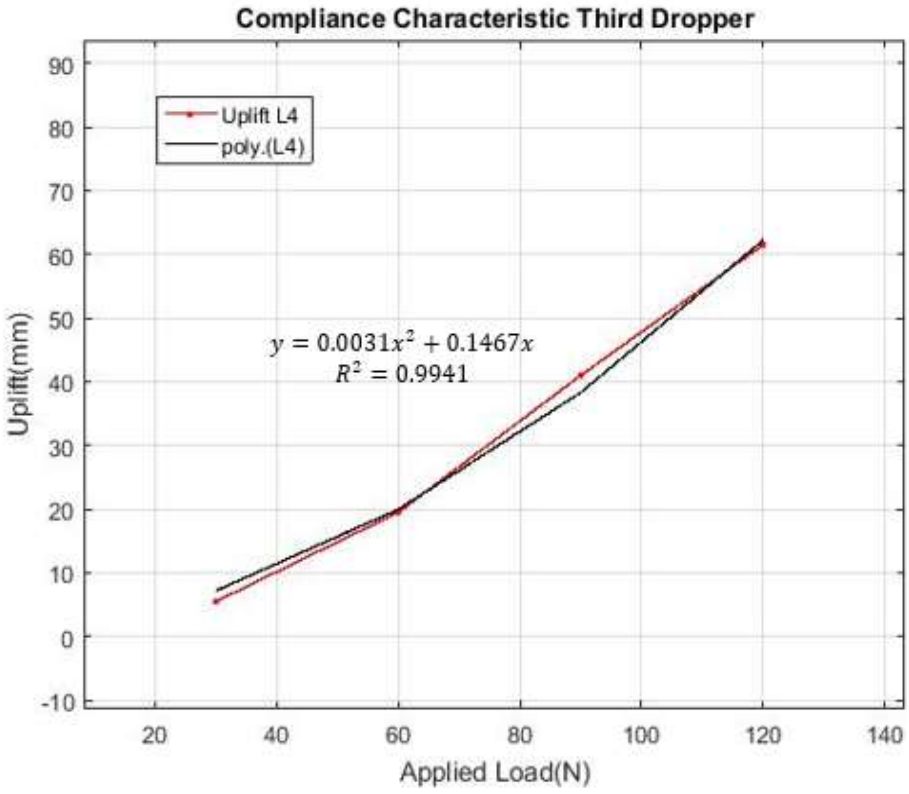


Figure 5-16: Uplift data (location: third dropper)

5.4.4.1 First Trial

Figure 5-17 demonstrates the impulse response of the contact wire after processing of the first video, recorded at the third dropper.

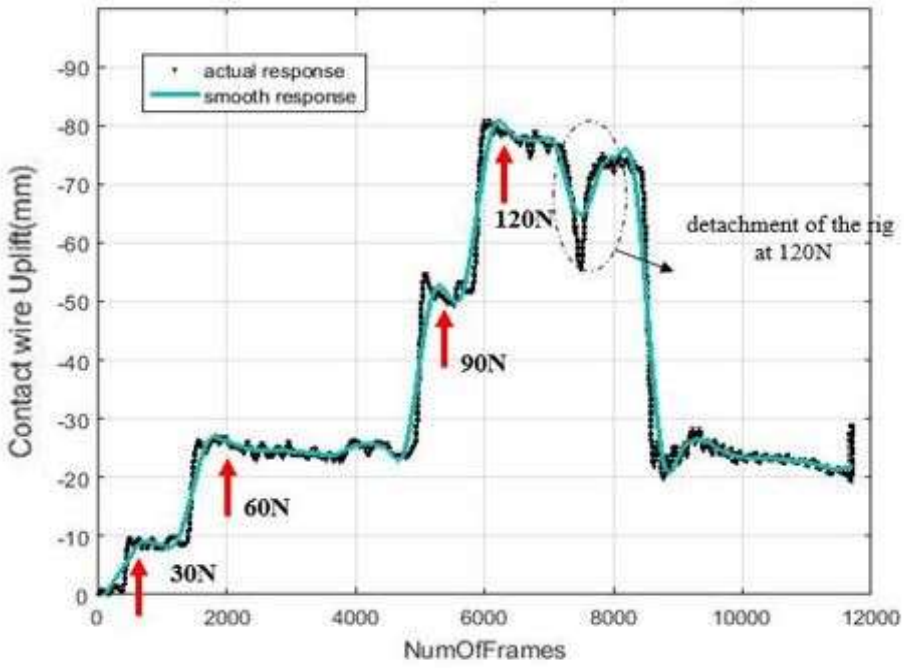


Figure 5-17: CW response characteristics at the third dropper

Figure 5-18 demonstrates the variations of the contact wire uplift under each load, recorded through both methods.

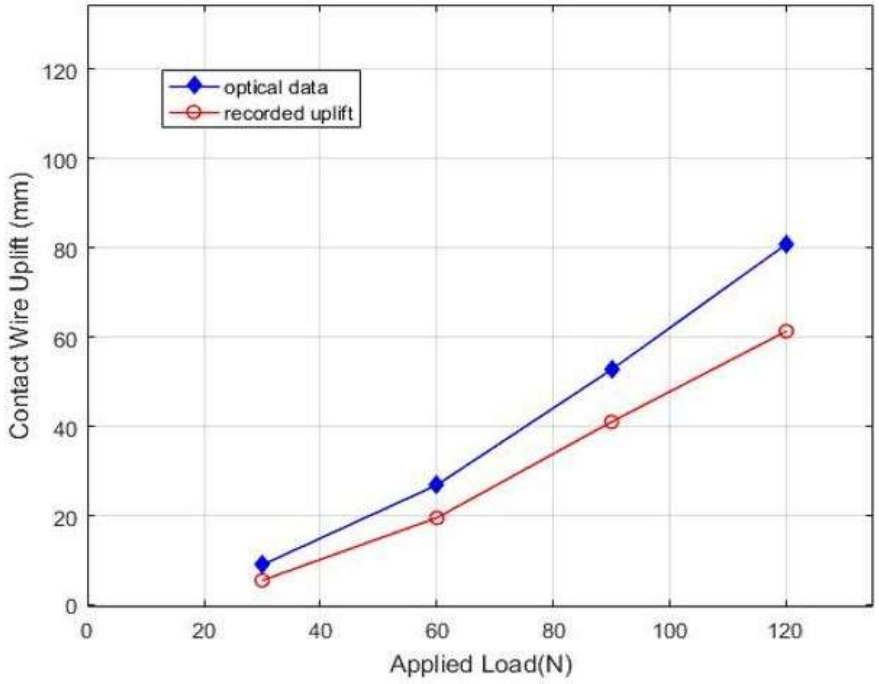


Figure 5-18: Variability of the recorded uplift at the third dropper

According to Figure 5-18, the variability of the contact wire displacement in between the lifts corresponding to the applied loads is as follows:

- As the force increases from 30 N to 60 N, the recorded uplift increases by 254 % and 159 % respectively for the apparatus and camera.
- As the force increases from 60 N to 90 N, the recorded uplift measured by the apparatus and the camera respectively increases by 110% and 108%.
- As the force increases from 90 N to 120 N, the recorded uplift measured by the apparatus and the camera increases by 50 % and 48 % respectively.

5.4.4.2 Second Trial

Figure 5-19 demonstrates the impulse response of the contact wire after processing of the second video, recorded at the third dropper.

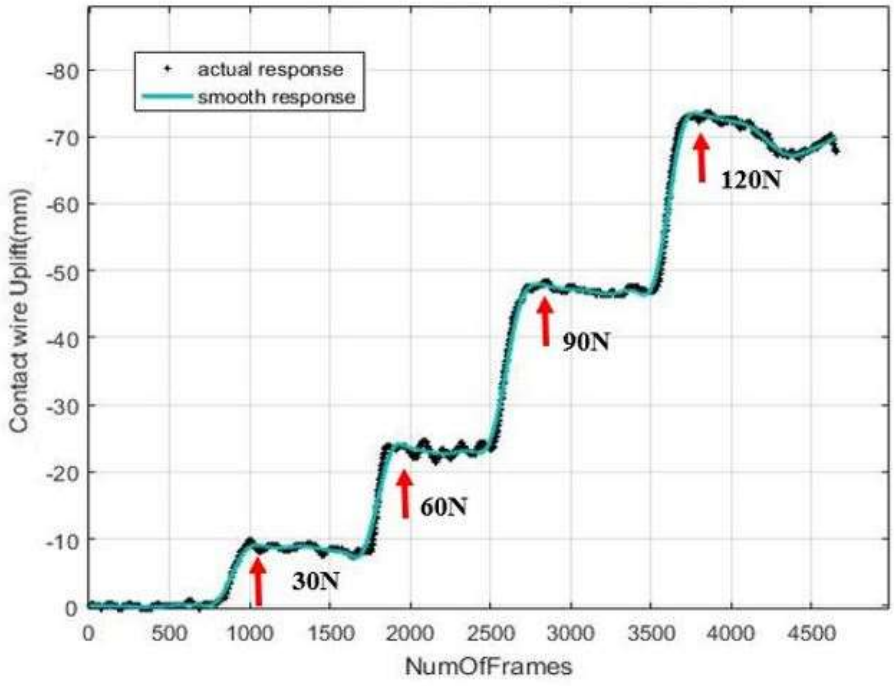


Figure 5-19: CW response characteristics at the third dropper

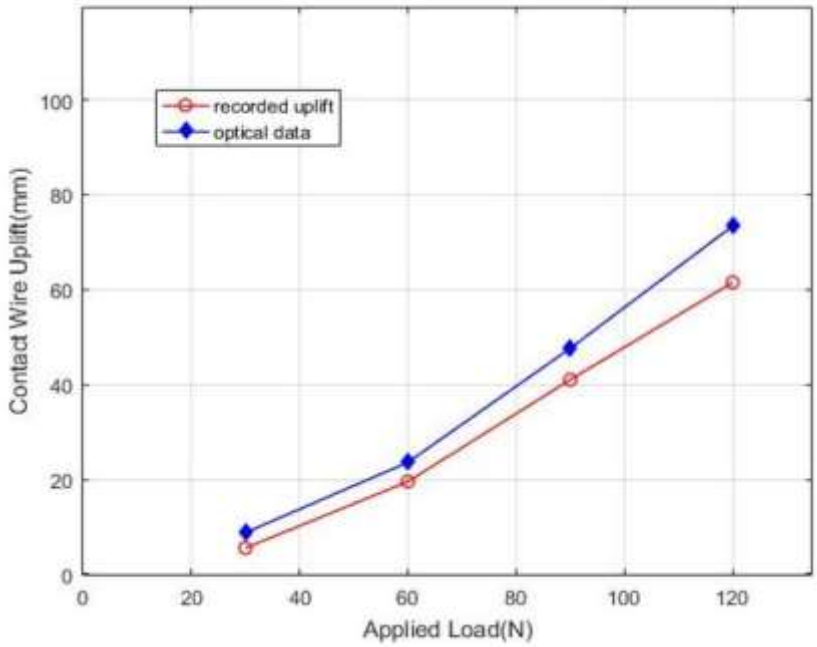


Figure 5-20: Variability of the recorded uplift at the third dropper

Using Figure 5-20 the following are the variability of the contact wire displacement in between the lifts:

- As the force increases from 30 N to 60 N, the recorded uplift measured by the apparatus and the camera increases by 254 % and 145 % respectively.
- As the force increases from 60 N to 90 N, the recorded uplift measured by the apparatus and the camera increases by 110% and 93% respectively.
- As the force increases from 90 N to 120 N, the recorded uplift measured by the apparatus and the camera increases by 50 % and 53 % respectively.

5.4.4.3 Third Trial

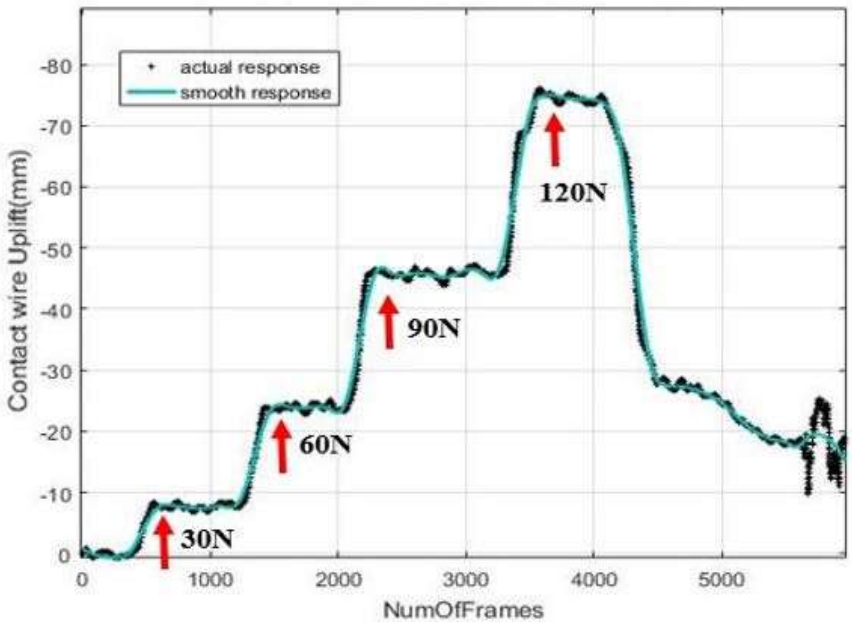


Figure 5-21: CW response characteristics at the third dropper

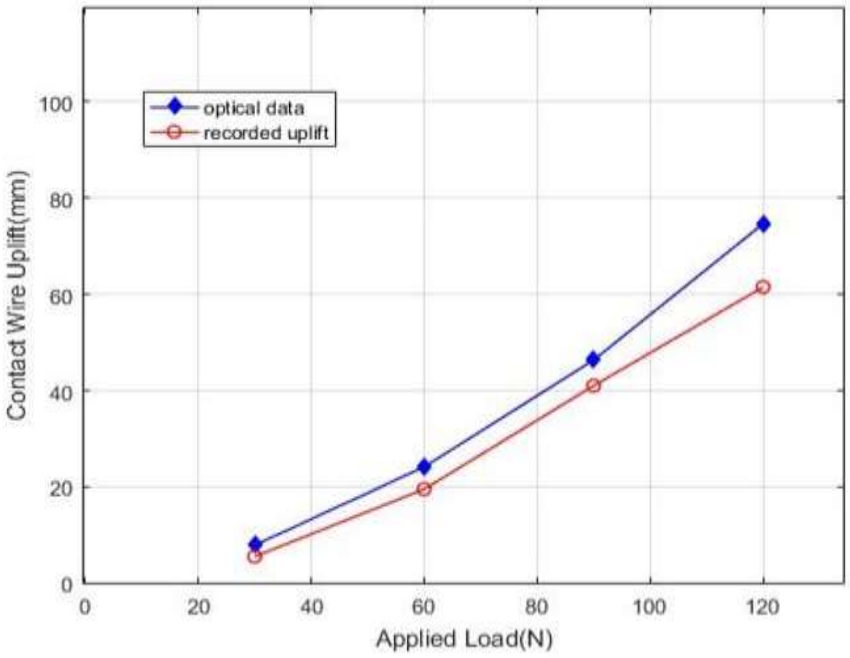


Figure 5-22: Variability of the recorded uplift at the third dropper

Figure 5-22 shows, the variability of the contact wire displacement in between the lifts and is described in the following:

- As the force increases from 30 N to 60 N, the recorded uplift measured by the apparatus and the camera increases by 254 % and 188 % respectively.

- As the force increases from 60 N to 90 N, the recorded uplift measured by the apparatus and the camera increases by 110% and 87% respectively.
- As the force increases from 90 N to 120 N, the recorded uplift measured by the apparatus and the camera increases by 50 % and 65 % respectively.

5.4.5 Fourth Dropper

The measured variability of the recorded uplift during each carried test to the mean of the data recorded under each load is less than 2 millimetres. The recorded uplift under 90 N and 120 N with 1.1 mm and 1.58 mm standard deviation determine the smallest and the largest variability of the recorded data, respectively. Figure 5-23 shows the recorded uplift at the second dropper.

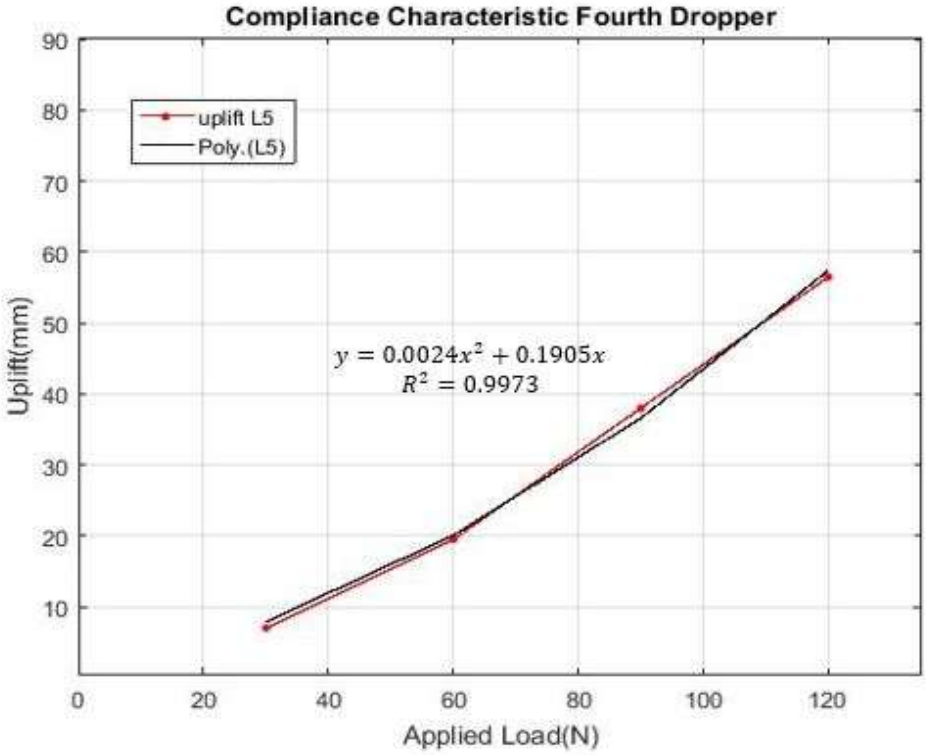


Figure 5-23: Uplift data (location: fourth dropper)

Figure 5-24 demonstrates the impulse response of the contact wire after processing the video, recorded at the fourth dropper.

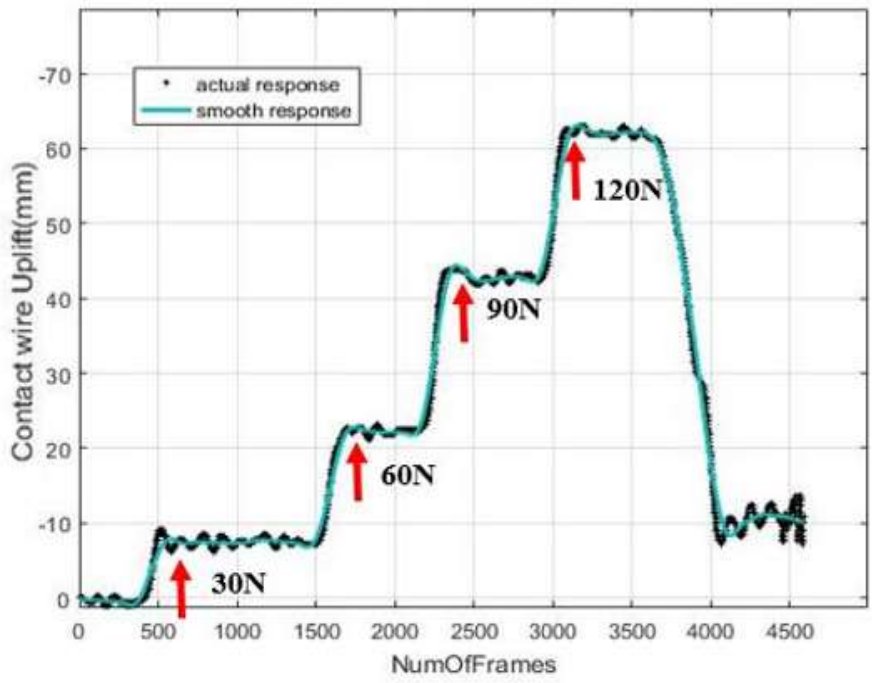


Figure 5-24: CW response characteristics at the fourth dropper

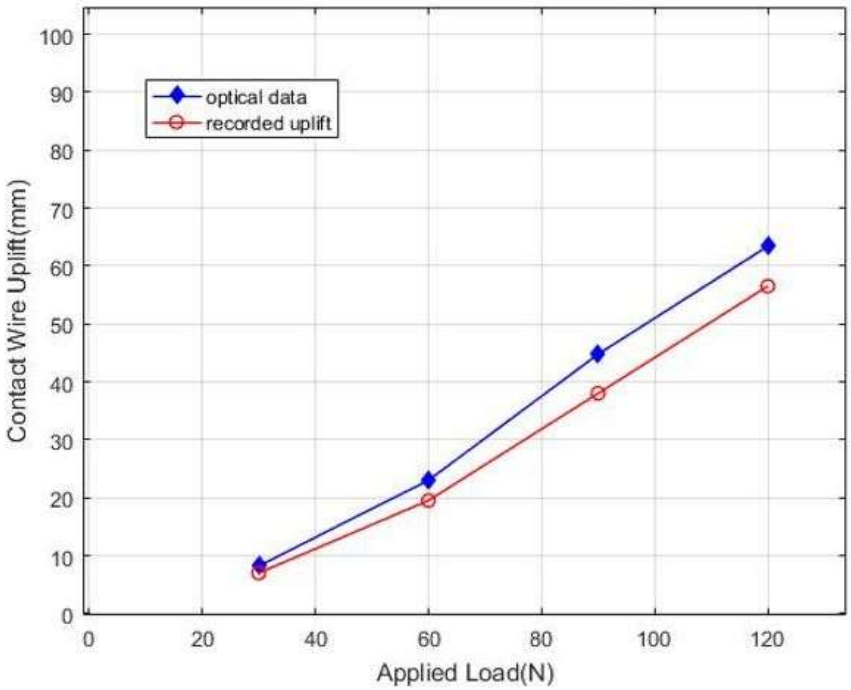


Figure 5-25: Variability of the recorded uplift at the fourth dropper

According to Figure 5-25, the variability of the contact wire displacement in between the lifts with regards to the applied load is as follows:

- As the force increases from 30 N to 60 N, the recorded uplift measured by the apparatus and the camera increases by 178% and 153 % respectively.

- As the force increases from 60 N to 90 N, the recorded uplift measured by the apparatus and the camera increases by 94% and 96% respectively.
- As the force increases from 90 N to 120 N, the recorded uplift measured by the apparatus and the camera increases by 48 % and 39 % respectively.

5.4.6 Fifth Dropper

The variability of the recorded uplift during each test to the mean of the data recorded under different loads is measured as less than 7 millimetres. The recorded uplift data against 30 N and 60 N with 2.77 mm and 6.69 mm standard deviation respectively determine the smallest and the largest variability of the recorded data. Figure 5-26 shows the recorded uplift at the fifth dropper.

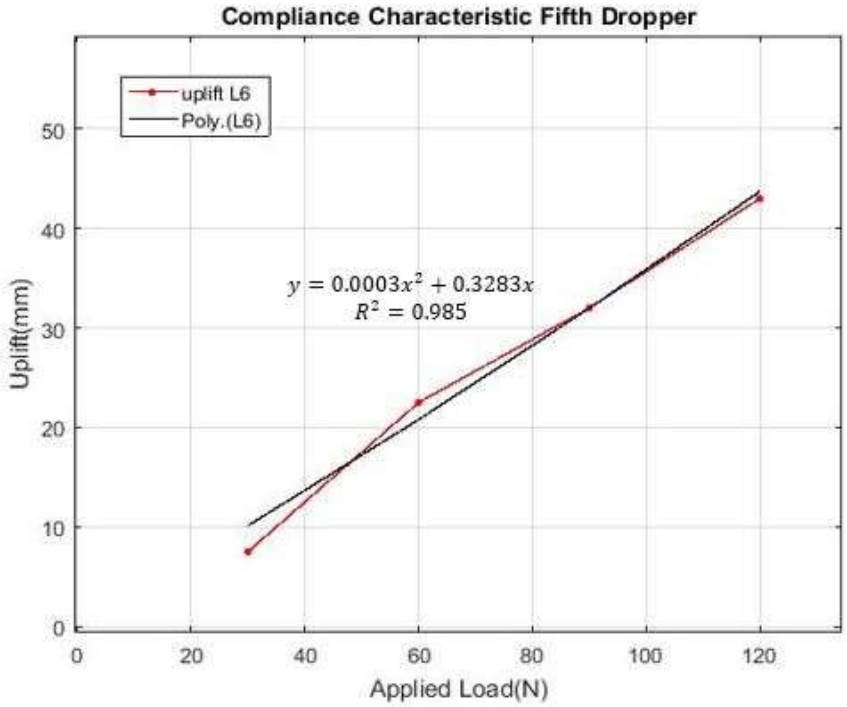


Figure 5-26: Uplift data (location: fifth dropper)

5.4.6.1 First Trial

Figure 5-27 demonstrates the impulse response of the contact wire after processing of the first video recorded at the fifth dropper.

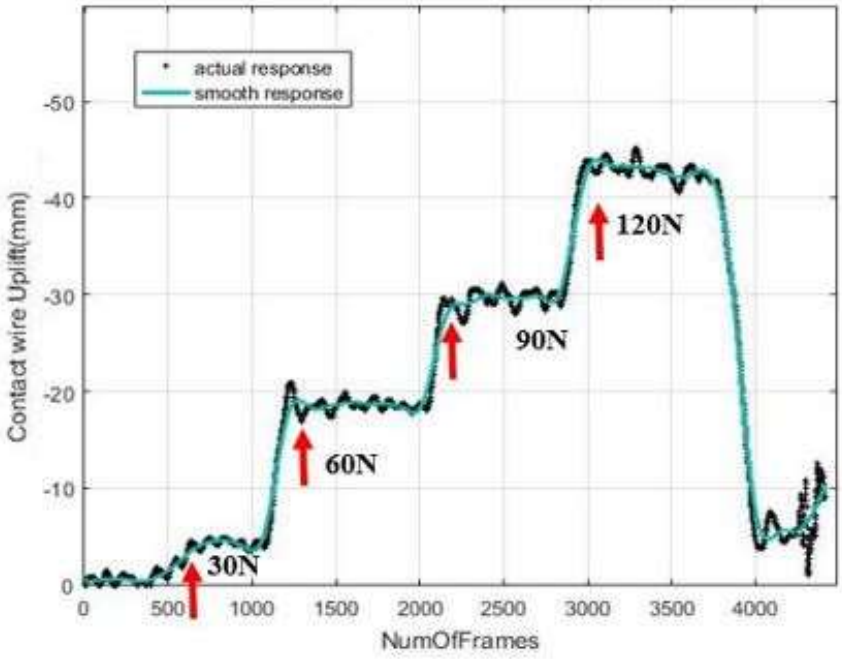


Figure 5-27: CW response characteristics at the fifth dropper

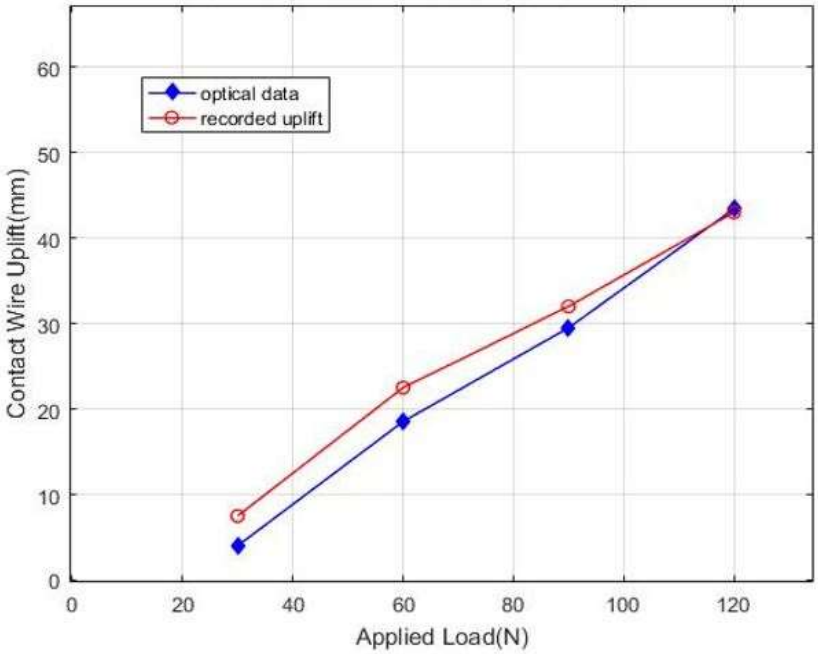


Figure 5-28: Variability of the recorded uplift at the fifth dropper

The variability of the contact wire displacement in between the lifts corresponding to each load shown in Figure 5-28, is as follows:

- As the force increases from 30 N to 60 N, the recorded uplift measured by the apparatus and the camera increases by 200% and 630% respectively.
- As the force increases from 60 N to 90 N, the recorded uplift measured by the apparatus and the camera increases by 42% and 36 % respectively.
- As the force increases from 90 N to 120 N, the recorded uplift measured by the apparatus and the camera increases by 34 % and 48 % respectively.

5.4.6.2 Second Trial

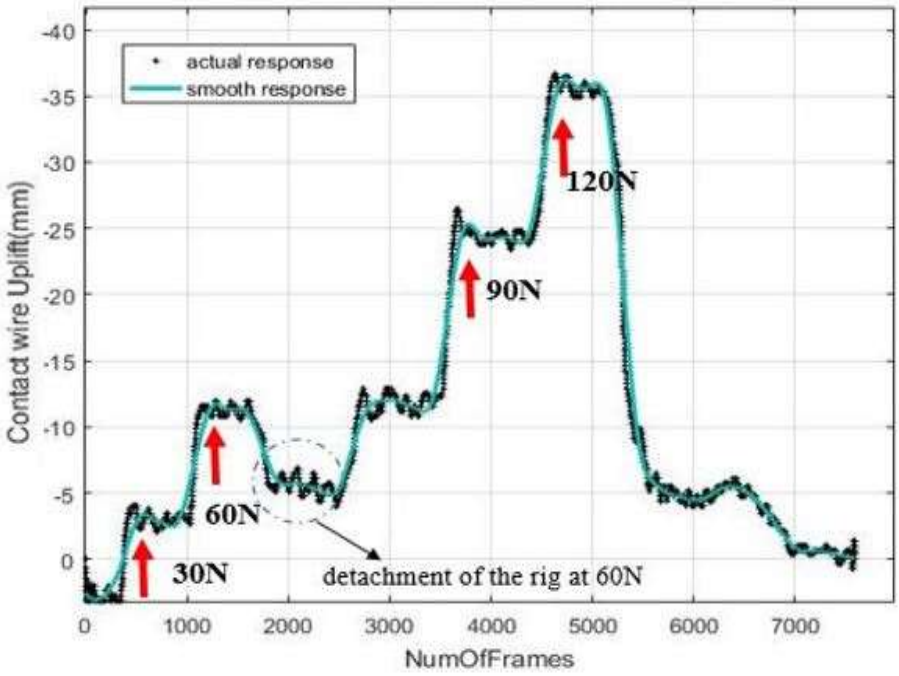


Figure 5-29: CW response characteristics at the fifth dropper

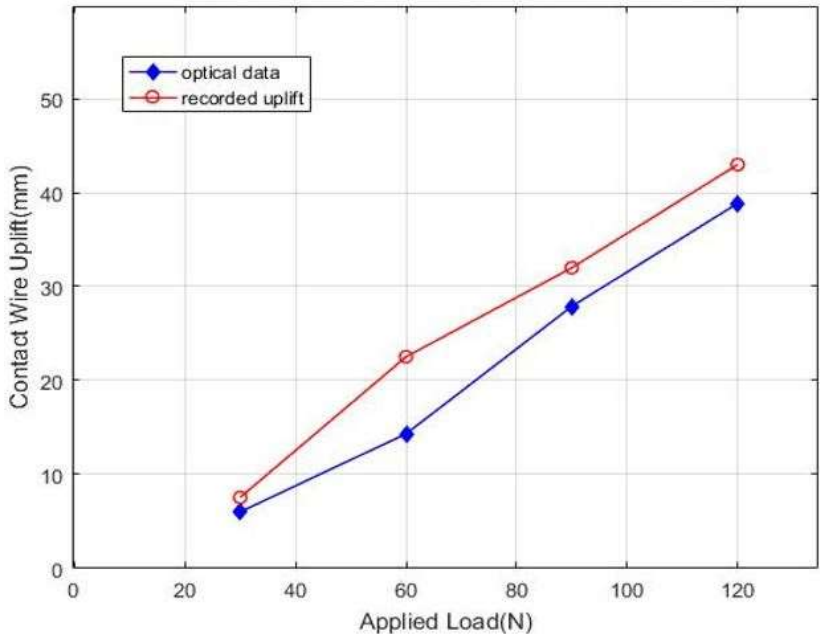


Figure 5-30: Variability of the recorded uplift at the fifth dropper

According to Figure 5-28, the following describe the variability of the contact wire displacement in between the lifts under each load:

- As the force increases from 30 N to 60 N, the recorded uplift measured by the apparatus and camera increases by 200 % and 210% respectively.
- As the force increases from 60 N to 90 N, the recorded uplift measured by the apparatus and the camera increases by 42% and 112% respectively.
- As the force increases from 90 N to 120 N, the recorded uplift measured by the apparatus and the camera increases by 34 % and 38 % respectively.

5.4.6.3 Third Trial

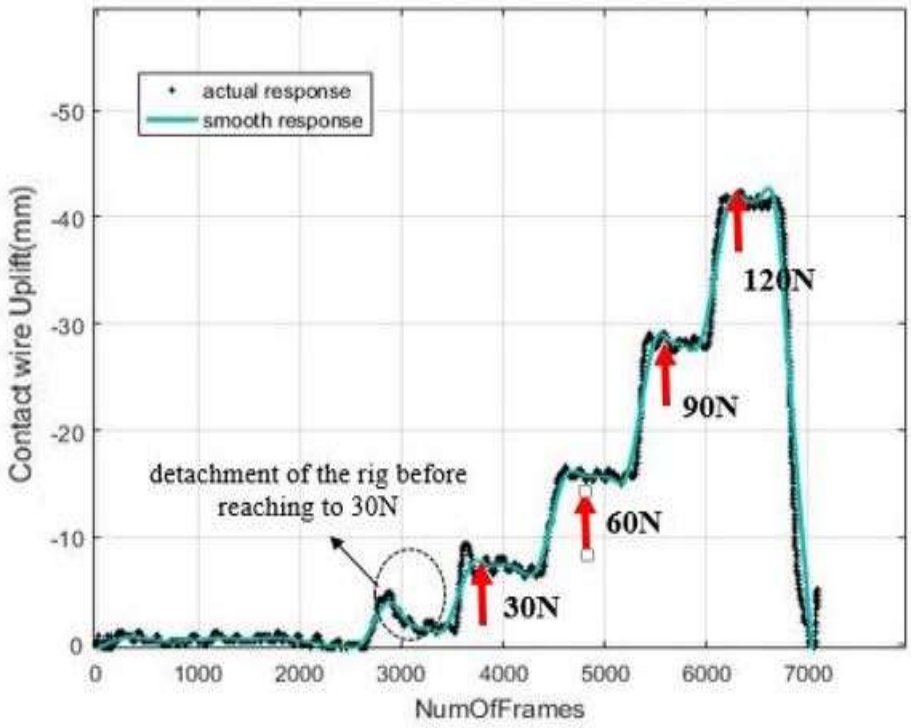


Figure 5-31: CW response characteristics at the fifth dropper

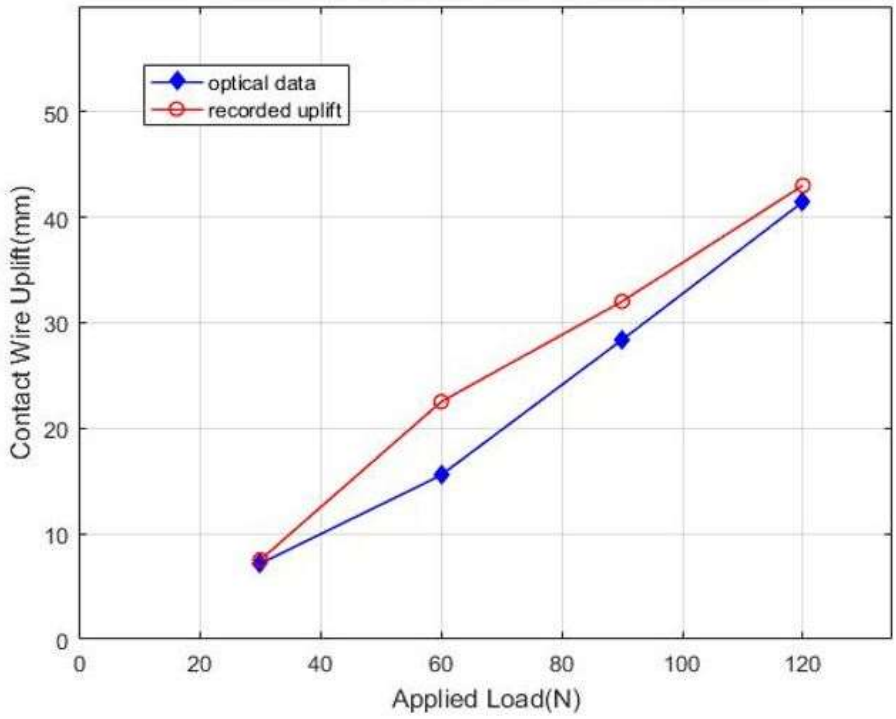


Figure 5-32: Variability of the recorded uplift at the fifth dropper

The variability of the contact wire displacement in between the lifts under each load according to Figure 5-32, is:

- As the force increases from 30 N to 60 N, the recorded uplift measured by the apparatus and camera increases by 200% and 128% respectively.
- As the force increases from 60 N to 90 N, the recorded uplift measured by the apparatus and the camera increases by 42% and 83% respectively.
- As the force increases from 90 N to 120 N, the recorded uplift measured by the apparatus and the camera increases by 34 % and 43 % respectively.

5.4.7 Second Registration Arm

The variability of the recorded uplift during each carried test to the mean of the data recorded under each load is measured as less than 5 millimetres. The uplift data recorded under 60 N and 120 N with 1.14 mm and 4.6 mm calculated standard deviation determine the smallest and the largest variability of the recorded data respectively. Figure 5-33 shows the recorded uplift at the fifth dropper.

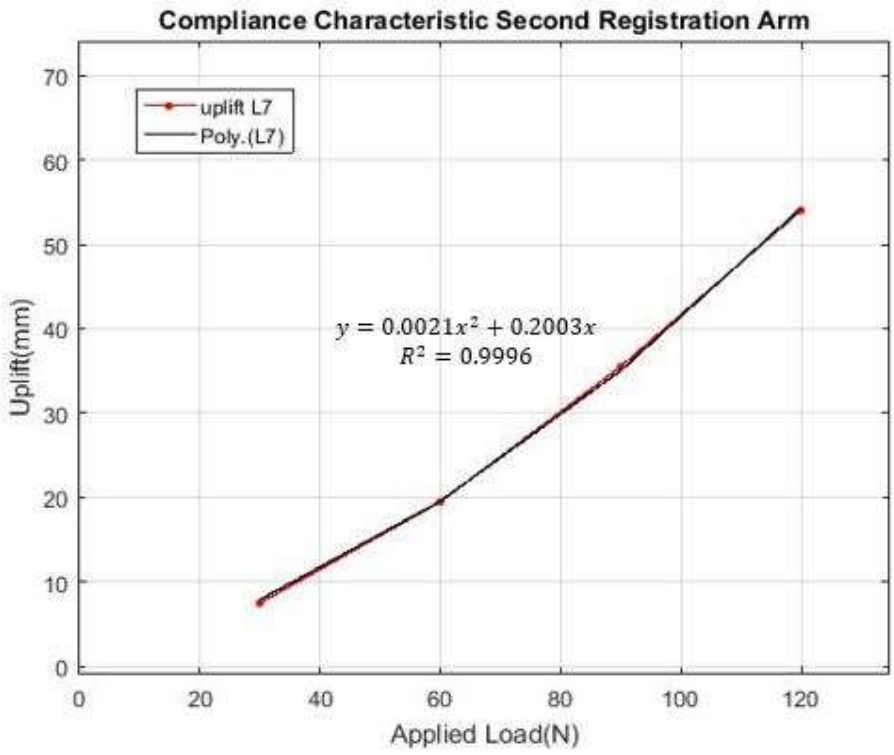


Figure 5-33: Uplift data (location: second registration arm)

5.4.7.1 First Trial

Figure 5-34 demonstrates the obtained contact wire response through the processing of the first video, recorded at the second registration arm.

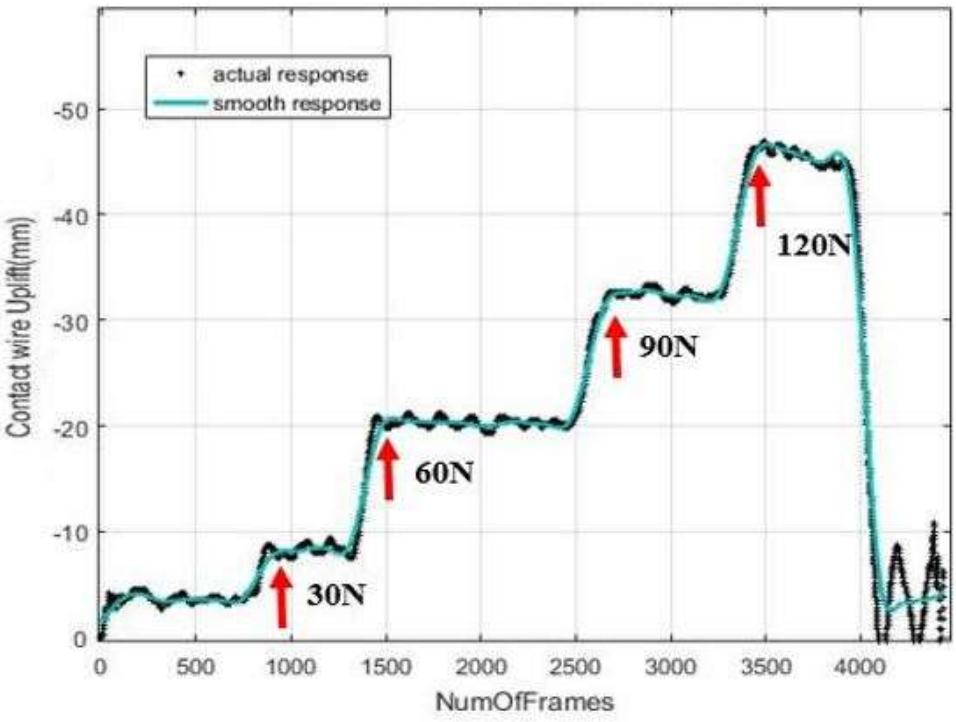


Figure 5-34: CW response characteristics at the second registration arm

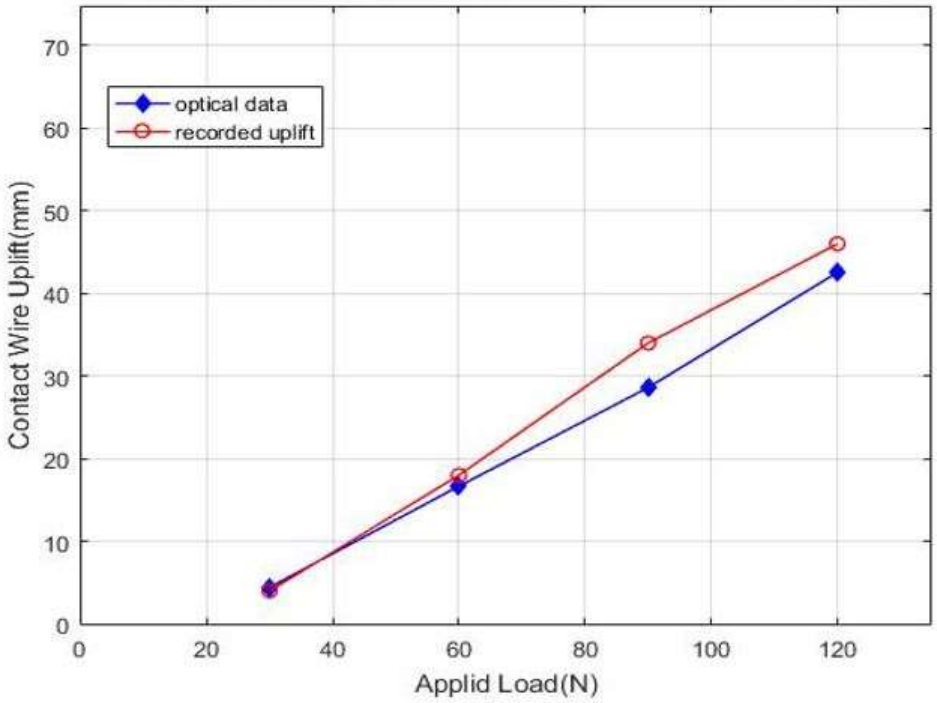


Figure 5-35: Variability of the recorded uplift at the second registration arm

According to Figure 5-35, the variability of the contact wire displacement in between the lifts corresponding to the applied load is as follows:

- As the force increases from 30 N to 60 N, the recorded uplift measured by the apparatus and camera increases by 160% and 144% respectively.
- As the force increases from 60 N to 90 N, the recorded uplift measured by the apparatus and the camera increases by 82% and 56% respectively.
- As the force increases from 90 N to 120 N, the recorded uplift measured by the apparatus and the camera increases by 52 % and 42 % respectively.

5.4.7.2 Second Trial

Figure 5-36 demonstrates the obtained contact wire response through processing of the second video, recorded at the second registration arm.

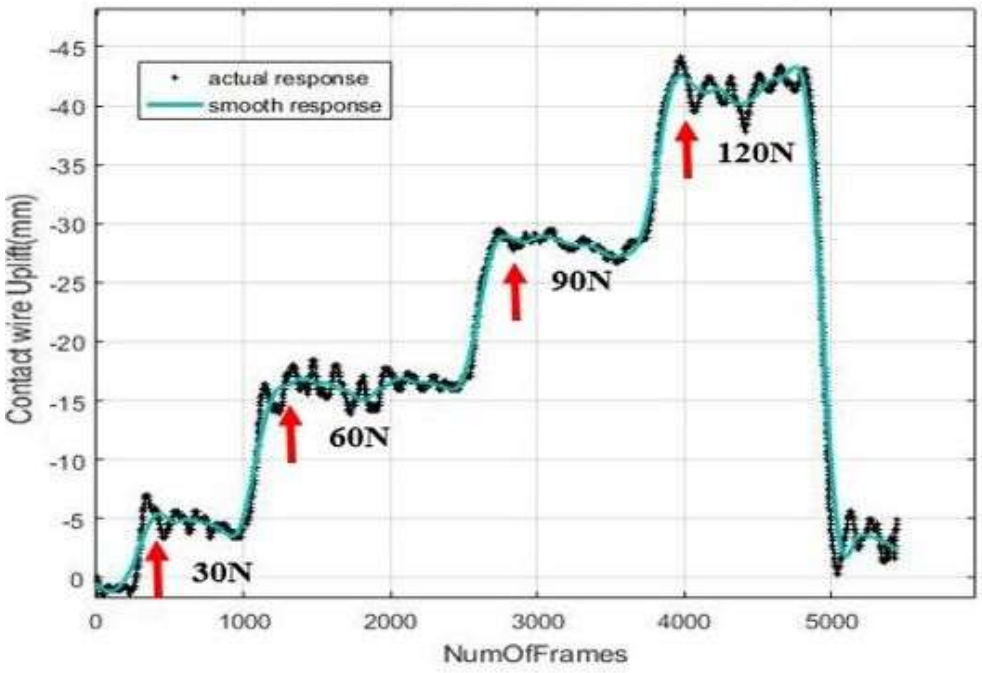


Figure 5-36: CW response characteristics at the second registration arm

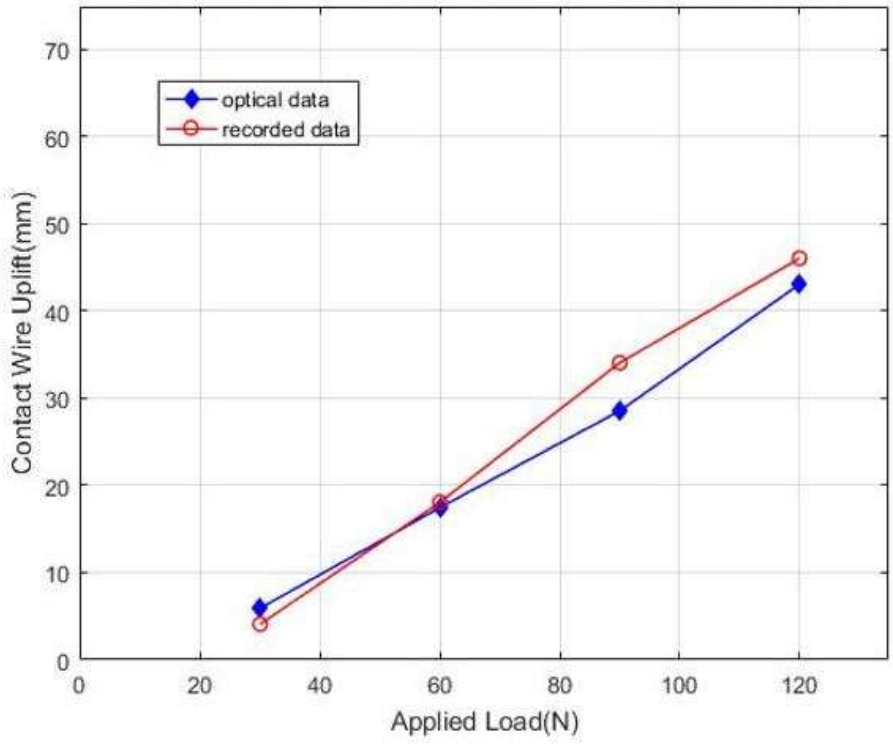


Figure 5-37: Variability of the recorded uplift at the second registration arm

Based on Figure 5-37, the following are achieved for the variability of the contact wire displacement in between the lifts against the applied load:

- As the force increases from 30 N to 60 N, the recorded uplift measured by the apparatus and camera increases by 160 % and 114% respectively.
- As the force increases from 60 N to 90 N, the recorded uplift measured by the apparatus and the camera increases by 82% and 85% respectively.
- As the force increases from 90 N to 120 N, the recorded uplift measured by the apparatus and the camera increases by 52% and 47 % respectively.

Figure 5-38 demonstrates the variations of the contact uplift recorded by the apparatus along the selected span.

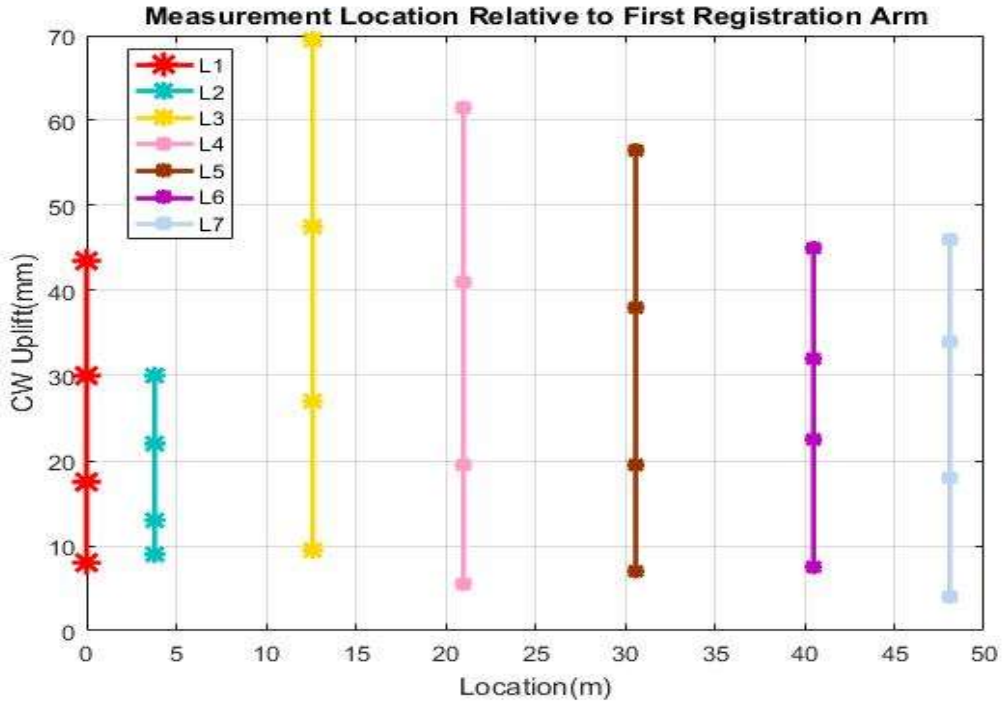


Figure 5-38: Recorded Uplift at each test location

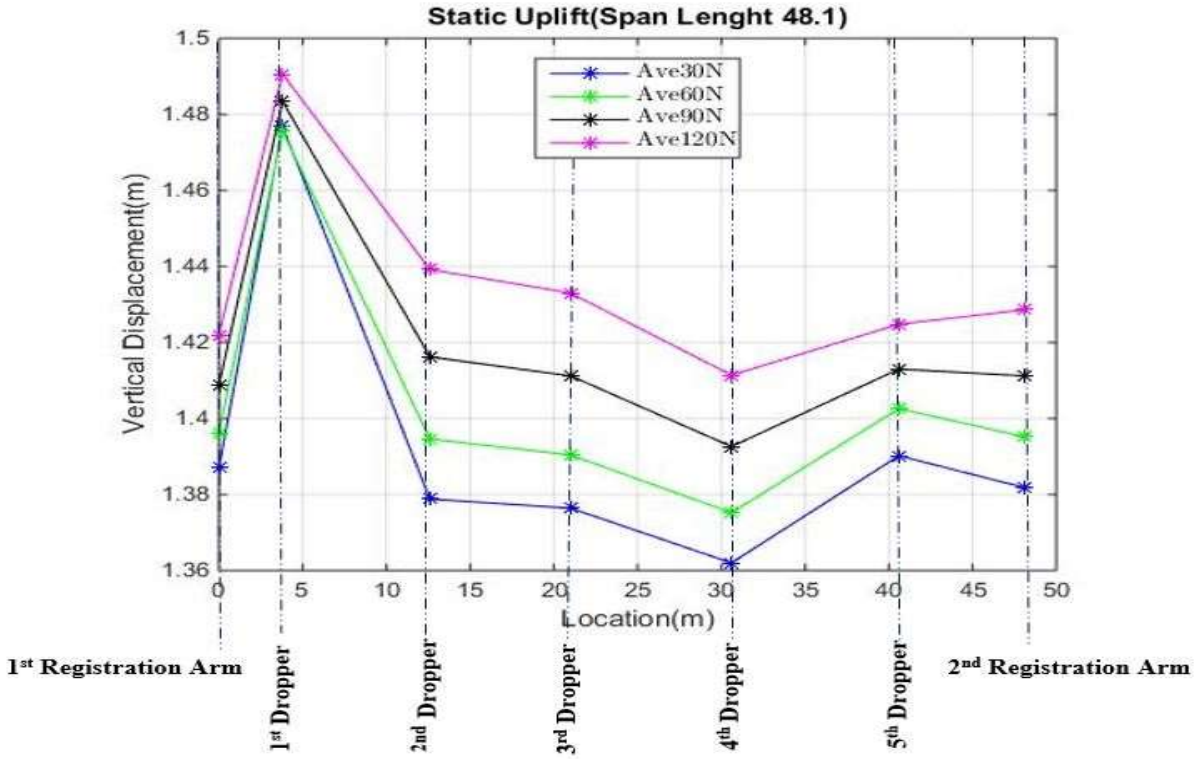


Figure 5-39: Static uplift of the contact wire under each load along the selected span

Figure 5-40 demonstrates the variations of the contact uplift recorded by the camera along the selected span.

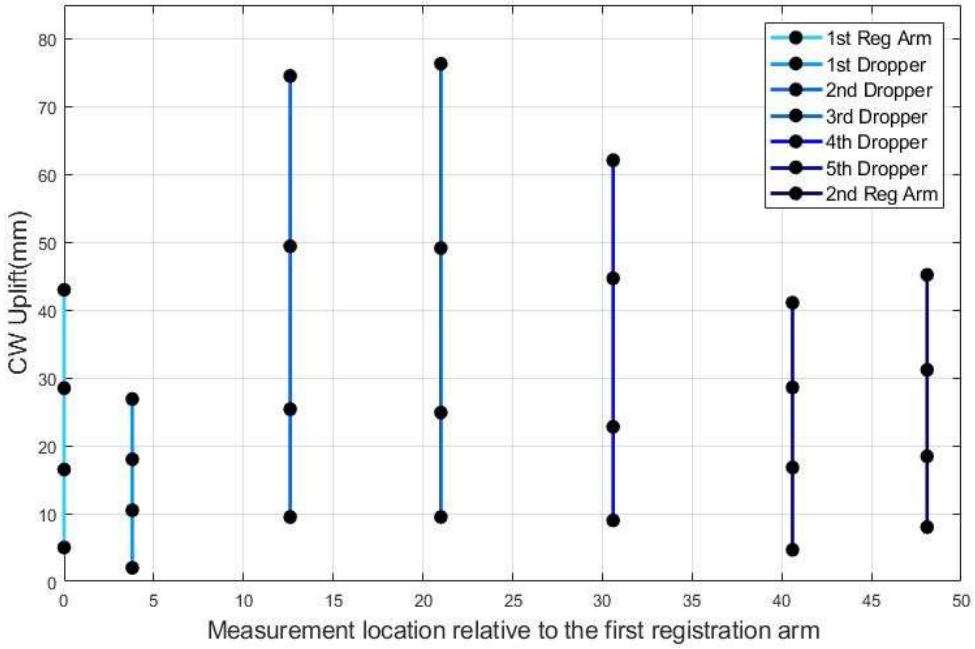


Figure 5-40: Recorded Uplift at each test location

From the experimental results presented throughout Section 5.4, it can be concluded that the load/uplift characteristics are generally linear. In the majority of the carried experiments, both utilised methods demonstrated the same trend of the contact wire uplift. The observed variations between the recorded uplifts are due to considering the median of the recorded uplift instead of the actual readings at each test location. Furthermore, the observed variations of the contact wire uplift are undoubtedly affected by the distance of the camera from the centre of the track and its elevation angle. One known disruption in manually measuring the uplift was to assure the stability of the lifting arm of the apparatus once it initiated the contact with the contact wire. The detachment of the apparatus from the contact wire repeatedly occurred throughout the experiments, which is mainly found to be due to the following causes:

- Loose catenary construction at Long Marston
- The height of the contact wire
- The height and weight of the mechanical arm
- The narrow holding surface of the hook

5.4.8 Investigation of the Contact Wire Stiffness Parameter

Knowing the applied forces and the recorded vertical displacement in response to each force, the contact wire vertical stiffness is achievable through Equation 5.3 (Woo Kim, et al., 2007):

$$K\underline{d} = \underline{f} \tag{5.3}$$

where K denotes the stiffness (N/m), $\underline{f}$ and $\underline{d}$ are the force vector and displacement vector respectively. Figures 5-41 to 5-47 are the demonstrations of the contact wire stiffness at each test locations.

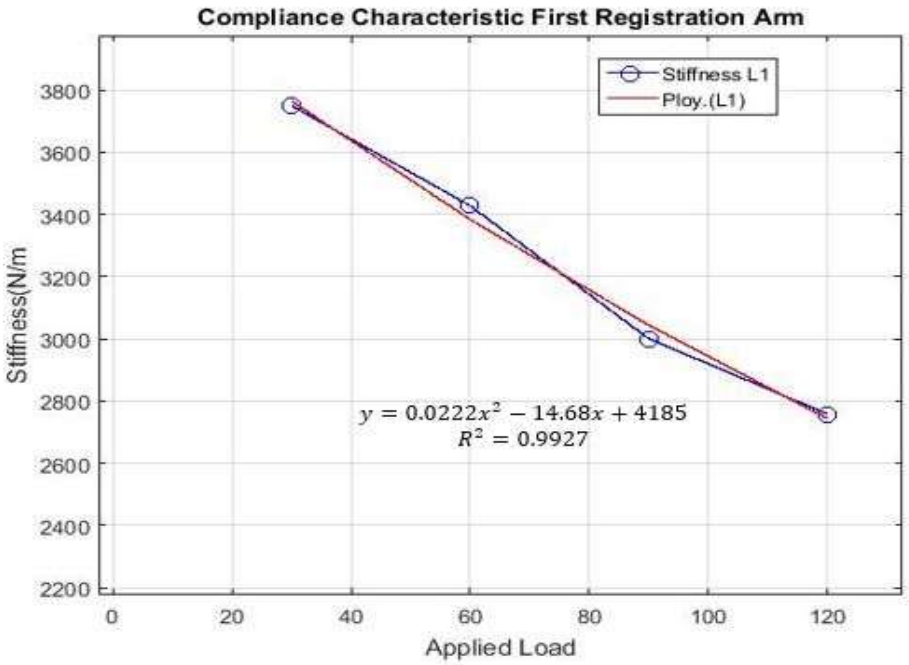


Figure 5-41: CW Stiffness at the first registration arm

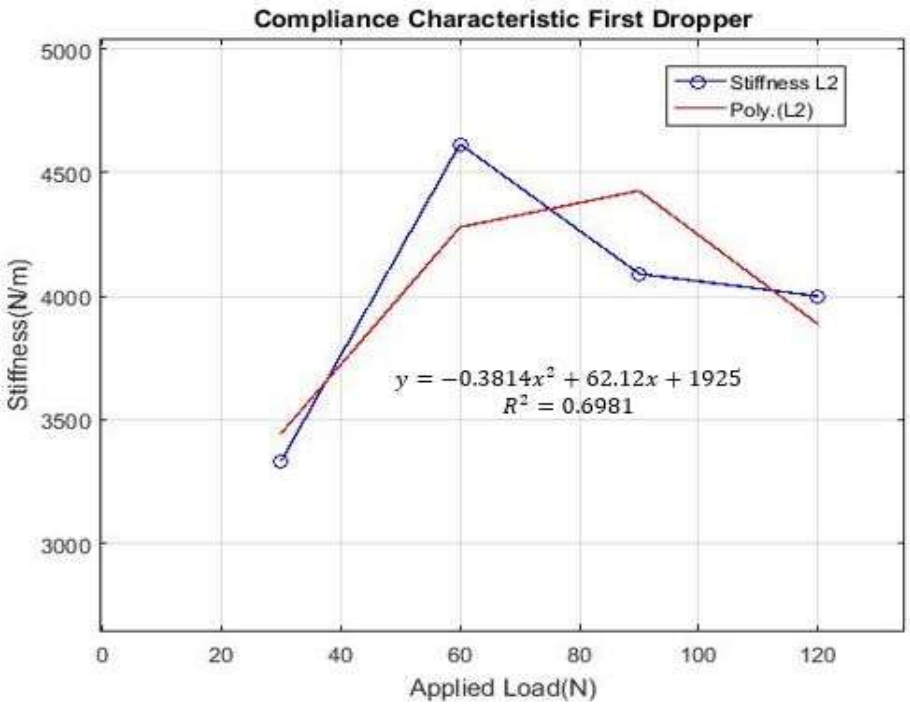


Figure 5-42: CW stiffness at the first dropper

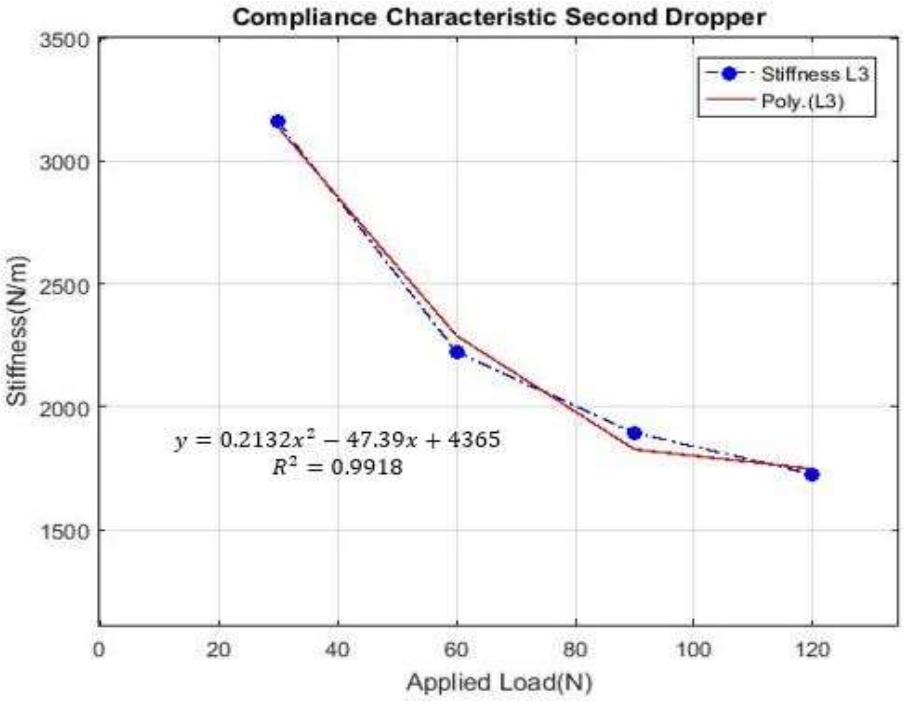


Figure 5-43: CW stiffness at the second dropper

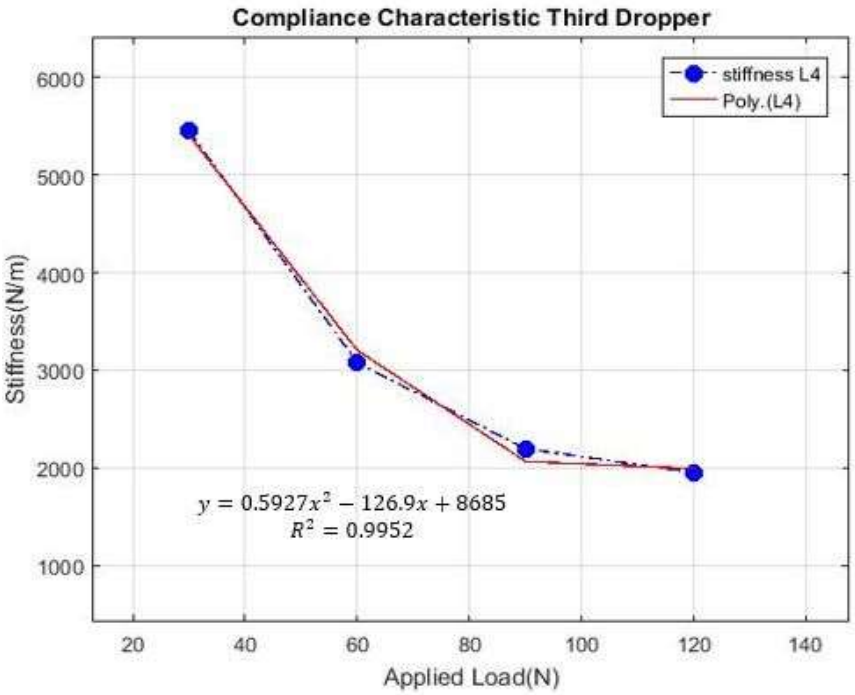


Figure 5-44: CW stiffness at the third dropper

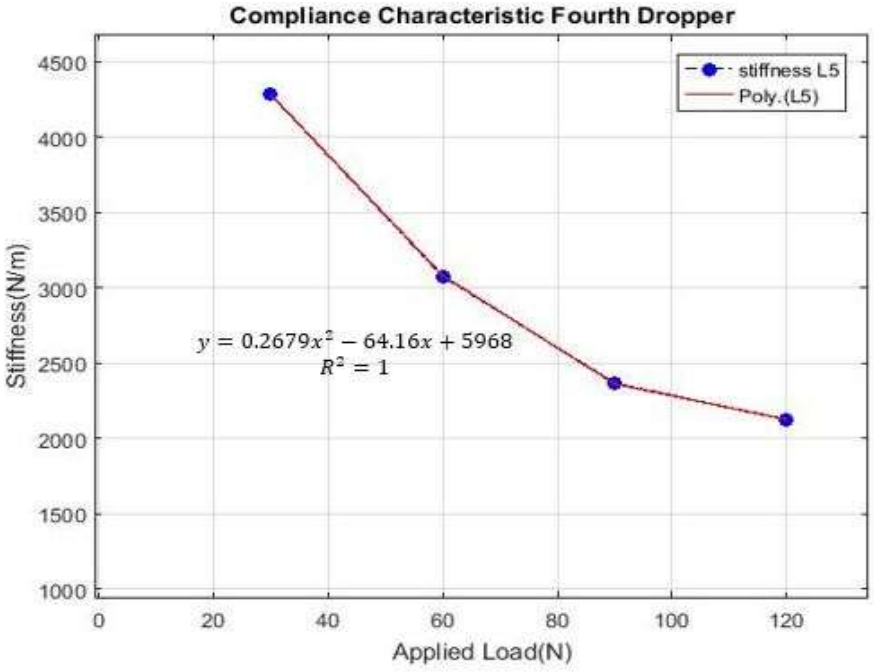


Figure 5-45: CW stiffness at the fourth dropper

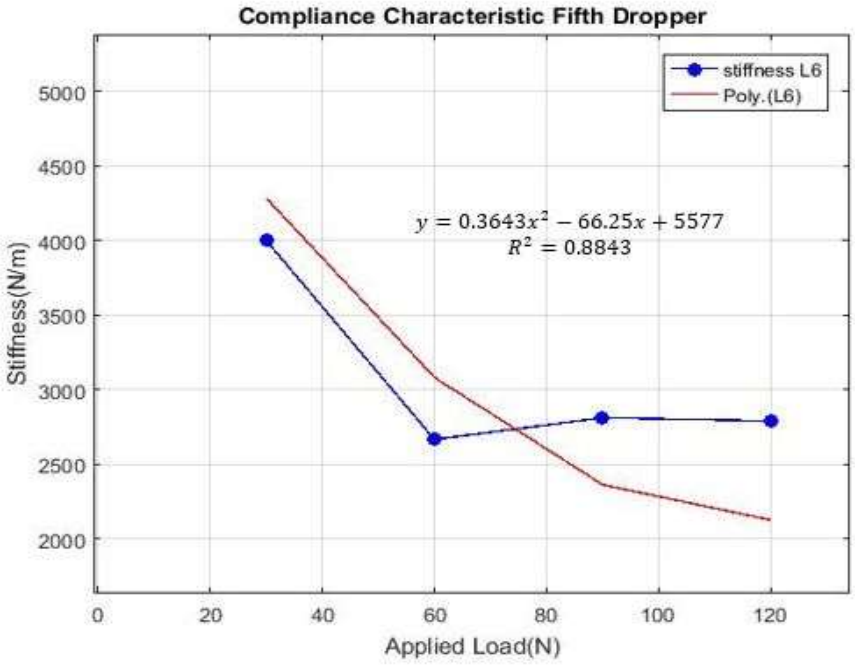


Figure 5-46: CW stiffness at the fifth dropper

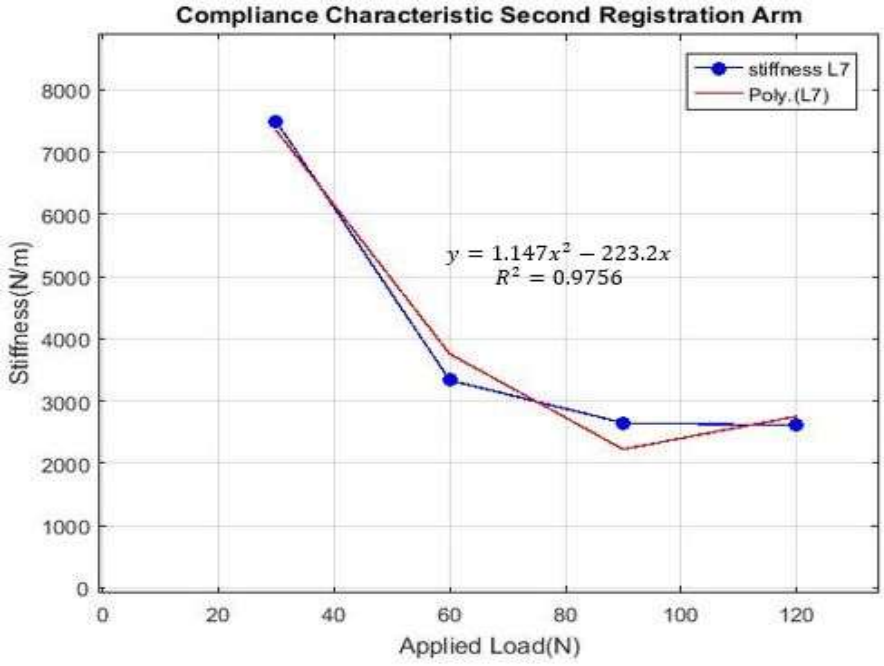


Figure 5-47: CW stiffness at the second registration arm

Figure 5-48 demonstrates the contact wire stiffness along the selected span.

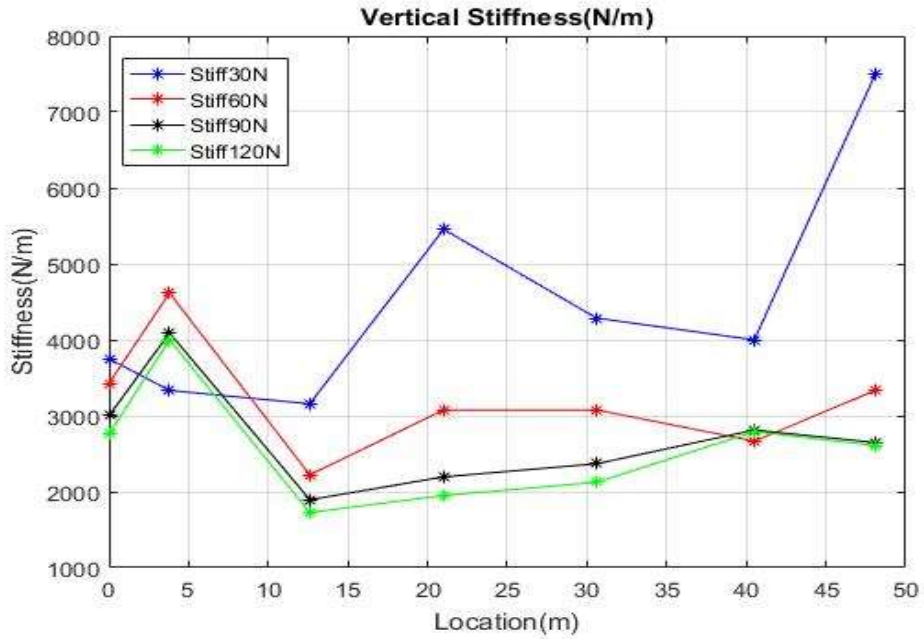


Figure 5-48: CW vertical stiffness along the span

Despite expecting a symmetrical trend of the contact wire stiffness from mid-span to each registration arm, an asymmetrical trend of stiffness is observed. In general, the first and fifth droppers are expected to be positioned at half a distance of the dropper spacing (i.e. about 4.5 metres) from the registration points at either ends of the span. The intermediate droppers are typically located at nine-metre intervals. The catenary construction at Long Marston is unevenly based on this setup, and the spacing of the last dropper is around eight metres to the second registration arm. Furthermore, an unknown tensioning of the contact wire, uneven tensioning in between the droppers are other potential reasons for the asymmetrical trend of stiffness along the selected span.

5.5 Summary

This chapter indicated the validity of the point-based analysis of trackside footages and the reliance on the image data in determining the contact wire uplift. The recorded static uplift through use of the apparatus and processing of trackside footages were compared and the variations of the component response under each loading condition were assessed. Analysis of the contact wire response using the recorded uplift by both monitoring methods showed larger variations under 30N which is attributable to stiffness of the contact wire according to its tensioning, and contribution of the spring friction. Despite observing good similarities between the recorded uplift using both methods at some of the test locations, the limitations of the

apparatus (i.e. bending of the lifting pole and its instability) led to variations between the measurements.

The practicality of the developed vision-based monitoring approach was indicated using the proposed framework which determines the pantograph contact force from the range that the contact wire lifts under different loading conditions.

As mentioned in Section 2.6.2.4 monitoring of the contact force involves measurement of three forces including the aerodynamic force. The contribution of the aerodynamic force increases at high speed runs and its measurement under service condition is a challenge. The application of the proposed trackside technique in monitoring of the contact force is limited to low speed test runs, where the impact of the aerodynamic force on the measurement of the contact force becomes negligible. Within the industry low speed test runs are usually performed when commissioning new OHL or when testing a new/ recently maintained pantographs. In addition to requirement for installation of transducers/sensors on either the OHL structure or the pantograph, the contact-based measurement of the uplift and the contact force at low speed test runs are disruptive, time consuming and prone to errors.

Once the camera is properly calibrated, using the uplift of the contact wire under different forces, the proposed trackside approach is effective in measuring the contact force of the pantograph. This is done through a non-disruptive, reliable and fast operation with no/less requirement for human intervention.

Chapter Six

6. MEASUREMENT OF CONTACT WIRE UPLIFT USING ON-BOARD VIDEO DATA

6.1 Introduction

This chapter introduces a novel technique of monitoring that enables OHL asset managers and senior decision makers to assess the degradation of contact wire through trending analysis of its uplift variations, obtained after each monitoring cycle. In contrast to the trackside monitoring of contact wire, that determines the uplift at a certain location of the contact line, the on-board monitoring approach provides wider insight about stability of the asset across the full catenary length. In the on-board data, detection of contact wire based on its line features does not provide information regarding its height variations. This is due to the viewing direction of the on-board camera and the location of the contact wire with respect to the camera lens (refer to Section 3.4.2.5). For this reason, feasibility of using the uplift data, obtained from detecting the pantograph, in determining means to mimic degradation is investigated.

The chapter describes the adopted procedures to processing and post-processing of the on-board data, and evaluates the performance of the adopted technique in recognition and detection of the pantograph from the background objects in the on-board videos. Using the

obtained results, the application of the proposed technique in using uplift as a measure of condition to determine degradation is explained. Three scenarios are discussed through which the trending analysis of the contact wire uplift enables comparison to be made to better specify the probable causes of defects.

6.2 Current Application of the On-board Video Data

On-board monitoring systems aid railway engineers to more precisely assess the reliability of the catenary-pantograph system by enabling them to observe the performance of the pantograph. Although the recorded videos are potentially appropriate for uplift measurement, the application of uplift measures in determining the reliability of wires is not included in existing monitoring systems. As stated by a senior member of Network Rails OHL team, the only use of this data at the moment is manually watching and focusing on functioning of the pantograph which can be very time consuming, exhausting and prone to human errors. The visual assessment of on-board videos aid in identifying causal factors linked to incidents and system failures and liable parties for damages. Due to huge size of data and their current limited application, the majority of data are erased from the data mass-storage unit after a short period without being assessed. Figure 6-1demonstrates detachment of the pantograph captured by an on-board camera. This incident and its consequences on the train operation cost the train operator company £500K.



Figure 6-1: Breakage of the pantograph and its detachment from the train

6.3 Monitoring of Contact Wire Height Variations

The strength of any detection and tracking algorithm is in processing of the images as fast as possible whilst maintaining high detection rate. Recognition and detection of the pantograph from the on-board data is a challenging task. The main reason is, as the camera moves with the train, the background features are in constant change throughout the video. The properties of the background, variations of the pantograph location, non-uniform movement of the pantograph and the requirement of the system to process the data in near real-time, narrows the selection of methods suitable for the desired task. To overcome the processing complexities in detecting the pantograph from a dynamic scene, Cho & Park (2016) suggested the use of limited number of frames (i.e. 300 frames from three test runs over three days) and categorising them based on common background features.

Determining the contact wire height variations along the entire catenary length requires frame by frame processing of the videos and estimation of the contact wire height from the returned coordination information of the pantograph. The utilised method to enable classification of the panhead from the background objects is a machine learning approach, developed based on the Viola-Jones method (discussed in Section 3.4.5.2). Despite initial application of the Viola-Jones method in detecting the human faces, the real-time performance level offered through this method led to its further practicality in other vision-based applications such as vehicle tracking system for analysis of the traffic scene (Moghimi, et al., 2019). The proposed on-board monitoring in this chapter enables recognition of the pantograph discriminant features from the background objects by a strong classifier that is constructed using the Viola-Jones method. Figure 6-2 is the block diagram of the system developed to extract the contact wire height from the on-board video.

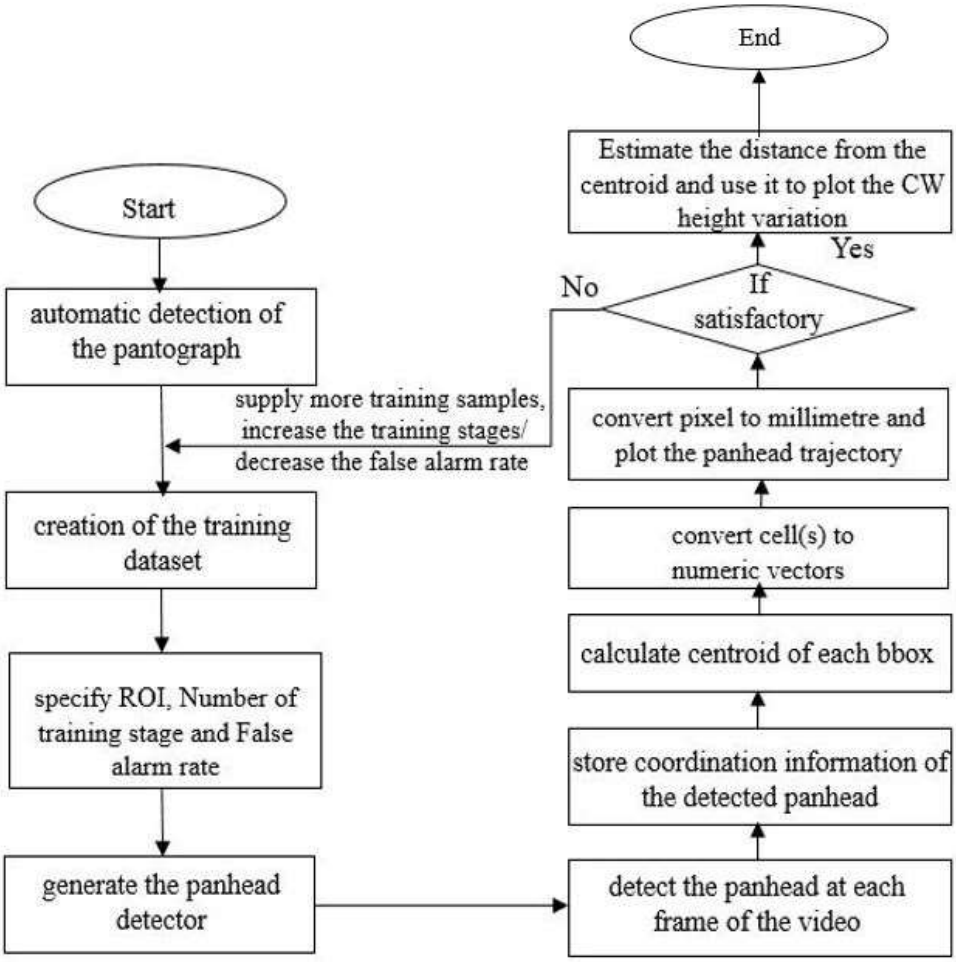


Figure 6-2: System Processes

The classification of the pantograph from background objects is performed using the following steps:

1. **Creation of a training dataset**: Training dataset is created from the extracted video frames. The training samples are generated for the pantograph and background objects separately. Data is in a range of thousands of samples obtained by applying different size of masks to different regions of the images as well as changing the contrast and brightness level of samples.
2. **Training:** AdaBoost is the adopted algorithm through which the best features with minimum error rate are selected to build a strong classifier.
3. **Evaluation:** the performance of the generated classifier is examined by observing the detection results in the videos that were not fully used to create the training samples.

Training of the classifier is performed in number of different stages. Each stage is formed by simple classifiers that enable efficient classification of the image regions. Each stage of the classifier filters one Haar-like feature. AdaBoost (see Section 3.4.5.2) gives weights to these stages, and the stage with the highest weight comes first. At each stage, the current region of the sliding window can be labelled as either positive or negative. If the region is labelled as negative, the classification of that region is completed and the classifier slides the window to the next region. If the region is labelled as positive, the training of that particular stage is completed so the classifier passes the region to the next stage.

Since majority of windows do not contain the object of interest, the negative samples containing the background objects are swiftly excluded at the first training stages. Once training of each stage completes, the image regions that successfully passed the filter, enter to the next stage with a more complex filter. Accordingly, those image regions that successfully pass the final stage contain the object of interest (Viola & Jones, 2001). Depending on the number of training stages and that of supplied samples, early termination of training is possible. Reducing the number of training stage and retraining of the classifier does not yield to same results since the required positive and negative samples are recalculated corresponding to the defined training parameters.

6.3.1 Processing of the First Video

To train a strong classifier it is necessary to establish a training dataset with sufficient samples to be used at each training stage. To achieve a high detection rate, training is performed over a high number of stages either by supplying more training samples or selecting a low false alarm rate (i.e. portion of negative samples incorrectly classified as positive sample) for each stage. In the case of latter, as soon as the object is labelled incorrectly as negative the classification of the training stage terminates.

The procedure of training a strong classifier with good generalisation involves a lot of troubleshooting and tuning of parameters to gain the desired detection rate. However, through use of a strong classifier a higher detection rate is achieved.

The first classifier to detect the pantograph was trained over eight stages with false alarm rate of 0.5. Figure 6-3 demonstrates the trajectory of the pantograph height obtained after processing of the video using the first classifier.

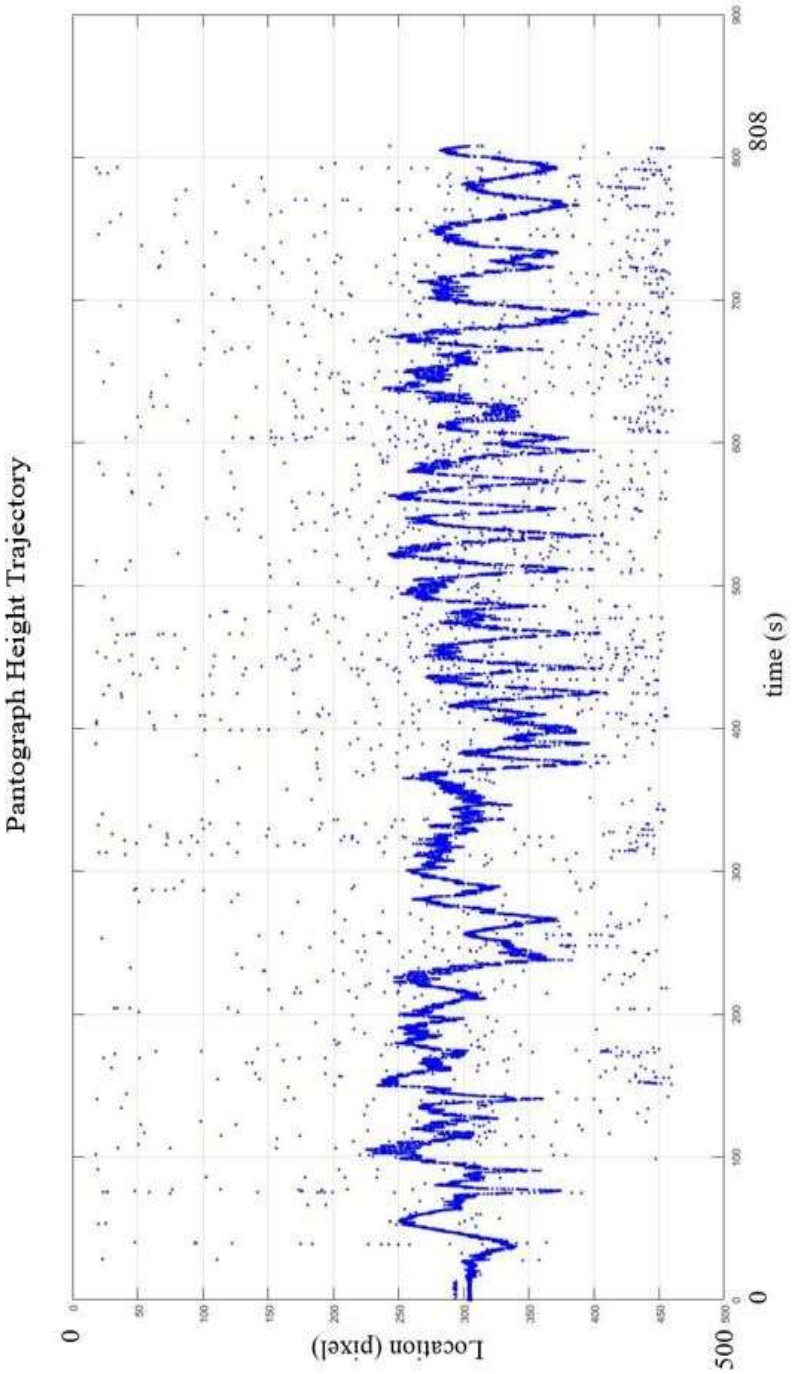


Figure 6-3: Pantograph Height Trajectory(8stages of training at 0.5 FAR)

With this setting and the current number of true positives (correct classification of the pantograph), false positives (classification of background objects as pantograph), and false negatives (classification of pantograph as a background object) the estimated locations of the pantograph can be identified (see Figure 6-3). However, the number of false tracks in proximity of the panhead trajectory creates uncertainty in determining its actual location.

To achieve a higher detection rate the number of training stages increased to twelve. To avoid overfitting and reduce computational complexity at each training stage the false alarm rate remained the same.

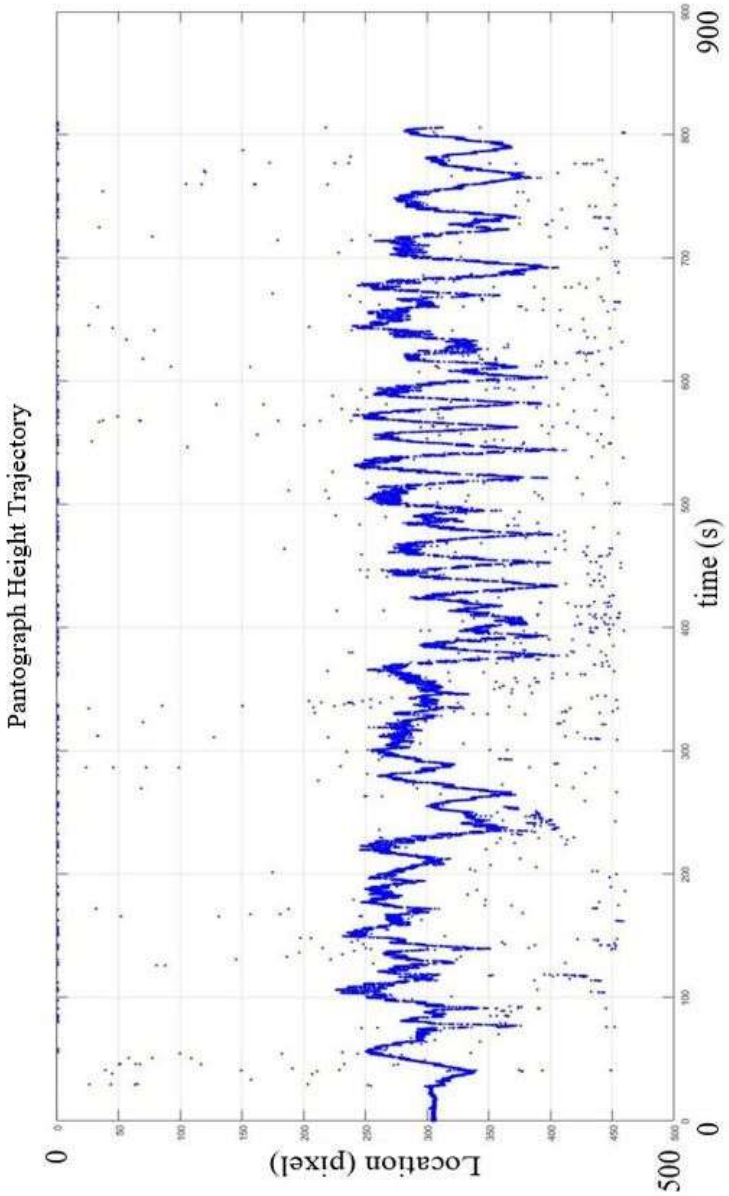


Figure 6-4: Pantograph Height Trajectory (12 stages of training at 0.5FAR

To gain further higher detection rate, the training stages were set to twenty and false alarm rate reduced by 0.3. Using these settings, the estimated pantograph height trajectory is shown in Figure 6-5.

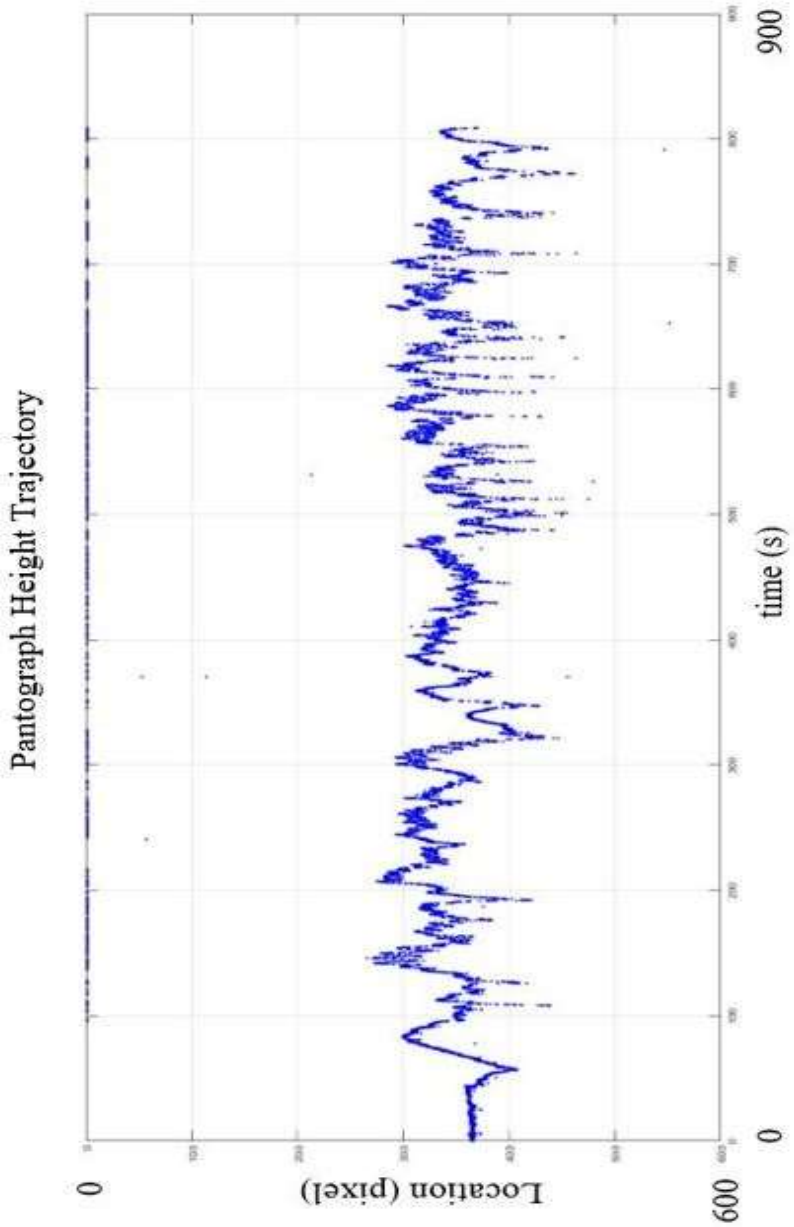


Figure 6-5: Pantograph Height Trajectory (20 stages of training at 0.2FAR)

After assessing the detection results, it is found that the majority of the false and missing tracks are corresponding to the following locations:

- Near portal frames: structural similarity of portal frames and pantograph in some of the video frames resulted in false/missing tracks.
- Entering to the tunnels: low contrast between the pantograph and brick wall of the tunnel caused camouflage and resulted in missing tracks.
- Inside tunnels and bridges: lack of sufficient illumination led to fewer colour information and resulted in missing tracks.

- Exiting tunnels: very limited colour information due to severe brightness level resulted in missing tracks.

6.3.1.1 Detection Results

Figures 6-6 and 6-7 show the performance of the system in detecting the pantograph in some of the open-route backgrounds.

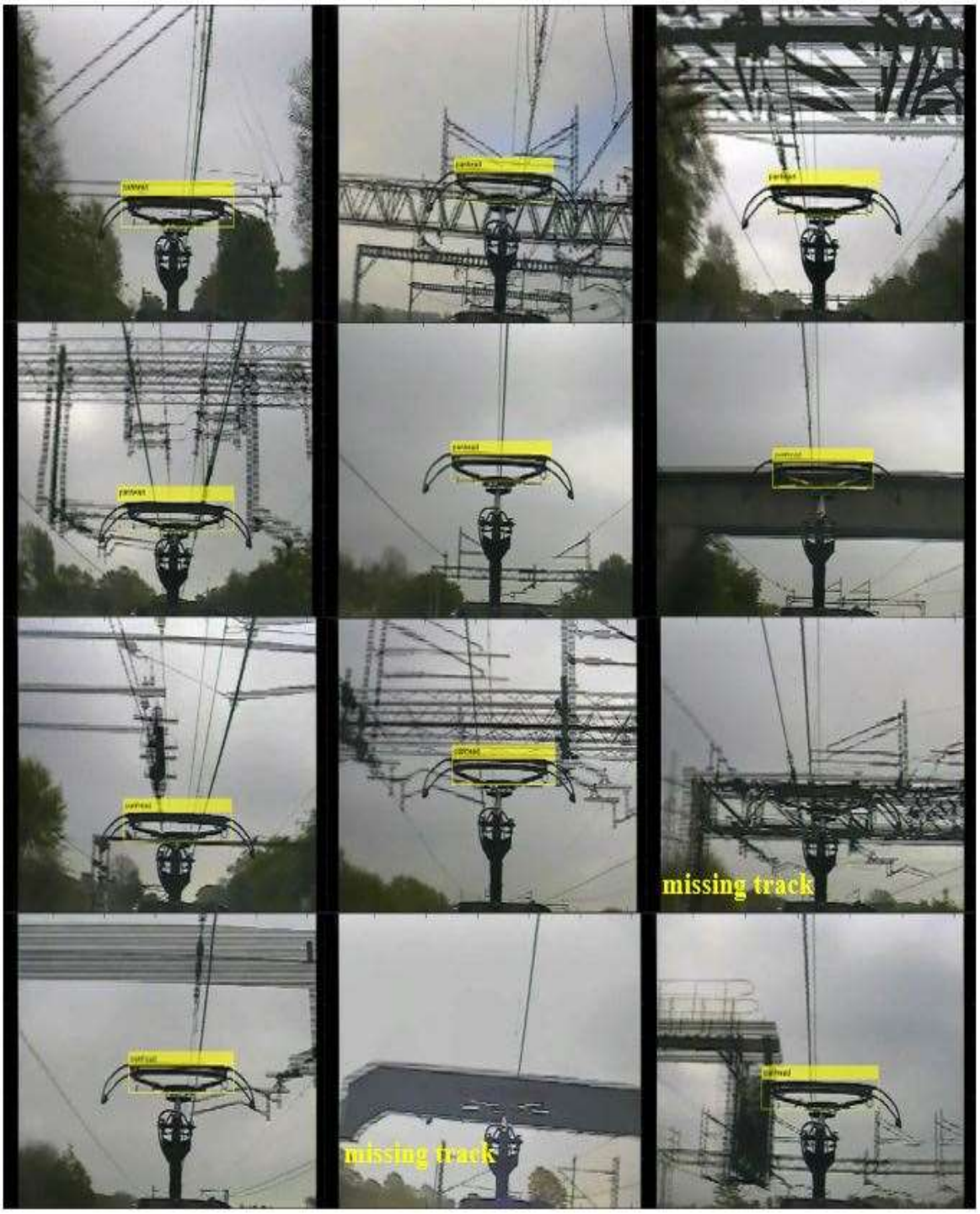


Figure 6-6: Performance evaluation on open-route equipment



Figure 6-7: Performance evaluation on open-route equipment

Figures 6-8 to Figure 6-12 shows the performance of the system near structures, throughout tunnels and bridges.



Figure 6-8: Performance evaluation at the first structure,(a) missing track due to the low contrast



Figure 6-9: Performance evaluation at the second structure, (a) missing track due to brightness severity

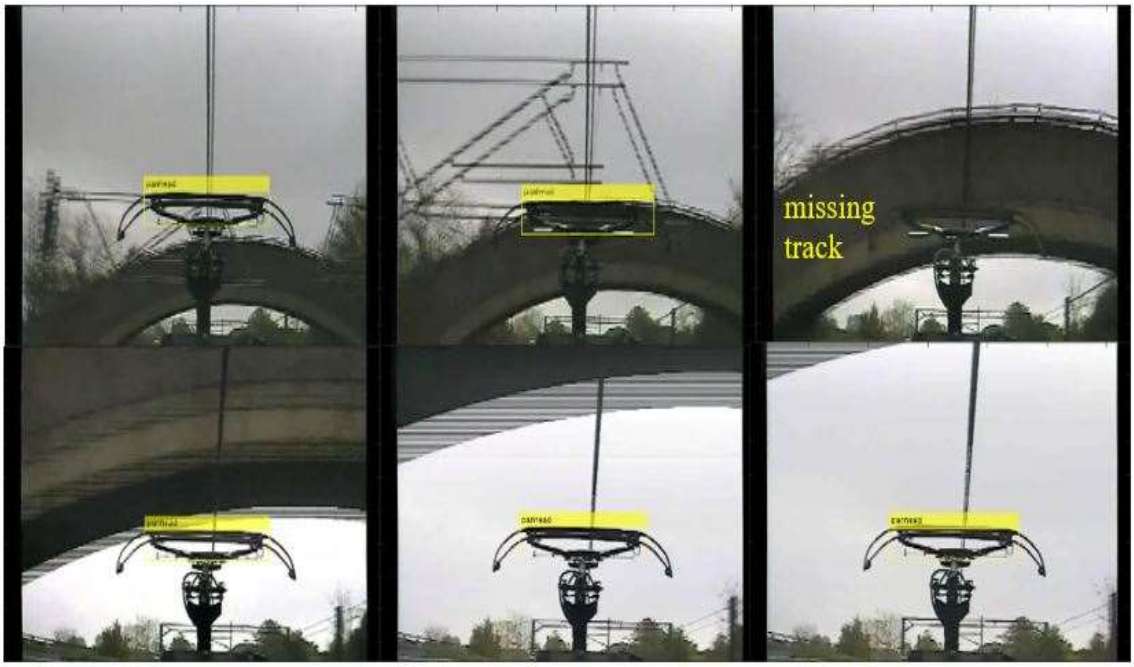


Figure 6-10: Performance evaluation at the third structure



Figure 6-11: Performance evaluation at the fourth structure



Figure 6-12: Detection challenges in poor and severe brightness level at the bridges

6.3.1.2 Performance Evaluation

The performance of the developed system is evaluated by three measures; precision, recall and quality. As in Section 3.4.5.2, these measures are defined by quantitative metrics that categorise the detection results into TP (i.e. correct detection of the object), FP (i.e. detection of a background object as object of interest) and FN (i.e. wrong labelling of the object that appears as a missing track). Due to limitations of the leading platform used in the design of the suggested system, automatic computation of the defined metrics was not possible. Thereby, the performance of the system is evaluated by observing the detection results in one thousand frames. These were selected from output frames featuring the effectiveness of the system amongst both open-route equipment and throughout a tunnel. Table 6-1 describes performance of the system.

Table 6-1: System Performance

Classifier	TP	FP	FN	Precision	Recall	Accuracy
8stages at 0.5 FAR	692	216	92	76	88	69
12stages at 0.5 FAR	767	163	70	82	91	76
20 stages at 0.2 FAR	947	14	39	98	96	94

6.3.1.3 Contact Wire Height Variations

To covert the pantograph height variations from pixel to millimetre the length of the collector strip was used as a guide. Knowing the length of the collector strip (~ 39 centimeters), the $calib\left[{}^{pixel}/_{mm}\right]$ is calculated by counting the number of pixels featuring the collector strip in image data.

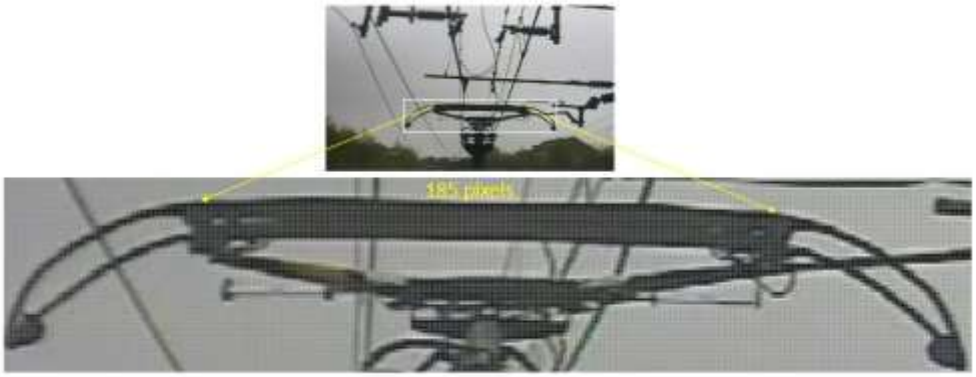


Figure 6-13: Measurement of the conversion coefficient

Figure 6-14 shows the pantograph height variations after converting each pixel value to millimetre.

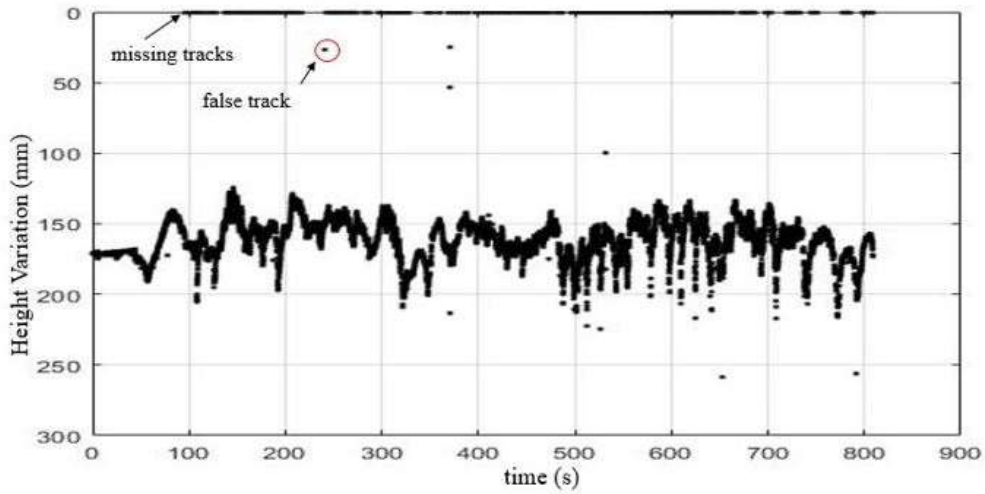


Figure 6-14: Pantograph Height Variations (mm), calib=0.4683

The results in Figure 6-14 involves two types of uncertainties. The first uncertainty is due to estimation of the length of collector strips and the second is attributable to observations taken by camera from the movement of the pantograph.

To estimate the real vertical movement of the pantograph from the images, camera properties such as; its distance and elevation angle to the pantograph must be known. By calculating the camera coverage area at a certain distance, the vertical displacement of the pantograph from the sequences of the video frames can be calculated based on the vertical resolution of images. Figure 6-15 illustrates the geometry involved in the calculation of camera coverage area.

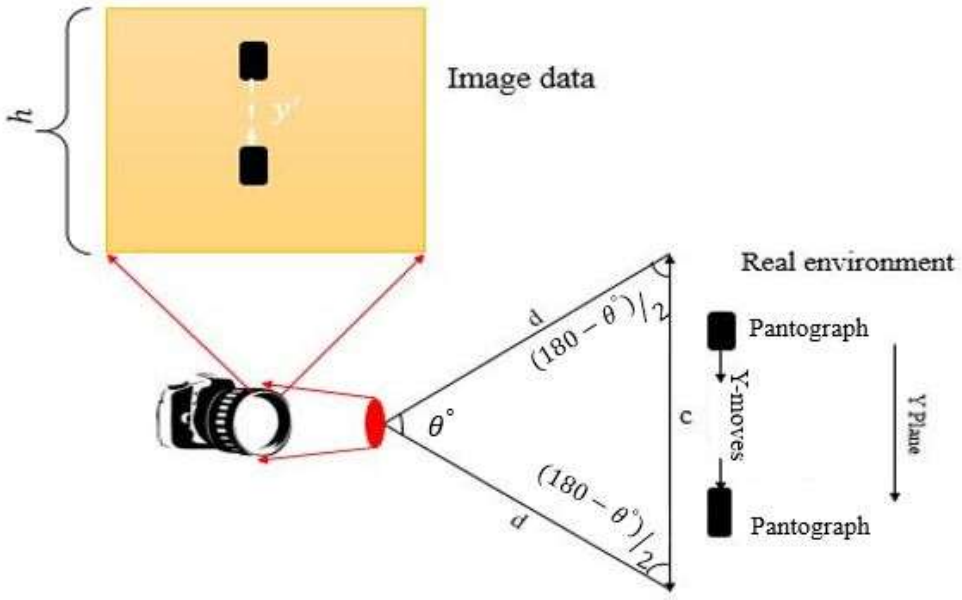


Figure 6-15: Image mapping technique

Where d is the distance between the camera lens and pantograph, c is the camera coverage area and θ is the degree of the camera span. The coverage area of the camera can be calculated using Equation 6.1 (Das, et al., 2012).

$$\frac{c}{sin\theta} = \frac{d}{\sin((180-\theta)/2)} \qquad (6.1)$$

$$c = \frac{d \times \sin\theta}{\sin(90-\theta/2)}$$

As an example, if $\theta = 60^{\circ}$ and $d = 4\,m$, the camera coverage area c is calculated as:

$$c = \frac{4000 \times sin60^{\circ}}{cos60^{o}} = 6928\,mm$$

By knowing the coverage area and the vertical resolution h, in reality the vertical displacement of the panhead in pixel is equal to $^{c}/_{h}$. Accordingly, if the total displacement of panhead y' across two successive video frames is 3 pixels, the real displacement of the panhead can be calculated as:

$$\mathrm{y} = \frac{\mathrm{c}}{\mathrm{h}} \times \mathrm{y}' = \frac{6928\ \mathrm{mm}}{576\ \mathrm{pixel}} \times 3\mathrm{pixel} = 36\ \mathrm{mm}$$

Figure 6-16 is a demonstration of the pantograph height variations after estimating the actual displacement of each pixel using the camera coverage area and image vertical resolution.

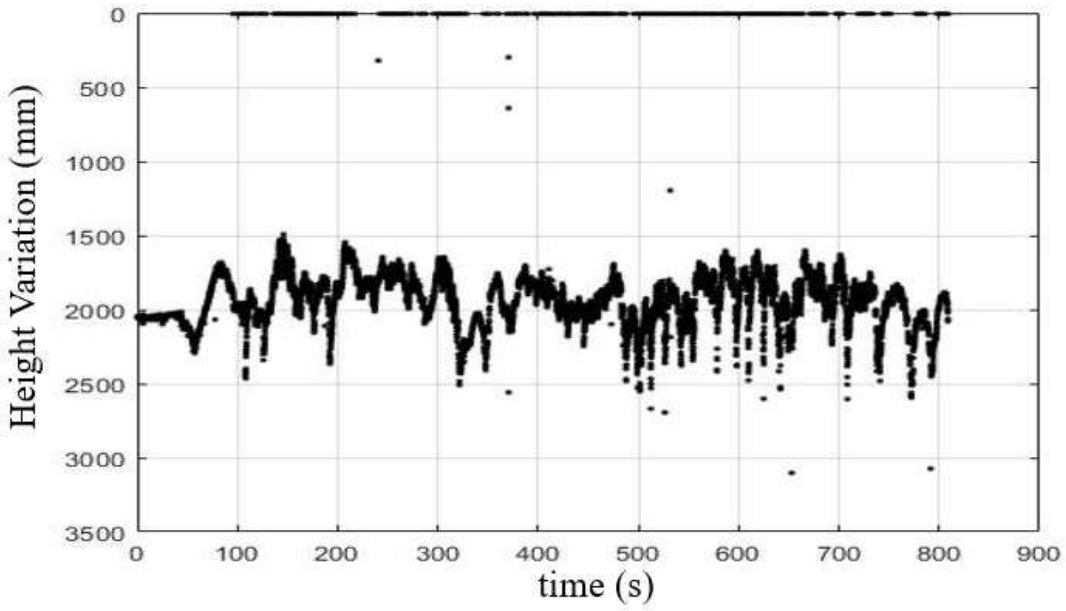


Figure 6-16: CW height variations considering movement of each pixel in reality

The contact wire height variation is achieved corresponding to the number of pixels between the centroid of the bounding box and upper edge of the collector strips.

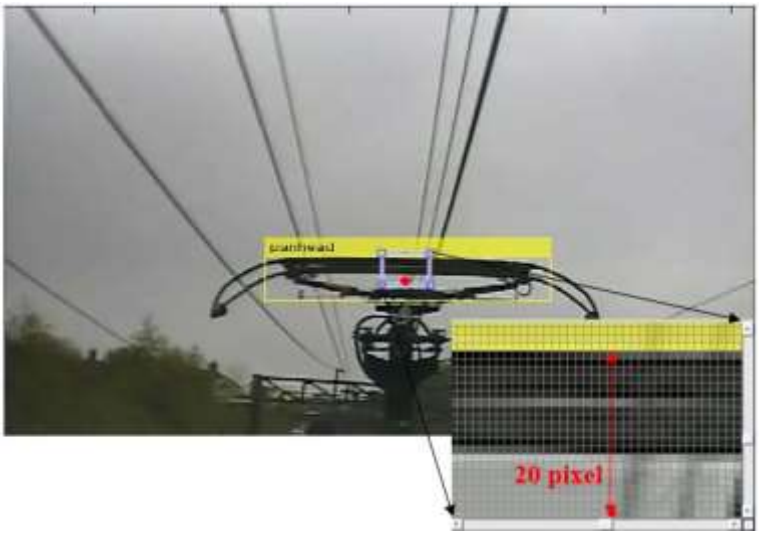


Figure 6-17: Calculation of the conversion factor

Using the calculated number of pixels from the computed centroid of the bbox to the upper edge of the collector strips, and the value of each pixel in millimetres, the contact wire height is estimated from the obtained location of the pantograph at each video frame.

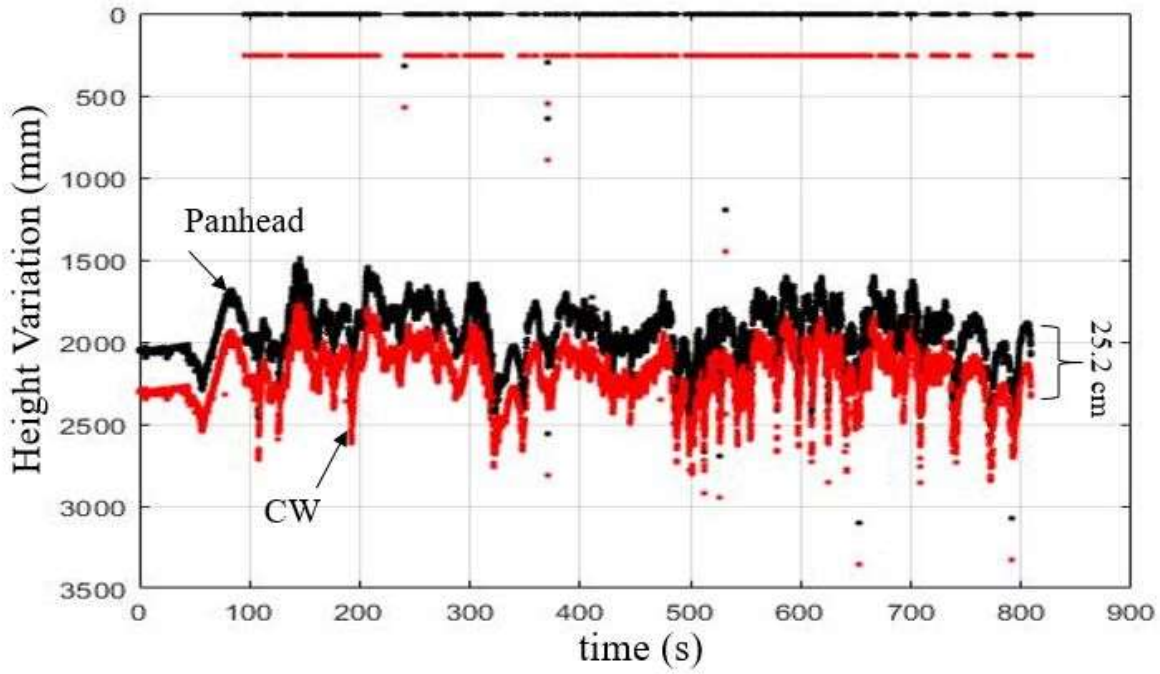


Figure 6-18: Estimation of the CW height variations

6.3.2 Processing of the Second Video

The performance of the utilised technique on the second video from a different line is examined. Figure 6-19 demonstrates the performance of the system in recognition and detection of the pantograph from the background objects.



Figure 6-19: Performance evaluation of the system and its sensitivity to deviation of the pantograph

The contact wire height variation is estimated according to location of the pantograph using the post-processing procedures in Section 6.3.1.3. Figure 6-20 demonstrates the contact wire height variations, achieved through analysis of the second video.

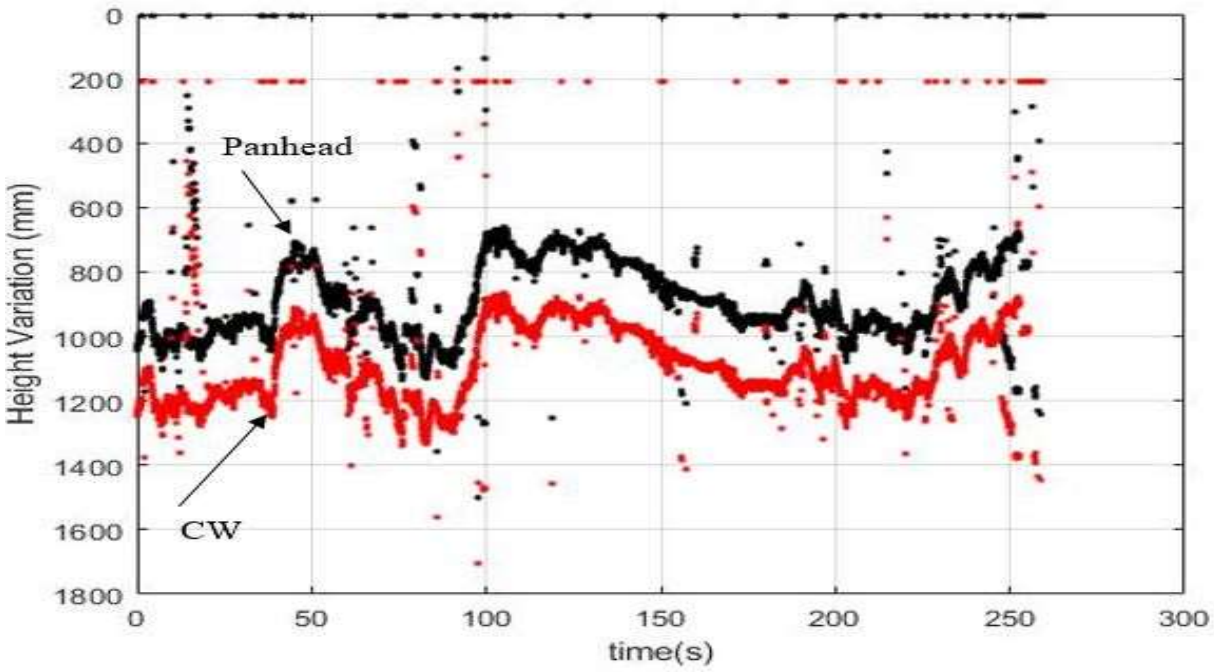


Figure 6-20: Estimation of the CW height variation from detected locations of the pantograph (89% estimated accuracy based on detection results in 1000 output frames)

6.3.3 Trending Analysis of the CW Height Variations

Using the available on-board data and processes explained in Section 6.3, Figure 6-21 is generated to illustrate the amount of uplift for each point over a selected length of the line. As discussed in Section 6.2, the on-board video is recorded frequently. However, the video is only played by maintenance engineers in cases of accidents to manually investigate the root cause of faults. It is possible to categorise these recorded video data in a manner that recordings over time of a particular length of the line are classed together. The generated uplift trends can be analysed to provide an insight of degradation or defects in contact wire.

Due to unavailability of such data, theoretical datasets were generated after consultation with a senior member of OHL team within Network Rail. Accordingly, three case studies are defined to explain the use of uplift measurements in determining the condition of the contact wire.

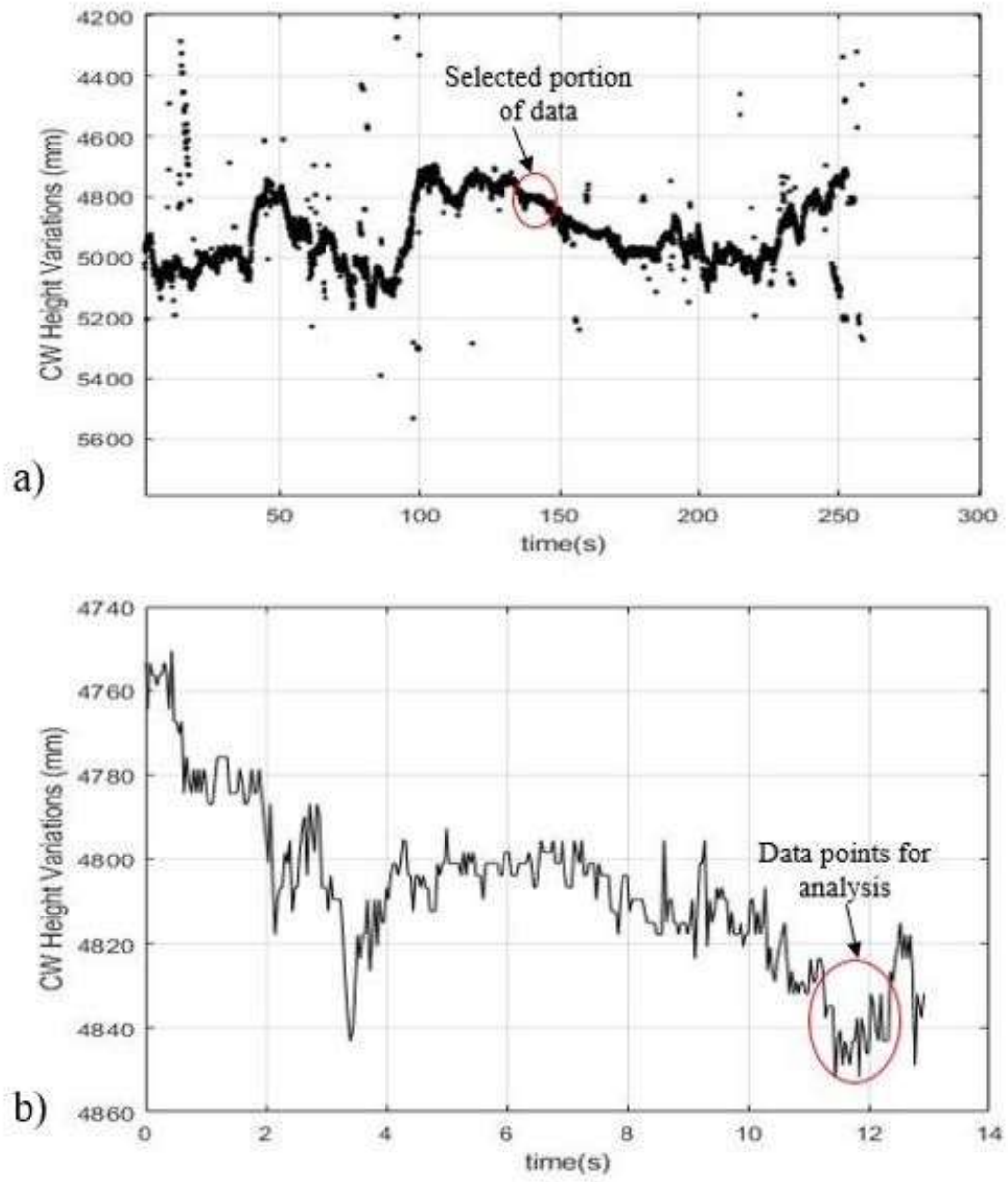


Figure 6-21: Selected data for trending analysis of the CW uplift

6.3.3.1 First Scenario

In this scenario, reasonable theoretical datasets regarding the measurements of uplift of contact wire, similar to that of Figure 6-21 (b), are generated. The data are measurements of uplift over a single span over time. To achieve this, measurements in Figure 6-21 (a) were used and it was assumed that, the train speed is 200 km/hr, however the acceleration is unknown and therefore not considered. Based on the calculated duration of 259.32 seconds (see Figure 6-21(a)) it was assumed that the overall measurements were carried over 14.9 km of track. Considering a standard length of each span is 50 metres, it was assumed that the overall monitoring length comprises 298 spans.

Figure 6-22 shows the measurements of uplift over a single span recorded at six different times.

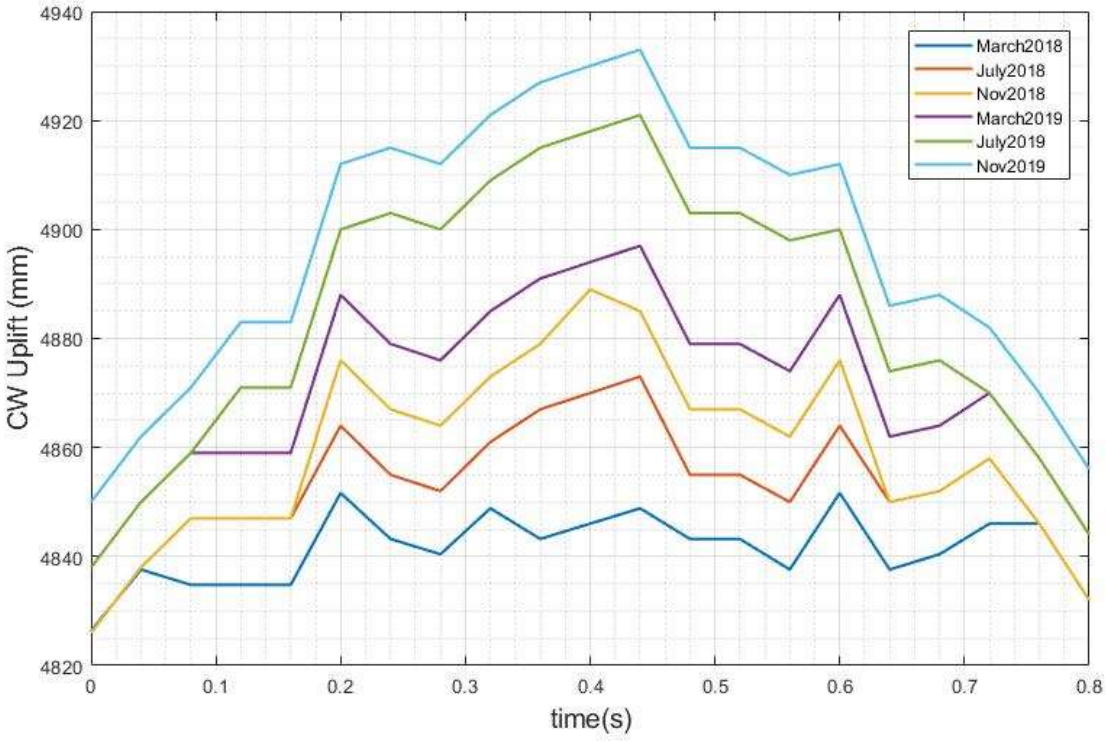


Figure 6-22: CW uplift over a single span

Maintenance treatment to rehabilitate the contact wire is mainly renewal. Therefore, in case of contact wire having defects or reaching the end of its useful lifecycle, it is removed and replaced with a new one. Replacements are in range of tens of meters to connect the newly replaced contact wire to the rest of the contact line. In practice one method to determine the condition of the contact wire and contact force of the pantograph is to measure the amount of uplift (see Section 2.6.4). It was advised by a senior member of a OHL team within Network Rail that when the uplift of the contact wire reaches or exceeds 200 mm an immediate inspection must be carried out. The inspections are mostly performed by sending an inspection crew to visually check the line from side of the track and complete a survey regarding the possible causes of failure. In Section 2.5.1 it was discussed that the increase in contact wire uplift indicates poor performance/ degradation of the wire. For this reason, it is reasonable to set the uplift of 200 mm as a threshold value to indicate a poor condition of the contact wire. Accordingly, any value equal or higher than this threshold indicates unhealthy conditions. To this end it is decided to use the mean of the selected data over the length of the span to represent its overall uplift value. The initial plot of the contact wire height variations that was obtained

after processing of the video is used as a reference line to determine the level of change in uplift over time. Figure 6-23 determines the mean of uplifts over time along the length of span.

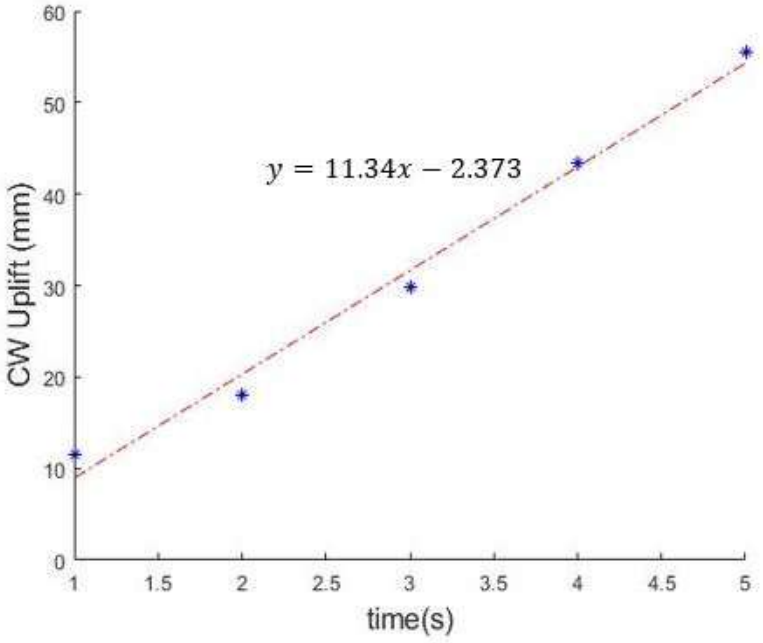


Figure 6-23: Variations of mean of uplift over time

According to Figure 6-23 it can be seen that the mean of uplifts is increasing over time. To define a relationship between the mean of uplifts and time linear regression is applied.

Accordingly, a linear function as $Y_i = ax_i + b + \epsilon_i$ is fitted to the calculated uplift variations. Where Y is the random variable representing the dependent observed values y_i for the independent predictor values x_i and is distributed as $f_{Y_i}(y)$. a and b are the slope and intercept respectively, and ϵ_i is the error term with zero mean $E[\epsilon_i] = 0$, variance $V[\epsilon_i] = \sigma^2$, and $V[\epsilon_i \epsilon_j] = 0$ for $i \neq j$. With these assumptions the following is derived (Sa & P, 2007).

- ϵ_i are independent and identically distributed with $E[Y_i] = ax + b$. Therefore, $E[Y] = aX + b$ expresses the regression of Y dependent on X. The density of observed values $f_{Y_i}(y)$is the density of errors, $f_\epsilon(\epsilon)$, with mean $E[Y_i]$.
- $V[\epsilon_i] = \sigma^2$ therefore, $V[Y_i] = \sigma^2$
- Y_i and Y_j are uncorrelated.

To estimate the regression function Least Squared Errors (LSE) is used to minimise the total sums of the squared errors (deviations) between the observed values and the estimated $\hat{y} = Ax_i + B$, where A and B are estimates of a and b respectively.

(6.2)

$$E = \sum_{i=1}^{n} \epsilon_i^2 = \sum_{i=1}^{n} (y_i - B - Ax_i)^2$$

Using LSE *(6.3)*

$$\begin{cases} \sum y_i = nB + B \sum x_i \\ \sum x_i y_i = B \sum x_i + A \sum x_i^2 \end{cases}$$

Accordingly, $A = \frac{\sum(x_i - \bar{x})(y_i - \bar{y})}{\sum(x_i - \bar{x})}$ and $b = \bar{y} - A\,\bar{x}$.

The goodness-of-fit parameter is $R^2 = \frac{SSR}{SST} = 1 - \frac{SSE}{SST}$, where $SSE = \sum(y_i - \hat{y}_i)^2$ is the sum of squared errors which determines the total residual values obtained from the regression. The total sum of the squares is $SST = \sum(y_i - \bar{y})^2$ and sum of squared to the regression is $SSR = \sum(\hat{y}_i - \bar{y})^2$.

With this trend fit performed it enables the inversion of the uplift against time relationship to determine the time that any particular uplift value is reached the defined threshold value for the span under consideration. Distribution of times to a particular uplift value can be obtained. The uplift level of interest is set as 200 mm. For the samples the trend curve is then inverted to provide a sample time to reach that threshold. These samples of times are then used to generate the best-fit distribution to the process.

Weibull distribution is commonly used for such tasks due to their flexibility to represent many shapes of distributions and are common for degradation/ failure modelling (Andrews, 2012). In addition, Weibull distribution is very effective in situations where data samples size is small (Abernethy, 2001).

The Cumulative Distribution Function (CDF) of Weibull distribution is (Abernethy, 2001):

$$F(x) = 1 - e^{-(\frac{x}{\alpha})^{\beta}} \quad (6.4)$$

Where $F(x)$ is the fraction failing CDF, x is time, α is scale parameter and β is slope.

Rearranging Equation 6.4 gives:

$$1 - F(x) = e^{-(\frac{x}{\alpha})^{\beta}} \tag{6.5}$$

Taking the natural log of both sides of Equation 6.5 gives:

$$ln\big(1 - F(x)\big) = -\left(\frac{x}{\alpha}\right)^{\beta} \tag{6.6}$$

By multiplying both sides of Equation 6.6 by -1 and taking the natural log one more time provides:

$$ln\big(-ln\big(1 - F(x)\big)\big) = \beta\, ln\, x - \beta\, ln\, \alpha \tag{6.7}$$

This can be expressed as the linear equation

$$y = \beta x' + \alpha \tag{6.8}$$

where $y - \ln\big(-\ln\big(1 - F(x)\big)\big), x' = \ln x$ and $\alpha = -\beta \ln \alpha$. In this manner the calculated coefficients of Weibull distribution are $\alpha = 1.1200 \times 10^6$ and $\beta = 0.1925$. The reliability function of Weibull distribution is one minus its CDF. Accordingly, Figure 6-24 is derived.

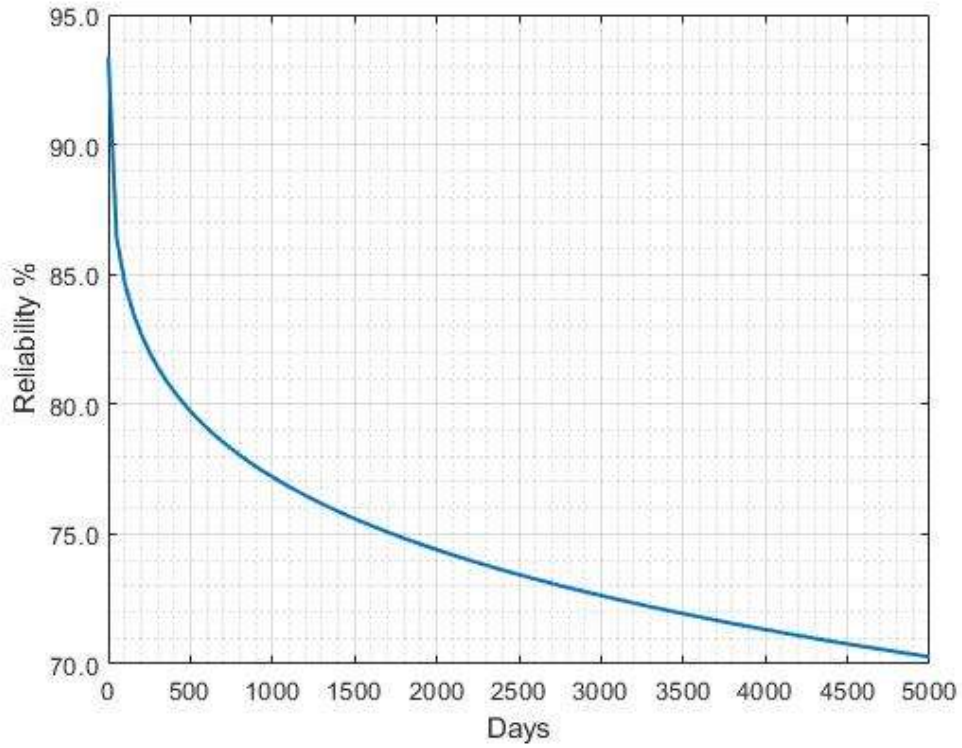


Figure 6-24: Prediction of the CW reliability

According to the graph it can be seen that after 5000 days the reliability of the contact wire reduces to 70%. As consulted this with a senior member within a central route performance

team of Network Rail, it was found that the aim within the company is maintaining 100% performance of assets at all times. Therefore, it seems reasonable to indicate that after approximately 13 years the performance of the contact wire reduces to 70%. This number is very low in terms of performance within the company and imposes risk of failure. This is considering that no maintenance activities were undertaken on this section of the line to demonstrate the progression of increase in uplift over time. This indicates that the contact wire condition/ performance comparing to its initial stage has degraded. This graph can be used by OHL maintenance engineers and asset managers to better plan for maintenance inspection intervals before the contact wire uplift reaches critical conditions. For instance, to keep the reliability at 80% level every 400 days maintenance should be carried. Whereas to maintain the performance at 85% this value is 100 days.

6.3.3.2 Second Scenario

The first scenario suggested a method that can predict the future reliability of the contact wire overtime using its uplift value as a measure. In this scenario a different method of analysis is explained in order to determine the condition of the contact wire.

As shown in Figure 6.21, the uplift of the contact wire can be evaluated over the full catenary length. If monitoring video of each line is recorded over time, which is done in practice, by comparing the uplift variations of a same line recorded at different times the performance of the contact wire can be determined. Taking into account the calculated movement of each pixel (see Section 6.3.1.3), a series of reasonable random numbers were generated to mimic the contact wire uplift variations. Using the generated theoretical dataset, the graph of contact wire height variation after performing six monitoring rounds is shown in Figure 6-25.

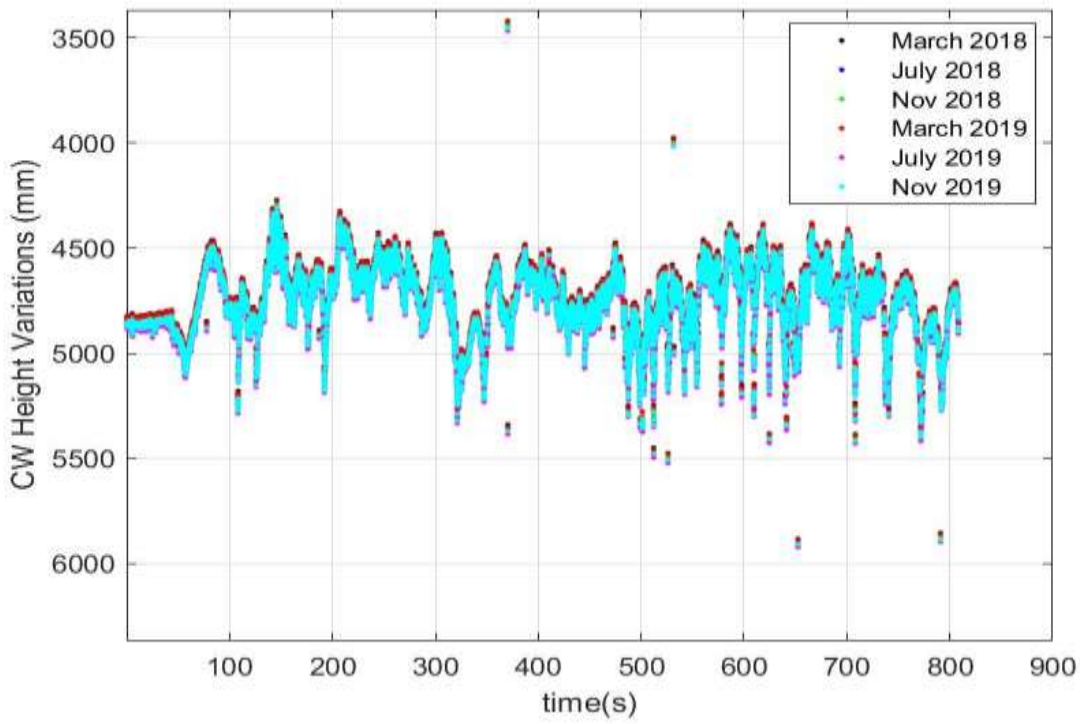


Figure 6-25: Trending analysis of the CW uplift over the full catenary length

The graphs in Figure 6-25 are accumulation of data points from the contact wire height calculated based on the location of the pantograph at each frame of the video recorded at different monitoring intervals. Although the graphs show slight differences within the contact wire uplift, it is very difficult to precisely assess the condition of the contact wire. For example, the result of the carried monitoring in July 2019 demonstrates higher uplift compared to the monitoring results in November 2019. However, this is not easily identifiable from the graph. For this reason, the difference plots are generated that compare the contact wire uplift at different monitoring times with respect to the initial uplift recorded at the beginning of the monitoring. Accordingly, the trending analysis of the contact wire uplift over the full catenary length is:

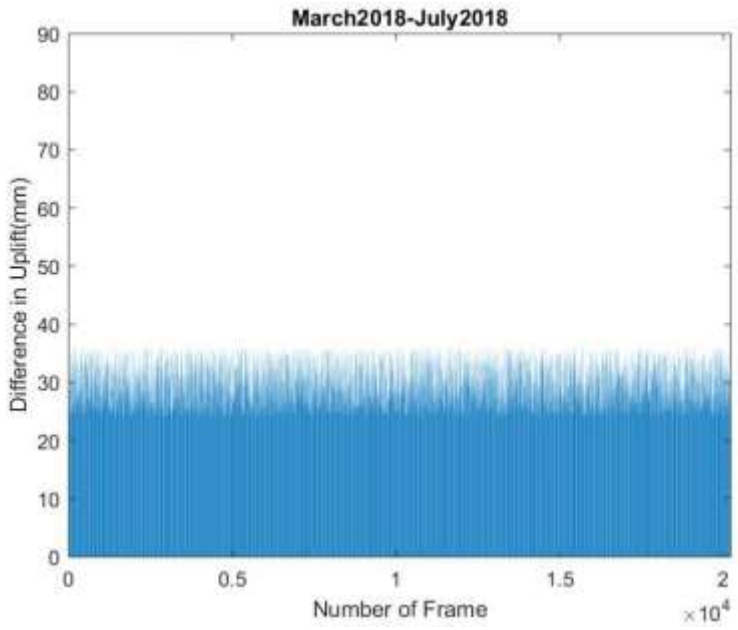


Figure 6-26: Difference graph of the CW uplift

According to Figure 6-26, it can be seen that the point to point uplift difference from March 2018 to July 2018 is roughly between 24 to 36 mm.

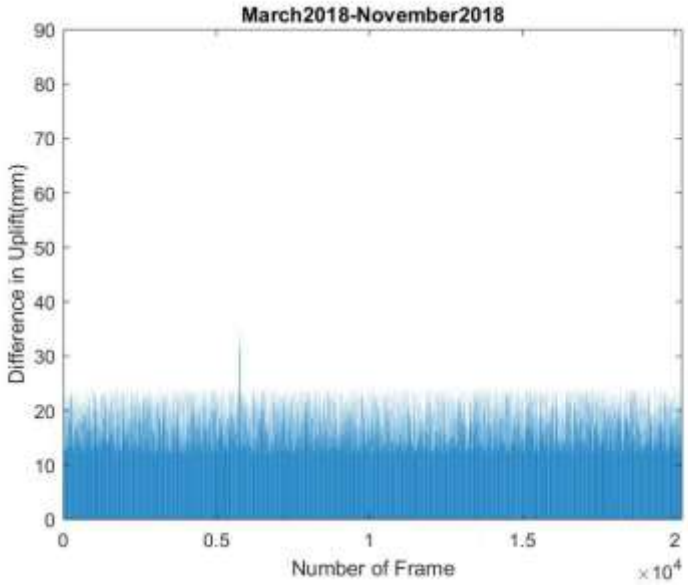


Figure 6-27:Difference graph of the CW uplift

From Figure 6-27, the majority of point to point difference in the uplift is approximately between 12 to 24 mm. In addition, a spike of 30 mm over a particular section of span is observed.

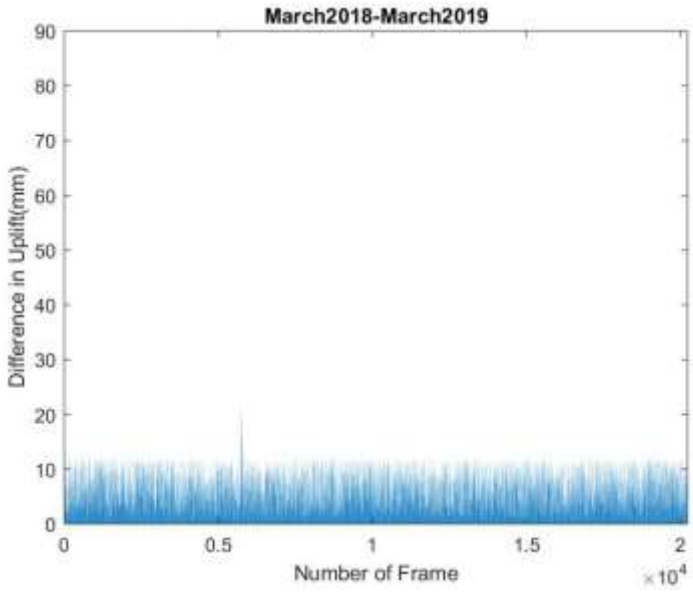


Figure 6-28: Difference graph of the CW uplift

From March 2018 to March 2019, the uplift of the contact wire increased by 12 millimetres. The spike occurred at Figure 6-27 also exists in Figure 6-28, although with a slightly less difference value. The reoccurrence of the spike can raise concern regarding a potential defect. Therefore, this issue can be flagged and monitored routinely over the subsequent monitoring cycles.

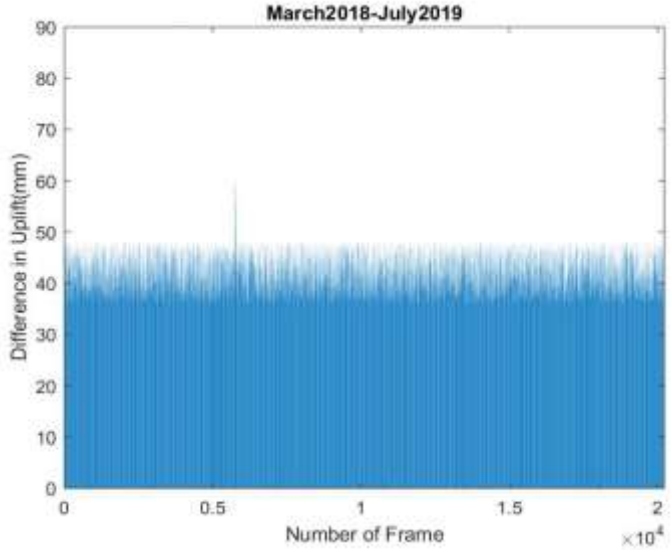


Figure 6-29:Difference graph of the CW uplift

From March 2018 to July 2019, the contact wire uplift increased between 36 to 48 mm. The suspicious peak also increased by nearly 60 mm (see Figure 6-29).

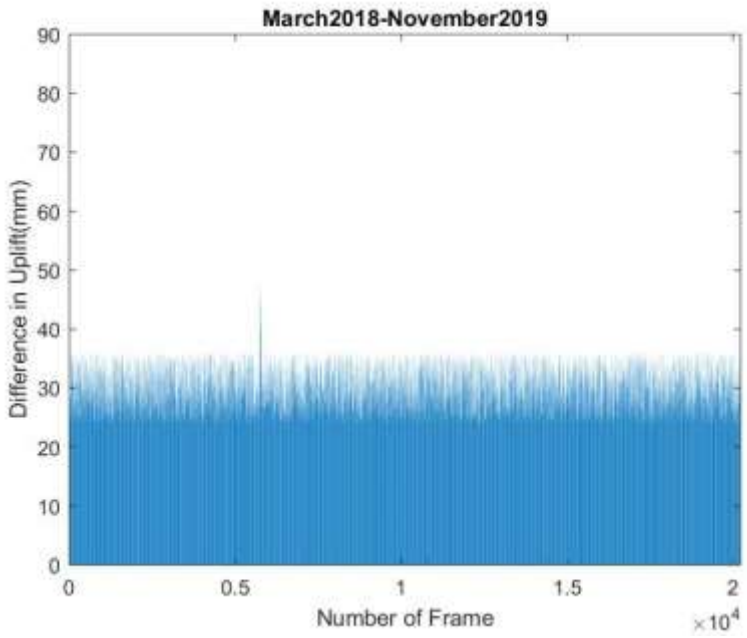


Figure 6-30: Difference graph of the CW uplift

From Figure 6-30, the contact wire uplift increased around 24 to 36 mm in November 2019, and the spike in Figure 6-30 is of less value than in Figure 6-29.

According to Network Rail expert in OHL team, 140mm excess from the planned uplift of 60mm gives cause for concern that the asset is reaching its critical threshold. Measuring the scale of contact wire uplifts can help in diagnosis of the defect type. In the example under consideration, monitoring intervals are scheduled in a manner to mimic the condition assessment of the contact wire in mild, hot and cold seasons. Temperature related impact on uplift for lines equipped with auto-tensioning mechanism is insignificant. Lines with fixed terminations are more sensitive to temperature variations (see Section 2.4.1). In the given scenario, from the trend of the uplift observed between March 2018 to November 2019, it can be concluded that the differences can be linked to seasonal changes. This is because there is a uniform difference throughout the length of the track. However, from Figure 6-27 to 6-30, it can be seen that although the entire length of the line experienced increase and decrease in uplift, there exists a sharp spike. This spike indicates a very large difference which is not normal compare to the rest of the line and remained uncompensated until the end of two years monitoring.

Identification of defects nature requires line specification such as; line traffic, line speed, age of the contact wire, type of tensioning (AT or FT) and track condition to be known. Assuming the length of the affected section of the contact wire in this scenario falls within a span, to

identify and rectify the uplift based on the condition of the contact wire itself the following two actions are required:

- To check the date of last renewal programme to identify if the wire is undergoing fatigue/crack initiations.
- If the tensioning is via fixed terminations, it is beneficial to check the latest date that tensioning of the wire was performed. Depending on the contact wire operational lifecycle and type of alloy used for its fabrication, the distributed contact wires over sections with fixed terminations run out of their elastic memory every ten to twelve years. To maintain the uplift of the contact wire within the planned range, the tensioning of the contact wire is usually performed every eight to ten years.

6.3.3.3 Third Scenario

Figure 6-31 shows the plot of the contact wire uplift obtained through performing four monitoring activities on a line under consideration. On the contrary to the second scenario that variations of the contact wire uplift were noticeable from the monitoring graphs (see Figure 6-25), the monitoring results from Figure 6-31 seem to be identical. To better analyse the change in uplift, the difference graphs of contact wire uplift are generated (see Figures 6-32 to 6-34).

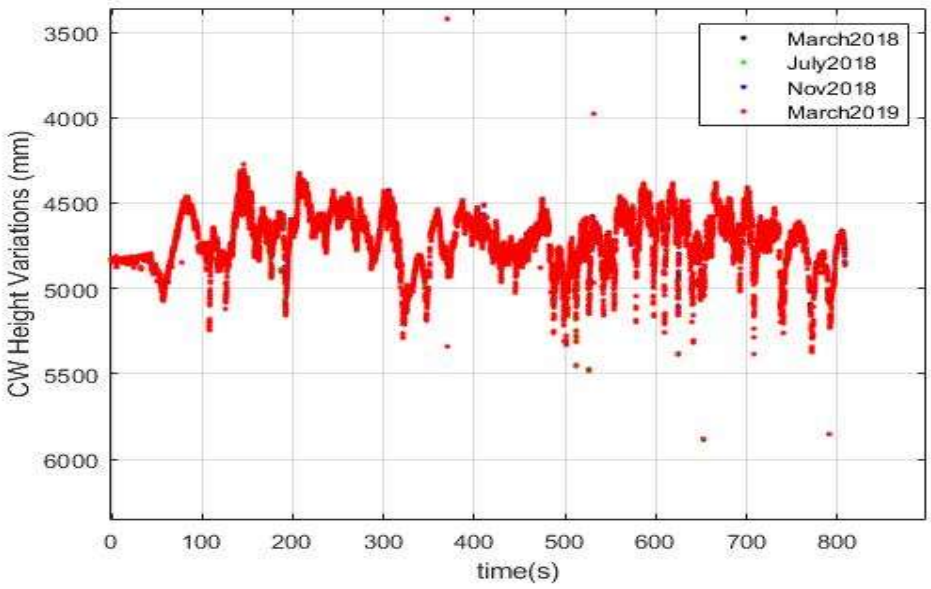


Figure 6-31: Trending analysis of the CW uplift over the full catenary length

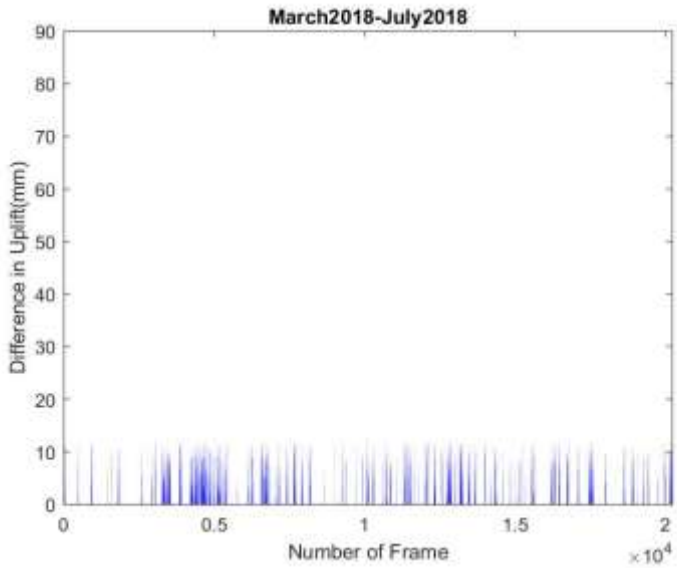


Figure 6-32: Difference graph of the CW uplift

According to Figure 6-32, the contact wire uplift obtained from the first monitoring time, on March 2018, to the second monitoring carried on July 2018 shows either negligible or increased by 12 millimetres on some points. This indicates the contact wire condition is roughly to its condition in March 2018.

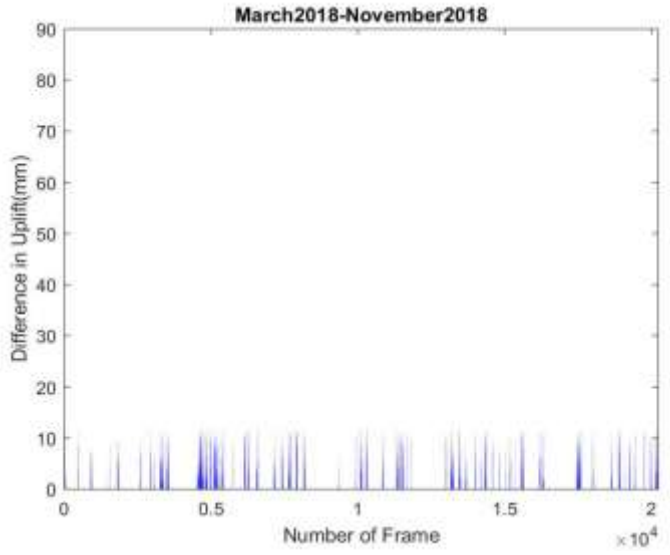


Figure 6-33: Difference graph of the CW uplift

Comparing the measured uplift on March 2018 to the uplifts on November 2018 (see Figure 6-33) the same situation as in Figure 6-32 exists. The excess 12 millimetre uplift at some sections of the line is modified.

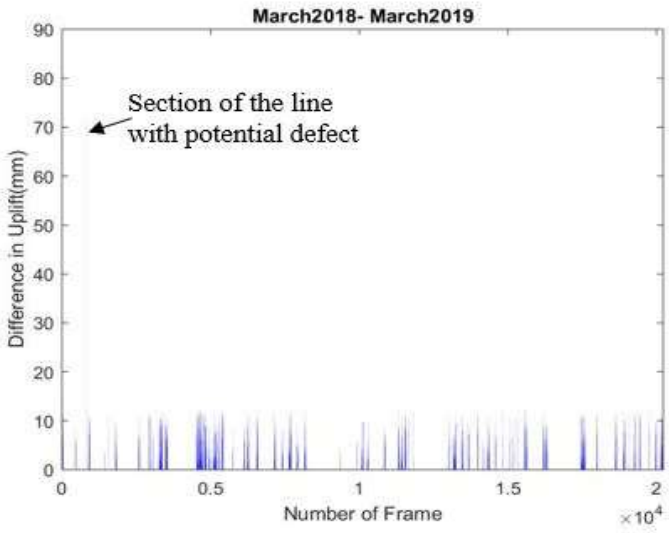


Figure 6-34: Difference graph of the CW uplift

Based on the monitoring results in Figure 6-34, the uplift of the contact wire at a certain location of the line increased by 60 millimetres. Such a sudden change in this variation can be attribution to an existing fault (for example: slackening/breakage of dropper). In this situation, immediate action is required. Figure 6-35 maps the location of this sudden change of the contact wire uplift on March 2019 monitoring graph.

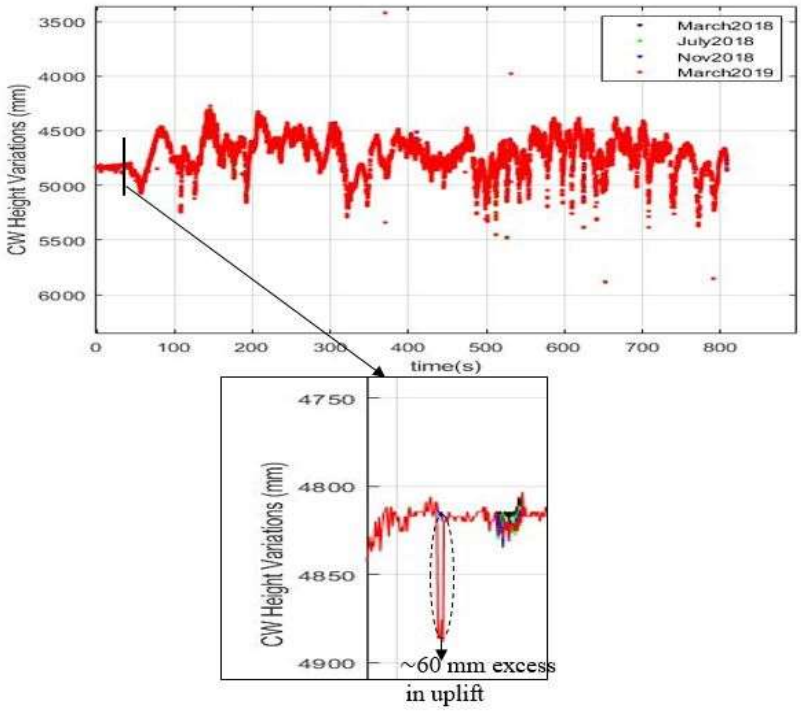


Figure 6-35: Trending analysis of the CW uplift

6.4 Summary

A novel monitoring approach that uses the on-board videos and determines the contact wire height variations according to detected location of the pantograph was discussed. The system processes along with the employed post-processing approach to achieve the contact wire height were explained. Detection results on open route equipment, in the vicinity of structures having similar features and throughout tunnels/ bridges where visibility significantly reduces were show cased.

Evaluation of the system performance is done by calculating three measures of precision, recall and quality. This is based on observing the number of TP, FP and FN amongst one thousands output images. It was found that the performance of the system degrades in poor lighting conditions. This leads to missing tracks at locations with low visibility. Two frameworks were proposed that enables condition assessment of the contact wire through trending analysis of its uplift.

Statistical analysis is applied to the obtained uplift results in order to produce the graphical reliability of the contact wire. To achieve this, an uplift value is set as a threshold indicating the maximum allowable uplift. In this manner, a relationship between the mean of uplift over a span and time was established. The relationship was then inverted to provide distribution of times to reach that particular threshold value. Using the distribution of times to reach the threshold, the reliability of the contact wire is calculated in a graphical format over time. This graph can be very valuable to maintenance managers and asset engineers in terms of specifying reasonable maintenance intervals to maintain acceptable reliability level.

In different scenarios, the uplift of the entire length of the line was calculated over different time periods. Comparing and analysing the uplift results provide point to point differences in uplifts. Any observed abrupt difference indicates a potential problem with the contact wire. Although the graphs do not provide information regarding the exact defect/ fault within the contact wire, they are quite useful in determining any great and abnormal changes in uplift. Accordingly, appropriate actions can be taken by maintenance engineers and asset managers to further investigate into the problem.

This developed vision-based system is a pioneer step in using the recorded on-board videos and processing them to produce uplift measurements of contact wire over time.

Chapter Seven

7. Discussion

7.1 Introduction

The aim of this research project was to propose a feasible methodology that determines the contact wire uplift through analysis of the video data. Two vision-based monitoring approaches of trackside and on-board were proposed.

The purpose of former is to measure the dynamic uplift through processing of video footages with static backgrounds. As the wire undergoes structural deformity, the reduction of its cross-section affects its stability against external forces and results in high amplitude oscillations. This method enable assessment of the contact wire condition based on its uplift, frequency of oscillation and damping ratio.

The on-board approach determines the contact wire height variations according to height of the pantograph. Data required for this approach are the videos recorded by cameras installed on the trains. These data are stored by Network Rail and TOCs, therefore highly available. Unfortunately, due to lack of adequate monitoring system, data are only assessed in case of incidents and failures. A responsible engineer manually plays the videos to identify causal factors. This task is very time consuming and prone to human error. The data are not kept for a long time and gets deleted. This is because keeping them requires a huge hard-drive storage

and assessing them manually is exhausting. The proposed on-board monitoring method in this project enabled analyses of these data to produce contact wire uplift in a graphical format. Depending on the frequency of data recordings over each line, the uplift measurement of each line over time can be achieved. Therefore, using trending analysis and expert knowledge comparison is made between the measurements at each time to examine the condition of contact wire.

To date there has been no preceding literature or monitoring systems that enables condition assessment of the contact wire through measurement of its uplift. This highlights the challenges involved in the completion of this research project.

7.2 Requirements for Vision-based Condition Monitoring of Contact Wire

According to the aim of this project (see Section 1.2) the developed vision-based monitoring systems are designed by considering the following requirements:

- Measurement of the contact wire uplift from data
- Ease of use

To achieve the requirements, measurement of contact wire uplift is described for track and trackside approaches in Sections 7.2.1 and 7.2.2 respectively.

7.2.1 Trackside Measurement of Dynamic Uplift

Trackside video are used to analyses the vertical movement of the contact wire in order to measure the amount of uplift. This was achieved through segmentation of the images and identification of contact wire location at each video frame.

7.2.1.1 Segmentation of Image Data

The colour intensity distribution of the contact wire and background pixels in trackside footages were sufficiently distinct and the histogram of the grayscale image was identified as bimodal. Although bimodality of the histogram means segmentation can be performed through global thresholding, identification of a suitable threshold value for segmentation operation was challenging. This was due to properties of the produced valley bottom in between two modes of the histogram (see Section 3.4.3.1). To select a suitable threshold value and minimise the effect of illumination variations on copper surface of the wire, the separability of the classes was maximised through minimising the intra-class intensity variance. The utilised threshold value was computed from the intensity values of the pixels in between the two boundaries of

the wire instead of its edges. Accordingly, the goodness of the selected threshold value was assessed through segmentation of the images using the stored amount of red, green and blue colours in pixels at the edges of contact wire. Analysis of the contact wire response plot obtained through thresholding over each colour channel (see Section 4.3.4) showed less than one-millimetre difference within the measured uplift compared to the response plot produced through thresholding over the gray channel.

7.2.1.2 Extraction of Contact Wire Motion Information

To extract the contact wire motion information, three most common motion detection techniques in the literature were examined (see Section 3.4.4). These are background subtraction, optical flow and difference over time. By taking into account the appearance feature, movement of the contact wire and the required information from images, it was concluded that these techniques are not suitable to be employed for processing of trackside footages. The weakness of these methods in extracting the contact wire motion information from the images, resulted in developing of a heuristic approach. Analysis of the contact wire response over a single column of the image matrix not only enabled trace of the contact wire motion trajectory from the video images, it also minimised the level of possible disturbances arising from occlusion of the contact wire by the pantograph on the displacement graphs.

7.2.1.3 Ease of Use

The advantages of the proposed monitoring approach comparing to existing methods currently used within the industry are as follows:

- Automatic processing of the videos
- Generation of the response graphs and measurement of the dynamic uplift
- Not requiring installation of sensors or markers to the wire

Depending on the video resolution, the processing time of each video frame was from 0.01 to 0.03 second. Processing time of the videos was almost twice as fast as the video actual streaming time. Once the processing is completed user can have instant access to the contact wire displacement graphs. This allows the user to inspect the amount of uplift with respect to any desired location. Thus, according to the maximum allowable uplift any extreme uplift can be identified.

The developed system is a GUI format, which allows processing of the data in an easy manner. Figure 7-1 demonstrates the functionality of the system.

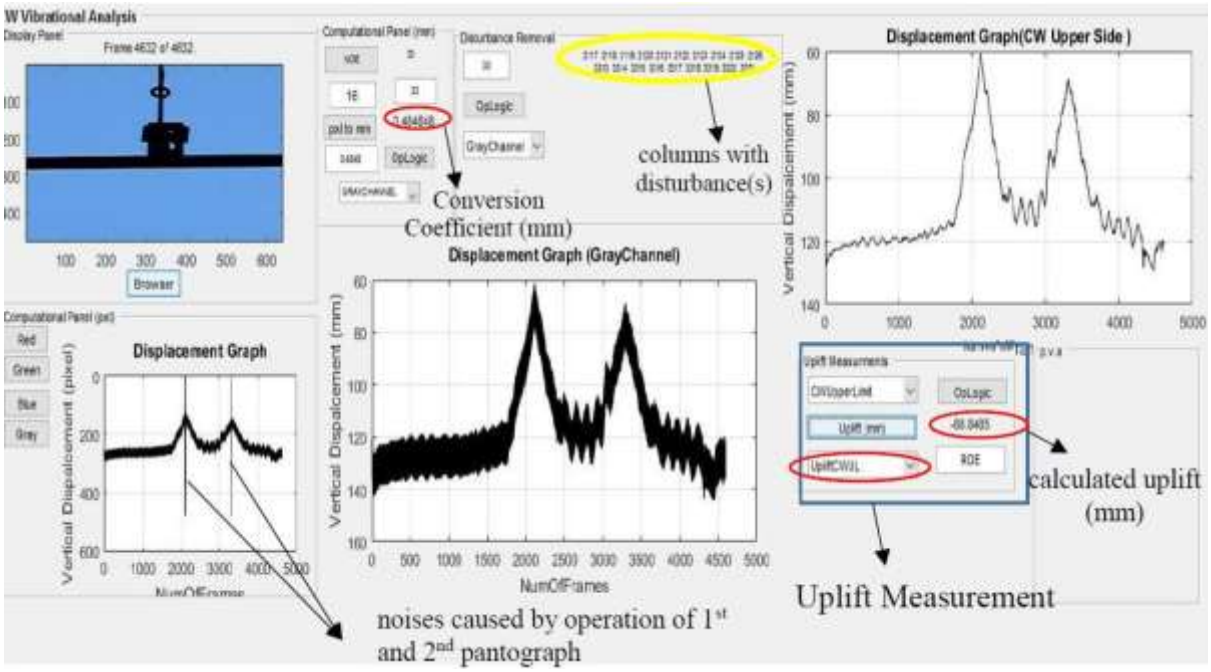


Figure 7-1: Prototype of the trackside uplift measurement system

7.2.1.4 Validation

Reliance on both the image data and utilised processing technique in determining the amount of uplift was examined by creating a dataset from the contact wire static uplift. For this reason, an apparatus was designed and fabricated. After performing field trials, comparison was made between the measured uplift values obtained through processing of the footages and the ones recorded using the apparatus. Although the results were satisfactory for the purpose of evaluating the feasibility of the method, there were some drawbacks. Due to the limitations of the designed tool and loose catenary structure at Long Marston, the manually recorded uplift values at some of test locations showed large variations.

At some test locations, good similarities were observed between the results obtained using each method. However, due to variations in the manually recorded data, median of uplifts was selected to be compared to uplift values calculated through the GUI. This led to higher differences between the measured uplift using each method. Despite the differences in the measured uplift, analysis of the component displacement in between two forces of 90N to 120N using each method showed less than 10% variations in majority of the carried tests.

7.2.1.5 Application

The proposed trackside system is aimed to be used to monitor the state of the contact wire from it uplift range. The system enables analyses of the wire oscillations after passage of the pantograph. Higher amount of uplift under identical lifting forces can be an indication of an

uncompensated sag or reduction/deformity of the contact wire cross-section. Depending on defect severity, instability of the contact wire because of its sag or wear leads to irregularity of the contact force. In some cases, this can impose speed restrictions otherwise it damages both to the pantograph and train. According to Network Rail senior engineer in OHL team, in August 2020 after experiencing couple of hot days, excessive sag of the contact wire at a certain section of the line in Birmingham New Street damaged the pantograph and led to service cancelation. Therefore, using this system, analysis can be carried on desired sections to early detecting on possible faults. This can be achieved through prioritising lines based on their traffic and failure history. For instance, in sections with high probability of wear higher priority is given. The following are some of these locations:

- Locations where the gradient of the wire changes
- Overlap sections
- Locations where the track is curved /canted lines
- Locations with frequent fault and failure obtained from history report in FMS

Another advantage of the proposed system is its potential in becoming an alternative to measure the uplift and contact force in low speed test runs. Low speed test runs are usually carried out when commissioning OHL or testing pantographs and currently involves high disruption level and complexity.

The system has its own limitations described in the following:

- The colour intensity distribution of the foreground and background pixels plays a vital role in identification of a suitable threshold value for segmentation of image data. In terms of functioning under different lighting conditions, as long as the contrast between the background and foreground is appropriate the system can determine uplift. This can restrict application of the system to daylight conditions. It might also highlight the requirement for image enhancement prior to segmentation operation.
- The effectiveness of the proposed approach was examined under static background without presence of any moving objects but the pantograph. Accordingly, if the movement of contact wire correlates with movement of any other object within the scene the system performance might degrade.
- Low visibility inside tunnels and bridges as well as safety considerations restrict application of the proposed system at these locations.

7.2.2 Contact Wire Height Variation Using On-board Data

Object detection is a complex process comprising of two interrelated analysis functions. The first function is for detecting the object of interest in sequential video frames. The second is for tracking the object according to its motion and spatial changes in the video. Because of the appearance features of the contact wire in on-board data, detection based on line features only determines the contact wire lateral movement across the collector strip. Accordingly, height of the contact wire was achieved based on its location on top of the collector strip through detection of the pantograph.

7.2.2.1 Detection of the Pantograph from Dynamic Scene

Detection of the pantograph was achieved through a classifier that was trained over a series of training samples using Viola-Jones method. Three key parameters of this method that facilitated construction of a strong classifier for detection of the pantograph from the background objects are identified as:

- Integral image that helps in fast computation of Haar-like features
- AdaBoost learning algorithm that enables selection of a small number of discriminant visual features of the pantograph and construction of an efficient classifier for its detection.
- The attentional cascade that combines the strong classifiers and increases the detection performance.

The functionality of the designed classifier in detecting the pantograph was carefully examined under backgrounds with different levels of complexities. Based on observed detection results, performance of the detector was improved by supplying of more training samples by varying the contrast/brightness level of the samples and increasing the number of training stages. Increasing the training stages increased the training time. On the other hand, it resulted in construction of a classifier with higher detection rate. One of the challenges when developing object detection system is evaluating the accuracy. This is usually performed using the returned confidence rate. Due of the limitations of the leading platform, the performance of the system was alternatively examined according to the observed number of TP, FP and FN amongst one thousand output samples.

The contact wire height was achieved according to its distance from the centre of the pantograph. The value of each pixel in millimetres was calculated according to the actual length of the collector strip as well as the number of pixels featuring it the image data. Variations of

the pantograph height were estimated through calculating the camera coverage area in accordance with the video vertical resolution.

7.2.2.2 Ease of Use

The pre-processing stage of the utilised approach in detecting the pantograph comprises creation of a dataset and supervising the training of the classifier. This was achieved by supplying training samples and tuning of the parameters for construction of a strong classifier. The processing stage involves frame by frame detection of the pantograph. This is performed without requirement for human supervision. To distinguish the height of the contact wire from height of the pantograph in the post-processing stage minor human intervention is required.

The training time varies according to the number of training stages and the selected false alarm rate. Training time of the first stage was done faster than the rest of the stages as no negatives were trained. At the beginning of next training stage, the learning algorithm checks the rejected negatives from the previous training stage. The algorithm identifies the negatives that were wrongly classified in the previous training stages and corrects them. For this reason, the training time of the final stages increased significantly. The overall training time of the last classifier which was constructed over 20 stages was about seven hours. Processing of the video with duration of 13:28 minutes took 2 hours and 40 minutes.

7.2.2.3 Limitations

The developed method for detection of the pantograph has offered high detection rate. This was achieved through sophisticated feature selection and construction of an invariant detector which locates scales. Notwithstanding the advantages, this method has some limitations. One is sensitivity to object orientation. For example, when the pantograph is tilted it will result in missing track. The other is illumination variations. Illumination variations severely affect the detection performance. Such limitations resulted in tracking of the pantograph to become lost at locations with poor lighting condition for example, inside the tunnels. Lastly, there is a possibility of different detections of the pantograph because of sub windows overlapping.

7.2.2.4 Application

The developed system allows analysis of the on-board footages and provides OHL asset managers with an access to the contact wire height variations. This valuable information can be used to evaluate the stability of the asset over the full catenary length. Using the recorded video data, measurements of uplift throughout the length of the track is achieved. Since data are recorded frequently this process can be done over same length of track at different intervals. In this manner, a comprehensive data base can be established which include over time

measurements of uplift at different length of track. Based on the processed data, point based uplift over length of each span is determined in a graphical format (see Section 6.3.3).

This information was used to determine the reliability of the contact wire over time. For this reason, statistical analysis was performed to the system output. In particular Weibull distribution was used for this process. This function has applications in system reliability and failure analysis and is widely used in different fields of engineering such as railways. There are two main advantages of using this distribution for reliability analysis. One is ability of Weibull function to transform to other forms distributions and the other is providing accurate results even with small sample range. To achieve this a sample of uplift measurements over a length of a span was considered. Mean of the uplift values at each measurement interval was used for analysing the progression of uplift over time. Based on the available information from Network Rail it was assumed that the critical uplift value is 200 mm. Accordingly, data was analysed to provide distribution of time to reach this threshold value. This way, the reliability of the contact wire over the specific span was achieved over time. Using this information reliability in percentages can be set as a threshold and maintenance intervals can be scheduled accordingly. The allowable values can be set based on track specifications and category which includes traffic and speed.

The other application of the system is enabling monitoring of point-based uplift over the length of the track over time. In this manner, uplift differences at different times can be achieved with respect to the reference. This way, comparison can be made by the user between the measured uplifts differences. The user can carefully observe the graphs and flag any abnormalities in the differences for requiring further inspection. This provides valuable information to OHL engineers in determining the condition of the contact wire.

The current processing time restricts the application of the proposed system to offline monitoring of the contact wire height variations. Once the data is fully recorded at each inspection interval, it can be feeded to the system to be processed. The outputs are then saved accordingly to track specifications, ELR and asset number. Overtime measurements are accumulated to provide comprehensive database for analysing the condition of the contact wire considering the amount of its uplift.

7.3 Summary

Considering the aim of the project, two vision-based approaches for condition assessment of the contact wire were proposed. Both approaches enabled an automated contact-less

measurement of the contact wire uplift. Neither of the approaches required the need for hazardous, costly, time consuming and ambiguous conventional inspection methods currently in use in the industry. The chapter provided a thorough review regarding the procedures adopted to develop these measurement systems and discussed the usefulness of each approach for the rail industry. Although limitations included in both systems, the output of the system contains valuable information for engineers to assess the performance of the contact wire and helps infrastructure managers in better management of their assets.

Chapter Eight

8. Conclusion

8.1 Accomplished work

The work presented in this thesis may be regarded as the first stage in the development of vision-based monitoring systems that enable condition assessment of the contact wire through analysis of its uplift under service condition. The research programme has focused on establishing whether it is feasible to extract the contact wire uplift through automatic analysis of the video images. To this end, two video image analysis systems consisting of the following items were considered:

8.1.1 Trackside

- Extraction of the contact wire motion information from the trackside videos.
- Analysis of the video images through:
    - Identification of a suitable threshold value for segmentation of the image data.
    - Extraction of the contact wire motion information through frame-by-frame processing of the video images.
    - Generating the contact wire displacement graph.
    - Removing of the disturbances caused by occlusion of the monitoring point by the pantograph.
    - Measurement of the dynamic uplift

8.1.2 On-board

- Extraction of the contact wire height through processing of the on-board videos.
- Generating ground truths and creating dataset for training of a classifier.
- Offline augmentation to increase number of the training samples and to help the classifier to generalise well.

- Calculation of the pantograph discriminant features through integral image and use of adaptive boosting.
- Troubleshooting in the training phase to achieve a faster inference time and higher detection rate.
- Frame-by-frame detection and tracking of the pantograph across the entire length of the video.
- Generating plot of the pantograph height trajectory using coordination information of the pantograph locations achieved through processing of the video.
- Estimating the contact wire height according to the location of the pantograph.
- Generating plot of the contact wire height trajectory.

8.1.3 Conclusions

The key conclusions of the work using the two systems are as follows:

8.1.3.1 Trackside

- The system has been able to locate the contact wire at every video frame.
- The system was successful in calculating the uplift of the contact wire at the moment of interaction with the pantograph in both slow-motion and real-time videos.
- The system generates graph of the contact wire vertical vibrations as consequences of passing of up to two pantographs by the selected monitoring point.
- The system enables faster than real-time processing of the trackside footages and generates the plot of the contact wire height variation in near real-time.
- The system enables calculation of the contact wire natural frequency and damping ratio through analysis of its oscillations after passage of the pantograph.

8.1.3.2 On-board

- The system showed high detection rate at a reasonably fast inference time.
- The system was successful in distinguishing and detecting the pantograph from objects having similar Haar-like features present in the background.
- In cases where system loses detection in locations with poor lighting, rapid detection is regained as soon as the illumination slightly stabilised.
- The system provides graphical plot of the contact wire height variation, estimated based on height of the pantograph.

8.1.4 Findings

The followings are the main findings of this thesis:

- The major link between degradation of the contact wire and line traffic as well as complexities involved in scheduling the inspection programme emphasise the need for more routine assessment of this railway asset at the lowest possible risk and disruption to train services.
- The uplift of the contact wire beyond the specified range can be an indication of existing or developing fault, which if not addressed on-time can adversely affect reliability of OHL and efficiency of the railway operation. From speed restrictions and service cancellations as result of an uncompensated sag to high amplitude oscillations as result of failure of the droppers, deformation of the wire cross section or its wear, measurement of the uplift helps in identifying potential faults within the system before they developed into service-affecting asset failures.
- Non-quantifiable contribution of the effect of draw string potentiometers and frictional damping on uplift of the wire make conventional measurement using displacement transducer prone to error and less suitable for this task. Thereby, a considerable advantage can be gained through developing a monitoring system capable of determining the contact wire uplift without attaching markers or sensors to the light high-current wire.
- Pattern detection based on object history of motion across the video frames is the way of displaying the object motion when the background is static. Aperture problems and non-trajectory nature of the classic motion estimation techniques made them inefficient in determining movement of the contact wire and calculation of its uplift. This was mainly due to appearance features of the contact wire in trackside data and its relatively fast up and down movements at the moment of coupling with the pantograph. Heuristics approach developed based on prior understanding of object of interest enables fast extraction of the desired parameter from the images. This is an important point to be considered when developing a system with near real-time application.
- The proposed approach for extraction of the contact wire dynamic uplift from the trackside data was established by considering the shape of the contact wire, its thickness, colour and direction of motion. Analysis of the trackside videos have shown that as long as the intensity values of foreground and background pixels are consistent application of global thresholding for segmentation of the images is valid.

- The standard approach of selecting a threshold value for segmentation of the image data is through assessing the image histogram. Analysis of the histogram of trackside data and bimodality of the image histogram in the trackside data proven the suitability of Otsu's method in handling the variations of foreground pixel values which enabled an automated yet fast computation of an optimal threshold value for global thresholding of images. The comparison between the contact wire responses achieved through processing of the trackside video through each colour channel approved the reliance on Otsu's method in segmentation of the video images.
- The reliance on the image data was assessed by conducting a static uplift measurement test. Analysis of the recorded data using the designed apparatus in conjunction with the extracted response through processing of the video images revealed some variations in measurement of the static uplift under identical measurement condition. Larger variations were observed under lower forces that is attributable to stiffness of the contact wire at the test location, contribution of the spring friction, bending of the lifting pole and loose catenary construction at the test location. Despite the observed variations, analysis of the contact wire response under higher forces shown less than 10% variations within the calculated uplift.
- Extraction of the contact wire stagger from the video data needs detecting the contact wire and the collector strips of the pantograph based on their line features. Hough transform enables detection of line features from the edge images produced after applying edge detection operation. Contact wire stagger graph can be generated by locating the contact point at each video frame that helps in identifying the wear point on the collector strips. The illumination variation causes the edge images to be generated differently, which affect the efficiency of Hough transform in handling such variations and in detecting the desired lines. Overnight monitoring and restriction of the camera observation zone can significantly improve line detection operation.
- Estimation of the variations in the contact wire height according to the location of the pantograph at each frame of the on-board data was achieved through computation of the Haar-like features relevant to discriminant properties of the pantograph in the images. Haar-like features are efficient in encoding information about the object of interest that is hard to be extracted from raw pixel data. However, computation of these rectangular features is time consuming. The Viola and Jones method adopted to detect the pantograph from other background objects in the on-board data addressed the complexity involved in calculating the Haar-like features through use of integral image

and adaptive boosting. Adaptive boosting (AdaBoost) is greatly used in computer vision to solve object detection problems using machine learning approaches. Training a classifier is a slow process and involves a lot of troubleshooting to achieve high detection rate. Despite being one of the first released competent framework in addressing object detection problems, the efficiency of the Viola and Jones method is still comparable to more recently released object detection models such as RCNN and its variants.

- Using the proposed method for analysing the on-board video data, the generated graph of the contact wire height variations can be classified according to track category (i.e. traffic and speed) and route specifications. Statistical analysis can be then applied for degradation/failure modelling of the contact wire according to its uplift recorded at different monitoring rounds. Considering the limited data accessible from processing of the videos, the reliability of the contact wire in this work was examined by applying Weibull distribution that enabled prediction of the asset reliability according to its uplift.

8.1.5 Remaining Problems

Although the systems enabled extraction of the contact wire height variations from the video data, there are some outstanding problems:

- Due to lack of sufficient trackside data the tolerance of the adopted segmentation technique in handling variations in videos with more challenging background could not be examined.
- The reliance of the image data was assessed by performing a static test on the contact wire. The mechanical tool used for this purpose showed instability issue during the measurement. This led to variations within the uplifts recorded under identical condition and test locations. Although the problem could be addressed through modifying the tool by means of fitting a recording device and load cell to enable continuous recording of the uplift data, due to lack of sufficient funding this problem remained outstanding.
- Despite the intention of performing the excitation test on the contact wire to further analyse its vibrational response under each load while performing the static test, limitation of the hook of the apparatus and loose catenary construction at the site restricted this experiment from happening.

- In the construction of an object recognition and tracking system using machine learning algorithm data plays the most vital role. Training of a powerful detection system requires a suitable dataset in which instances are not repeated. Although limited data were available, through careful creation of training samples, data augmentation and laborious troubleshooting an excellent detection performance under background with high complexities was achieved. Despite the high detection rate, detection of the pantograph due to its occlusion at some of the video images was not possible. Occlusion is still one of the biggest challenges in computer vision that in majority of object detection problems it is either not considered at all or minimised by applying some assumptions.
- Although a good detection performance was observed inside tunnels and bridges with shorter length, poor lighting conditions and the inability of the camera to adjust the exposure resulted in fewer colour information that affected the efficiency of the system in detecting the pantograph at such locations. Thereby, it is envisaged to achieve a better detection performance through provision of an independent lighting unit and extending application of the system to overnight monitoring.

8.2 Recommendations for Future Work

To enable a fully working vision-based uplift measurement system to be developed the following future work are recommended:

- The suggested on-board monitoring system in this work determines variations of the contact wire height as a function of time. To determine contact wire height variations as a function of distance travelled along the track, it is beneficial to use cameras that have facility to record GPS location and train speed.
- Computational complexities involved in processing of the video images can be mitigated through restricting the camera observation zone and overnight recording of the footages. To enable good feature extraction, a camera with suitable CCD sensor and brightness resolution must be utilised.
- Depending on the severity, the effect of occlusion on the object recognition can be addressed by means of suitable dataset augmentation for the classification algorithm.
- To seek for suitable data processing algorithm that enables estimation of the pantograph locations where the system loses its tracking extended Kalman filter and CONDENSATION are two algorithms that might address such a problem.

- Marking of the pantograph with a specific colour that is different from other colours in the background can help in detecting the pantograph at locations where visibility degrades. Using the colour range in a colour space that can separate colour information from intensity a mask can be created. The mask can be used to detect the pantograph from the video.

9. References

Abernethy, R., 2001. *The new weibull handbook.* 4th ed. North Palm Beach : s.n.

ADS, et al., 2016. *Increasing the Resilience of Power Supply Infrastructure To Changing Climate* , Sheffield : NeTIRail.

Agarwal, A., Gupta, S. & Singh, D., 2016. *Review of Optical Flow Technique for Moving Object Detetion.* s.l., IEEE.

Aggarwal, R., Johns, A. & Jayasinghe, W., 2000. An overview of the condition monitoring of overhead lines. *Electric Power System Research,* Volume 53, pp. 15-22.

Ahad, A. R., Jie, T. M. & Kim, H., 2010. *Motion History Image: Its Variants and Application* , Fukuoka: Springer.

Ahmed, M., 2017. *Appendices to Network Rail's Consulation on Variable Charges and Station Charges in Control Period 6 (CP6),* s.l.: Netwrok Rail .

Allen, C. E. & Emerson, A. H., 1962. The development of and field tests on different types of high-voltage overhead traction equipment. *The Institution of Electrical Engineers* , 109(4), pp. 257-264.

Andrews, J., 2012. A modelling approach to railway track asset management. *Rail and Rapid Transit* .

Arnold, M. & Simeon, B., 2000. Pantograph and Catenary dynamics: A benchmark problem and its numerical solution. *ELSEVIER,* 34(4), pp. 345-362.

Aydin, I., Karakose, M. & Akin, E., 2014. A New Contactless Fault Diagnosis Approach for Pantograph-Catenary System Using Pattern Recognition and Image Processing Methods. *Advances in Electrical and Computer Engineering,* 14(3), pp. 79-88.

Baker, C. et al., 2019. *Train Aerodynamics Fundamentals and Applications.* First ed. Oxford : ELSEVIER.

Ballard, D. H., 1981. Generalizing the Hough Transform to Detect Arbitrary Shapes. *Pattern Recognition,* 13(2), pp. 111-122.

BARWELL, F. T., 1960. *Research for a.c. traction.* london , British Transport Comission , pp. 158-198.

Beagles, A. et al., 2016. *Validation of a new model for railway overhead line dynamics.* Sheffield, Thomas Telford.

Bhargavi, K. & Jyothi, S., 2014. A Survey on Threshold Based Segmentation Technique in Image Processing. *Internation Journal of Innovative Research & Development,* 3(12), pp. 234-239.

Bishop, C. M., 2006 . *Pattern Recognition and Machine Learning.* Cambridge: Springer .

Bobick, A. & Davis, J., 1996. *An Appearance-Based Representation of Action.* Cambridge, IEEE.

Borromeo, S. & Aparicio, J., 2002. *Automatic System for Wear Measurement of Contact Wire in Railways.* Madrid, IEEE.

Borromeo, S. & Aparicio, J., 2005. *Application of Computer vision systems to the inspection of contact wire wear ,* Madrid: Urban Transport .

Borromeo, S., Aparicio, J. L. & Martinez, P. M., 2003. MEDES: Contact wire wear measuring system used by the Spanish National Railway (RENFEE). *Journal of Rail and Rapid Transit ,* 217(3), pp. 167-175.

Brahimi, M., Medjaher, K., Leouatni, M. & Zerhouni, N., 2017. *Prognostics and health Management for an Overhead Contact Line System.* France, s.n.

BritishTransportCommission, 1955. *Modernisation and Re-Equipment of British Railways,* London: The Curwen Press.

BritishTransportCommission, 1960. *Railway Electrification at Industrial Frequency.* London, British Transport Commission.

Bruno, O., Landi, A., Papi, M. & Sani, L., 2001. Phototube Sensor for monitoring the quality of current collection on overhead electrified railways. *Journal of Rail and Rapid Transit,* 215(3), pp. 231-241.

Bucca, G. & Collina, A., 2015. Electromechanical interaction between carbon-based pantograph strip and copper contact wire: A heuristic wear model. *Tribology International,* Volume 92, pp. 47-56.

Buksch, R., 1979. Contribution to Understanding the Vibration Behaviour of an Overhead Contact Line Equipment. *WiessenschaJtliche Berichte AEG-Telefunken,* Volume 5, pp. 250-262.

Chapel, M. N. & Bouwmans, T., 2020. *Moving Objects Detection with a Moving Camera,* La Rochelle: Elsevier.

Cheng, H., Jiang, X., Sun, Y. & Wang, J., 2001. Color image segmentation: advances and prospects. *Journal of the Pattern Recognition Society ,* 34(12), pp. 2259-2281.

Cho, J. C. & Park, Y., 2016. New Monitoring Technologies for Overhead Contact Line at 400 km/h. *ELSEVIER,* pp. 360-365.

Choras, R., 2007. Image Feature Extraction Techniques and Their Applications for CBIR and Biometrics System. *International Journal of Biology and Biomedical Engineering,* 1(1), pp. 6-15.

Chow, C. & Kaneko, T., 1972. Automatic Boundary Detection of the Left Ventricle from Cineangiograms. *Computers and Biomedical Research,* Volume 5, pp. 338-410.

Cho, Y. H. et al., 2010. Influence of Contact Wire Pre-Sag on the Dynamics of Pantograph-Railway Catenary. *International Journal of Mechanical Sciences ,* 52(11), pp. 1471-1490.

Collina, A. & Bruni, S., 2002. Numerical Simulation of Pantograph-Overhead Equipment Interaction. *Vehicle Mechanics and Mobility,* 38(4), pp. 261-291.

Cox, P., 2015. *Network Rail Weather Analysis Report ,* s.l.: NetworkRail.

Dahlberg, T., 2007 . Catenary, Pantograph and Their Interaction. *International Journal of Vehicle Mechanics and Mobility,* 44(8), pp. 591-593.

Das, P., Kole, K. D., Ghoshal, R. & Ghosh, R., 2012. Measurement of Displacement and Velocity of a Moving Object from Real Time Video. *International Journal of Computer Application ,* 49(13), pp. 12-16.

Dearman, P., 2019. *Overhead Line Equipment Inspection Maintenance and Renewal.* [Online]
Available at:
https://www.thepwi.org/technical_hub/presentations_for_tech_hub/190522_hds_understanding_asset_life/07_ohle_perspective_p_dearman
[Accessed 15 06 2020].

Desai, H. M. & Gandhi, V., 2014. Background Subtraction techniques. *Journal of Scientific & Engineering Research,* 5(12), pp. 1365-1367.

Duncan, S. & Arthington, M., 2018. *OLE Video Analyser.* Oxford: University of Oxford .

Dupuy, J., 1981. 389 km/h, Rails of the world. *Railway Gazette International ,* 137(6), pp. 495-497.

Efanov, D., 2016. Becoming and development prospects of concurrent error detection and monitoing systems of railway automation and remote control devices. *Automation on Transport ,* 2(1), pp. 124-148.

Efanov, D. et al., 2016. *Monitoring system of vibration impacts on the structure of overhead catenary of high-speed railway lines.* Yerevan, IEEE East-West Design & Test Symposium .

ELAND CABLES, 2018. *RAILWAY CONTACT WIRE.* [Online]
Available at: https://www.elandcables.com/cables/railway-contact-wire-107-120
[Accessed 27 01 2019].

Engquist, B. & Majda, A., 1977. Absorbing boundary conditions for numerical simulation of waves. *Applied Mathematical Sciences,* Volume 74, pp. 1765-1766.

EuropeanUnionAgencyforRailways, 2016. *Technical Specifications for Interoperability.* [Online]
Available at: https://www.era.europa.eu/activities/technical-specifications-interoperability_en
[Accessed 15 12 2018].

Evans, J., Johnson, T. & Clark, R., 1990. *Dewirement Dynamics ,* United Kingdom: British Rail Research .

Flore, S. & Tobben, F. J., 2015. *Study on Universal Overhead Contact Line Design ,* s.l.: ARCADIS NEDERLAND BV.

Forrest, P., Provost, M. & Lovell, J., 2010. *Diagnostic system and method for monitoring a rail system.* GB, Patent No. US2010/0204857 A1.

Freund, Y. & Schapire, R. E., 1999. A Short Introduction to Boosting. *Journal of Japanese Society for Artificial Intelligence .*

Fumi, A. & Forgione, A., 2001. *A New Complete System for catenary's Checking* , Rome: WCRR.

Galeotti, G. & Toni, P., 1997. Overhead contact line elasticity optimization for railway high speed running. *Journal of Computers and Structures*, 65(5), pp. 975-983.

Ghobadi, S. E., 2010. *Real Time Object Recognition and Tracking Using 2D/3D Images* , Siegen: s.n.

Ghobadi, S. E. et al., 2010. 2D/3D Image Data Analysis for Object Tracking and Classification. In: S. Ao, B. B. Rieger & M. Amouzegar, eds. *Advances in Machine Learning and Data Analysis.* s.l.:Springer , pp. 1-14.

Gonzalez, F. J., Chover, J. A., Suarez, B. & Vazquez, M., 2008. Dynamic analysis using finite elements to calculate the critical wear section of the conatct wire in suburban railway overhead conductor rails. *Journal of Rail and Rapid Transit ,* 222(2), pp. 145-157.

Guennouni, S., Ahaituof, A. & Mansouri, A., 2015. A Comparative Study of Multiple Object Detection Using Haar-Like Feature Selection and Local Binary Patterns in Several Platforms. *Modelling and Simulation in Engineering*, 2 December, pp. 1-8.

Harprecht, W., Seifert, R. & Kiessling, F., 2002. *Traction power supply at German Federal Railway's 400 km/h runs.* Philadelphia, IEEE.

Heyun, L., Xiaosong, G. & Wenbin, T., 2012. Icing and Anti-icing of Railway Contact Wires. In: D. X. Perpinya, ed. *Reliability and Safety in Railway.* Hunan,China : Intech, pp. 295-313.

Hoefler, H., Seib, M., Dambacher, M. & Jetter, V., 2001. *High Speed Overhead Wire Monitoring,* Cologne: WCRR'01.

Horn, B. K. & Schnuck, B. G., 1981. Determining Optical Flow. *Artificial Intelligence,* 17(1-3), pp. 185-203.

Kang, B. H., 2007. A Review on Image & Video Processing. *Multimedia and Ubiquitous Engineering,* 2(2), pp. 49-63.

Kaur, N. & Kaur, Y., 2014. Object Classification Techniques using Machine Learning Model. *Journal of Computer Trends and Technology,* 18(4), pp. 170-173.

Keenor, G., 2016. *Overhead Line Electrification for Railways,* s.l.: s.n.

Keen, P., 1998. *Using condition monitoring systems to improve the reliability of overhead electrified railway operations.* London, IEEE.

Kiessling, F., Pucshmann, R., Schmieder, A. & Schneider, E., 2002. Description of Systems. In: *Contact Lines for Electric Railways.* Paris: SIEMENS, pp. 123-135.

Kiessling, F., Pucshmann, R., Schmieder, A. & Schneider, E., 2009. Requirements and Specifications. In: *Contact Lines for Electric Railway* . Paris: SIEMENS, p. 94.

Kiessling, F., Puschmann, R., Schmieder, A. & Schneider, E., 2000. Rating overhead contact lines. In: B. a. M. Siemens Aktiengesellschaft, ed. *Contact Lines for Electric Railways.* Germany: Publicis Publishing , pp. 280-287.

Kiessling, F., Puschmann, R., Schmieder, A. & Schneider, E., 2009. Construction, management and maintenance . In: B. a. M. Siemens Aktiengesellschaft, ed. *Contact Lines for Electric Railways.* Germany: Publicis Publishing,Erlangen, pp. 875-951.

Kiessling, F., Puschmann, R., Schmieder, A. & Schneider, E., 2009. Interaction of Pantograph and Overhead Contact Line . In: second, ed. *Contact Lines for Electric Railways* . Paris: SIEMENS, pp. 597-599.

Kiessling, F., Puschmann, R., Schmieder, A. & Schneider, E., 2009. Interaction of the pantograph and overhead contact line . In: B. a. M. Siemens Aktiengesellschaft, ed. *Contact Lines for Electric Railways.* Germany : Publicis Publishing,Erlangen, pp. 563-656.

Kiessling, F., Puschmann, R., Schmieder, A. & Schneider, E., 2009. Project Design. In: B. a. M. Siemens Aktiengesellschaft, ed. *Contact Lines for Electric Railways.* Germany: Publicis Publishing, pp. 322-340.

Kiessling, F., Puschmann, R., Schmieder, A. & Schneider, E., 2009. Rating Overhead Contact Lines . In: *Contact Lines for Electric Railways.* Paris: SIEMENS, pp. 259-273.

Koyama, T. et al., 2014. Measurement of the Contact Force of the Pantograph by Image Processing Technology. *RTRI,* 55(2), pp. 73-78.

Kusumi, S., Fukutani, T. & Nezo, K., 2006. Diagnosis of Overhead Contact Line based on Contact Force. *J.Stage,* 47(1), pp. 39-45.

Lee, B., 2018. *Application of video data at East Ham depot* [Interview] (26 September 2018).

Lilien, J., 2013. *Power Line Aeolian Vibrations* , Liege, Belgium : University of liege Department of Electronics, Electricity and Computer Sciences .

Liu, W. et al., 2016. *Scene Background Estimation Based on Temporal Median Filter With Gaussian Filtering.* Cancun, IEEE.

Lucas, B. D. & Kanade, T., 1981. *An Iterative Image Registration Technique with an Application to Stereo Vision.* Pennsylvania, IJCAI.

Lykov, A., Efanov, D. & Vlasenko, S., 2012 . Technical diagnostics and monitoring of railway automation and remote control devices state. *Transport of the Russian Federation,* Issue 5, pp. 67-72.

Masset, J. et al., 2011. *Fatigue analysis of catenary contact wires for high speed trains.* France , the 9th World Congress on Railway Research .

MathWorks, 2018. *Train a Cascade Object Detector.* [Online]
Available at: https://uk.mathworks.com/help/vision/ug/train-a-cascade-object-detector.html
[Accessed 16 December 2018].

MathWorks, 2019. *Cascade Object Detector.* [Online]
Available at: https://uk.mathworks.com/help/vision/ref/vision.cascadeobjectdetector-system-object.html
[Accessed 17 02 2019].

MathWorks, 2020. *Hough transform.* [Online]
Available at: https://uk.mathworks.com/help/images/ref/hough.html
[Accessed 15 03 2020].

Michie, D., Spiegelhalter, D. & Taylor, C., 1994. *Machine Learning, Neural and Statistical Classification* , Cambridge: s.n.

Migliore, D. A., Matteucci, M. & Naccari, M., 2006. *A revaluation of frame difference in fast and robust motion detection.* California, VSSN '06 Proceedings of the 4th ACM international workshop on Video surveillance and sensor networks.

Moeller, H., Grebner, L. & Hofman, D., 2002. Pantograph diagnosis under operation by stationary uplift measurement. *Elektrische Bahnen,* 100(6), pp. 198-203.

Moghimi, M. M., Nayeri, M. & Pourahmadi, M., 2018. *Moving Vehicle Detection Using AdaBoost and Haar-Like Feature in Surveillance Videos,* Yazd: University of Yazd.

Moghimi, M. M., Nayeri, M. & Pourahmadi, M., 2019. *Moving Vehicle Detection Using AdaBoost and Haar-Like Feature in Surveillance Videos,* Yazd: University of Yazd.

NetworkRail, 2012. *Period Review 2013: Network Rail Consulation on Traction Electricity and Electrification Asset Usage Charges in CP5,* s.l.: s.n.

NetworkRail, 2015. *A Guide to Overhead Electrification,* London: Alan Baxter.

NetworkRail, 2017. *A Guide to Overhead Electrification,* London: Alan Baxer.

Ojala, T., Pietikainen, M. & Maenpaa, T., 2002. Multiresolution Gray Scale and Rotation Invariant Texture Classification with Local Binary Patterns. *IEEE Transactions on Pattern Analysis and Machine Intelligence* , 24(7), pp. 971-987.

Othman, Z., Haron, H. & Abdul Kadir, M. R., 2009. Comparison of Canny and Sobel Edge Detection in MRI Images. pp. 133-135.

Otsu, N., 1979. A Threshold Selection Method from Gray-Level Histograms. *IEEE Transactions on Systems, Man, And Cybernetics,* 9(1), pp. 62-66.

Pal, N. R. & Pal, S. K., 1993. A Review on Image Segmentation Techniques. *Pattern Recognition,* 26(9), pp. 1277-1294.

Papi, M. & Violi, A., 1997. *Pantograph–overhead line interaction: methods of measurement in experimentation on the line.* Florence,Italy, World Conference on Railway Research 97 .

Popa, G., Mihailescu, M. & Arsene, S., 2012. *Contact Line Oscillations Induced by the Pantograph Coupling.* Bucharest , IEEE.

Popescu, B. P., Cagnazzo, M. & Dufaux, F., 2016. *Motion Estimation Techniques,* s.l.: TELECOM ParisTech.

Pratt, W. K., 2007. *Digital Image Processing.* 4th ed. New Jersey: John Wiley & Sons, Inc.

Prewitt, M. S. & Mendelsohn, M. L., 1966. The Analysis of Cell Images. *Annals of the New York Academy of Sciences ,* 128(3), pp. 1035-1053.

Raju, D. R. & Neelima, G., 2012. Image Segmentation by Using Histogram Thresholding. *IJCSET*, 2(1), pp. 776-779.

Reiterer, A. & Olshausen, P., 2021. *Wire Wear Monitoring System WWS.* [Online] Available at: https://www.ipm.fraunhofer.de/en/bu/object-shape-detection/applications/railway-measurement/wire-wear-monitoring.html [Accessed 16 May 2021].

Ricardo-Rail, 2017. *Smart Monitoring - The PanMon pantograph monitoring system,* Belgium: Ricardo Rail.

Ritzberger, D., Talic, E. & Schirrer, A., 2015. *Efficient simulation of railway pantograph/catenary interaction uisng pantograph-fixed coordinates.* Austria, ELSEVIER.

Sachs, P., 1987. *Wind Forces in Engineeringg.* s.l.:Pergamon Pr.

Sa, M. D. & P, J., 2007. *Applied Statistic Using SPSS,STATISTICA, MATLAB and R.* 2nd ed. Berlin: Springer.

Savian, S., Elahi, M. & Tillo, T., 2020. Deep Biometrics. In: R. Jiang, et al. eds. *Optical Flow Estimation with Deep Learning, a Survey on Recent Advances.* Bolzano: Springer, Cham, pp. 1-26.

Sell, R. G., Prince, G. E. & Twine, D., 1964. An Experimental Study of the Ovehead Contact System for Electric Traction at 25kV. *Railway Overhead Contact Systems,* 179(25), pp. 765-777.

Sengar, S. S. & Mukhopadhyay, S., 2017. Foreground Detection via Backgorund Substraction and Improved Three-Frame Differencing. *Arabian Journal for Science and Engineering,* 42(8), pp. 3621-3633.

Shimada, T., Kohida, T. & Satoh, Y., 1997. Development of Solid Laser Measuring Apparatus of Contact Wire Wear. *Railway Technical Research Institute,* 38(1), pp. 19-24.

Shing, A. & Pascoschi, G., 2006. *Contact wire wear measurement and data management.* Hong Kong, IET International Conference on Railway Condition Monitoring.

Shing, A. W. C. & Wong, P. P. L., 2008. Wear of Pantograoh Collector Strips. *Journal of Rail and Rapid Transit,* 222(2), pp. 169-175.

Stickland, M., 2003. An investigation into the mechanical damping characteristics of catenary contact wires and their effect on aerodynamic galloping instability. *Rail and Rapid Transit,* Volume 2, pp. 63-71.

Stickland, M. & Scanlon, T. J., 2001. An investigation into the aerodynamic characteristics of catenary contact wires in a cross-wind. *Journal of Rail and Rapid Transit* , 215(4), pp. 311-318.

Stipanicev, D., 1994. *Introduction to Digital Image Processing and Analysis,* Zug, Switzerland: Chronolab Vision, Chronolab A.G. Zug Switzerland.

Takahashi, A., Kishi, T. & Yamamoto, H., 2014. *Overhead Contact Line Monitoring and Prediction of Contact Wire Localized Wear Points,* s.l.: Research and Development Center of JR East Group.

Taylor, G., 2013. *A bad wire day .Rail Engineer.* [Online]
Available at: https://www.railengineer.co.uk/2013/04/15/a-bad-wire-day/
[Accessed 16 11 2018].

Tharwat, A., Gaber, T., Ibrahim, A. & Hassanien, A. E., 2017. A Detailed Tutorial on Linear Discriminant Analysis. *AI Communications (SRGE),* pp. 1-22.

The, C. N. & Shashev, D., 2017. *Methods and Algorithms for Detecting Objects in Video Files.* Tomsk, EDP Sciences .

TheCommissionoftheEuropeanCommunities, 2002. The Trans-European High-Speed System Referred toin Article 6(1) of Directive 96/48/EC. *Official Journal of the European Communities*, pp. 22-27.

Thoresen, T., 2008. *System for measuring the uplift from all pantographs passing the installed system,* Oslo : Product information .

Tsunemoto, M., Shimizu, M., Saito, H. & Kajiyama, H., 2016 . Effect of Temperature Change and Contact-wire Wear on Current Collection Performance. 57(3), pp. 199-206.

Tsunemoto, M., Shimizu, M., Saito, H. & Kajiyama, H., 2016. *Effect of Temprature Change and Contact-wire Wear on Current Collection Performance,* Japan: Railway Technical Research Institute.

UK Climate Projections, 2009. *Climate Change Projections,* Exeter: UK Climate Projections.

Viola, P. & Jones, M., 2001. *Robust Real-time Object detection,* Vancouver: Second International Workshop on Statistical and Computational .

Viola, P. & Jones, M., 2001. Robust Real-time Object Detection. *Second International Workshop on Statistical and Computational theories of Vision-Modeling, Learning, Computing and Sampling ,* 13 July , pp. 1-24.

Wada, S., Ito, K. & Hayasaka, T., 2019 . *Current Estimation Method at the Time of a Contact-Wire Breakage During Standstill Below Insulated Overlap Based on Contact-Wire Necking Lenght ,* Japan : WIT Press.

Watanabe, S. & CYBEST, 1974. An Automated Apparatus for Cancer Prescreening. *Computer Graphics and Image Processing,* Volume 3, pp. 350-358.

Weszka, J., Nagel, R. & Rosenfeld, A., 1974. A Threshold Selection Technique. *IEEE Transactions on Computers ,* 23(12), pp. 1322-1326.

White, P. F., Gerig, K. & King, J. B., 2017. *Insulated Overlaps and Sectionners For Overhead Contact Systems.* s.l., AREMA 2017 ANNUAL CONFERENCE.

Woo Kim, J. et al., 2007. State sensitivity analysis of the pantograph system for a high-speed rail vehicle considering span length and static uplift force. *Journal of sound and vibration-ELSEVIER*, pp. 405-427.

Wordsworth, N., 2018. *Monitoring overhead lines.* [Online]
Available at: https://www.railengineer.co.uk/2018/12/14/monitoring-overhead-lines/
[Accessed 14 01 2019].

Wu, G. et al., 2016. Evolution of the electrical contact of dynamic pantograph–catenary system. *Journal of Modern Transportation* , pp. 132-138.

Young, P., Ki-Won, L., Shin-Young, P. & Choi, W. S., 2015. Implementation of Multi-functional Type Condition Monitoring System for Raiway Catenary Systems. *The Korean Institute of Electrical Engineers* , 64(9), pp. 1406-1410.

Appendix A

A.1 Long Marston Measurements

L1	30N	60N	90N	120N
T1	**1.3890**	1.3970	1.4120	1.4250
T2	**1.3850**	1.3960	1.4090	1.4210
T3	**1.3850**	1.3960	1.4090	1.4210
T4	1.3910	1.3960	1.4080	1.4260
T5	1.3850	1.3960	1.4060	1.4170

L2	30N	60N	90N	120N
T1	**1.4950**	1.4760	1.4820	1.4890
T2	**1.4840**	1.4810	1.4880	1.4940
T3	**1.4690**	1.4740	1.4830	1.4920
T4	1.4680	1.4720	1.4800	1.4880
T5	1.4680	1.4750	1.4840	1.4900

L3	30N	60N	90N	120N
T1	**1.3790**	1.3960	1.4160	1.4430
T2	**1.3789**	1.3930	1.4180	1.4410
T3	**1.3789**	1.3950	1.4140	1.4370
T4	1.3800	1.3920	1.4140	1.4370
T5	1.3790	1.3970	1.4190	1.4380

L4	30N	60N	90N	120N
T1	**1.3740**	1.3870	1.4070	1.4370
T2	**1.3770**	1.3920	1.4140	1.4310
T3	**1.3750**	1.3930	1.4110	1.4330
T4	1.3780	1.3890	1.4130	1.4310
T5	1.3780	1.3910	1.4110	1.4330

L5	30N	60N	90N	120N
T1	**1.3630**	1.3750	1.3940	1.4110
T2	**1.3600**	1.3750	1.3910	1.4110
T3	**1.3620**	1.3750	1.3940	1.4130
T4	1.3620	1.3770	1.3930	1.4110
T5	1.3630	1.3740	1.3910	1.4110

L6	30N	60N	90N	120N
T1	**1.3870**	1.4020	1.4120	1.4270
T2	**1.3970**	1.4000	1.4140	1.4250
T3	**1.3910**	1.4090	1.4150	1.4250
T4	1.3870	1.4000	1.4130	1.4240
T5	1.3890	1.4020	1.4110	1.4230

L7	30N	60N	90N	120N
T1	**1.3790**	1.3910	1.4100	1.4280
T2	**1.3830**	1.4000	1.4180	1.4370
T3	**1.3830**	1.3950	1.4100	1.4280
T4	1.3820	1.3940	1.4060	1.4260
T5	1.3820	1.3960	1.4120	1.4240

Recorded uplift by the apparatus

Force (N)	First Registration Arm					Data Statistic	
	Test1	Test2	Test3	Test4	Test5	Median	Sd
30	9.00	8.00	4.00	8.00	7.00	8	1.92
60	17.00	19.00	15.00	13.00	18.00	17.50	2.41
90	32.00	32.00	28.00	25.00	28.00	30.00	3.00
120	45.00	44.00	40.00	43.00	39.00	43.50	2.59
First Dropper							
30	44.00	9.00	9.00	8.00	5.00	9.00	16.29
60	25.00	6.00	14.00	12.00	12.00	13.00	6.49
90	31.00	13.00	23.00	20.00	21.00	22.00	6.47
120	38.00	19.00	32.00	28.00	27.00	30.00	6.98
Second Dropper							
30	11.00	7.00	9.00	4.00	10.00	9.50	2.77
60	28.00	22.00	26.00	16.00	28.00	27.00	5.10
90	48.00	47.00	45.00	38.00	50.00	47.50	4.62
120	75.00	70.00	68.00	61.00	69.00	69.50	5.03
Third Dropper							
30	3.00	4.00	2.00	7.00	8.00	5.50	2.59
60	16.00	19.00	20.00	18.00	21.00	19.50	1.92
90	36.00	41.00	38.00	42.00	41.00	41.00	2.51
120	66.00	58.00	60.00	60.00	63.00	61.50	3.31
Fourth Dropper							
30	7.00	7.00	6.00	5.00	8.00	7.00	1.14
60	19.00	22.00	19.00	20.00	19.00	19.50	1.30
90	38.00	38.00	38.00	36.00	36.00	38.00	1.10
120	55.00	58.00	57.00	54.00	56.00	56.50	1.58
Fifth Dropper							
30	13.00	7.00	6.00	8.00	7.00	7.50	2.77
60	28.00	10.00	24.00	21.00	20.00	22.50	6.69
90	38.00	24.00	30.00	34.00	29.00	32.00	5.29
120	53.00	35.00	40.00	45.00	41.00	43.00	6.27
Second Registration Arm							
30	9.00	2.00	7.00	8.00	4.00	7.50	2.92
60	21.00	19.00	19.00	20.00	18.00	19.50	1.14
90	40.00	37.00	34.00	32.00	34.00	35.50	3.13
120	58.00	56.00	52.00	52.00	46.00	54.00	4.60

Change in Displacement between the Lifts

1st Registration Arm

Δ Lift (mm)	Change in Displacement (mm)				
30-60	8	11	11	5	11
60-90	15	13	13	12	10
90-120	13	12	12	18	11

1st Dropper

Δ Lift (mm)	Change in Displacement (mm)				
30-60	-19	-3	5	4	7
60-90	9	7	9	8	9
90-120	7	6	9	8	6

2nd Dropper

Δ Lift (mm)	Change in Displacement (mm)				
30-60	17	15	17	12	18
60-90	20	25	19	22	22
90-120	27	23	23	23	19

3rd Dropper

Δ Lift (mm)	Change in Displacement (mm)				
30-60	13	15	18	11	13
60-90	20	22	18	24	20
90-120	30	17	22	18	22

4th Dropper

Δ Lift (mm)	Change in Displacement (mm)				
30-60	12	15	13	15	11
60-90	19	16	19	16	17
90-120	17	20	19	18	20

5th Dropper

Δ Lift (mm)	Change in Displacement (mm)				
30-60	15	3	18	13	13
60-90	10	14	6	13	9
90-120	15	11	10	11	12

2nd Registration Arm

Δ Lift (mm)	Change in Displacement (mm)				
30-60	12	17	12	12	14
60-90	19	18	15	12	16
90-120	18	19	18	20	12

Measured Stiffness

Location	Force(N)	Test 1 (N/m)	Test 2 (N/m)	Test 3 (N/m)	Test 4 (N/m)	Test 5 (N/m)
1st Registration Arm	30	3333.33	3750	7500	3750	4285.71
	60	3529.41	3157.89	4000	4615.38	3333.33
	90	2812.5	2812.5	3214.28	3600	3214.28
	120	2666.66	2727.27	3000	2790.69	3076.92
1st Dropper	30	681.81	3333.33	3333.33	3750	6000
	60	2400	10000	4285.71	5000	5000
	90	2903.22	6923	3913.04	4500	4285.71
	120	3157.89	6315.78	3750	4285.71	4444.4
2nd Dropper	30	2727.27	4285.71	3333.33	7500	3000
	60	2142.85	2727.27	2307.69	3750	2142.85
	90	1875	1914.9	2000	2368.42	1800
	120	1600	1714.28	1764.7	1967.21	1739.13
3rd Dropper	30	10000	7500	15000	4285.71	3750
	60	3750	3157.89	3000	3333.33	2857.14
	90	2500	2195.12	2368.42	2142.85	2195.12
	120	1818.18	2068.96	2000	2000	1904.76
4th Dropper	30	4285.71	4285.71	5000	6000	3750
	60	3157.89	2727.27	3157.89	3000	3157.89
	90	2368.42	2368.42	2368.42	2500	2500
	120	2181.81	2068.96	2105.26	2222.22	2142.85
5th Dropper	30	2307.69	4285.71	5000	3750	4285.71
	60	2142.85	6000	2500	2857.14	3000
	90	2368.42	3750	3000	2647.05	3103.44
	120	2264.15	3428.57	3000	2666.66	2926.82
2nd Registration Arm	30	3333.33	15000	4285.71	3750	7500
	60	2857.14	3157.89	3157.89	3000	3333.33
	90	2250	2432.42	2647.05	2812.5	2647.05
	120	2068.96	2142.85	2307.69	2307.69	2608.69

Computed uplift and stiffness through analysis of the recorded videos

First Registration Arm			
30N	**60N**	**90N**	**120N**
5	16.5	28.5	43
First Dropper			
2	10.5	18	26.9
Second Dropper			
9	25.2	51.8	80
11	24.8	46.2	69
8.5	26.2	50.3	74.6
Third Dropper			
10	25.9	54	80
10	24.5	47.5	73
8.5	24.5	46	76
Fourth Dropper			
9	22.8	44.7	62.1
Fifth Dropper			
4	12.5	25.5	36.7
7	16	29.3	42.1
Second Registration Arm			
8.5	20.8	32.5	46.4
7.5	16.1	29.9	44

First Registration Arm			
Stiff 30 N/m	**Stiff 60N/m**	**Stiff 90N/m**	**Stiff 120N/m**
6000	3636.36	3157.89	2790.69
First Dropper			
15000	5714.28	5000	4460.96
Second Dropper			
3333.33	2380.95	1737.45	1500
2727.27	2419.35	1948.05	1739.13
3529.41	2290.07	1789.26	1608.57
Third Dropper			
3000	2316.60	1666.66	1500
3000	2448.97	1894.73	1643.83
3529.41	2448.97	1956.52	1578.94
Fourth Dropper			
3333.33	2083.33	2013.42	1932.36
Fifth Dropper			
7500	4800	3529.41	3269.75
4285.71	3750	2047.78	2850.35
Second Registration Arm			
3529.41	2884.61	2769.23	2586.20
400	3726.70	3010.03	2727.27

Appendix B

Detection results at/near the structures



